INFORMATION TO USERS

This manuscript has been reproduced from the microfilm master. UMI films the text directly from the original or copy submitted. Thus, some thesis and dissertation copies are in typewriter face, while others may be from any type of computer printer.

The quality of this reproduction is dependent upon the quality of the copy submitted. Broken or indistinct print, colored or poor quality illustrations and photographs, print bleedthrough, substandard margins, and improper alignment can adversely affect reproduction.

In the unlikely event that the author did not send UMI a complete manuscript and there are missing pages, these will be noted. Also, if unauthorized copyright material had to be removed, a note will indicate the deletion.

Oversize materials (e.g., maps, drawings, charts) are reproduced by sectioning the original, beginning at the upper left-hand corner and continuing from left to right in equal sections with small overlaps. Each original is also photographed in one exposure and is included in reduced form at the back of the book.

Photographs included in the original manuscript have been reproduced xerographically in this copy. Higher quality 6" x 9" black and white photographic prints are available for any photographs or illustrations appearing in this copy for an additional charge. Contact UMI directly to order.

UMI

A Bell & Howell Information Company
300 North Zeeb Road, Ann Arbor MI 48106-1346 USA
313/761-4700   800/521-0600

STUDY OF ELECTRICAL DEGRADATION OF II-VI ZnSe-BASED SINGLE QUANTUM-WELL LIGHT-EMITTING DEVICES

BY

JONG RYUL KIM

A DISSERTATION PRESENTED TO THE GRADUATE SCHOOL
OF THE UNIVERSITY OF FLORIDA IN PARTIAL FULFILLMENT OF
THE REQUIREMENTS FOR THE DEGREE OF
DOCTOR OF PHILOSOPHY

UNIVERSITY OF FLORIDA

1996

UMI Number: 9703556

To my parents in heaven

ACKNOWLEDGMENTS

I would like to express my sincere appreciation to my advisor, Dr. Kevin S. Jones, for his guidance, support, and encouragement. Thanks are also due to my doctoral committee members, Dr. Paul H. Holloway, Dr. Robert M. Park, Dr. Rajiv K. Singh and Dr. Timothy J. Anderson, for their assistance and interest in my work.

This work would not have been possible without the samples provided by 3M company. I am grateful to Dr. Greg M. Haugen for his support of my work.

I would also like to thank Dr. Peter Zory for helping to fabricate LEDs and providing the electroluminescence microscopy and degradation experiment set-up. His advice and discussion during the experiments have been a major contribution in this work.

Thanks are due to Dr. Maggie Puga-Lambers for providing SIMS analysis and Dr. Matthias H. Ludwig for collecting low temperature photoluminescence data.

I am indebted to my friends and coworkers for their encouragement and friendship throughout my stay in Gainesville. My special appreciation goes to Dr. Viswanath Krishnarmoorthy for his advice and discussion in writing this dissertation.

iii

Finally, I thank my wife and two daughters, Sahrang and Harah, for their support.

TABLE OF CONTENTS

Abstract of Dissertation Presented to the Graduate School
of the University of Florida in Partial Fulfillment of the
Requirements for the Degree of Doctor of Philosophy

STUDY OF ELECTRICAL DEGRADATION OF II-VI ZnSe-BASED
SINGLE QUANTUM-WELL LIGHT-EMITTING DEVICES

By

Jong Ryul Kim

May, 1996

Chairperson: Dr. Kevin S. Jones
Major Department: Materials Science and Engineering

II-VI ZnSe-based light-emitting devices(LED) were fabricated from
various structures consisting of $Zn_{0.8}Cd_{0.2}Se$ single quantum wells on GaAs
substrates. LEDs were degraded by applying a pulsed direct-current. The
degradation rate was founded to depend on the current density and the pre-
existing defect density. The temperature of the quantum well (QW) during
operation was estimated to be about 250 °C.

Efficiency measurement on the LEDs showed that the nonradiative
recombination rate increased with increasing degradation. The thermal
expansion behavior of the lattice matched epilayers was investigated using
HRXRD with an in-situ heating stage. At 250 °C the epilayers expanded
in the perpendicular direction and the strain in the quantum well increased
by 15%. In the 50%-degraded LEDs, the strain remained constant,
however, after 80% degradation 1/3 of the strain in the QW was relaxed.

SIMS and PL studies did not show any measurable atomic interdiffusion of the QW during operation.

LEDs were degraded by the generation of dark spot defects(DSD) and dark line defects(DLD) that appear in the active region. DLDs were observed to be aligned in <100> directions. The light output intensity decreased with increasing DSDs and DLDs density. TEM analyses on the 80%- degraded LEDs showed that two major types of degradation-induced extended defects formed during operation. One type appeared to be rows of clusters of point defects and the others were distorted crystalline regions that correspond areas of dense networks of dislocations. The spacing of the defects (5 μm) was the same as the DLDs observed in EL microscopy. Some DLDs appeared to nucleate from the grown-in stacking faults.

In order to study the possible source of these defects, point defect formation during operation was studied. Generation of point defects were observed in the degraded LEDs by measuring PL quenching rate at higher temperatures and diffusion enhancement of Cd from the QW into the barrier layers upon post degradation annealing. Nonradiative recombination-induced point-defect generation at pre-existing defect sites and subsequent nucleation of extended defects is proposed as the major degradation mechanism in ZnSe-based II-VI LEDs.

ix

CHAPTER 1
INTRODUCTION

1.1 Motivation and Objectives

The development of compact short-wavelength light emitters (lasers and LEDs) is certain to have enormous effects on any technology using visible light. For example, bits of information are read and recorded by semiconductor lasers whose output is a focused, diffraction-limited spot in most of today's optical recording systems. Because the spacing of the dots that can be read is directly proportional to the wavelength of light used, a significant gain can be obtained in recording density as well as in data transfer rates simply by using lasers that operate at shorter wavelengths. The ZnSe based II-VI compound semiconductors have been considered a good candidate for producing such short-wavelength lights due to their direct, wide bandgap.

The first ZnSe-based diode lasers operating at liquid nitrogen temperature were reported in 1991 after successful p-type doping of ZnSe [1]. In 1993 the first demonstration of the blue-green laser diode at room temperature was presented and the turn-on voltage of the laser was around 20 V. Since then, two important breakthroughs were made, the realization

1

of lattice-matched separate-confinement heterostructure (SCH) and ohmic contacts to p-type ZnSe. The lattice mismatching between heterostructure layers and the GaAs substrate produced a poor crystal quality. Using the quaternary alloy ZnMgSSe, a Sony group successfully employed the SCH configuration in a pseudomorphic embodiment on the GaAs substrate [2]. Figure 1.1 shows the band gap and the lattice constant of II-VI compounds used in this SCH configuration.

Another problem was heat generation due to the voltage drop at the interface between metal contact and p-type ZnSe. The use of Zn(Se,Te)-graded contacts proved to be a promising ohmic contact. The ZnSe/ZnTe multiquantum well scheme was then realized to be another ohmic contact. By using these new contacts the threshold voltage decreased to around 4V range after employing new contacts [3].

Today there are at least two major obstacles remaining: (1) the poor p-type doping in ZnMgSSe and (2) the low lifetime of the lasers or light-emitting diodes (LED). The nitrogen doped ZnMgSSe layer has an increased acceptor activation energy and hence the resulting reduced free hole concentration limits the vertical current transport. The degradation of II-VI blue light emitters is now drawing much attention. The most recent report from SONY showed that a laser device lasted as long as 9 hour at room temperature under CW operation [4]. It was a significant leap from the lifetime of a few seconds reported in 1993 from Brown/Purdue [5]. The current emphasis of research in most laboratories is directed at improving

the crystalline quality of the structures with a view to increasing the device lifetime by reducing growth-related defects.

In order to increase lifetime of II-VI ZnSe-based light-emitting devices, a better understanding of the rapid degradation mechanism is necessary. Through investigation of the devices failure, we may be able to eliminate degradation mechanisms during operation of devices.

1.2 Scope of the Present Work

In an effort to understand the reasons why the lifetime of II-VI ZnSe-based optoelectronic devices is so short, degradation mechanism of light emitting devices were investigated. The degradation of lasers and LEDs were found to be similar in terms of the degradation defects generated during operation. Both lasers and LEDs fail due to the production of dark spots and dark line defects inside the device. In this study LEDs were exclusively used because the dimension of the device can be modified so that the characterization of degraded devices can be carried out in a more convenient way.

In chapter 1 the previous study on the degradation of II-VI devices is first reviewed. Since the blue-green light emitting devices were first made in 1991, there have been only a few studies of degradation reported. Therefore the degradation mechanisms of III-V devices are also summarized. The basic mechanism of light emission from the single quantum-well LED is also described. Chapter 2 provides the device

structures used in this work, LED fabrication, experimental setups for LED degradation and characterization methods used to study degradation process. In chapter 3 the degradation trends are presented. The general trends of the light output intensity as a function of time, degradation dependence on the pre-existing defect density, degradation dependence on the current density, efficiency change due to nonradiative recombination, I-V characteristics before and after degradation, and the estimation of temperature of the active region during operation are detailed. Chapter 4 discusses investigation of the strain relaxation and possible atomic interdiffusion during operation. In chapter 5 the structural investigations of the as-grown structure and degraded devices using transmission electron microscope (TEM) is presented. The nature of pre-existing defects and degradation-induced defects are described. Based on the degradation phenomena found in this work, Chapter 6 discusses a possible degradation mechanism by which II-VI ZnSe-based light-emitting devices fail. Finally the conclusions of this study are given in chapter 7.

1.3 Literature review on the study of degradation of lasers and LEDs

1.3.1 II-VI degradation

One of the major issues in II-VI semiconductor-based blue or blue-green lasers and LEDs has been the device degradation and lifetimes since the first demonstration of II-VI laser diodes. Although considerable efforts

have been made to obtain high quality semiconductor heterostructures for devices, there has been little work on addressing the issue of degradation of such devices. The following is a summary of studies on the II-VI device degradation.

Guha et al. [6] first published a detailed study of the degradation of II-VI blue-green light emitters. They examined structural defects in electrically degraded devices that consist of ZnCdSe quantum-well and ZnSSe barrier layers. The [100] dark line defects were observed using a optical microscope to study the electroluminescent output. Degradation defects appeared to occur initially by the formation of new crystal defects in the vicinity of pre-existing defects such as stacking faults as investigated using TEM. These new crystal defects then propagate along [100] directions and their evolution finally results in the formation of regions of nonradiative material spread out across the device and lying in the quantum well.

Hua et al. [7] did a structural investigation on the ZnCdSe /ZnSSe/ZnMgSSe pseudomorphic SCH structure carried out by TEM after electrical degradation. They observed triangular nonluminescence dark defects in EL microscopy and those defects were identified to be patches of dislocation networks developed at the quantum-well region. The dislocation networks were observed to be nucleated at threading dislocations originating from pairs of V-shaped stacking faults which are nucleated at or near the II-VI/GaAs interface.

Haugen et al. [8] examined structural defects in the photodegraded devices. The structure used in this study was a lattice-matched ZnSSe or ZnMgSSe barrier layer with a ZnCdSe quantum-well. The cladding layers were only Cl doped (n-type). They observed [100] dark line defects (DLD) in photoluminescence microscopy, which appear to be the same as those observed in the electrically degraded devices. The DLDs appeared to originate from pre-existing defects and it was concluded that nitrogen would not play a role in the degradation process.

Recently Tomiya et al. [9] carried out structural studies on the lattice-matched ZnCdSe/ZnSSe/ZnMgSSe structure grown by MBE. LEDs were degraded by current injection and [110] dark line defects and dark spot defects were observed in electroluminescence microscopy. During the test the [110] dark line defects did not change, however the dark spot defects were spread out in the [100] direction during current injection. These regions consisted of a high density of dislocation dipoles and dislocation loops in TEM observation. The source of the highly dislocated regions appeared to be the pre-existing stacking faults.

Some important points can be drawn from the previous studies. First, the degradation defects seem to originate from pre-existing structural defects. The major type of pre-existing defect is the stacking fault; these are usually developed in pairs at the interface between the GaAs substrate and the epilayer. Secondly, the degradation defects appear to grow during current injection in the vicinity of the quantum-well active region. Thirdly,

the degradation defects may be identified as dislocation-like defects and lie in the quantum well. Finally lasers and LEDs fail due to the same type of degradation defects, that is, mainly dark line defects.

Previous studies blame the pre-existing defects, which are developed during the growth process, for the source of the degradation defects. However, the relationship between the pre-existing defects and the degradation induced defects are not apparent yet. Previous studies have not determined the microstructural nature of the major degradation defects, or [100] dark line defects, which can be seen in electroluminescence microscopy. The nature of [100] dark line defects is not understood well and is still controversial as to whether they are dislocations or not. In addition, no studies about the effect of strain in the quantum-well on the rapid degradation have been conducted. The rapid degradation process may be related to the strain in the quantum-well since the quantum well layer is highly strained due to its composition.

1.3.2   III-V degradation mechanisms

1.3.2.1 Rapid Degradation

A large number of of studies on the degradation of III-V semiconductor-based lasers and LEDs have been done since 1970, when the first AlGaAs/GaAs double-heterostructure laser was achieved [10]. Reliability of many kinds of semiconductor lasers and LEDs has been drastically improving for about 20 years. Throughout this period, various

degradation mechanisms have been discovered and reliability improvements have been made. Here, major degradation mechanisms of III-V based devices and the method of suppression of those degradation mechanisms, which are related to the II-VI based devices, are summarized. The degraded regions of a device may be the facets, electrodes, bonding parts, heat sink and active region. Only the degradation mode of the inner active region due to dark line defect development and the facet melting of lasers will be surveyed.

DeLoach et al. [11] found that the rapid degradation in the AlGaAs/GaAs lasers was related to the [100] dark line defect (DLD) in the electroluminescence topography for the first time. Petroff and Hartman [12] observed the [100] dark line defect with transmission electron micrographs and concluded that [100] DLD is caused by the dislocation network. Many studies [13][14] by TEM indicate that a DLD in this material is formed of a network of interstitial-type helical dislocation dipoles usually originating from a single dislocation crossing the active layer.

The DLD growth mechanism is believed to be recombination-enhanced dislocation climb [15][16]. Dislocation climb is a process by which a dislocation increases its length by absorption or emission of point defects. The energy gained from non-radiative recombination and light absorption near the dislocation core and an existing point defect is transformed into lattice vibrations and give rise to the low-temperature defect motion [17]. As opposed to dislocation glide, dislocation climb does

not confine the dislocation line motion to its glide plane. So, DLDs can elongate in the [100] direction with this climbing motion by the observation from the direction perpendicular to active layer (100) plane. Petroff and Kimerling [18] suggested that the climb resulted from the absorption of interstitial point defects. O'Hara et al. proposed that the climb resulted from the emission of vacancy pairs at the dislocation [19].

On the other hand, [100] DLD growth is not as prevalent in InGaAsP/InP LEDs and lasers [20] and this system is sensitive to the existence of crystal defects [21]. InGaAsP/InP LEDs and lasers have been put on the market early without serious problems.

In addition to the [100] DLD, the [110] DLD is also a cause of rapid degradation in III-V based devices. This type of degradation scarcely requires the existence of dislocations and point defects in the active region and are generated in both AlGaAs/GaAs and InGaAsP/InP devices [22][23]. The cause of [110] DLD is the glide motion of a dislocation from the surface of the device. The [110] DLD glide is believed to be enhanced by non-radiative recombination. Recombination enhanced dislocation glide is characterized by the generation of a 60° dislocation along the [110] directions from a dislocation source. The gliding motions occur when the AlGaAs/GaAs LEDs and lasers are operated under a residual stress. The mechanical stress can originate from several sources including bonding region between the device chip and electrode, heat sink, or from the

dielectric film inserted between the electrode and cap layer to restrict the current injection area.

When rapid degradation is observed in InGaAsP/InP devices, the source appears to be the generation of dark spot defects (DSD) in the active region. Yamakoshi et al. [24] have reported that DSD included precipitation-like defects related to host atoms such as In. Ueda et al. [25] used TEM to study DSDs and they found bar-shaped precipitates lying in the [100] and [110] directions. The defect regions were In rich compared with the crystal matrix. The primary causes of those DSDs are identified with the precipitation of host atoms and the migration of electrode metal such as Au [26]. DSD generation due to Au migration has been also reported by Chin et al. [27] and this is a main cause of gradual degradation in InGaAsP/InP devices.

Another degradation area besides the inner active region is the mirror facet of a laser. In an atmosphere, oxide film grows as a result of oxidation reaction-enhanced by emitted light. When the temperature rise at the facet exceeds the melting point of the laser crystal, catastrophic damage occurs and the light output power suddenly decreases. The damage is called catastrophic optical damage (COD). Henry et al. [28] indicated that the absorption coefficient increases rapidly, and calculated that the temperature rise to around 1500 K (the melting point of GaAs) can be reached within about 100 nsec in a typical AlGaAs/GaAs DH structure having a light output power of 5 MW/cm^2. The sudden melting of the light-

emitting part at the facet is believed to occur because of heating through the nonradiative recombination process.

1.3.2.2 Suppression of Rapid Degradation

The [100] DLD growth, which is a main problem in AlGaAs/GaAs devices, can be suppressed by eliminating dislocation sources. The elimination of the sources is performed by employing a clean GaAs substrate having a dislocation density less than $10^3/cm^2$. In addition, the epitaxial growth of the DH structure should be performed in a clean vacuum and pure material should be used in order to reduce the introduction of impurities. Addition of small amount of Al or Mg to the active layer is an effective means of improving the quality because the added Al or Mg getters oxygen and Al releases thermal stress in the double-heterostructure layer and improves the stoichiometry [29]. Thus, the crystal growth process is used for suppression/elimination of [100] DLD.

In contrast, the suppression and elimination of [110] DLD's is principally the result of improvement in the fabrication process after crystal growth. A reduction of mechanical stress is necessary for suppression of [110] DLD.

Recently InGaAs/GaAs strained quantum-well lasers have been reported [30][31]. The primary issue of reliability in the InGaAs/GaAs strained QW laser is the existence of strain in the active region which is usually on the order of 1 to 3×10^{10} dyne/cm^2. This strain can usually cause [110] dislocations in normal AlGaAs/GaAs lasers. Such strain is

introduced by a lattice mismatch of about 1.5 %. In spite of the strain, the inner region of the In based lasers is quite stable and dark defects such as DSD and DLD are rarely observed during operation. The degradation in this InGaAs/GaAs strained QW structure seems to be only slightly influenced by the defect and growth related dislocations. This high reliability may be attributed to both lattice hardening and strain accommodation [32].

Several suppression and elimination methods for facet oxidation and COD have been developed and applied to actual devices, including a reduction of light absorption and separation of a facet from the atmosphere. Yonezu et al. succeeded in the elimination of facet oxidation and COD by reducing the light absorption at the facet [33]. The reduction was achieved by diffusing Zn into the active region except in the vicinity of the facet. Zn diffusion lowers the band gap energy. Thus the current injected into only the Zn-diffused region, the energy of the emitted light can be set to be smaller than the bandgap energy in the vicinity of the facet, In this situation, the absorption of emitted light at the facet is greatly decreased. For the separation of the facet from the atmosphere, a facet coated with dielectric film is generally used.

1.3.2.3 Gradual degradation

A characteristic of the gradual degradation is a uniform and featureless darkening of the active region accompanied by an increase in deep level defect concentration. Although DLDs or DSDs are not formed,

it is believed that nonradiative recombination takes place at existing defects and results in the generation of new defects. Both the defect density and the nonradiative recombination rate increase with time and lead to a reduced efficiency. Point defects generated in this long process can migrate and coalesce into defect clusters and microloops. This kind of gradual degradation most likely comes from intrinsic material properties and can be reduced by using a better crystalline quality materials [34][35][36].

1.4 General Background : Electrical Pumping

When a single quantum-well device is under forward bias as shown in Figure 1.2, the electrons and holes are injected into the quantum well. Most of the electrons and holes are confined in the well and a high concentration of electrons and holes is achieved, the electron-hole recombination process then takes place mainly in the quantum-well region and photons are produced due to this electron-hole recombination. There are two major recombination processes, radiative and non-radiative recombination. The physical phenomena related to radiative electron-hole recombination are spontaneous emission, stimulated emission, and absorption. These phenomena are closely related to each other and the relative importance of them depends on the device [37]. Another type of electron-hole recombination, non-radiative recombination, also occurs. The energy produced by nonradiative recombination does not create photons,

but is released by lattice vibrations (phonons). This phonon formation enhances the rate of the degradation of the devices. Thus the nonradiative recombination process plays an important role in the device degradation. For the LEDs, only spontaneous emission and non-radiative recombination are considered, because stimulated emission is not involved in the LED mode and the absorption would be remain almost constant during whole operation of the device.

Spontaneous emission. Electrons pumped into the conduction band recombine with holes in the valence. In this process, an energy corresponding to the gap between the electron state and hole state is emitted as photons. This phenomenon is spontaneous emission. The transition between the conduction band and valence band does not take place randomly in the quantum well. Transitions can take place only between the allowed energy states by Fermi's golden rule [38]. The energy state in the quantum well is quantized and there is only one energy state available in each conduction band and valence band in the quantum well for the structures used in this study. As shown in Figure 1.3, there exists the ground state of electrons in the conduction band and the ground state of heavy holes in the valence band. Because the band offset in both conduction band and valence band is relatively shallow, there is only one transition possible in spontaneous emission. In other words theoretically only one wavelength of the photons is generated from our devices.

Non-radiative recombination.   Non-radiative recombination occurs mainly as a result of crystalline defects, impurities and the Auger effect. This nonoradiative recombination is directly related to device degradation. The energy emitted through recombination enhances the degradation rate. Crystalline defects can include dislocations, stacking faults, point defects such as interstitial atoms and vacancies, their complexes, etc.   Many possible routes exist for nonradiative recombination through those defects. First, defects change the tight binding state between the electron and atom, and they give rise to the continuum of state joining the conduction band to the valence band. Through the continuum of state, electrons and holes recombine nonradiatively. Secondly, impurities existing as interstitial atoms or substitutional atoms produce deep levels in the forbidden band gap. Electrons and holes within a diffusion length of the carrier from the position of the defect are trapped and can radiatively or nonradiatively recombine. For the nonradiative process, heat can be generated by multiphoton generation [39] and as a result new defects can be also created [40]. This mechanism of nonradiative recombination induces reactions which will be explored in a later chapter.   Thirdly, the surface of a semiconductor can be a significant source of defects because many dangling bonds are generated and impurities from ambient exist at the surface. These defects and impurities may also introduce a continuum of state to the surface [41]. There is also the Auger recombination which is a nonradiative recombination process not related to defects. The energy released by

electron-hole recombination is transferred to another electron or hole during the Auger recombination process. This Auger process appears under high injection conditions and it becomes the more rapid and dominant nonradiative process in narrow band-gap semiconductors [42]. Among all of the above nonradiative recombinations, nonradiative recombination through defect sites by releasing energy as a form of multiphonon is considered to be most closely related to the degradation of LEDs and lasers. Nonradiative recombination-induced heating and related phenomena have been reviewed by Yassievich [43] and Abakumov et al. [44].

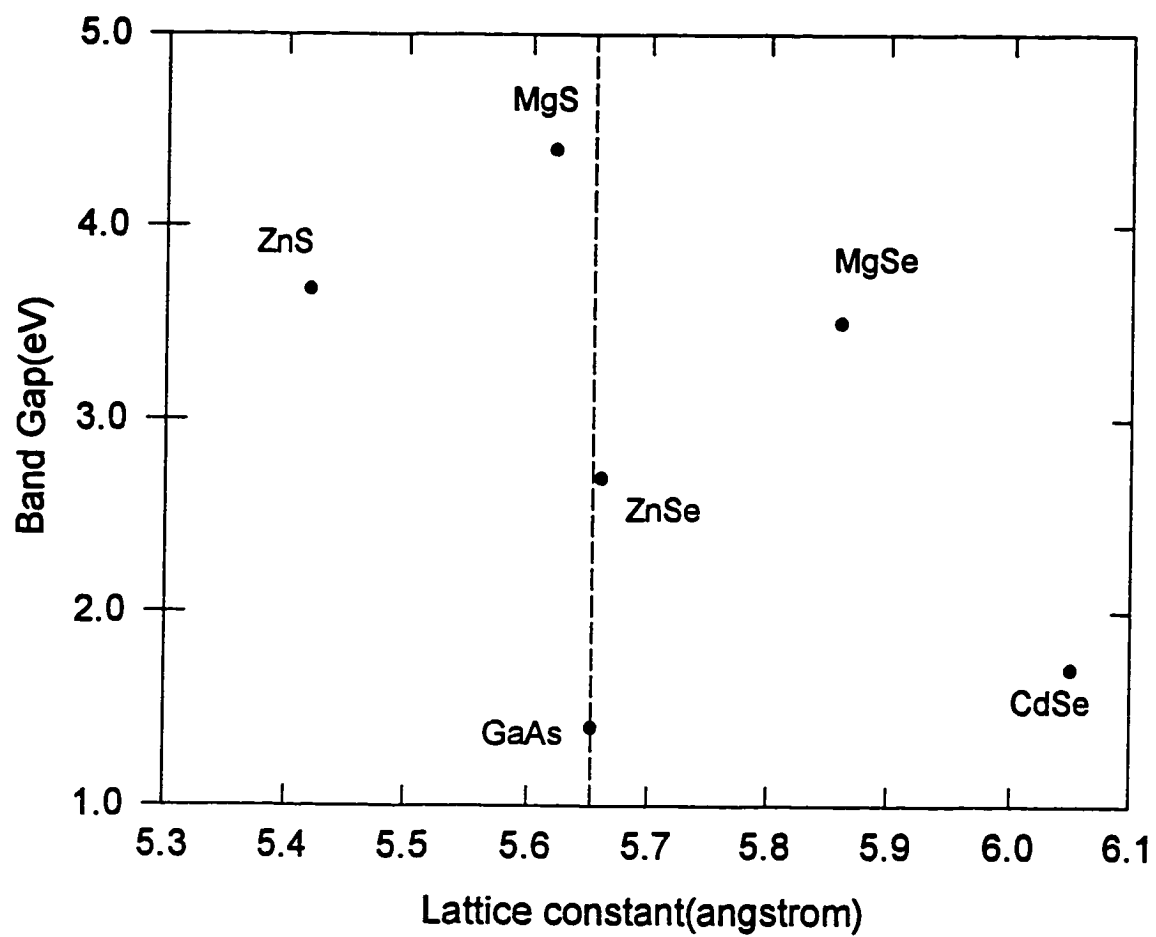Figure 1.1. Band gap energy and lattice constant of II-VI compounds

p-side electrode
p-type ZnMgSSe
p-type ZnSSe
Quantum well
n-type ZnSSe
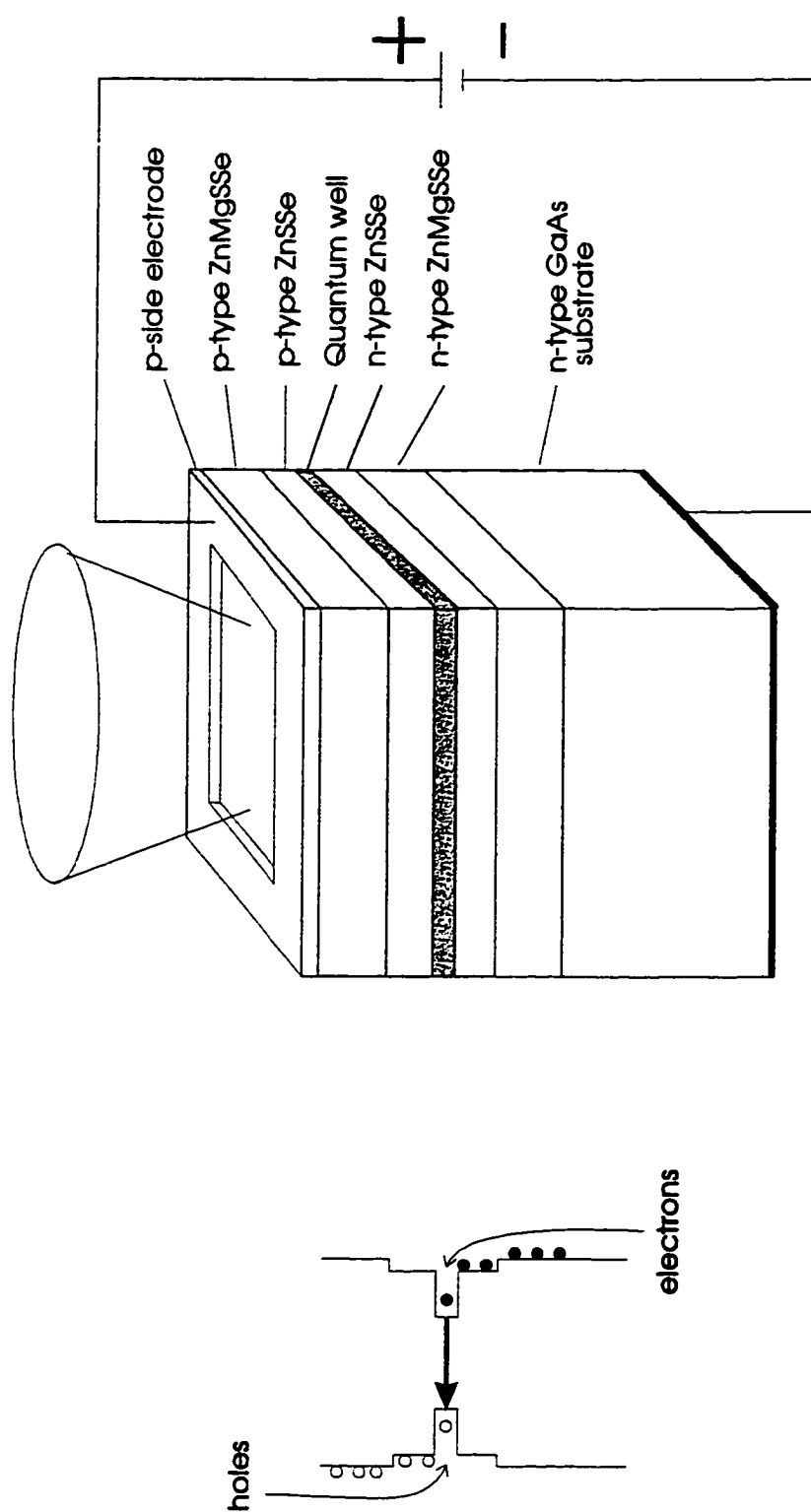n-type ZnMgSSe
n-type GaAs substrate

+ |

electrons

holes

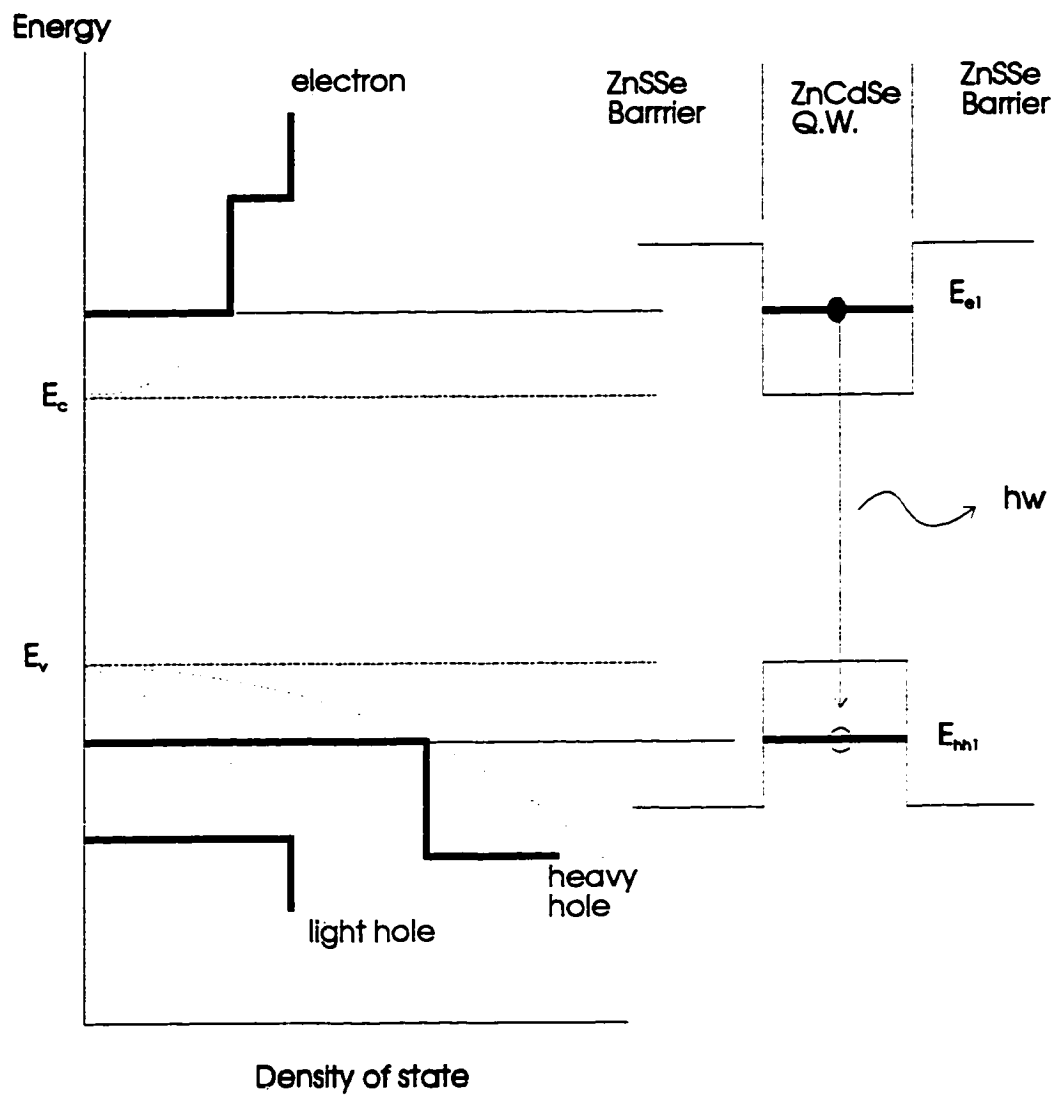Figure 1.2. LED under the forward bias condition

Figure 1.3. Electron and hole density of state and available energy states in the conduction and valence band

CHAPTER 2
EXPERIMENTS AND CHARACTERIZATION METHODS

All of the structures used for this study were grown by molecular beam epitaxy (MBE) in a research laboratory at 3M company. The characteristics of the as grown samples, such as lattice mismatch and crystalline quality, were examined by high resolution x-ray diffraction (HRXRD) and transmission electron microscopy (TEM). Light emitting devices (LED) were then fabricated in a clean room. The LEDs were degraded by applying an electrical current and the characteristics of these LEDs were investigated during operation using electroluminescence (EL) microscopy. These degraded devices were then further examined by photoluminescence (PL) spectroscopy both at low temperature and room temperature, secondary ion mass spectrometry (SIMS) and plan-view and cross-sectional TEM. The details of the device structure, LED fabrication, electrical degradation setup, and the characterization techniques used in this work are discussed in the following sections.

2.1 Device Structures

The samples were grown on (100) Si-doped n^+ -GaAs substrate in a modular Perkin-Elmer Model 430 system. The MBE system and the

20

substrate preparation technique are described in greater detail by Haase et al. [45] [46]. Three different sample structures were used in this study and are as follows.

2.1.1 A Ternary-Based Separate-Confinement Heterostructure

This sample is a separate-confinement heterostructure (SCH) with cladding layers of $ZnS_{0.06}Se_{0.94}$, barrier layers of ZnSe and quantum-well active layer of $Zn_{0.8}Cd_{0.2}Se$. A schematic of this structure (Structure I) is shown in Figure 2.1. The composition of the cladding layer in this structure was chosen to lattice-match to GaAs substrate in an effort to reduce the mismatch related defect density. The cladding layers are nearly lattice-matched to the GaAs substrate at the growth temperature. The ZnSe layers are used as guiding or optical field confinement because of their higher refractive index when compared to the $ZnS_{0.06}Se$ cladding layer. However, the structure produced in this fashion suffers from a lattice mismatch of 0.27 % between the cladding and barrier layers. The relaxation of this mismatch is accomplished by generation of misfit dislocations and other extended defects at the ZnSSe/ZnSe heterointerface. For electrical confinement a very highly strained quantum-well was utilized in this structure. In order to have a pseudomorphic quantum-well layer, the well thickness needed to be kept below 50 Å since the lattice mismatch between ZnSe and $Zn_{0.8}Cd_{0.2}Se$ is about 1.3 %.

The conduction band offset ΔEc and valence band offset ΔEv at the $ZnSe/Zn_{0.8}Cd_{0.2}Se$ heterointerface are 140-270 meV and 60-120 meV

respectively. The net acceptor concentration, N_A-N_D, in the p-type layers was around 6×10^{17} /cm^3 and free electron density in the n-type layers was about 1×10^{18} /cm^3.

2.1.2   A Simplified Ternary-Based Heterostructure

This light emitting device structure is a simpler version of the ternary-based SCH. In order to reduce the nucleation of structural defects, such as misfit dislocations and threading dislocations, during the growth, the layers were grown at a lattice matched (pseudomorphic) condition. The sample consists of a ZnSe buffer layer, a n-type $ZnS_{0.06} Se_{0.94}$ layer, a $Zn_{0.8}Cd_{0.2}Se$ single quantum well and a p-type $ZnS_{0.06} Se_{0.94}$ barrier layer and this structure (Structure II) is shown in Figure 2.2. The quantum-well is tetragonally distorted and the amount of strain in the ZnCdSe quantum-well is 1.6 %. In this structure only electronic confinement can be accomplished. Although all the layers grown are theoretically to be lattice-matched to the GaAs substrate, there appears to be a lattice-mismatch between ZnSSe layers and GsAs substrate.

2.1.3   A Quaternary-Bbased Separate-Confinement Heterostructure

One way to accomplish the lattice matching condition in the separate-confinement heterostructure(SCH) is to utilize the ZnMgSSe quaternary compounds. This alloy allows for the tuning of the lattice constant, band-gap of the layer, the band offsets and refractive indices. So that both electronic confinement and optical confinement can be accomplished. A schematic of such a sample (Structure III) is shown in

Figure 2.3. This is the third structure investigated. All the layers are supposed to be lattice matched to the GaAs substrate, however, high resolution x-ray diffraction indicated a slight mismatch at room temperature still exists. The compositions of the cladding and barrier layer is $Zn_{0.9} Mg_{0.1} S_{0.12} Se_{0.88}$ and $ZnS_{0.06} Se_{0.94}$ respectively. The composition of the quantum well is the same as other samples, $Zn_{0.8}Cd_{0.2}Se$. The doping levels (N_A-N_D) in the p-type ZnMgSSe and ZnSSe regions are about 5×10^{17} /cm^3 and 1×10^{17} /cm^3. The amount of strain in ZnCdSe quantum-well is the same as that of structure II. A special feature in this sample is that a graded ZnTe/ZnSe ohmic contact has been grown onto the p-type ZnMgSSe layer. The method utilizing a heavily doped ZnTe:N is described in detail by Fan et al [47].

2.2 Electrical Degradation of LEDs

Light emitting devices were fabricated as surface emitting types. Then the direct current (DC) was applied to LEDs, while the amplitude and repetition rate and duty cycle were kept constant. During operation the characteristics of light output, such as the output intensity and wavelength was monitored and stored by the optical multichannel analyzer controlled by a computer. At the same time the evolution of degradation defects which was appeared as dark spots and dark lines on the CRT screen was monitored.

2.2.1   LED fabrication for EL

Light emitting diodes were fabricated for the electroluminescence microscopy. The sample was cleaned by dipping into first TCE (Tetra-Chloro Ethane) solution then acetone and methanol subsequently for about 60 seconds each. The sample was then dried with N_2 gas by blowing on the surface followed by drying in a oven for 10 minutes at 60-70 °C. After cleaning a standard photolithography was performed to define the device pattern. Using a mask, an array of 300µm × 300 µm squares was opened up in the photoresist on the sample. The 100 angstrom-thick gold was evaporated on the whole sample. The standard lift off process was done to remove the photoresist outside of the squares. Using another mask, an array of electrical contact pads was opened up. The electrical contact areas were defined along the edges of squares with the width of 50 micron. About 1500 angstrom-thin gold was deposited onto the contact areas. The inside area enclosed by this thick gold band is transparent to photons emitted from the quantum well. Electroluminescence imaging was possible by passing the light exiting from the top surface of the LED through a optical microscope. Gold was deposited on the backside of the sample to provide the other contact. Figure 2.4 shows a flow chart of the LED fabrication process.

The sample was then mounted on a copper block which played a role of heat sink. A silver paste was used to adhere the sample to the copper block both thermally and electrically. The current was then applied to the

copper block and the gold pad on the surface of the sample using a sharp tungsten pin. A schematic after mounting is shown in Figure 2.5.

2.2.2 Experimental Setup for EL microscope

The EL from the active region of the device is focused on a CCD camera and a topography can be observed on the CRT monitor, where the image is enlarged by the optical microscope. This method allows easy observation of dark defect generation and growth (dark spot defect-DSD, and dark line defect-DLD) during operation in the active region of the device, LEDs or lasers. When the cladding layers are transparent against the emitting light from the active region or do not absorb much, this observation method is applicable. A schematic of the experimental setup for observing EL image and measuring parameters of the emitted light is shown in Figure 2.6.

Systems used in this setup are as follows; A voltage pulse generator was used to supply a voltage pulse of constant magnitude. The model is 214B Hewlett Packard and it generates direct current. The pulse repetition rate (Hz), duty cycle (%), pulse width (sec) and amplitude (volts) were controlled. These parameters were set constantly for a degradation process and a pulse shape is shown in Figure 2.7. An oscilloscope (model 2215 Hewlett Packard) was used to monitor the current pulse in ampere going through the LED device using a converter. The current density (ampere/cm^2) during operation was obtained using this oscilloscope. The C2400 Hamamatsu CCD camera was used to capture the

electroluminescence image through a optical lens (20X). The optical lens are used for focusing and enlargement of the image. The image was sent to the TR930B Panasonic video monitor to observe electroluminescence topograph. At the same time the parameters of the emitted light from a LED, such as wavelength and intensity, were measured using the model 1460 optical multichannel analyzer (OMA). The data acquisition and display with a signal processing were done by this computerized system. In front of the OMA system a photo detector (model 1453A EG & G Princeton Applied Research) was attached. This is a silicon photo diode detectors, which has 1024 elements photodiode array detector. The detectable range of wavelength is 371 nm to 669.3 nm with the resolution of 0.3 nm.

2.3 Characterization Methods

2.3.1 Transmission Electron Microscopy

Using a JEOL 200CX transmission electron microscope, as grown samples and degraded ones were analyzed by cross-sectional and plan-view transmission electron microscopy (XTEM and PTEM). XTEM was used to study structural defect evolution in the heterostructures. PTEM was used to determine extended defect densities in the layers and to investigate dark spot defects and dark line defects. The main efforts were directed to find

out those degradation related defects and characterize them. Some unique features of the preparation of TEM specimen is described in the following.

Cross-sectional TEM specimen preparation. The samples were cut into 250 micron thick strips using a diamond dicing saw. The epilayer surfaces of the two strips were coated with M600 Bond epoxy resin and brought together in such a way that these coated surfaces were closely contacted each other. The glued strips were then heated for 60 minutes at 100 °C for curing the epoxy resin. After curing the bonded strips were mechanically polished down to a thickness of about 40 micron using a Struers polishing jig and 5 micron size Al_2O_3 powder. In order to get a smooth polishing surface, the sample was lapped on a 1 micro size grid silicon carbide paper. A copper ring was then mounted on the thinned specimen to provide mechanical stability. The specimen was thinned further in a Gatan ion miller using the sputtering action of Ar^+ ion at a gun voltage of no more than 3 KV and a gun current of 0.5 mA until a small hole was obtained. The ZnSe based compound has been known to be damaged during ion milling. The gun voltage had to be kept below 3 KV in order to prevent any ion milling damages. However, there was still some damage observed in the TEM and it is necessary to differentiate this from degradation induced defects. The regions in the vicinity of the hole were thin enough for electron transparency and could be analyzed in the TEM.

Plan-view TEM specimen preparation. Ion milling method was used for the plan view TEM samples. The sample was cut into 2 mm × 2 mm

squares using a dicing saw again. Since the samples consist of many different layers on the GaAs substrate, the first step towards the preparation of a PTEM specimen involves polishing the substrate side of the sample. The sample was polished, using the same procedures as XTEM specimen preparation down to a thickness of 40 microns. A copper ring was mounted on the substrate side and thinned further in a Gatan ion miller. The substrate side was ion milled first using only one ion gun until a small hole was obtained. The Ar$^+$ ion gun voltage kept below 3 KV and the gun current also kept below 0.5 mA during the whole ion milling. After forming a small hole the epilayer side was ion milled gradually. Every 10 minutes ion milling was stopped and the specimen was investigated in the TEM until the electron transparent region is reached to the quantum well active area.

Chemical etching to get rid of ion milling damages. It is common for ZnSe based compounds that ion milling damage results in black dot contrast in TEM. In order to eliminate those ion milling induced damages a chemical etching was employed. After the sample was ion milled, the specimen was dipped into a 1 % Br$_2$/CH$_3$OH solution for 1 seconds, then rinse in methanol(CH$_3$OH) and in D.I. water consequently. This method appears to be the most effective one as described by Yu et al. [48]

2.3.2 High Resolution X-ray Diffraction

A Philips HRXRD was used to characterize the lattice mismatch among the epilayers and the degree of strain relaxation in the layers. Even

though all the epilayers were supposed to be lattice- matched to the GaAs substrate as they were grown, the lattice parameter each layer turned out to be different. Two basic methods of HRXRD analysis were performed for the as grown and degraded samples, i.e. rocking curves and diffraction space mapping.

Rocking curves. Both symmetric plane reflection and asymmetric plane reflection were used. A peak position of a symmetric plane, such as the (004) plane can be used to determine the lattice spacing between the (004) planes. The angular separation between the substrate and epilayer peaks can be used to determine the perpendicular lattice mismatch. In order to find the in-plane lattice mismatch, an asymmetric reflection must be measured. This is a reflection from a lattice plane inclined to the surface, such as the (224) plane. The more detailed methods and evaluation of the mismatch both in the perpendicular and parallel direction to the surface are described in chapter 4.

Diffraction space mapping. The inhomogeneous and or mosaicity of the epilayer can be obtained using the triple axis configuration. Figure 2.8 shows the diagram of the triple axis diffractometer. It is a regular high resolution diffractometer using a four crystal monochromator with an additional channel-cut crystal placed on the 2-theta arm, immediately before the detector. Both the in-plane and perpendicular lattice parameters can be derived from a single two-dimensional reciprocal-space map from a asymmetric plane. If an epitaxial film is misoriented or tilted at a certain

angle with respect to the substrate, at least 8 measurements of rocking curves have to be obtained to figure out the exact lattice tilt and lattice mismatch. Because this diffraction space map isolates the components of strain and tilt, the individual layer tilts can be determined and then used to correct the data obtained from the asymmetric rocking curves.

Measurement parameters. The X-ray tube generator was operated at 40 KV and 40 mA and produced Cu $k\alpha$ radiation at the wavelength of 1.54056 Å. The Bartels 4-crystal monochromator was set to Ge (440) planes. The sample were mounted on a glass slide with a scotch tape and care was taken to minimize any stresses on the sample. The glass slide and sample were then mounted on the goneometer with the mounting plate. The sample surface was aligned to the center of the optical axis of X-ray by using a dial gauge. The normal procedures for optimization were performed. For the rocking curves, the omega (ω) / 2theta (2θ) scan was chosen because it is most sensitive to differences in lattice plane spacing. Omega refers to the angle between the crystal surface plane and the optical axis of x-ray source. 2theta is the angular position of the detector relative to the same optical axis. For the reciprocal lattice mapping, an aerial, 2-dimensional scan was chosen. The combination of an omega scan and an omega/2theta scan was performed since this gives information on the oriental relationship between sets of lattice planes.

2.3.3   Photoluminescence

For the low temperature photoluminescence, samples were cooled down to 20-23 K in a cryostat of liquid helium. This low-temperature measurements were necessary to obtain spectroscopic information by minimizing thermally-activated recombination process and thermal line broadening. Since the offset in the conduction band and valence band is relatively small for the structures studied here, samples were excited with the focused beam of He-Cd laser in order to obtain a maximum output intensity.

PL measurements were used to investigate (1) the strain relaxation in the quantum well, (2) the temperature dependence of the quantum well material on temperature and (3) the atomic interdiffusion in the quantum well due to thermal annealing as will be discussed.

2.3.4   Secondary Ion Mass Spectrometry

Secondary Ion Mass Spectrometry(SIMS) was performed with a Perkin-Elmer 6600 system to get the depth profile of atomic interdiffusion around the QW active region. In order to resolve the small dimension of quantum well(50 angstrom), the following optimization conditions were used after many trials. The Cs^+ primary ion beam operated at a voltage of 3 keV and a beam current of 31 nA. The rastered area was 400 μm × 400 μm and the analyzed area was 300 μm × 300 μm. In order to improve the resolution of SIMS profile the quantum well should lie close to the surface.

Since the quantum well is located around 1 micron below the surface, the top surface of the samples for SIMS were lapped down mechanically using Syton. This solution is a mixture of 0.01 micron size of SiC and water. The depth profile mode was used to scan for preselected species as a function of time.
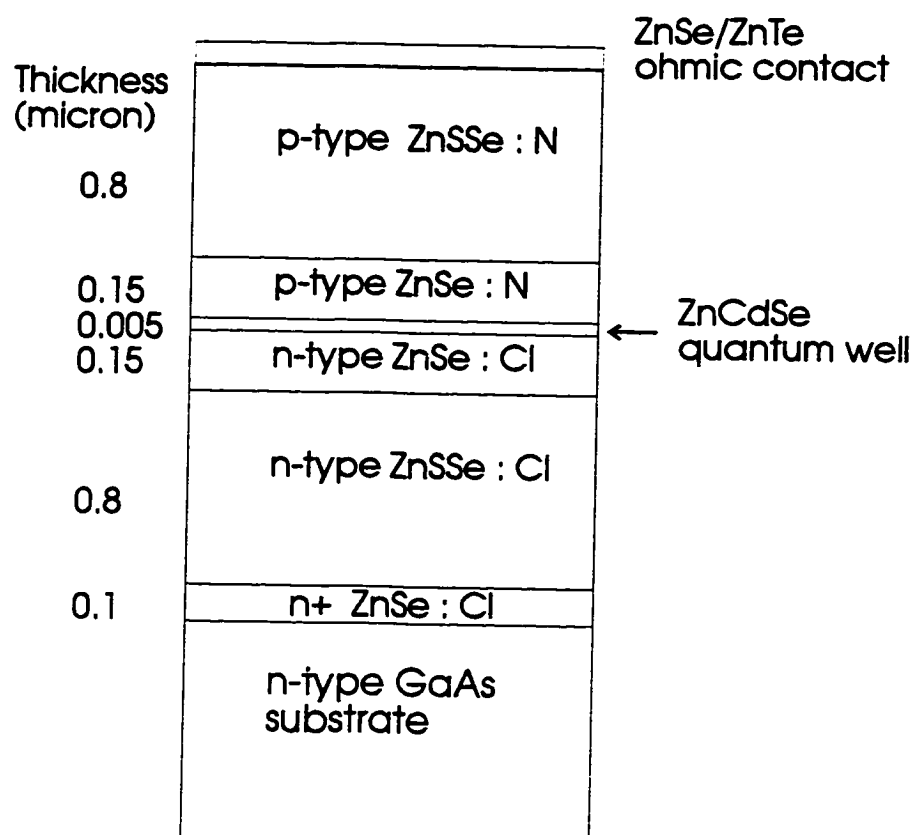
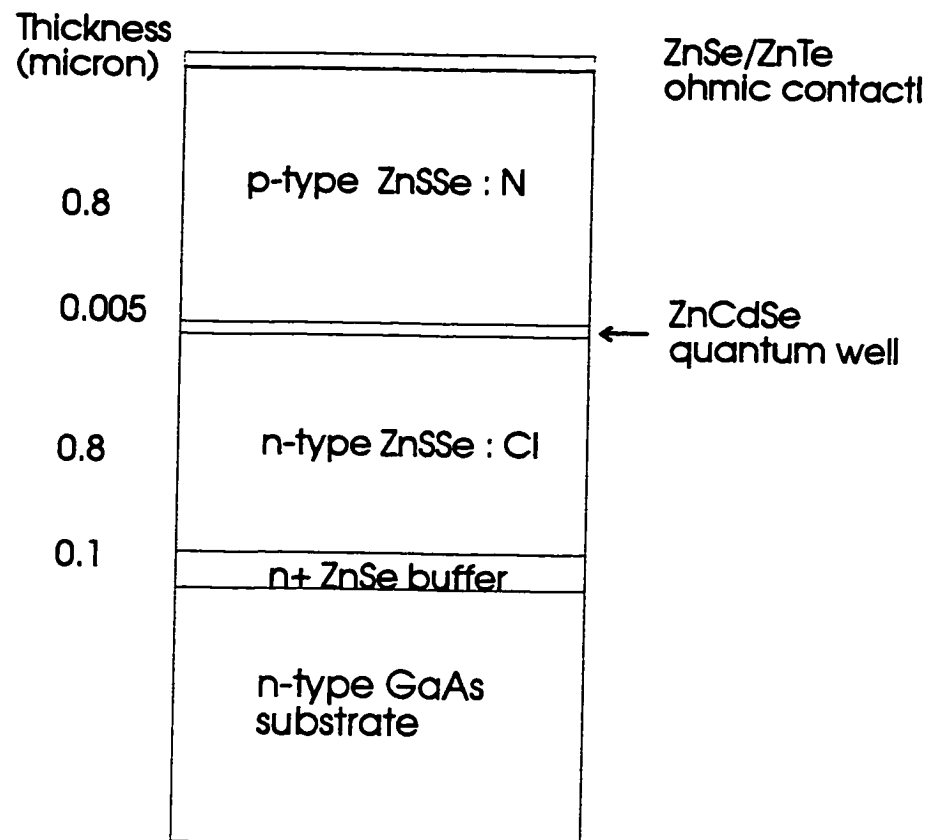Figure 2.1. Ternary-based separate-confinement heterostructure (Structure I)

Thickness (micron)		
		ZnSe/ZnTe ohmic contactI
0.8	p-type ZnSSe : N	
0.005		← ZnCdSe quantum well
0.8	n-type ZnSSe : Cl	
0.1	n+ ZnSe buffer	
	n-type GaAs substrate	

Figure 2.2.   Simplified ternary-based heterostructure (Structure II)

Thickness (micron)

Thickness	Layer
0.1	ZnSe/ZnTe ohmic contact
0.8	p-type ZnMgSSe : N
0.15	p-type ZnSSe : N
0.005	(ZnCdSe quantum well)
0.15	n-type ZnSSe : Cl
0.8	n-type ZnMgSSe : Cl
0.1	n+ ZnSe : Cl
	n-type GaAs substrate
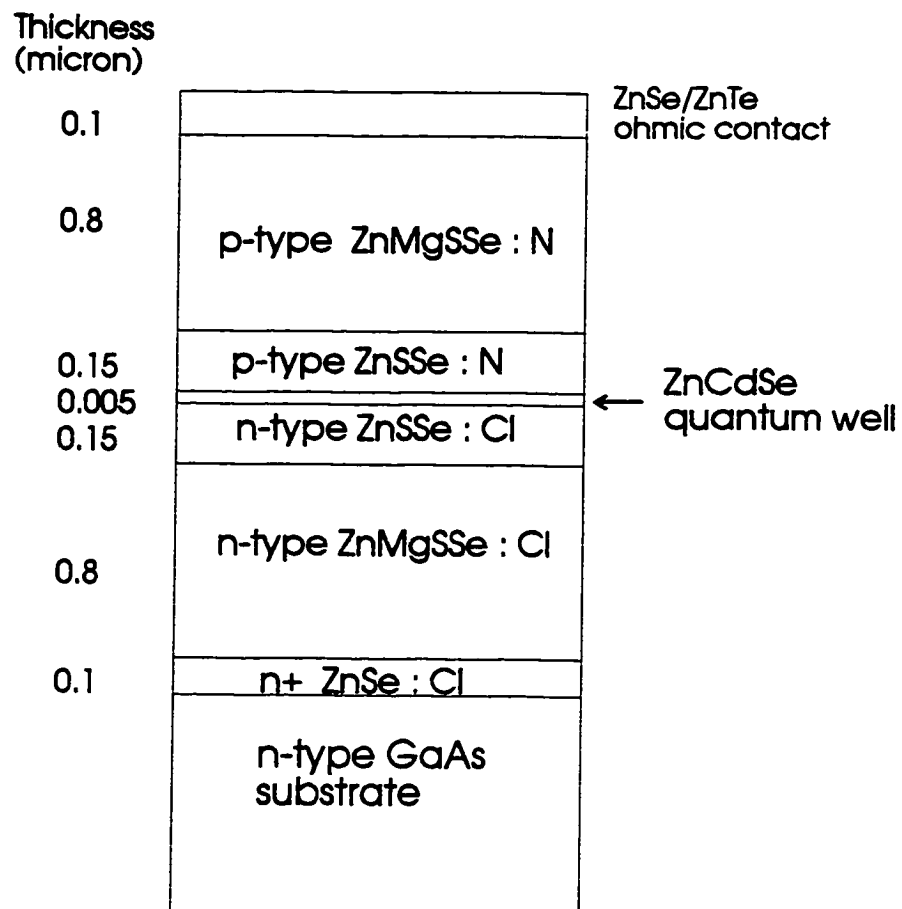
Figure 2.3.   Quaternary-based separate-confinement heterostructure (Structure III)

surface cleaning
TCE, acetone, methanol (60 sec each)

↓

drying
(N_2 blowing, 60 °C, 10 min)

↓

coating with photoresist

↓

mask 1
array of 300 μ* 300 μ squares opened up

↓

gold deposition : 100 angstrom thick

↓

removal of remained photoresit

↓

coating with photoresist

↓

mask 2
50 μ wide pads along the edge of squares opened up

↓

gold deposition(electrical contact): 0.15 μ

↓

removal of remained photoresist

↓

electrical contact (back side) : gold 0.15 μ
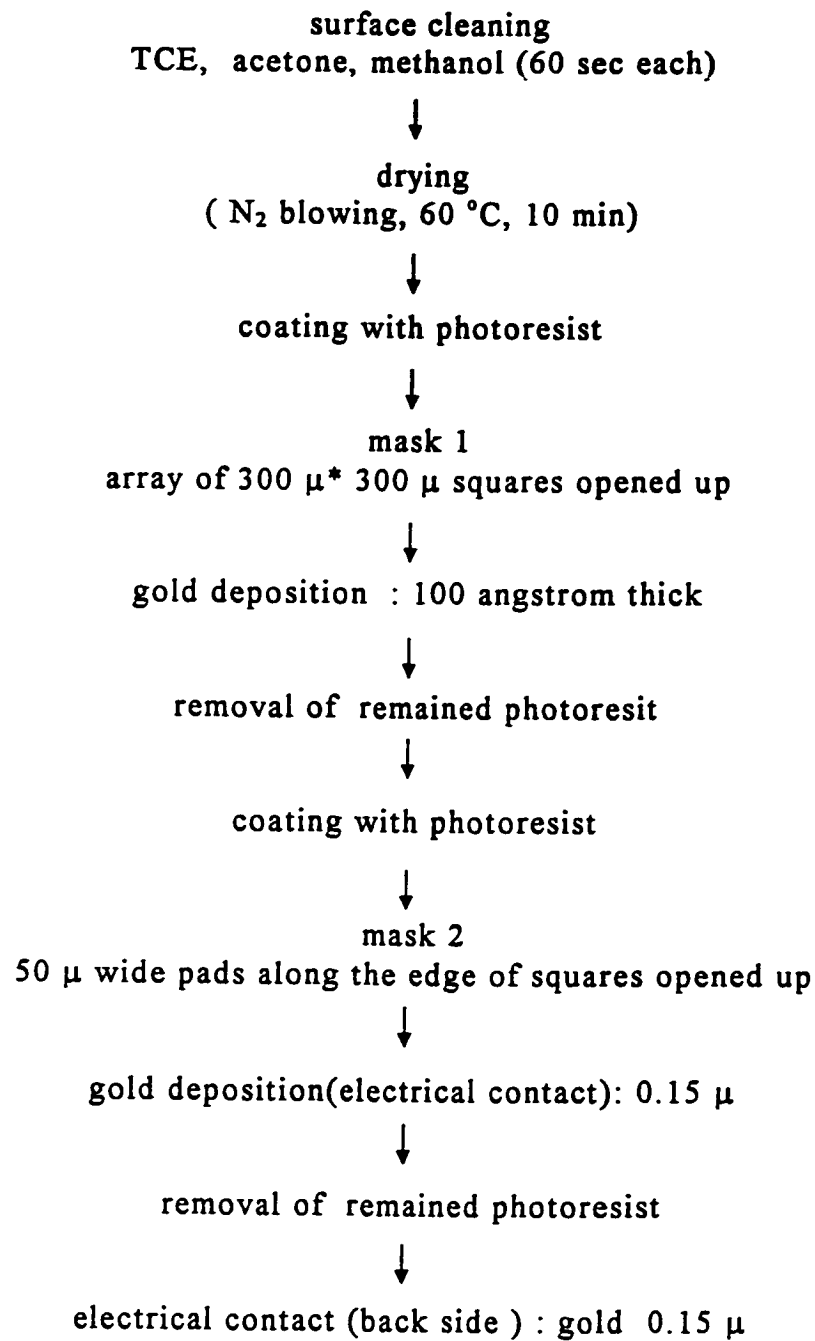
Figure 2.4.   A flow chart of LED fabrication

LED dimension
   A=200 micron
   B= 300
   C=1.0
100 angstrom thick (middle)

C

B A

LED array
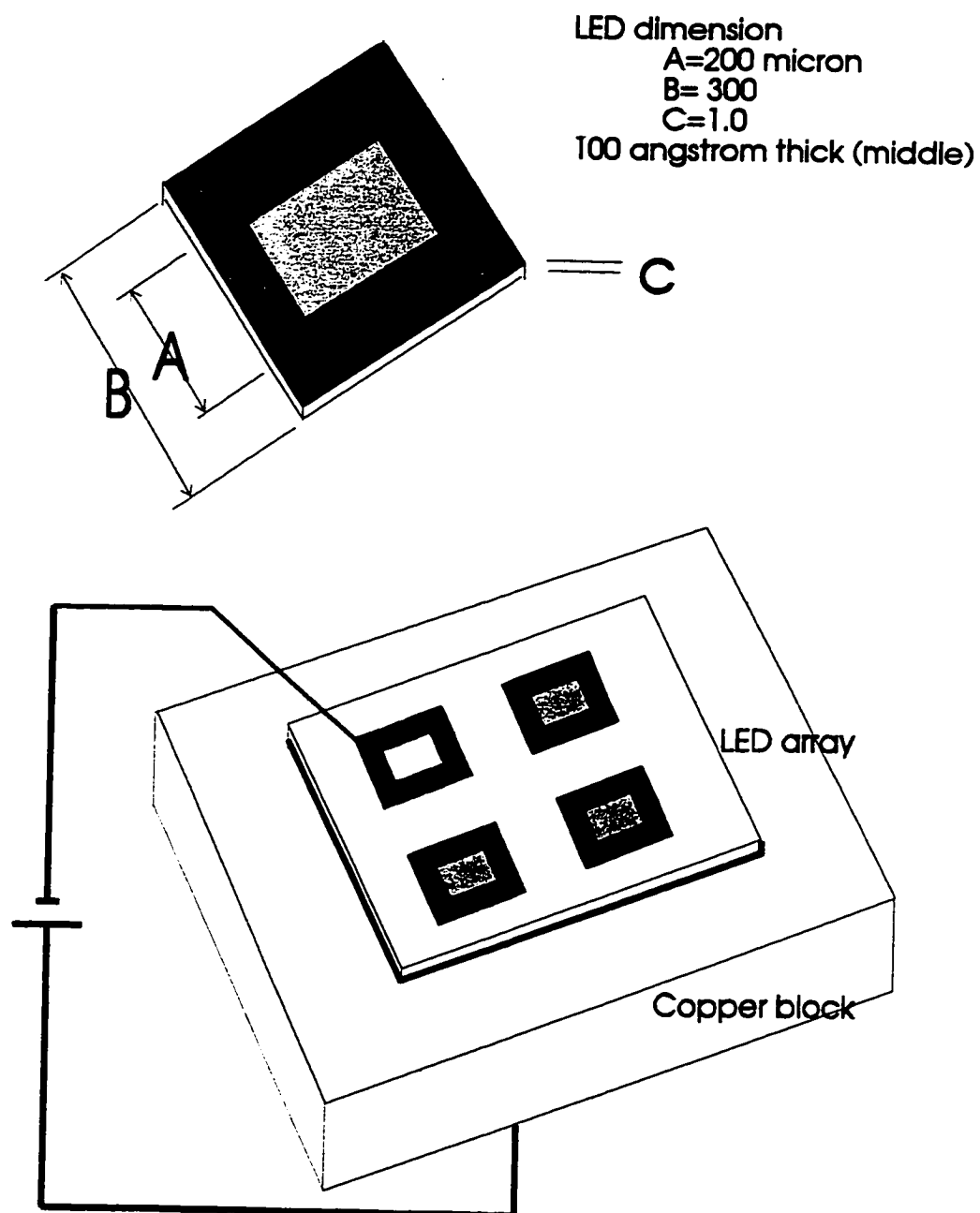
Copper block

Figure 2.5.   Mounting LEDs on a copper block and the dimension of LED
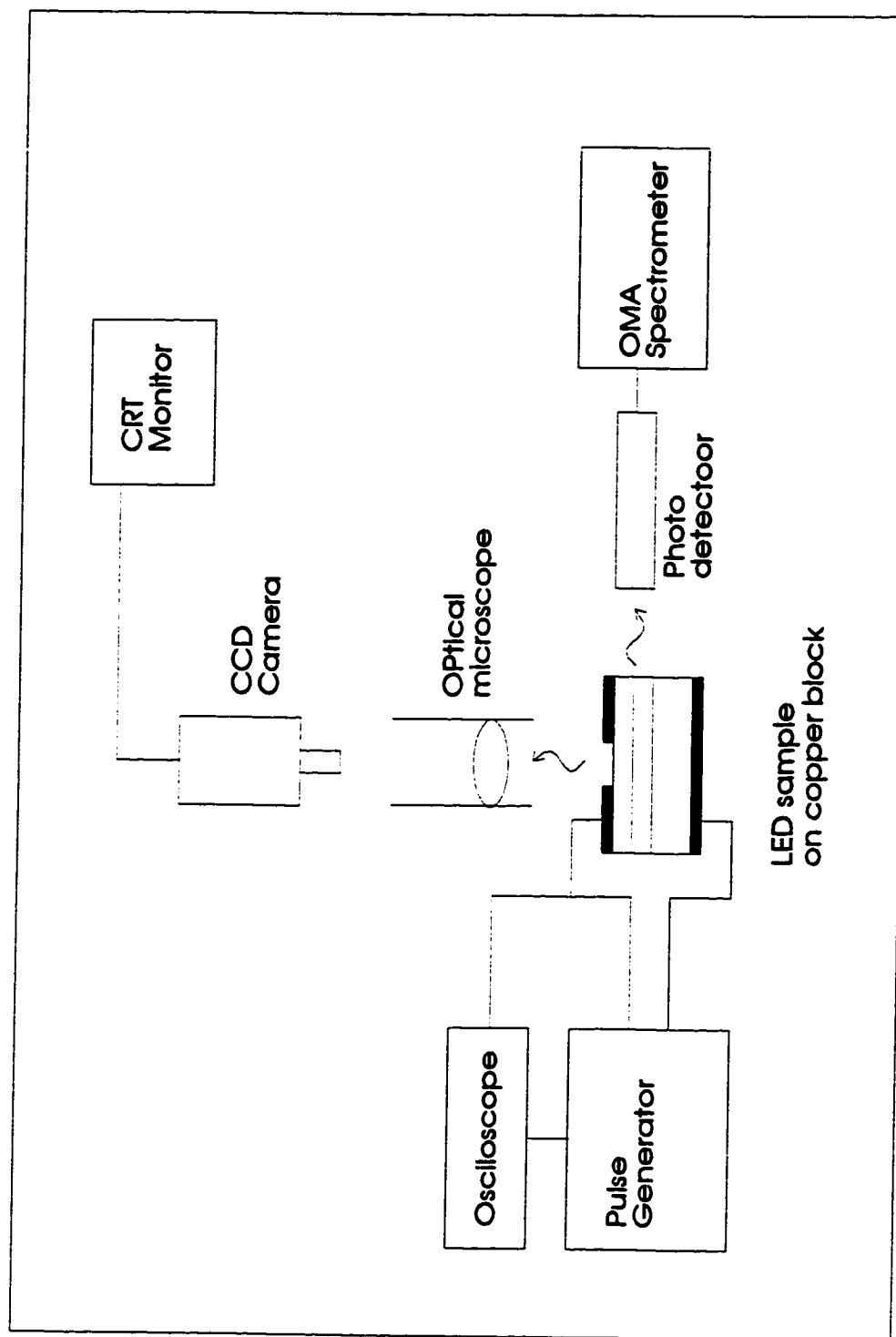
Figure 2.6. Experimental setup for electrical degradation of LEDs
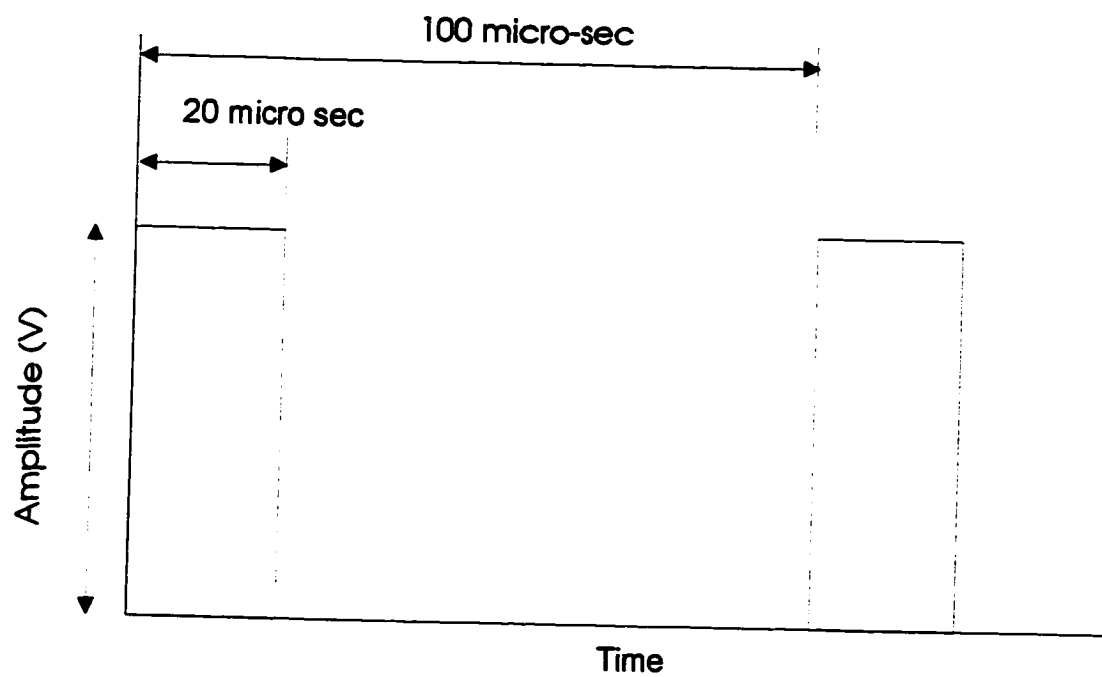
Figure 2.7. Schematic of a dc pulse: 20 % duty cycle and 10 Khz repetition rate
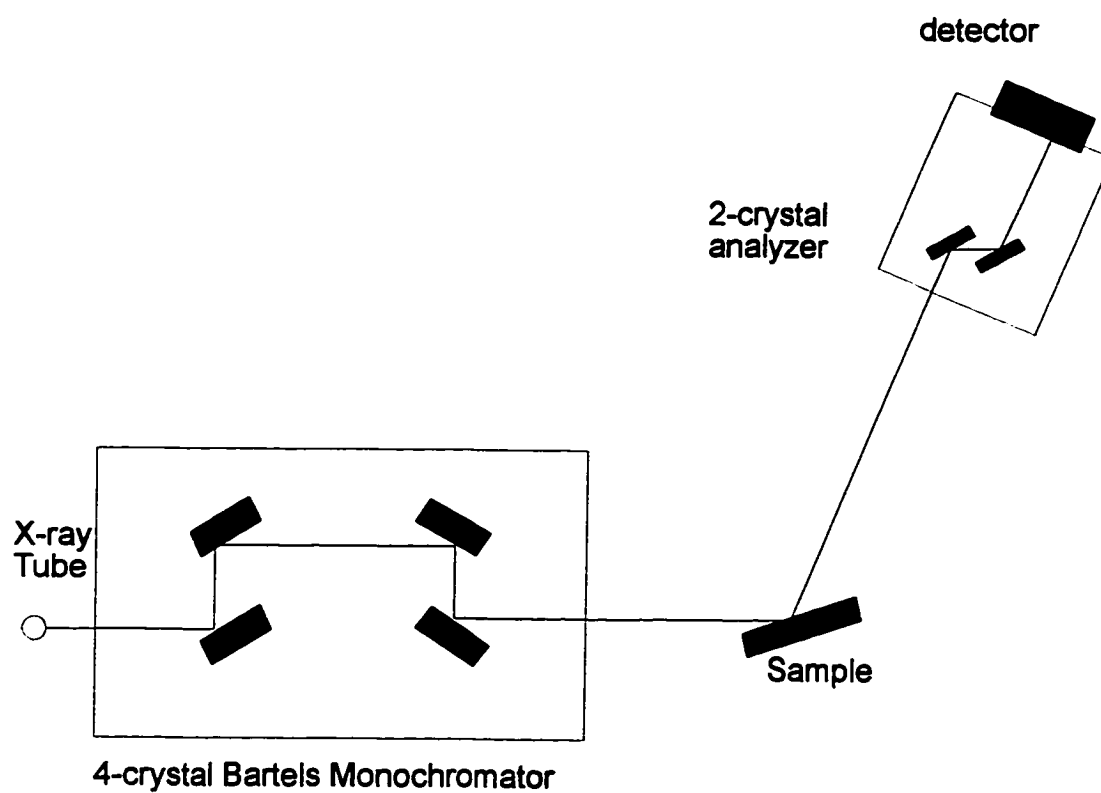
detector

2-crystal
analyzer

X-ray
Tube

Sample

4-crystal Bartels Monochromator

Figure 2.8.   Cofiguration of HRXRD for two-dimentional area scan

CHAPTER 3
DEGRADATION TRENDS

The characteristics and trends of LED degradation may depend on the intrinsic properties of materials comprising the device. The laser structures of II-VI ZnSe devices were observed to be degraded by dark line defects formation whether being operated in the LED mode or laser mode [49]. In the LED mode only spontaneous emission takes place. Lasers can be produced by stimulated emission above a threshold current density. The EL spectra of LEDs fabricated from each structure are shown in Figure 3.1. In order to see investigate the LED degradation phenomena, the changes in wave length and output intensity of the emitted light were measured during the LED operation. The experimental set up was explained in chapter 2.

The degradation trends which depend on the pre-existing defect density and driving condition are reported. The external efficiency curves were surveyed before and after degradation. The efficiency decreases after degradation. This is attributed to an increase of the concentration of nonradiative electron-hole recombination sites. I-V characteristics were obtained during the degradation and related to the structural changes. It was not possible to measure the temperature of the active region during

41

LED operation directly. To estimate the temperature of the quantum-well region, the temperature dependence of band gap was utilized.

3.1 General Degradation Trends

Driving conditions for the measurement of output power change as a function of time are shown in Table 3.1.

Table 3.1. Current driving conditions

Conditions	values
current density	16.7 A/cm2
repetition rate	10 K Hz
pulse width	40 μsecs
duty cycle	40%

The operating ambient temperature was room temperature(300K). The output power was measured during operation and the driving conditions were maintained a constant during degradation. The result of degradation trend of ternary based SCH (structure I) is shown in Figure 3.2. LEDs degraded rapidly at the initial stages of the aging period with the output power decreasing exponentially. The decrease in the light output power has been previously reported for III-V compound-based LEDs and is given by [50]

$$P(t) = P(0) \exp(-\beta_d t) \qquad (3\text{-}1)$$

where P(0) and P(t) are initial output power and output power after time t, respectively. The degradation coefficient, β_d , indicates the slope of the decreasing line of optical power with degradation time and hence the rate of decrease in the output power. This value of β_d usually depends on the driving conditions and the structural quality of the devices.

The output power calculation was done by obtaining a sum of all the energies of photons detected by the Si detector array. The output intensity detected by the OMA system is the number of photons in 16 msec for each wave length interval (3 nm). The output power was calculated using the following formula,

$$P = \int \hbar w f(w) dw \qquad (3-2)$$

where $\hbar$ is reduced Plank constant and the function f(w) is the angular frequency which is a function of wavelength. w is equal to $2\pi c/\lambda$, where c is the velocity of light and λ is the wave length. The wave length distribution of emitted light from the ternary based SCH (structure I) is shown in Figure 3.3. This figure also shows the output intensity changes as a function of the degradation time. The calculated output power using this method is a small portion of the total external output power. The measured intensity was obtained through a slit in front of the detector, as such all the light emitted was not detected. Only a small portion of the emitted light was detected. It is assumed that the power measured in this

way is proportional of the total power produced in the quantum-well over the course of degradation.

3.1.1 Degradation Dependence on Current Density

To investigate degradation dependence on the current density, LEDs were degraded while monitoring output intensity. The driving conditions used were the same as shown in Table 3.1 except for varying the current density. Increasing current density flowing through the LED increased the rate of degradation. This degradation dependence on the current density is shown in Figure 3.4 and Figure 3.5. Dark spot and dark line defects were observed in the electroluminescence microscope during degradation. These defects appeared to develop more rapidly with increasing current density. These dark defects has been considered a major problem in the II-VI ZnSe-based light emitters. The generation and propagation of DLDs appear to be strongly dependent on the current density.

If the current density were to be increased to that for laser operation, the device would degraded much more rapidly. The current density for laser operation is typically between 0.5 and 2 KA/cm^2 [49] [51][52]. After development of the more efficient ohmic contact onto the p-type upper layer by utilizing resonant tunneling multiple quantum-well structure, the threshold current density for ZnSe-based lasers is in the range of 0.5 KA/cm^2 for lasing. If the current density is projected to that of the lasing level, the time for lasing operation would be a few seconds as shown in the Figure 3.6. This figure shows that the time for LEDs to be

degraded down to the 30% of the initial output intensity as a function of current density. The time for lasers to stop lasing is on the projection line of the LEDs and is on the order of few seconds. This indicates that the degradation of lasers would be the same as that of LEDs. The structures may also be extremely vulnerable to the higher current flow.

3.1.2 Degradation Dependence on Pre-existing Defect Density

In order to compare the dependence of degradation on the as-grown defect density, the ternary-based SCH (structure 1) and simplified ternary-based heterostructure (structure II) were used for this study. The ternary-based SCH has more defects around the quantum-well than the simplified ternary-based heterostructure. The density of the extended defects (mainly stacking faults) in the structure was determined from plan-view TEM analysis. The extended defect density near the active quantum well region of the ternary-based SCH on the order of 10^9 /cm^2 while it was less than 10^6/cm^2 for the simplified ternary-based heterostructure. This was calculated using the length of partial dislocations in an observed unit volume near the quantum well. LEDs were fabricated as detailed in chapter 2 and were operated under the same driving conditions. The driving conditions were that the repetition rate was 10 KHz, duty cycle was 40% , pulse width was 40 μsec and the current density was 15 A/cm^2.

The degradation of LEDs was found to be strongly dependent on the extended defect density in the structure. The more the as-grown structural defects, the more rapid the output power decreased as shown in

Figure 3.7. When the current density was changed, the time for 70% degradation, that is time to degrade the output intensity down to 30% of the initial intensity, was much shorter for higher defect density structure. This trend is shown in Figure 3.8. Therefore the pre-existing crystal defects play an important role in the degradation process. In III-V devices, dark line defects were observed to form readily at defects such as threading dislocations and other structural extended defects. Stacking faults, which are the major type of defects in II-VI ZnSe-based structure, may act as sources of degradation-induced defects.

3.2 Efficiency

3.2.1 LED Efficiency Change due to Nonradiative Recombination

The external efficiency is usually proportional to the internal efficiency and also should be proportional to the injected current. The external efficiency was measured before and after degradation. LEDs fabricated from the simplified ternary based heterostructure was degraded down to 50% of the initial output intensity (50% degradation) The reason why 50% degradation was chosen was that even though dark line defects were observed at this level of degradation in electroluminescence microscopy, no new extended defects were found by TEM. This observation will be described more in the chapter 5. The conclusion is that some changes in the crystalline structure around the active region have taken place but are not observable in TEM for the 50% degraded LEDs.

The external efficiency was obtained by measuring the output power of light emitted as a function of current density for the as-grown state LED and degraded LED. The driving conditions for the this measurement were a 10 KHz of the repetition rate, a 20% of duty cycle and a 20 μsec pulse width. The power-current (P-I) curves are shown in Figure 3.9. This graph clearly shows the output efficiency was substantially decreased after 50% degradation. This decrease in output efficiency could be explained by a decrease in the nonradiative recombination lifetime as a result of submicroscopic defects generated during operation.

To better understand why the nonradiative lifetime is decreasing, one must look at the light emission process more detail. Spontaneous emission takes place when the electrical current flows through the active quantum well. When a certain density of electrons are injected into the active layer, an equal density of holes are also injected because of the requirement of charge neutrality. Under constant driving conditions, such as dc operation, (If injected electron and hole densities are expressed by Δn and Δp), the density of electron (n) and hole (p) can be expressed by

$$n = \Delta n = \tau_n \frac{J}{qd} \qquad (3\text{-}3)$$

$$p = \Delta p = \tau_p \frac{J}{qd} \qquad (3\text{-}4)$$

where τ_n and τ_p are electron and hole lifetimes and they correspond to the time when the density of the excited carriers is reduced by recombination to $1/e$ of the initial value. Usually, the carrier life time is divided into two terms: for radiative recombination, τ_r, and for nonradiative recombination, τ_{nr}. The carrier life time is expressed by

$$1/\tau_n = 1/\tau_r + 1/\tau_{nr} \tag{3-5}$$

where τ_r is for determined by spontaneous emission as follows

$$\tau_r = \Delta n / Rr$$

where Rr is the radiative recombination rate.

The efficiency of radiative recombination (internal quantum efficiency) is expressed by

$$\eta_i = \frac{\tau_{nr}}{\tau_r + \tau_{nr}} \tag{3-6}$$

where, τ_r is the carrier lifetime for radiative recombination and τ_{nr} is the carrier lifetime for nonradiative recombination.

The emitted light output power is proportional to the emitted light from the active layer. The output power is less than a few percent of the total emitted light from the active region. The emitted light power from the quantum well layer is given by the product of the emitted photon number and its energy, $h\nu$. The photon number created by recombination in a unit volume of the active layer is a product of injected carrier density (Δn) and an internal quantum efficiency (η_i), corresponding to the ratio of emitted

photon number to injected electron number. Therefore the power emitted from a unit volume of the active layer, P_i, can be expressed by

$$P_i = h\nu\eta_i \left(\frac{J}{qd}\right)$$

$$= h\nu\left(\frac{J}{qd}\right)\left(\frac{1}{1+\tau_r/\tau_{nr}}\right)$$

<div align="right">(3-7)</div>

where J is the current density, q is the charge of electron and d is the thickness of the active layer. The radiative recombination lifetime does not change and it is a intrinsic property of material. So this equation indicates the decrease in the light output power during device degradation is basically caused by the decrease in carrier lifetime due to a decrease in the nonradiative recombination lifetime.

The main cause of the reduced carrier lifetime is the poor quality of materials [53]. In general, a high quality semiconductor with few defects usually has a long carrier lifetime. On the other hand, poor quality semiconductors have a short carrier lifetime and a large defect density. During degradation, dark line defects and other types of degradation induced defects are generated and they act as nonradiative recombination centers. The decrease in carrier lifetime due to these degradation-induced defects results in a lower output power.

3.2.2 Analytical Calculation of Efficiency

A relationship between light output power and current density for a LED has been derived based on semiconductor theories in the following. A

theoretical calculation of the output power was evaluated as a function of radiative and non-radiative recombination rate. This calculated value was compared with those obtained from experiments. The main purpose of this section is to show that the output power of emitted light is reduced due to the non-radiative recombination.

Before lasing in a laser diode, light emission takes place in the LED mode. In other words, the change from spontaneous emission to stimulated emission occurs at a threshold current density. Figure 3.10 shows that a laser device operates in the LED mode (spontaneous emission) below the threshold current density and it runs in the stimulated emission mode above the threshold current density. The optical gain during stimulated emission for lasers has been well established theoretically. The spontaneous emission, however, has been less investigated.

If we apply the nonradiative recombination rate of bulk semiconductors to a quantum well device, a general expression for the net nonradiative recombination rate at a thermal equilibrium can be expressed by a simplified equation,

$$R_{nr} = AN \tag{3-8}$$

where, R_{nr} is the nonradiative recombination rate, A is the nonradiative recombination coefficient, and N is the carrier density. The radiative recombination rate (spontaneous emission rate) in a quantum-well is given by [54]

$$R_{sp} = (\frac{1}{\hbar\omega})\frac{\pi e^2 \hbar}{n^2 \varepsilon_o m_o^2}|M_{ave}|^2 \rho_{red}(E_{eh} - E_g)\rho_{opt}(\hbar\omega)f_c(1-f_v) \qquad (3\text{-}9)$$

where e is the electron charge, ε_o is the electric permittivity, n is the refractive index, m_o is the free electron rest mass, $|M_{ave}|^2$ is the transition matrix element, ρ_{red} is the reduced density of states, $E_{eh} = \hbar\omega$, ρ_{opt} is the optical density mode, f_c and f_v are the fermi distribution function of conduction band and valence band, respectively. This radiative recombination rate can be simplified as

$$R_{sp} = C(E_{eh} - E_g)f_c(1-f_v)N^2 \qquad (3\text{-}10)$$

where C represents all the material constants combined for the equation. E_{eh} and E_g are fixed values and f_c (f_v) is related to the carrier density N. The carrier density in the quantum-well can be given by [55]

$$N = \frac{m_c k_B T}{\pi \hbar^2 L}\ln\{1 + \exp[-E_{c1} - E_{fc})/(k_B T)]\} \qquad (3\text{-}11)$$

where E_{fc} (E_{fv}) is the quasi-Fermi level of the conduction (valence band), L is the thickness of the quantum-well layer, E_{c1} is the quantized electron level in the conduction band., and f_c (f_v) is the fermi distribution function for the conduction (valence) band. They are expressed by

$$f_c = \frac{1}{1 + \exp[(E_{c1} - E_{fc})/k_B T]} \qquad (3\text{-}12)$$

$$f_v = \frac{1}{1 + \exp[(E_{h1} - E_{fv})/k_B T]} \qquad (3\text{-}13)$$

The ZnCdSe single quantum-well in our structures has only one quantized energy level in the conduction and valence band. For a 50 angstrom thick quantum well, the quasi-Fermi level in the conduction and valence band was calculated as a function of carrier density and is plotted in Figure 3.11 and Figure 3.12.

The total recombination rate at a given carrier density is the sum of the nonradiative and radiative recombination rates and it is expressed as

$$R_{tot} \quad = \quad R_{nr} + R_{sp}$$

$$= \quad AN \quad + \quad BN^2 f_c(1-f_v) \tag{3-14}$$

assuming that all the electrons ejected into the quantum well recombine either nonradiatively or radiatively and N=P due to the charge neutrality. Therefore the injected current density J can be related to the radiative and non-radiative emission rate and output power P as follows

$$\frac{J}{eL} = \int R_{tot}(\hbar\omega)d(\hbar\omega)$$

$$= \int [AN + BNf_c(1-f_v)]d(\hbar\omega) \tag{3-15}$$

$$= \alpha P$$

This simplified equation was used to calculate the output power P as a function of the current density J by varying two parameters, A and B. Figure 3.13 shows the calculated output power as a function of carrier density when Aa=0.2 , Ba=0.4 (before degradation) and Ad=0.5 , Bd=0.12

(after degradation). This figure matches well with the experimental results. The non-radiative recombination coefficient after degradation has increased 2.5 times that of the as-grown value (Ad/Aa =2.5) and the radiative recombination rate has decreased 3.3 times (Ba/Bd =3.3). Therefore the observed decrease in the external efficiency of the LED after degradation could be explained by an increase of nonradiative recombination centers such as dark line defects and other types of degradation-induced defects.

3.3   I-V Characteristics

The current -voltage curves were measured before and after degradation for the sample structure I and the results are shown in Figure 3.14.   After 70% degradation, that is, the output intensity has been reduced down to 30% of the initial intensity, the the forward biased slope of the I-V characteristic decreased.   One reason for the reduction in slope may be an increase in the space-charge recombination component of current [50]. Another cause may be the deterioration of the ohmic contact during degradation. The effective barrier height at the metal/semiconductor interface might be increased by degradation .   The other reason might be the resistance of the layers has increased due to the defects generated near the active region [56].

The diode current is conventionally given by

$$J_d = J_s[\exp(qV_d/nk_BT)-1] \tag{3-16}$$

where Js is the saturation current density of the diode and the factor n equals 2 when the recombination current dominates. The saturation current density, Js, depends on the crystalline quality of the heterostructure near the active layer. If we assume that there is no change in the barrier height in the metal/semiconductor interface, there might be changes in the crystal structure such as point-defect generation and accumulation of point defects. So that the value of Js and n in the above equation may change after degradation. A plot of the equation (3-16) for different values of Js and n is shown in Figure 3.15, and can be compared with the experimental values. This comparison shows that the slope change in I-V curve after degradation may be due to changes in the crystalline structure near the quantum-well active region.

3.4 Temperature in the Active Region during Operation

The temperature of the copper block, on which the LED was mounted, was about 60 °C. The dimension of heat sink was large enough compared to the heat source (300 μm by 300 μm) that the heat might easily be dissipated into the surroundings. The temperature of the copper block may be significantly different from that of the active region of the device. The temperature of a III-V laser diode were estimated by Fukuda et al. [57] and it was around 150 °C at the current density of 5 KA/cm^2. The energy released during the operation of blue light-emitters should be larger

because of the large band gap energy of ZnSe-based II-VI materials. We can suppose that the temperature of the active region would be higher. A method of estimating the temperature of the active region is developed utilizing the fact that the band-gap energy is a function of temperature.

As the current injection level was changed, the wavelength of the emitted light was shifted. Figure 3.16 and 3.17 show that the emission wavelength decreased at higher current levels. Other driving conditions were maintained a constant for this experiment. Figure 3.18 shows that when the duty cycle was increased while the other conditions (5 A/cm^2 current density, 10 KHz repetition rate) were fixed, then the emission wavelength decreased. There are two factors which affect the change of bandgap in the single quantum-well, the free carrier (electron and hole) density and the temperature. The quasi-fermi level in the conduction band goes up as the electron density is increased in a quantum well. On the other hand the quasi-fermi level in the valence band goes down as the hole density is increased. These changes are plotted in Figure 3.11 and Figure 3.12, which show the fermi level change as a function of free carrier density. The increase in current density, therefore broadens the band gap in the single quantum-well. Hence the wavelength would be smaller as the current density increases if only the free carrier density is considered. However, the emission wavelength has be decreased as the current density increases. The amount of bandgap change due to the carrier density can be ignored compared to the band gap change due to the temperature. The

injected current heats the device due to the intrinsic resistance of the whole layers or due to heating from nonradiative recombination at localized defect sites. The temperature of the lattice in the active quantum-well during operation at a certain current density could be important to the degradation process.

In order to estimate the temperature of the active region, the bandgap change at different temperatures was used. First, the emission wavelength was measured with a very small pulse width (less than 1% duty cycle) and a very low current density (0.1 A/cm^2), while the device was heated externally on the heating stage. So that the driving current for measuring the wavelength shift has as little effect as possible on the temperature of the active region due to electron scattering. The result is shown in Figure 3.19 where photon emission wavelength decreases as the external ambient temperature is raised. The band-gap energy was calculated from the peak emission wavelength.

The relationship between the energy band gap and temperature is usually expressed for bulk materials by [58]

$$E_g(T) = E_g(0) - \frac{\alpha T^2}{\beta + T} \tag{3-17}$$

where T is the temperature (K), α and β are the material constants. This equation is applicated in the low temperature regime for low injection levels as in photoluminescence. If we assume that this relationship is valid

at higher temperatures at higher injection levels, then this equation needs to be modified for the single quantum-well case. It can be expressed by

$$E_{e-h}(T) = E_{e-h}(r.t.) - \frac{\alpha T^2}{\beta + T} \qquad (3-18)$$

where E_{e-h} is the energy gap between the electron energy level and heavy hole level. Figure 3.20 shows the experimental data of the relation between the energy gap and the external temperature. The alpha and beta values used to calculate the band gap energy were 310 and 7.5e-4 [eV/°C] respectively and they are fitted well to the experimental data. The actual temperature of the lattice in the quantum well region can therefore estimated from the emission wavelength using Figure 3.20. By extrapolating the curve to higher temperature value, the actual temperature of the active region was estimated to be about 250 °C at a current density of 12.5 A/cm^2 , 20% duty cycle and 10 KHz repetition rate.

This temperature during the device operation a LED mode is relatively high when compared to similar III-V devices. The local temperature at a defect site might be much higher than 250 °C. Kobayashi et al. [59] measured the temperature rise of the dark line spot area during a InGaAsP/InP laser operation. The current density was about 7 KA/cm^2. The infrared thermometer was used and the temperature of the dark spot defect area was much higher than the surrounding area. The temperature difference was about 50 °C.

This high operating temperature in the active region can be explained by many reasons: First, the electrical contacts to the device have barrier heights at the top and bottom electrodes. The turn-on voltage for the LED whose size was 1.5 mm× 2 mm was around 1.8 V. Heating can take place at the metal (Au) / semiconductor interface and the temperature of the active region can be raised by thermal conduction. Secondly the emitted light can be absorbed in the lattice. The energy of the emitted light is large and the temperature rise due to absorption would also be large. Thirdly the temperature increase is believed to occur through nonradiative recombination at crystal defect sites. The process of nonradiative recombination of electron-hole pairs is accompanied by energy transfer to the lattice of the order of the energy band gap. This energy transfer takes place in the form of phonons, that is, lattice vibration which in turn increases the temperature. Finally, the thermal conductivity of II-VI materials is poor. The thermal conductivity of GaAs is 0.5 W/cm-°C and that of Si is 1.3 W/cm-°C at 300 K. On the other hand the thermal conductivity of ZnSe is around 0.1 W/cm-°C. Therefore the temperature can be significantly higher in localized regions.

3.5 Summary

Degradation studies of II-VI ZnSe based LEDs show similar behavior to III-V devices, i.e., the output power decreases exponentially as a function of degradation time. However, II-VI LEDs appear to be much

more sensitive to the current density. If the current density necessary for lasing (0.5-1 KA/cm^2) is applied to LEDs, the LEDs degrade in a period of time similar to that of lasers, implying the degradation of both LED and lasers is similar.

The external efficiency decreases significantly after 50% degradation in electroluminescence. This indicates that the nonradiative recombination rate increases and the radiative recombination rate decreases. This may be as the result of the generation of nonradiative recombination sites in the quantum well. The major nonradiative recombination sites are dark spot defects and dark line defects which can be observed in EL microscopy at 50% degraded LEDs. However, these sites are not visible in the TEM. The I-V characteristic of the degraded devices also implies that the crystalline quality near the quantum well may be damaged.

A method of estimating the temperature of the active quantum-well during LED operation has been established using the band gap dependence on temperature. It was estimated that during LED operation the quantum-well may rise to temperatures as high as 250 °C. This is significantly greater than temperatures of quantum-well in III-V lasers, which typically do not exceed 150 °C.
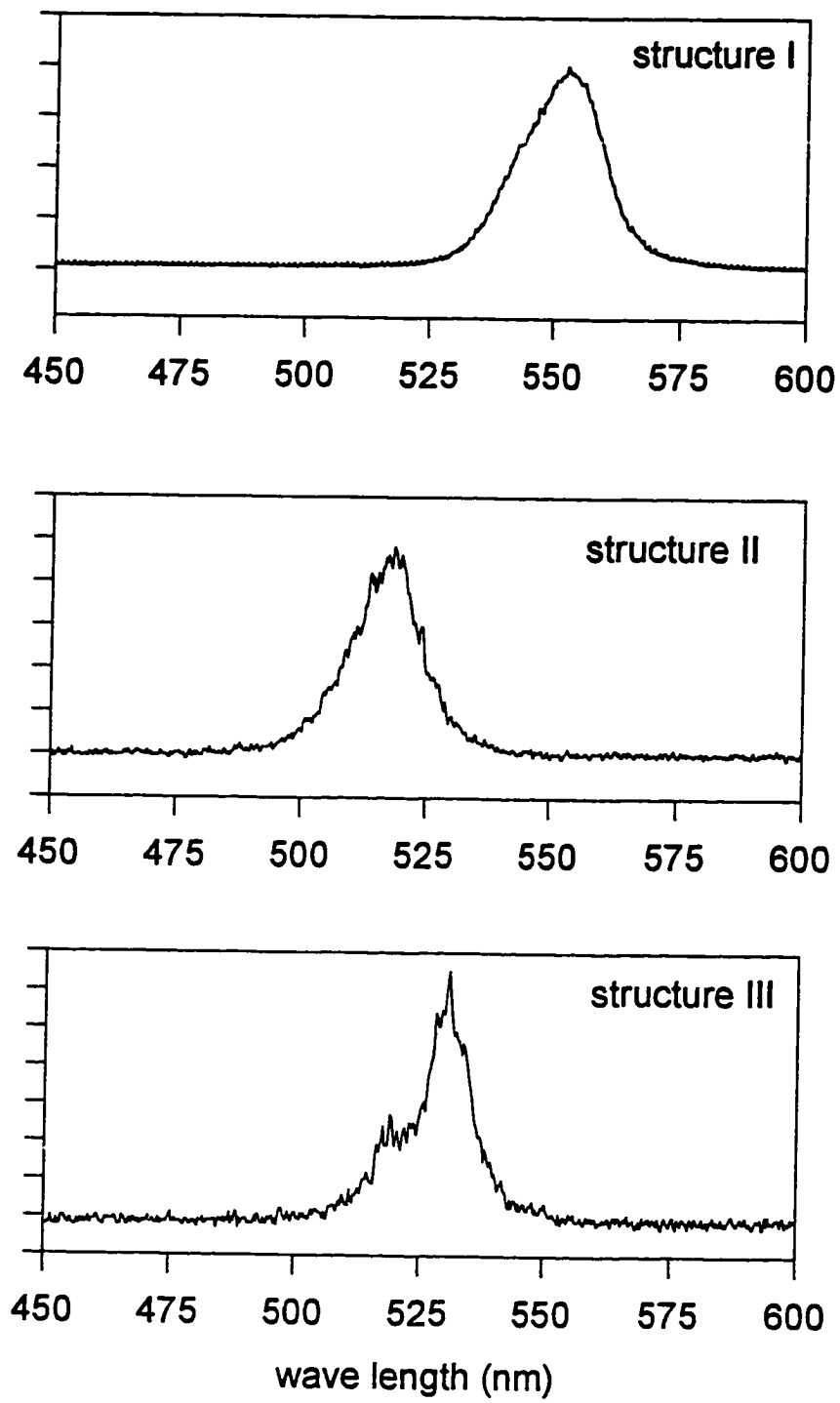
Figure 3.1.   Wavelength of emitted lights form ternary-based SCH (top), simplified ternary-based heterostructure (middle) and quaternary-based SCH (bottom)
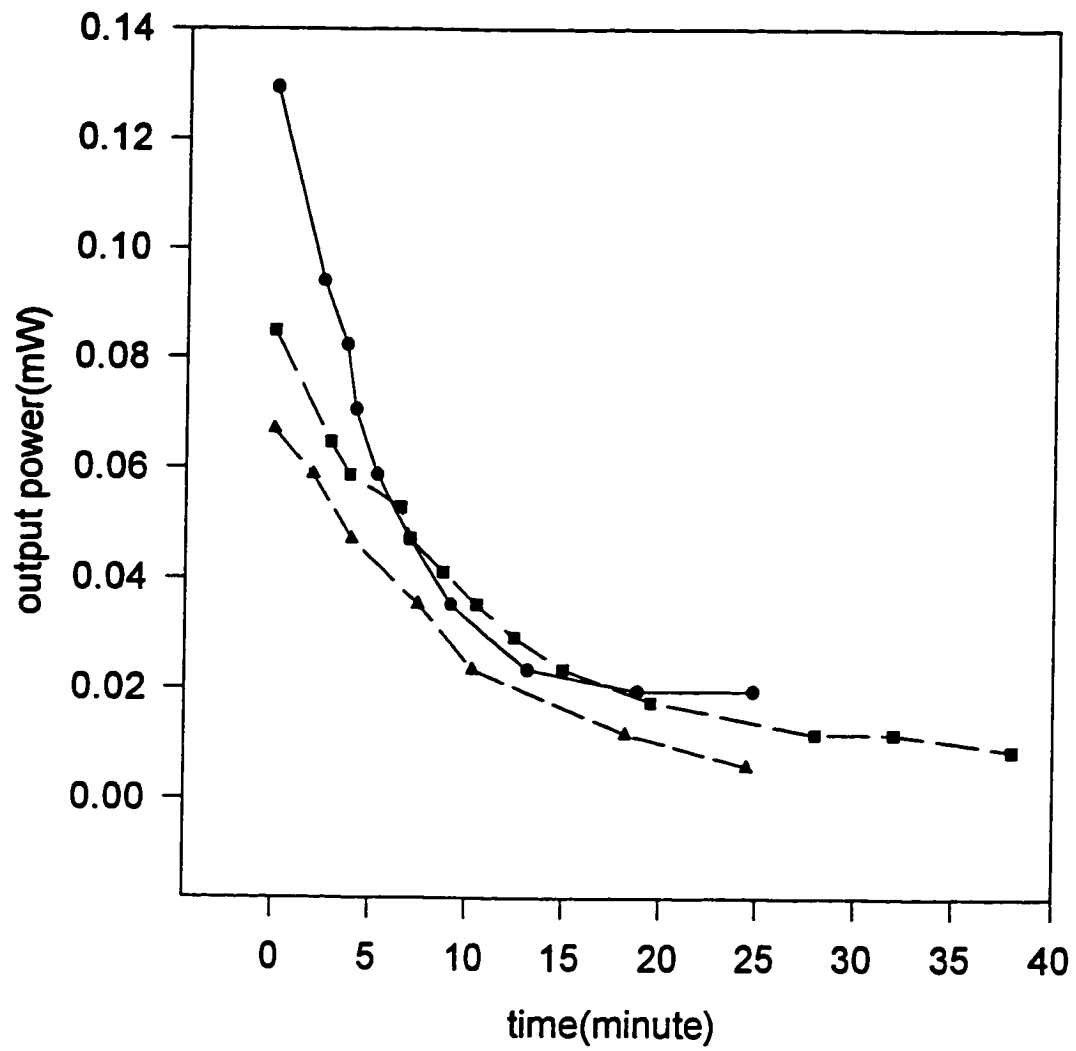
Figure 3.2.   General degradation trend showing that the output power decays
exponentially as function of time for ternary-based SCH
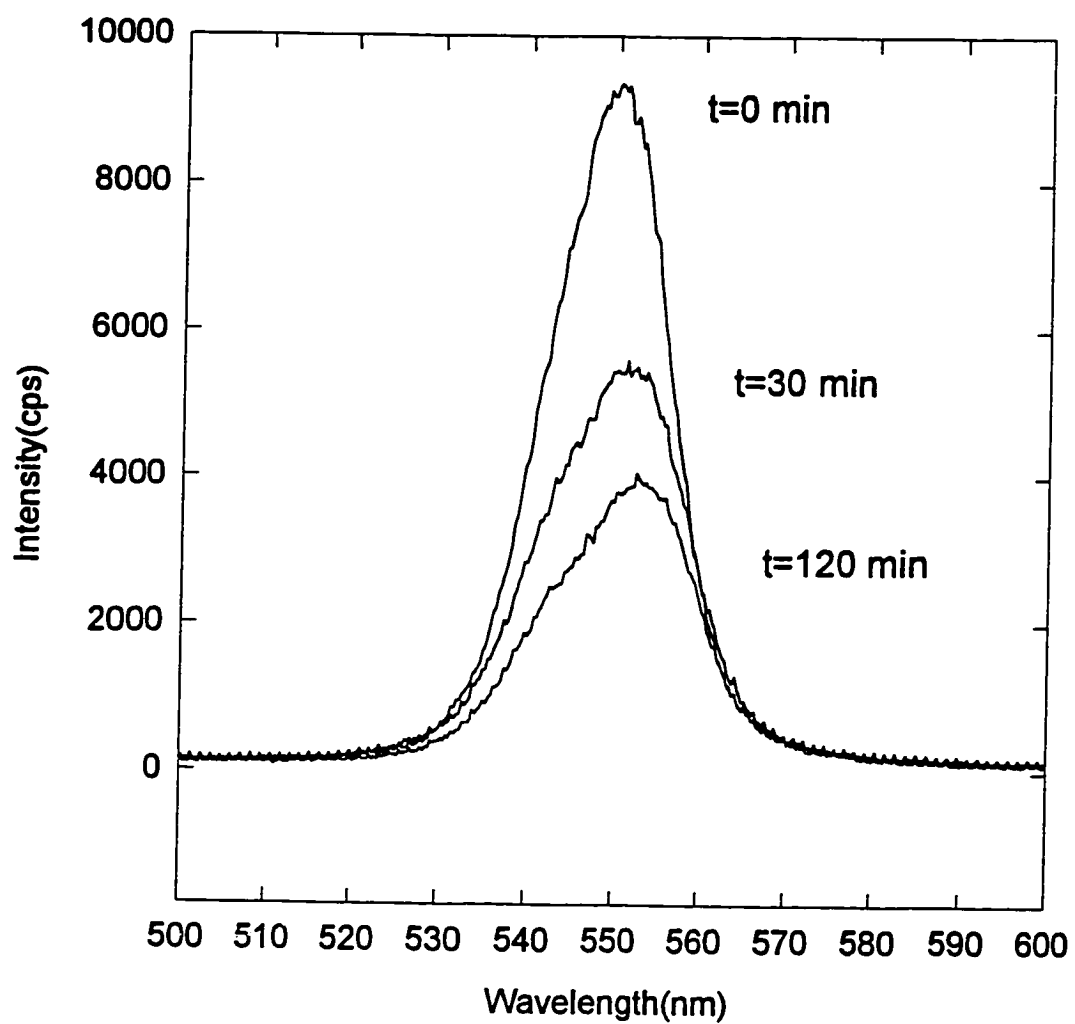
Figure 3.3.   Output intensity decrease as a function of time during operation of a LED fabricated from the ternary-based SCH.
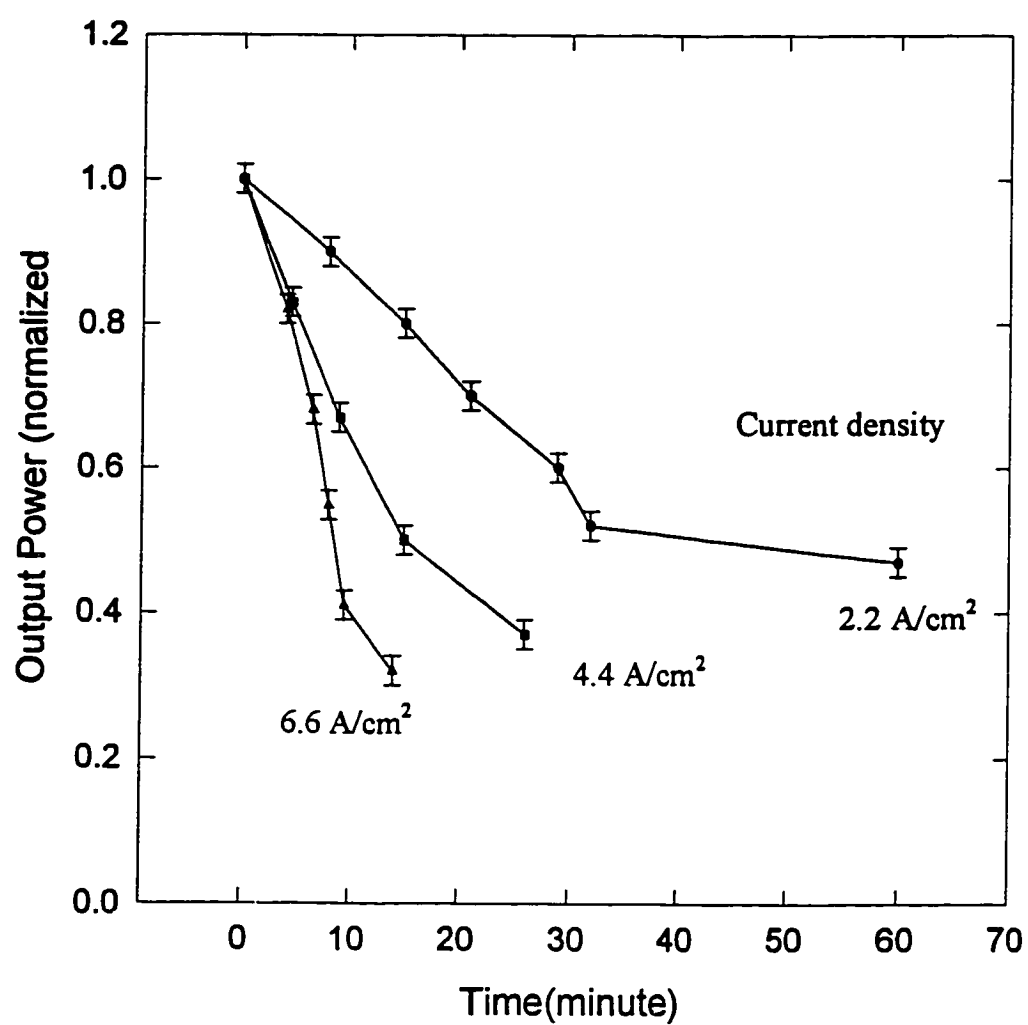
Figure 3.4.   Output power dependence on the current density. LEDs were fabricated from the ternary-based SCH.
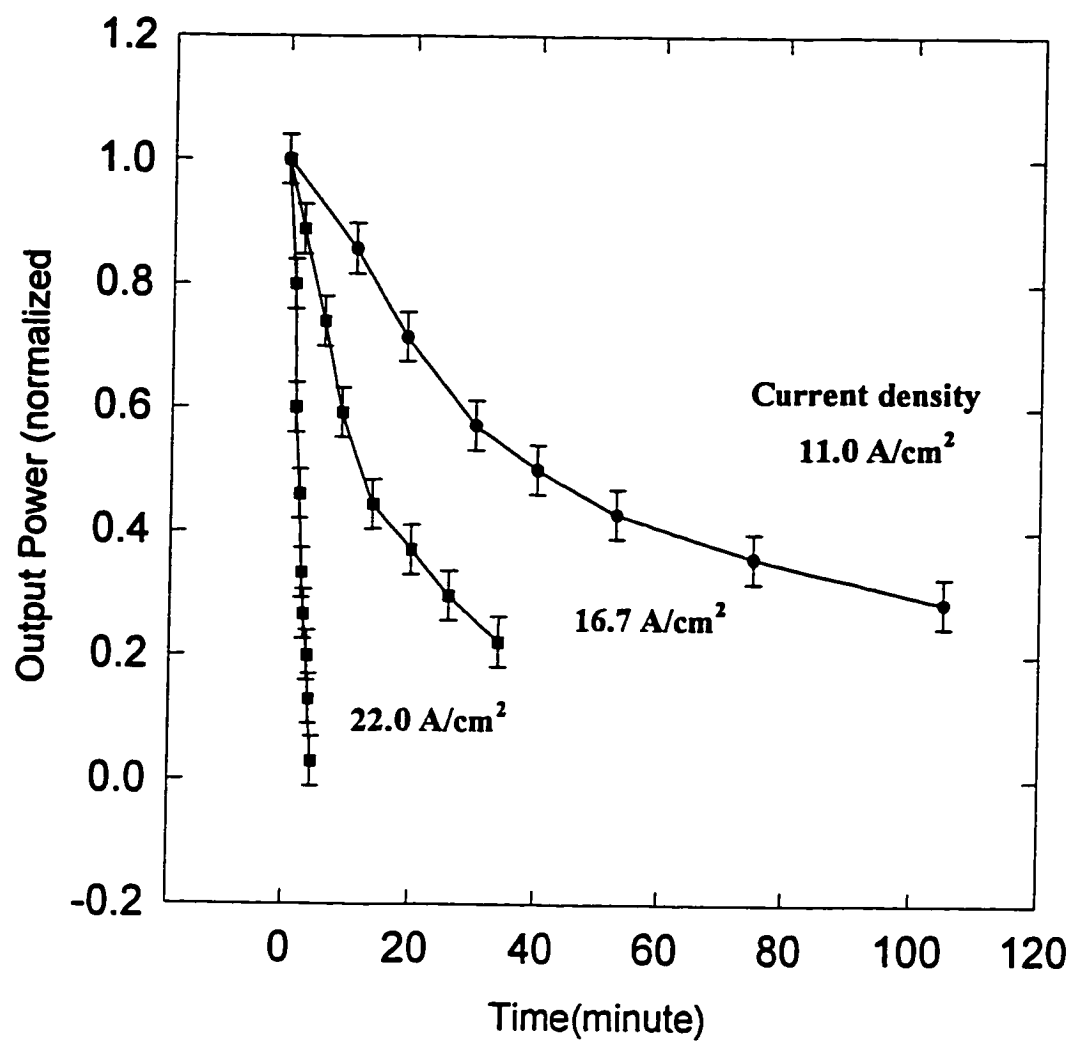
Figure 3.5.   Output power dependence on the current density. LEDs were fabricated from the simplified ternary-based heterostructure.
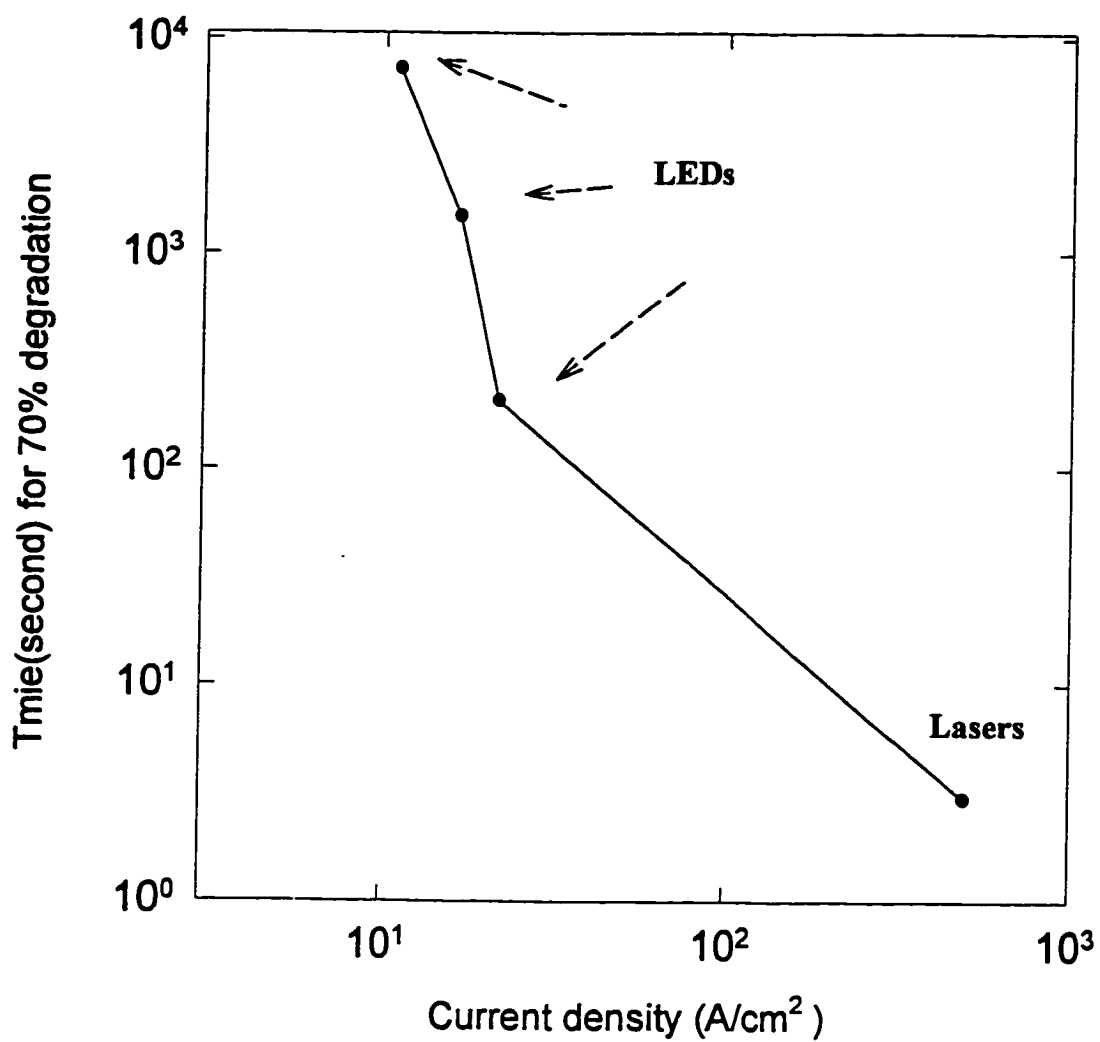
Figure 3.6.   Current density projection to the level of threshold current density of lasers
for 30% degradation for the simplified ternary-based heterostructure
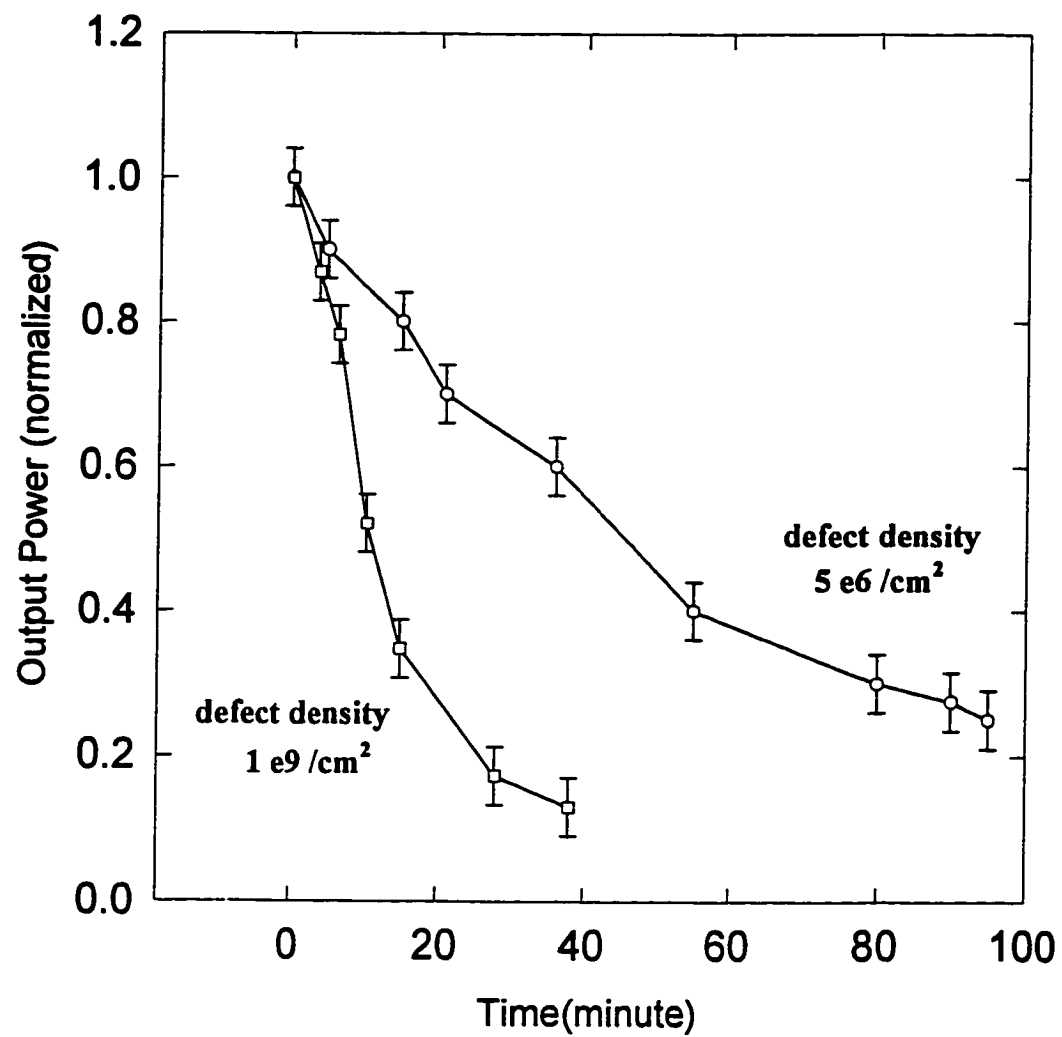
Figure 3.7.   Degradation dependence on the pre-existing defect density
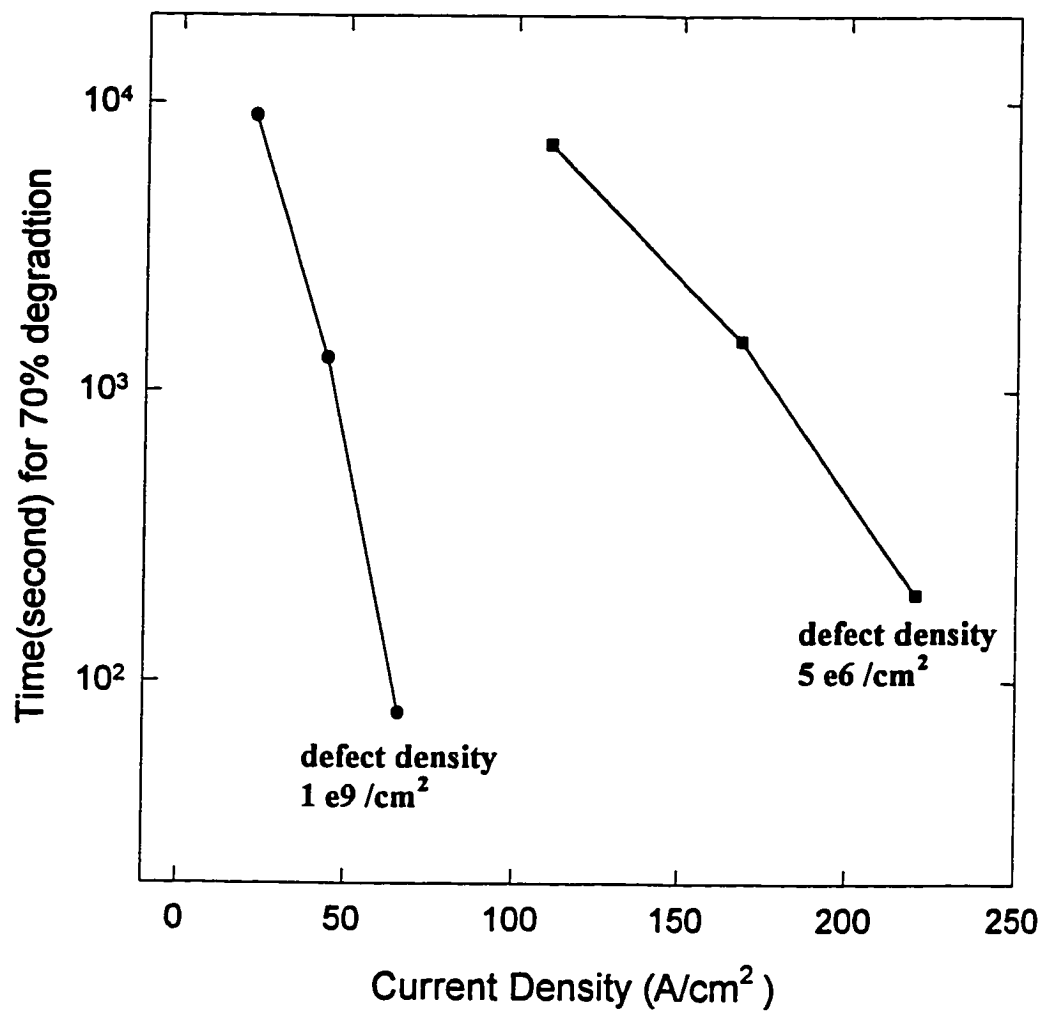
Figure 3.8. Comparison of the time for 70% degradation at different defect densities
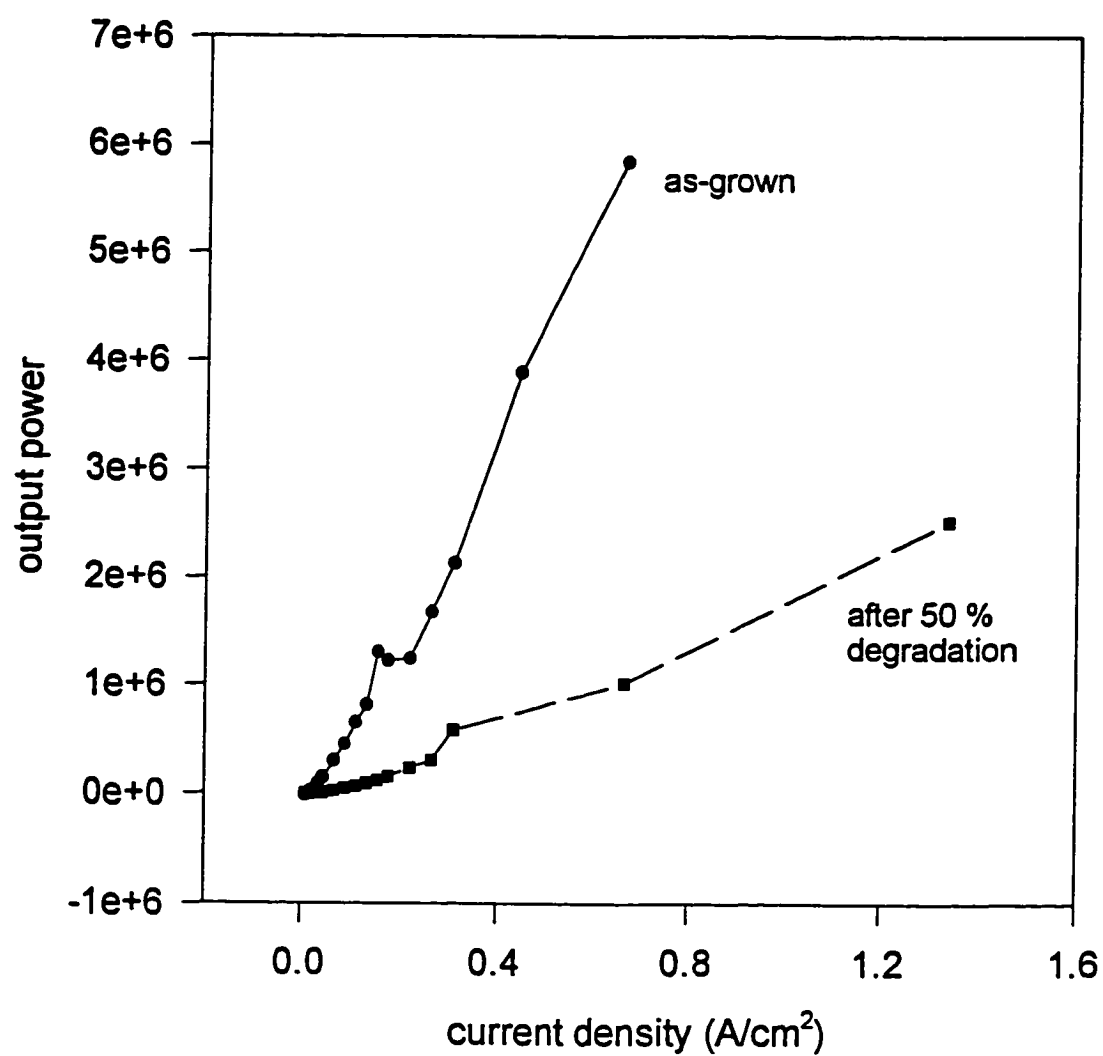
Figure 3.9.   Light output power-current density relation (Efficiency) measurements before and after 50% degradation for quaternary-based SCH

light output power

Spontaneous
emission
(LED mode)

Stimulated
Emission
(laser mode)

←

Threshold Current
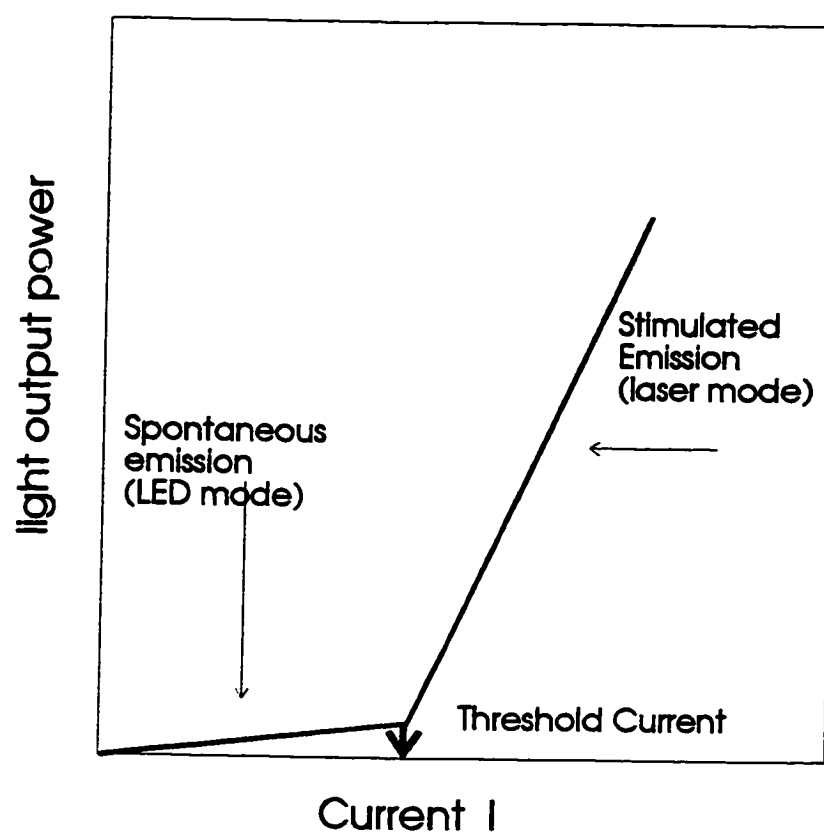
Current I

Figure 3.10.   Typical relation between current and light output power for lasers
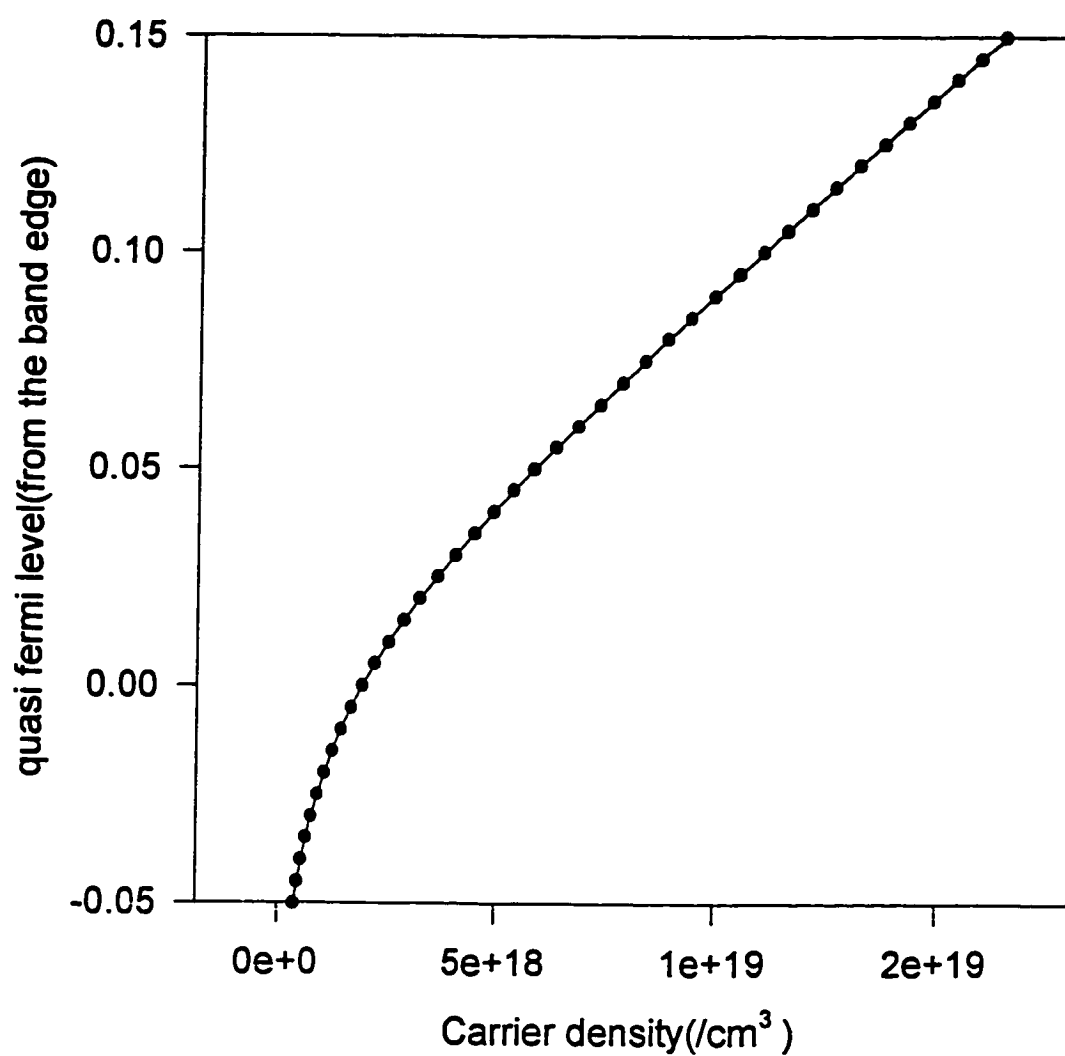
Figure 3.11.   Quasi-fermi level as a function of electron density in the conduction of the ZnCdSe quantum-well
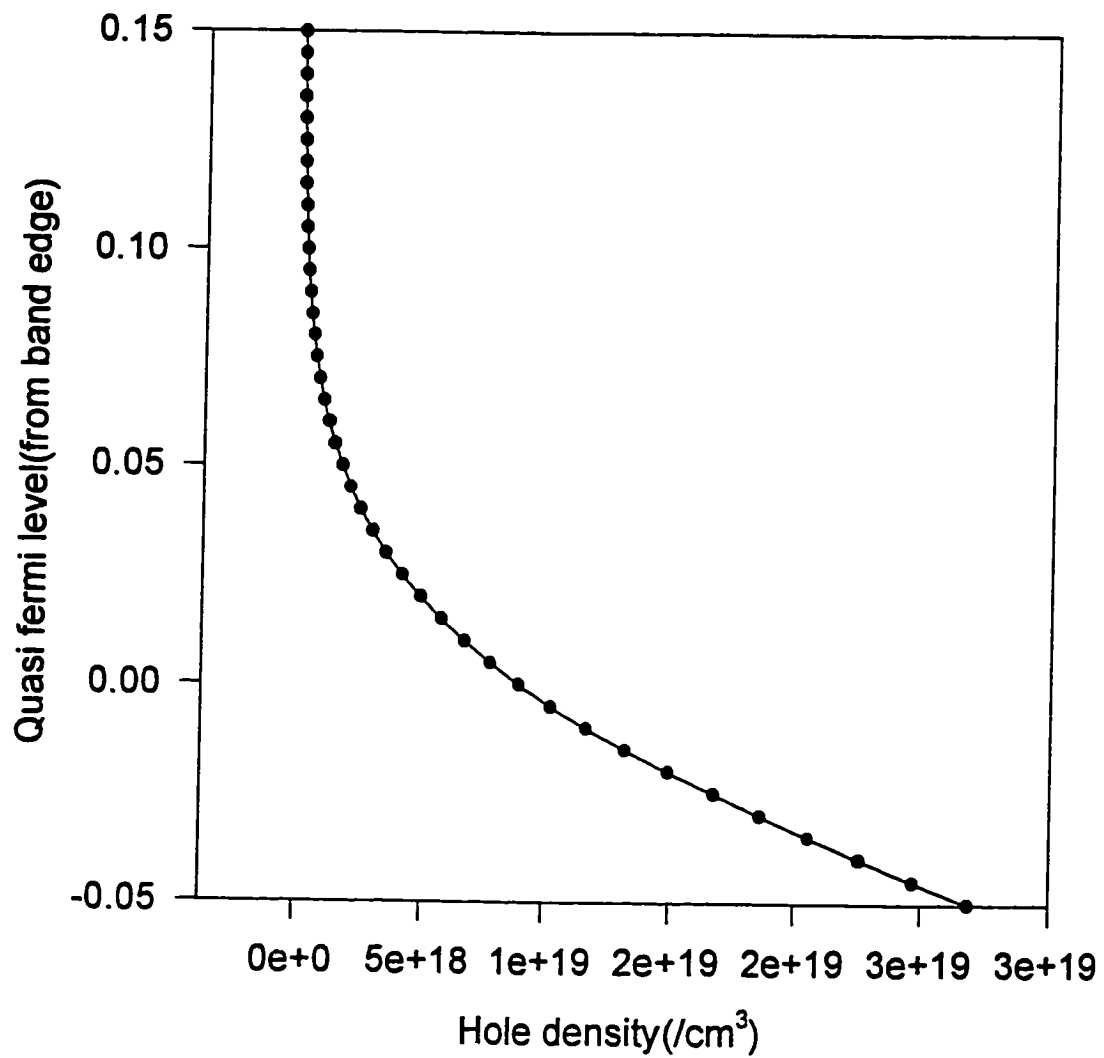
Figure 3.12. Qusi-fermi level as a function of hole density in the valence band of the ZnCdSe quantum-well
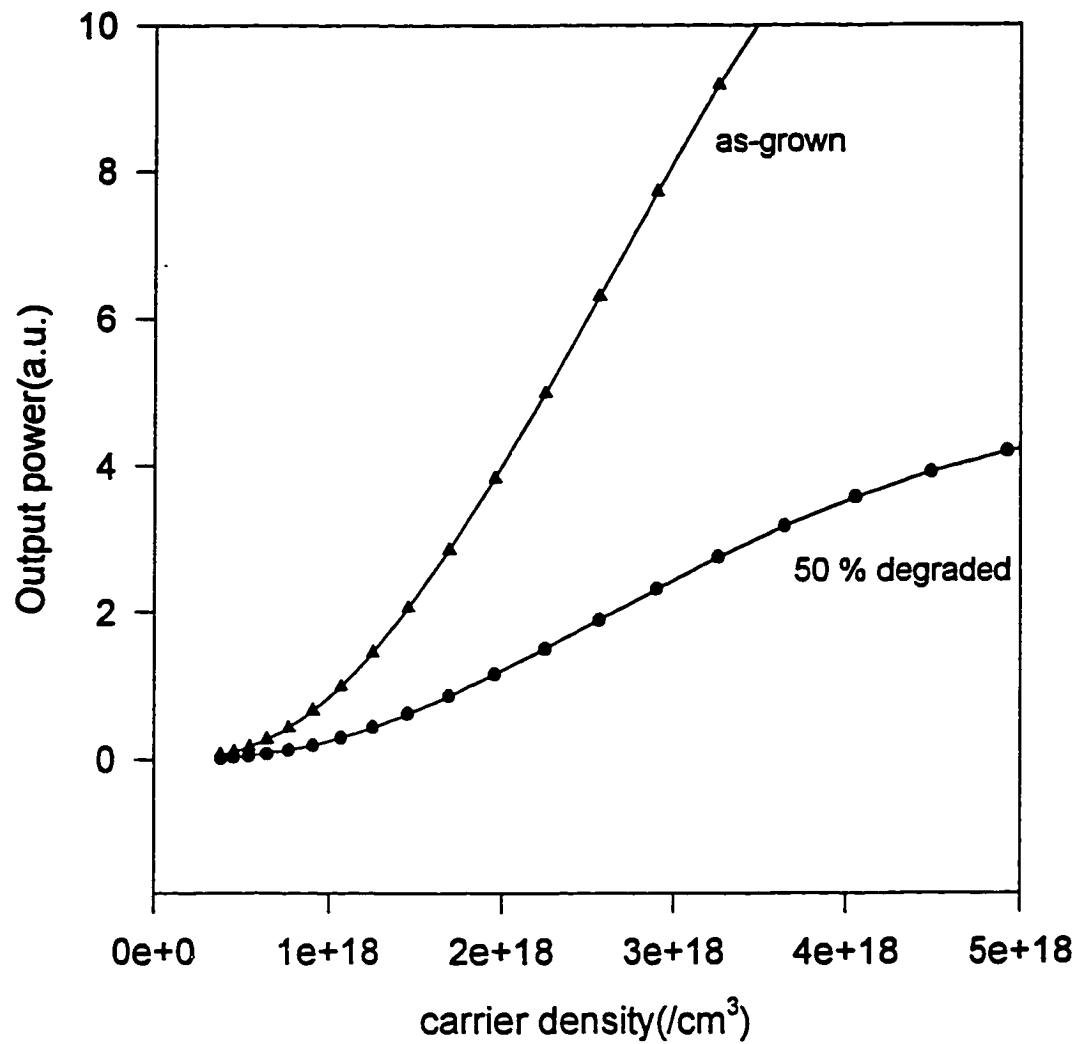
Figure 3.13.   Calculation of Light output power vs carrier density using the analytical equation (3-15) being Aa= 0.2, Ba=0.4 for the as-grown device and Ad=0.5, Bd=0.12 for the 50%-degraded quaternary-based SCH
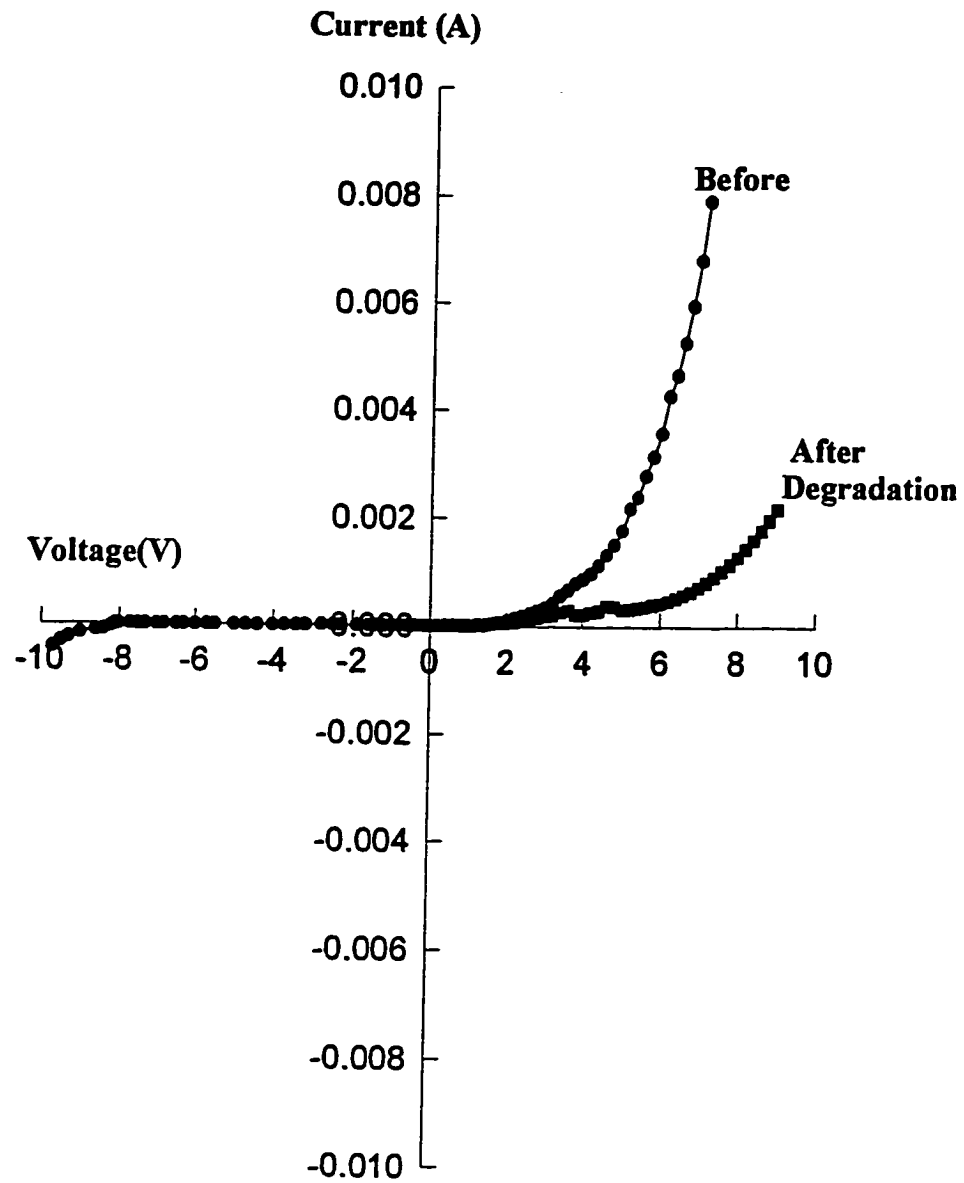
Figure 3.14. Current- voltage characteristics of as-grown LEDs and 80%-degraded LEDs fabricated from ternary-based SCH
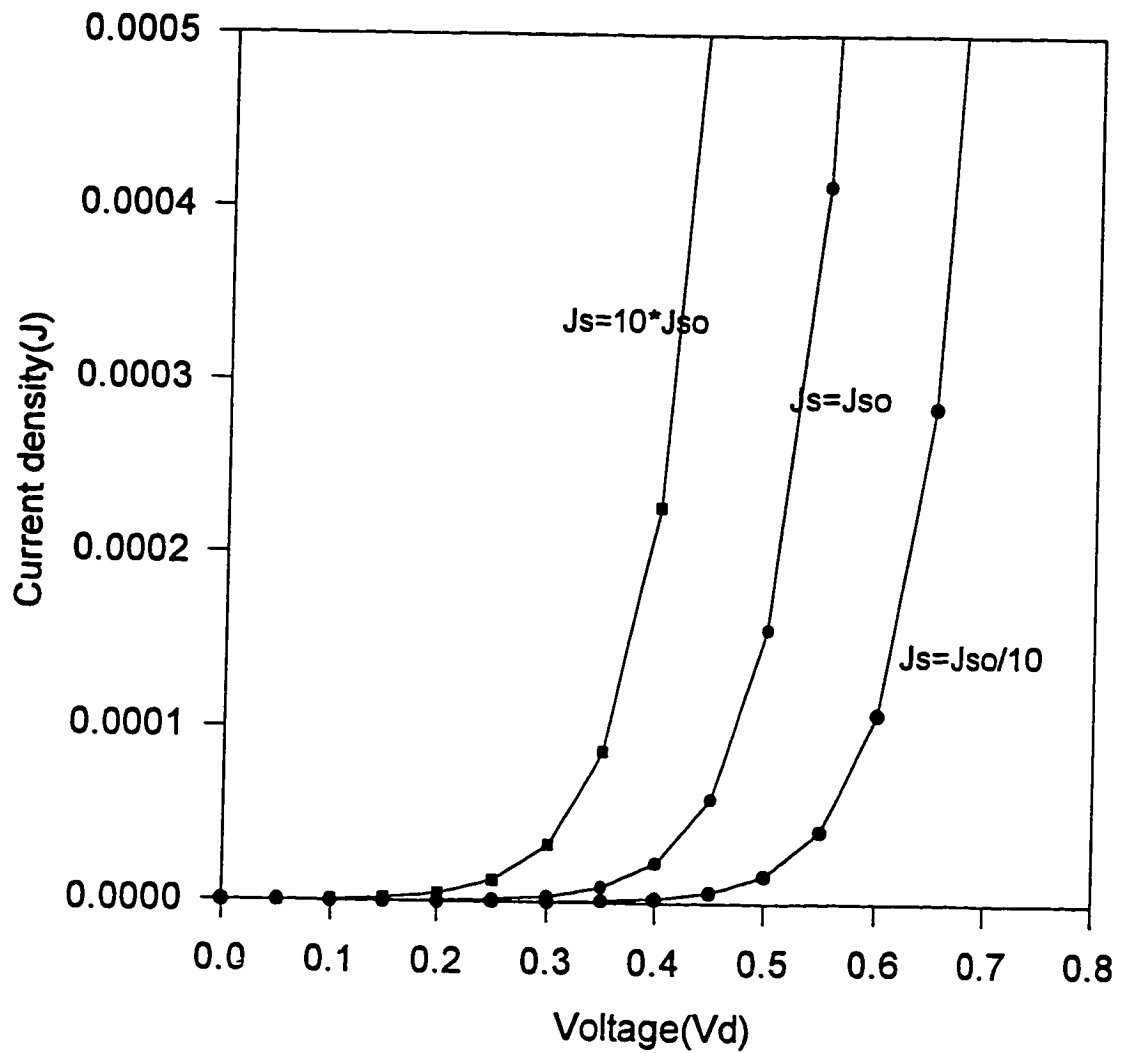
Figure 3.15.   Calculation of I-V characteristics for different values of Js according to equation (3-16)
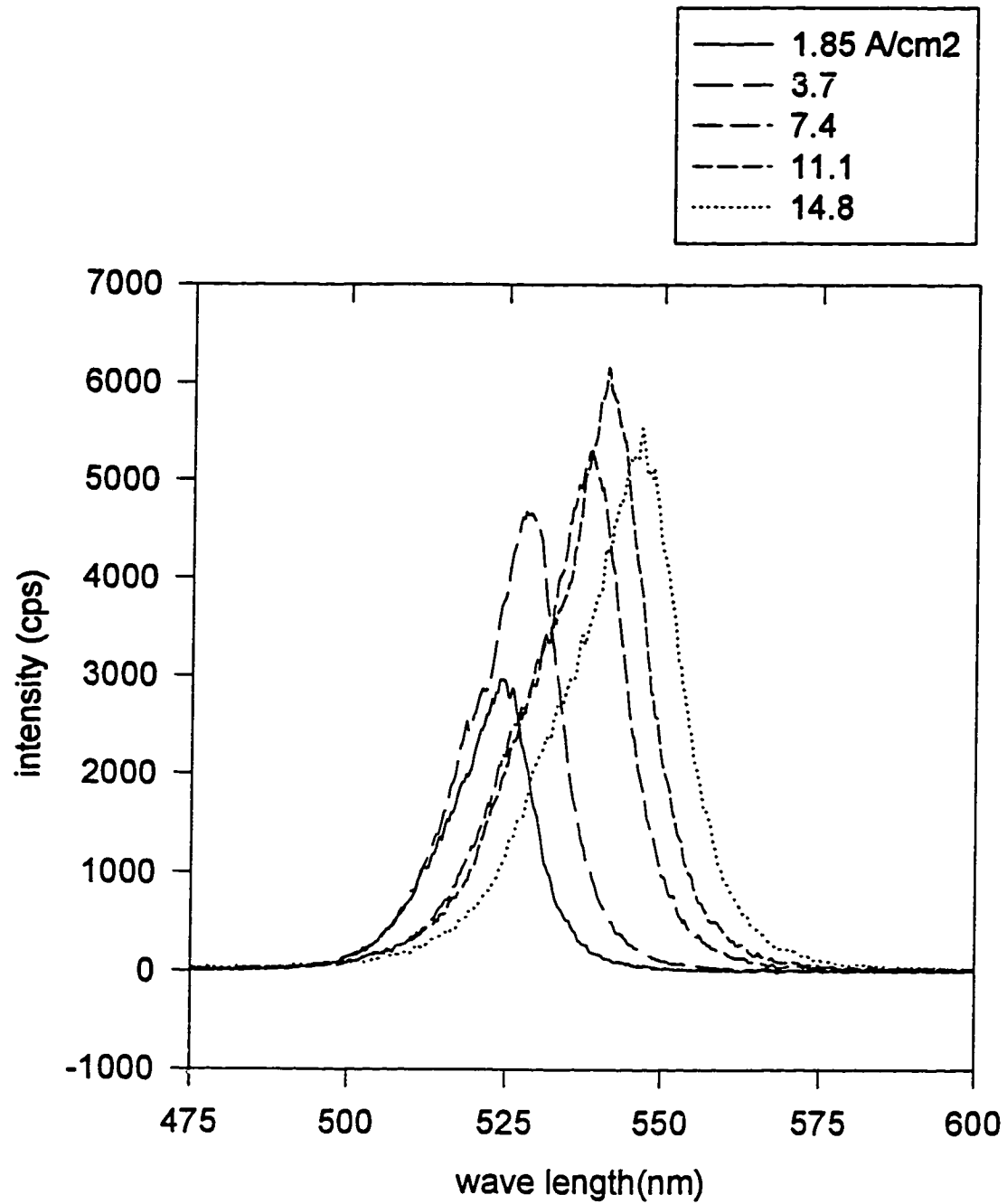
Figure 3.16. Wavelength change of the output light at different current densities (at 40% duty cycle and 10 KHz repetition rate) for quaternary-based SCH
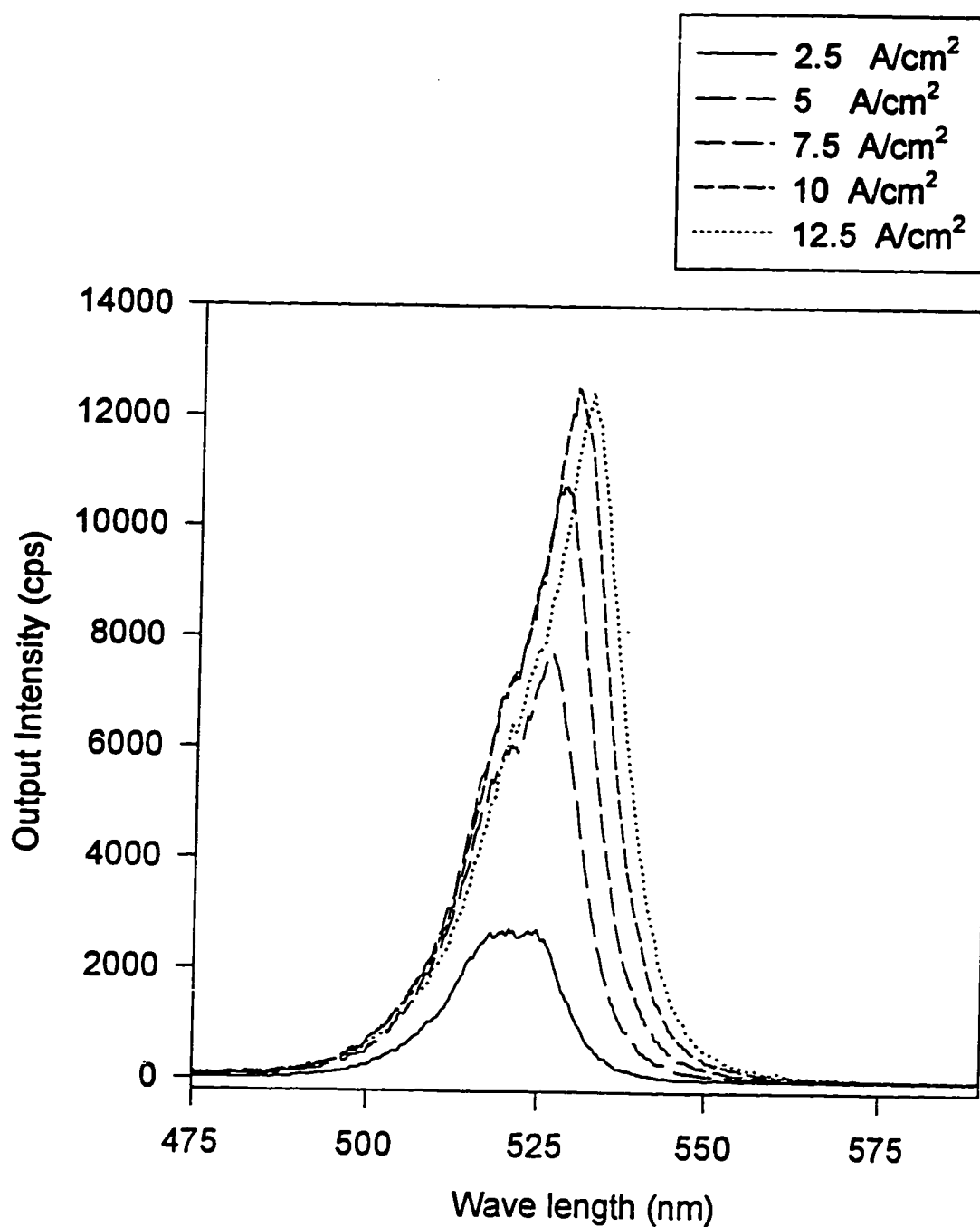
Figure 3.17. Wavelength change of the output light at different current densities (at 10% duty cycle and 10 KHz repetition rate) for quaternary-based SCH
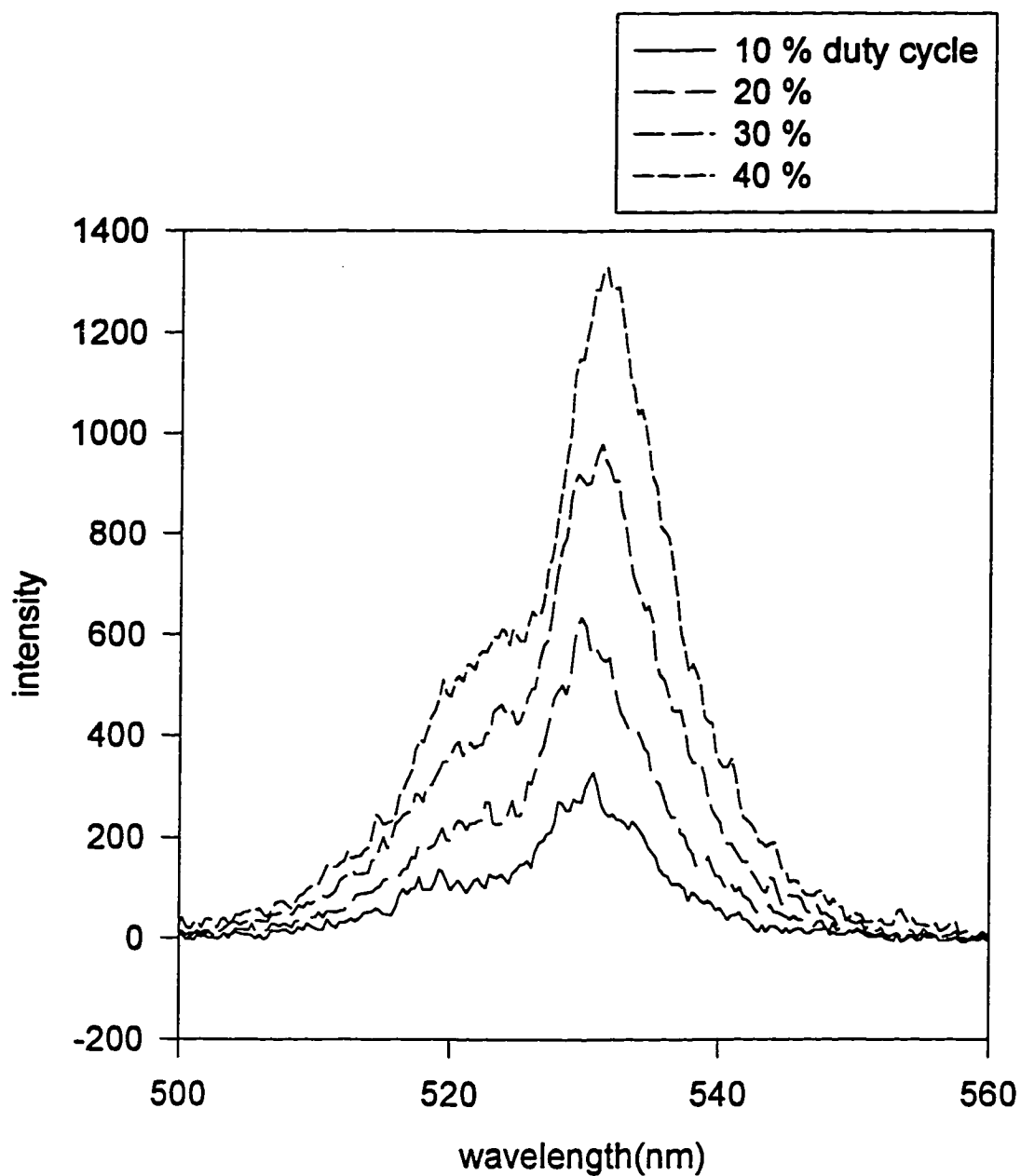
Figure 3.18.   Wavelength change at various duty cycle at the other driving
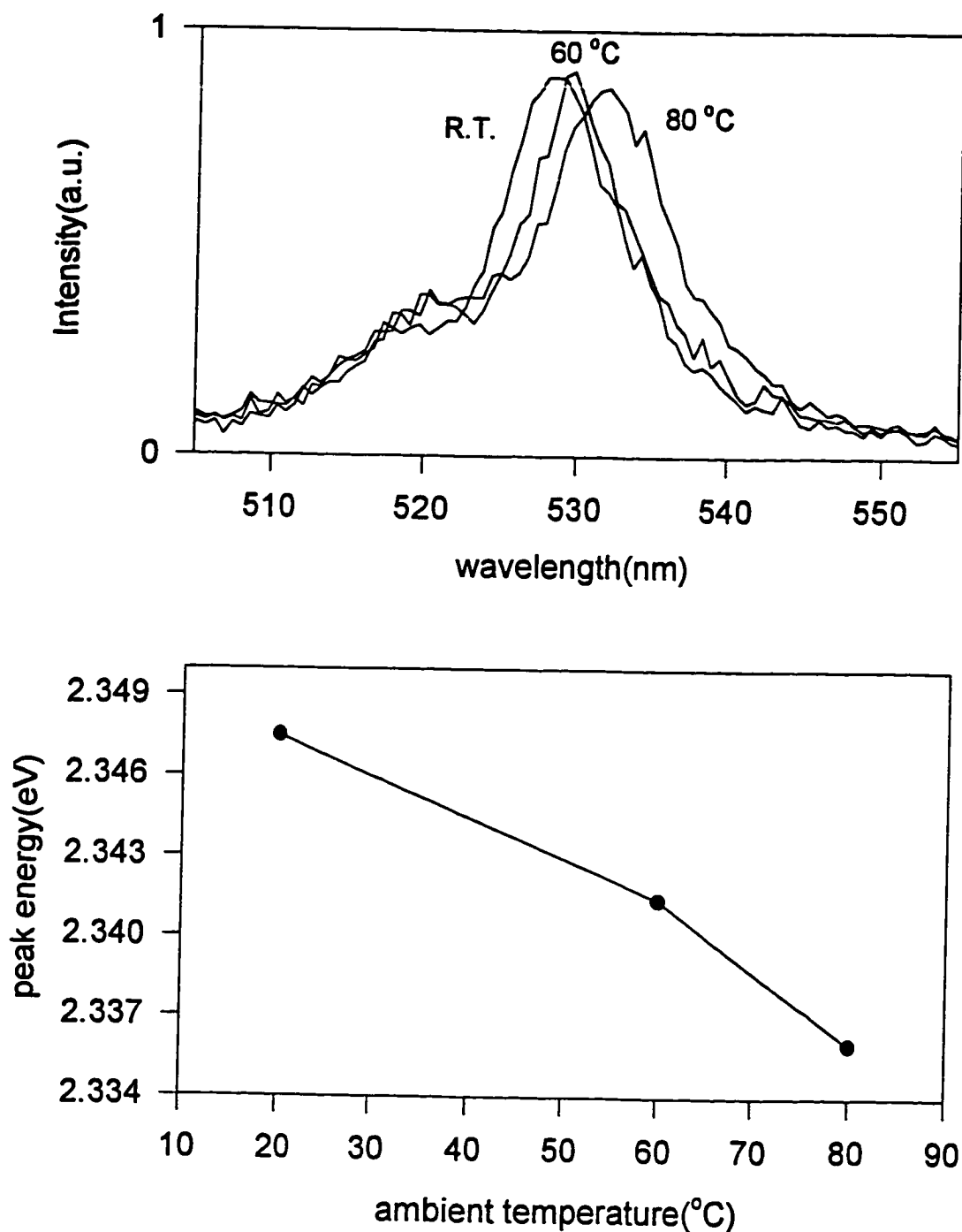conditions constant for the quaternary-based SCH

Figure 3. 19.   Wavelength at various ambient temperatures of the device (above) and peak energy of the emitted light at those ambient temperatures(below). LEDs were fabricated from the quaternary-based SCH.
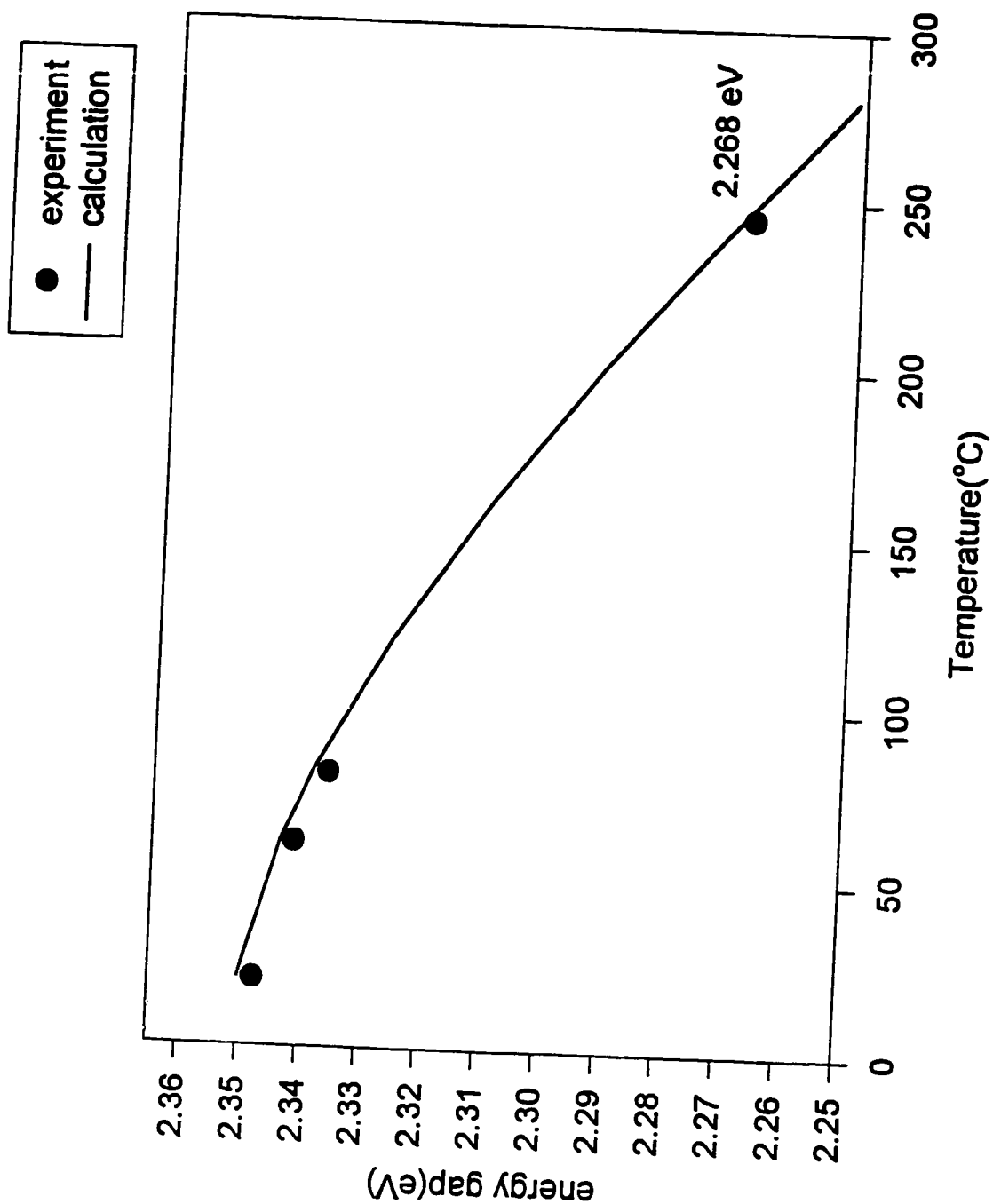
Figure 3.20.　Relationship of temperature and band-gap (calculated using the equation (3-18))

CHAPTER 4
INTERDIFFUSION AND STRAIN RELAXATION IN THE QUANTUM-WELL

The temperature of the active region of LEDs during operation was estimated to be about 250 °C in the previous chapter. The temperature of the active area for II-VI LEDs is typically much higher than that of III-V devices. This high temperature may play an important role in the rapid degradation of in II-VI light emitting devices. Parbrook et al. [60] investigated interdiffusion in ZnS/ZnSe, ZnSe/CdSe and ZnS/CdS superlattices by annealing in purified hydrogen flow. They showed that the interdiffusion of anions is not found to be significant at temperatures below 550 °C. On the other hand, Zn and Cd interdiffusion was observed at temperatures as low as 400 °C. This suggests that such interdiffusion may lead to disordered or graded interfaces at temperatures of about 400 °C.

Although the temperature of the over all area is around 250 °C during LED operation, temperatures may be higher locally at the vicinity of defect sites. Since it is believed that nonradiative recombination at crystal defects can occur which in turn transfers thermal energy to the surrounding lattice in the form of phonons [61]. The amount of energy transferred is of the order of the energy band gap. If this phonon energy is accumulated in the vicinity of the defect, the temperature may increase locally at the defect

80

site. This heating by nonradiative recombination via defects would induce defect reactions, such as defect annealing, defect diffusion and clustering, and new defect generation. Defects with near mid-gap levels are liable to have a particularly strong electron-lattice interaction and the recombination enhanced defect migration for such centers has been observed in Si, GaAs and GaP [62][63][64].

The band-gap of materials used in the present study is around 2.5 eV which is of the order of the activation energy for metal self diffusion in II-VI compounds [65]. Thus the nonradiative recombination induced reaction can take place more easily in II-VI compounds. Possible reactions in the active region during LED operation were investigated in this chapter, that is, atomic interdiffusion at the interfaces of the quantum-well and the strain change in the quantum-well. In order to understand the strain state of the quantum well during operation, it is necessary to understand the thermal expansion behavior of epilayers at the normal operation temperature.

4.1 Thermal Expansion Behavior of the Epilayers

The thermal expansion of ZnSe has been known to be higher than that of GaAs [66][67]. Figure 4.1 shows the difference in the coefficient of thermal expansion (CTE) between GaAs and ZnSe as a function of temperature with the CTE increasing with increasing temperature. The difference in thermal expansion coefficients existing in the heterojunction

causes the lattice to be strained. If the coherency of the heterojunction is maintained at the operating temperature, then the quantum well would be under more strained at the higher operating temperature than the original strain state (at room temperature). The thermal expansion is a material characteristic and can not be controlled. The effect of the thermal expansion in the strain state was investigated by measuring the lattice parameter of the epilayer at higher temperatures using HRXRD rocking curves. Because of the small dimension of the single quantum well in the real LED structure, it is very difficult to isolate diffracted x-ray signal from the 50 $\overset{\circ}{A}$ thick quantum well. A single layer structure of ZnSSe on GaAs was therefore used for this measurement.

p-type and n-type $ZnS_{0.6}Se_{0.94}$ layers were grown on the GaAs substrate by molecular beam epitaxy. The single epilayers were grown at around 275 °C and doped with nitrogen and chlorine respectively. The thickness of both these epilayers was 1.5 μm. The content of sulfur was measured using electron microprobe analysis. An average of five measurements across the surface of the specimen were made to evaluate the sulfur content. Using ZnSe and ZnS standards the sulfur content was determined to be 6.0 atomic %. At this composition the epilayer is either theoretically lattice matched to the GaAs or the mismatch is accommodated by tetragonal distortion. The net acceptor concentration in the p-type $ZnS_{0.06}Se_{0.94}$ layer was around 10^{17} /cm^3 and the free carrier concentration

in n-type $ZnS_{0.06}Se_{0.94}$ was about 10^{18} /cm^3, which are comparable to those used in actual devices.

In order to measure the lattice parameter of the epilayer at high temperatures, a sample heating stage was designed and installed on the high resolution x-ray diffractometer. A schematic of the sample heater is shown in Figure 4.2. The sample temperature was controlled and monitored by an Omega CN7600 temperature controller during x-ray analysis. The temperature of the sample was raised up to 250 °C, which is about the temperature of the active region of the device. The fluctuation of sample temperatures was less than ±3 °C.

4.1.1 Measurement and Calculation Procedure

Since the epilayer unit cell is tetragonally distorted, the lattice parameter of the layer parallel and perpendicular to the interface needs to be measured. The procedures used were as follows:

(1) The lattice parameter of the GaAs substrate (a_{sub}) was determined at different temperatures from 20 °C to 250 °C using Bond's method [68]. Only the (004) symmetric reflection was used because the GaAs substrate is considered as bulk and the shape of unit cell would remain cubic at different temperatures. Every reflection is taken twice, once directly (ω_d) and once with incident and reflected beams reversed (ω_r). Then the Bragg angle can be calculated by

$$\theta_B = 90^o - \frac{(\omega_d - \omega_r)}{2} + \phi \qquad (4-1)$$

where θ_B is the Bragg angle, ϕ is the angle between the surface and reflection plane($\phi = 0$ for (004) plane) and ω_d, ω_r are the peak positions. From the Bragg angle the spacing, d, between (004) planes is simply obtained by

$$n\lambda = 2d\sin\theta_B \qquad (4-2)$$

where λ is the wavelength of the incident radiation.

(2)   The relative lattice mismatch in both parallel and perpendicular directions were determined using an asymmetric reflection and assuming tetragonal distortion of the epilayer [69][70]. As shown in Figure 4.3, the Bragg condition for an asymmetric plane making an angle ϕ with the crystal surface is satisfied at two different ω angles, $\omega_1 = \theta - \phi$ and $\omega_2 = \theta + \phi$. Before obtaining asymmetric rocking curves, An optimization procedure was performed which is described in the manual [71] to accommodate for miscut of the substrate and mistilt of the epilayer. From x-ray rocking curve scans, the values of ω_1 and ω_2 were determined for both epilayer and substrate and subsequently the values of θ and ϕ for both epilayer and substrate were obtained. The mismatches were then determined as follows:

Parallel lattice mismatch:

$$\left(\frac{\Delta a}{a}\right)_{\text{II}} = \left(\frac{a_{epi} - a_{sub}}{a_{sub}}\right)_{\text{II}} = -\Delta\phi\cot\phi_{sub} - \Delta\theta\cot\theta_{sub} \qquad (4-3)$$

Perpendicular lattice mismatch :

$$\left(\frac{\Delta a}{a}\right)_{\perp} = \left(\frac{a_{epi} - a_{sub}}{a_{sub}}\right)_{\perp} = \Delta\phi \tan\phi_{sub} - \Delta\theta \cot\theta_{sub} \, t \qquad (4\text{-}4)$$

where $\Delta\theta = \theta_{epi} - \theta_{sub}$, $\Delta\phi = \phi_{epi} - \phi_{sub}$.

(3) The lattice constant of the deformed unit cell of the epilayer ($a_{epi(\perp)}$ and $a_{epi(ll)}$) was determined from the substrate lattice parameter obtained from (1) and the mismatch determined from procedure (2).

(4) The values of the relaxed lattice constant (a_o) of the epilayers were calculated by [72] [73]

$$a_o = \frac{a_{epi(\perp)} + 2(c_{12}/c_{11})a_{epi(ll)}}{1 + 2(c_{12}/c_{11})} \qquad (4\text{-}5)$$

The elastic constants for ZnSe are that $c_{11} = 8.5 \times 10^{10}$ N/m^2 and $c_{12} = 5.0 \times 10^{10}$ N/m^2. For ZnS $c_{11} = 10.4 \times 10^{10}$ N/m^2 and $c_{12} = 6.4 \times 10^{10}$ N/m^2 [74][75]. The elastic constants of ZnSSe was obtained by interpolation assuming there is a linear relationship.

4.1.2 Result and Discussion

The lattice mismatches and the relaxed lattice constant evaluated at different temperatures are shown in Table 4.1. For ZnS$_{0.06}$Se$_{0.94}$ /GaAs lattice-mismatched epilayer, the lattice-mismatch in the perpendicular direction increases as the temperature is raised. On the other hand, the lattice-mismatch parallel to the surface is not as significantly temperature dependent. The x-ray rocking curves were presented in Figure 4.4 and Figure 4.5 show that the ZnSSe layer appears to be closely lattice-matched at room temperature, however, a lattice-mismatch is clearly observed at

250 °C (since the separation between peaks increases) in both (004) symmetric reflection and (115) asymmetric reflection. As the temperature is increased the parallel mismatch remains the same which means that the coherency at the interface is maintained at 250 °C. The lattice matched structure of ZnSSe/GaAs can therefore remain lattice matched up to 250 °C. The increased lattice mismatch as observed in the various rocking curves is mostly accommodated in the perpendicular direction to the interface. It is to be noted that if the lattice constants are well matched at the growth temperature by changing the epilayer composition, the lattice constants will be significantly mismatched at room temperature and the epilayer lattice will be distorted and thus additional strain can be introduced solely due to the difference in thermal expansion.

In the structures used in this study, a $ZnS_{0.06}Se_{0.94}$ layer employed as the barrier layer. However, thermal expansion of the entire II-VI epilayer structure would take place in the fashion described above, that is, we can assume that the II-VI ZnSe-based epilayers on the GaAs substrate expand almost entirely in the perpendicular direction. The coherency at the heterojunctions also be sustained in our structures at the operation temperature of 250 °C. At this normal operating temperature the amount of strain in the ZnCdSe quantum-well would be increased by about 15%, assuming the thermal expansion of ZnCdSe is about the same as that of ZnSSe. The strain in the quantum-well for the as-grown structure at the room temperature is 1.3%. Therefore, the strain in the quantum-well during

operation would be about 1.5%. Therefore two factors, that is, high operating temperature and increased strain introduced during operation should be considered in the degradation mechanism.

Table 4.1. Lattice mismatch at higher temperatures

Sample temperature	room temp.	100 °C	250 °C

Lattice mismatch(ppm)
    parallel direction
    perpendicular direction
	10
	150
		10
		600
			10
			1400

Relaxed lattice constant
($\overset{\circ}{A}$)
    ZnSSe
    GaAs
	5.6534
	5.6533
		5.6567
		5.6556
			5.6645
			5.6612.

4.2 Atomic Interdiffusion During Operation

In order to investigate possible atomic interdiffusion near the quantum well, LEDs were degraded down to 50% of the initial output intensity. Low temperature PL measurements and SIMS depth profiling were performed on the as-grown and degraded structures LEDs were fabricated from the simplified ternary-based heterostructure (structure II) and quaternary-based SCH (structure III). No changes were observed in the PL peak position of the ZnCdSe quantum-well as shown in Figure 4.6 and Figure 4.7 after 50% degradation. If there was any interdiffusion at the

interface between ZnCdSe and ZnSSe, a ZnCdSSe quaternary layer would have formed. The PL peak from the quantum-well depends on the band-gap and hence the composition. Thus changes in the shape and position of the quantum well peak would be expected for any change in composition. A theoretical calculation of the band-gap energy for the quaternary $Zn_{1-x}Cd_xS_ySe_{1-y}$ compound is shown in Figure 4.8. If a graded layer of the quaternary compound had formed at the interface, the PL peak would be shifted or broadened to the higher energies. No such change was observed suggesting very little interdiffusion.

A comparison of the full width at half maximum (FWHM) between the as-grown and degraded structure shows no broadening of the quantum-well peak after 50% degradation. Low temperature PL spectra of the quantum-well is usually influenced by the interface abruptness, compositional variation and disordered and/or graded heterointerfaces [76]. These inhomogeneous contributions to the linewidth can be monitored by low temperature PL because the quantum well luminescence is dominated by excitonic transitions. At low temperature purely excitonic transitions are believed very narrow and ideal for monitoring small inhomogeneous characteristics of the structure. The FWMH line width from the ZnCdSe quantum well is the same for both as-grown and 50%-degraded LEDs. This indicates that the compositional fluctuations and the interface abruptness were maintained even after 50% degradation.

SIMS depth profiling was performed on as-grown and degraded samples. The samples were degraded down to 50% and 30% of the initial output intensity. No significant change in the Cd composition profile was observed at the ZnCdSe quantum-well as shown in Figure 4.9.

4.3 Relaxation of Strain in the Quantum-Well

The ZnCdSe quantum-well is only layer in the ternary and quaternary based SCH that is strained and tetragonally distorted. The quantum well layer is under the biaxial compression. The strain in the quantum-well could be relaxed during degradation. Strain in the epilayer is usually relaxed by generation of misfit dislocations at the interface. In order to see if there is a relaxation of strain in the quantum-well, a series of low temperature photoluminescence measurements were performed on both as-grown and degraded structures. When the biaxial compressive strain in the quantum well is relaxed, the band-gap energy of the quantum-well should change. Figure 4.10 shows how changes in the conduction and valence-band edges under a biaxial compression can in turn shift the wave length of the low temperature PL peaks. The theoretical calculation of changes in the electron hole transition energy due to the strain relaxation will be shown in the following section.

4.3.1 Strain Dependence of the Band Gap

The conduction band offset (ΔEc) and valence band offset(ΔEv) in the quantum-well change when the layer is strained. This change arises

from the difference in the energy gap between the strained and unstrained quantum-well. Therefore, the amount of strain relaxation during operation can be detected by measuring PL peak shifts at a low temperature.

There are two theories that are commonly used to estimate the band offsets of heterostructures. One is the linear combination atomic orbital (LACAO) theory and the other is the electron affinity rule.

According to the LACAO theory, the valence band edge is given by [77]

$$E_c = (E_s^c + E_s^a)/2 + [\{E_s^c - E_s^a)/22\}^2 + V_{ss}^2]^{1/2} \tag{4-6}$$

where $V_{ss} = 5.60\hbar^2/(m_e d^2)$ and is the Hamiltonian Matrix of the s orbital of the nearest neighbor atoms, $\hbar$ is the reduced Planck constant, m_e is the electron mass and d is the distance between an anion and a cation. E_s^c, and E_s^a are the energies of the s orbital of cation and anion respectively.

The conduction band edge can be calculated by adding the band gap to the valence band edge, where the band gap was given by the well known expression using bowing parameters, which for a ternary compound $A_xB_{1-x}C$ is given by

$$E_g = xE_{AC} + (1-x)E_{BC} - b_{bow}x(1-x) \tag{4-7}$$

where E_{AC} and E_{BC} are the band gaps of AC and BC, respectively, and b_{bow} is the bowing parameter.

However, some parameters are not available yet for II-VI compounds. The conduction and valence band edges can be estimated using the electron affinity rule. The vacuum level used as a reference and

relative positions of the conduction band edge was determined for ZnSSe and ZnCdSe. The electron affinity of each material is the energy to remove an electron from the conduction-band minimum to vacuum level. The electron affinity for these compounds was estimated from the binary materials (ZnS, ZnSe, CdSe) assuming a linear relationship as a function of composition. Then the valence band offset was derived by subtracting the energy band gap from the conduction band edge for each compound.

The above mentioned estimations were for band lineups in bulk materials. In the strained heterostructure, the constituent layers are under stress which considerably influences the band lineups. Since the ZnCdSe quantum well is under biaxial compression these strain effects should be taken into account in determining the band diagram. The amount of strain is defined as

$$\varepsilon = \frac{a_{barrier} - a_{well}}{a_{well}} \qquad (4\text{-}8)$$

where a is the lattice constant of the material used. For (001) oriented epilayers and substrate, where both have a zincblend structure, the strain tensors ε_{ij} are given by [78]

$$\varepsilon_{xx} = \varepsilon_{yy} = \varepsilon$$

$$\varepsilon_{zz} = -(2C_{12}/C_{11})\,\varepsilon$$

$$\varepsilon_{xy} = \varepsilon_{yz} = \varepsilon_{zx} = 0 \qquad (4\text{-}9)$$

where C_{12} and C_{11} are the elastic constants. The strain tensors indicated above can be divided into uniaxial and hydrostatic components. For a compound with a zincblend structure, the hydrostatic component shifts the center of gravity of the conduction and valence band edges. The energy shifts due to the hydrostatic strain are expressed as [79]

$$\Delta E_c = a_c(\Delta\Omega/\Omega) \text{ for conduction band}$$

$$\Delta E_v = a_v(\Delta\Omega/\Omega) \text{ for valence band} \tag{4-10}$$

where a_c and a_v are the hydrostatic deformation potentials for the conduction and valence band edges, respectively. $\Delta\Omega/\Omega$ corresponds to the volume change under hydrostatic pressure and is given by

$$\Delta\Omega/\Omega = \varepsilon_{xx} + \varepsilon_{yy} + \varepsilon_{zz} = -2(C_{11}-C_{12})/C_{11} \tag{4-11}$$

The uniaxial component of the strain splits the degeneracy of the valence band at the Γ peak. The valence band edge splits into heavy hole and light hole edges and the energy shifts of heavy and light hole states are expressed by [80][81]

$$\Delta E_{hh} = \frac{1}{2}\delta E_{001}$$

$$\Delta E_{lh} = \frac{1}{2}\delta E_{001} - \frac{1}{2}(\delta E_{001})2/\Delta_o \tag{4-12}$$

where $\delta E_{001} = 2b(\varepsilon_{zz} - \varepsilon_{xx})$, Δ_o denotes the spin-orbit splitting energy and b is the uniaxial shear deformation potential. Table 4.2 shows those values used in this calculation.

Table 4.2. Physical parameters used in the estimation of band lineups [82]

Parameters	ZnSe	ZnS	CdSe
Lattice constant (angstrom)	5.6681	5.4093	6.050
Energy gap at RT (eV)	2.70	3.73	1.69
Valence edge (eV)	-10.58	-11.40	-10.35
Electron affinity (eV)	4.090	3.810	4.950
Elastic constant (10^{11} dyne/cm^2)			
C_{11}	8.10	10.46	
C_{12}	4.88	6.53	
Deformation potential (eV)			
a_c	-4.17	-4.09	
a_v	1.65	2.31	
b	-1.20	-1.25	

The diagram of band line ups for the unstained quantum-well and strained quantum-well is shown in Figure 4.11. Based on these calculations, if the preexisting strain in the ZnCdSe quantum-well is fully relaxed during LED operation, there would be about a 30 meV difference in the electron-hole transition energy which would be correspond to a shift in emission length.

4.3.2 Low Temperature PL Measurement

Low temperature PL measurements were performed on the ternary-based heterostructure (structure II) and quaternary-based SCH (structure III) before and after degradation. The LEDs were degraded down to 50%

of the initial output intensity. As shown in Figure 4.6 and Figure 4.7, the PL peaks from the quantum-well remain in the same position. The strain in the quantum-well did not relax during degradation. However, dark line defects were observable in the 50%-degraded LEDs from both the ternary-based heterostructure and the quaternary-based SCH in electroluminescence microscopy. This result indicates that the DLD formation does not result in a measurable strain relaxation in the quantum well. This is consistent with the fact that no extended defects were observable in the TEM.

Another LED was fabricated from the quaternary-based SCH. degraded down to 20% of the initial output intensity (80% degradation). Low temperature PL spectra were obtained before and after degradation. Although the strain in the quantum well remains for the 50%-degraded LEDs, the strain is relaxed in the 80%-degraded LEDs. Figure 4.12 shows that the PL spectra at 22 K for the as-grown structure and the 80%-degraded LED. Since the ZnCdSSe quaternary has a larger band-gap energy than that of ZnCdSe, atomic interdiffusion would cause decrease in the peak wavelength. However, the ZnCdSe quantum-well peak is shifted toward a larger wavelength indicating that the strain in the quantum-well has been relaxed. The peak energy change is about 10 meV between the as-grown and 80%-degraded LEDs, which translates as about 33% relaxation of strain. This strain relaxation does not take place in the early stage of degradation but in the later stage. In the heavily degraded LEDs

we may expect to see some extended defects as a result of structural deformation related to the strain relaxation. TEM analysis showed that some dislocations and other degradation induced extended defects were observed in the 80% degraded LEDs. The more details of structural changes will be discussed in the chapter 5.

4.4 Summary

The thermal expansion difference in ZnSe based compound and GaAs makes the epilayer structure more strained at the LED operating temperature. The thermal expansion is almost entirely accommodated in the perpendicular direction in the lattice-matched ZnSSe/GaAs system. This makes the quantum-well more biaxially compressed and the amount of strain can be increased by 15%.

The atomic interdiffusion at the interface between the ZnCdSe quantum well and ZnSSe barrier layer was not able to be observed during LED operation. The low temperature PL spectra showed that neither the position nor the FWHM of PL peak from the quantum well changes after 50% degradation. The SIMS depth profile of the degraded LEDs indicates that any changes in composition did not occur near the quantum well and the abruptness of the interface between the quantum well and barrier layer appears to remain the same during the degradation process.

The strain in the quantum well was observed to remain a constant in the 50%-degraded LEDs, however, one third of the strain was relaxed in

the 80%-degraded LEDs. This indicates that the native strain in the active layer does not appear to be a direct cause of the early stages of degradation.

These results suggest that degradation takes place by 2 major mechanisms. In the early stages of degradation, point defects are generated and do not form extended defects and the strain in the active layer remains. However, DSDs and DLDs are formed. In the later stages of degradation, the strain in the quantum-well relaxes and extended defects form.
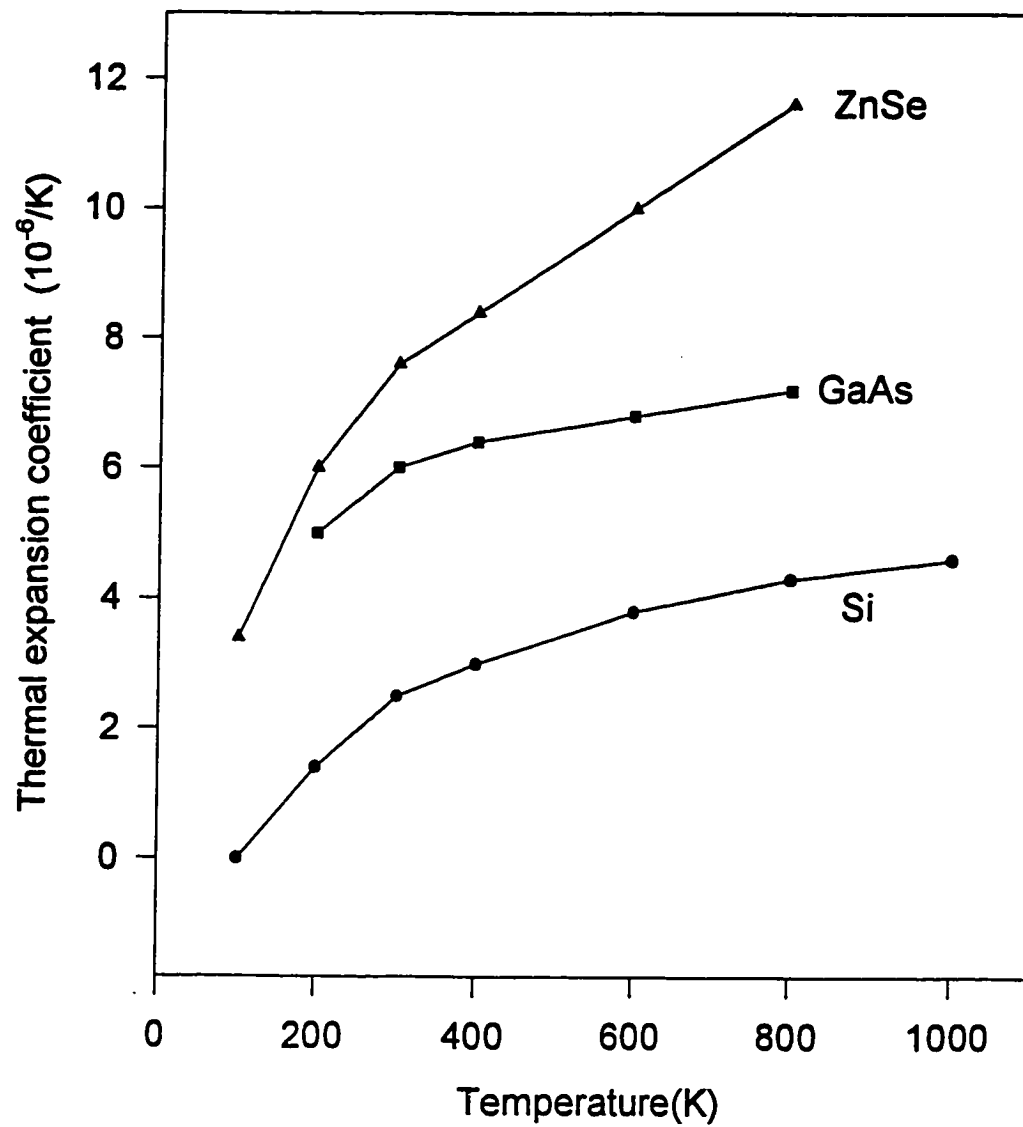
Figure 4.1.   Difference in thermal expansion coefficient between GaAs and ZnSe at various temperatures [66][67]
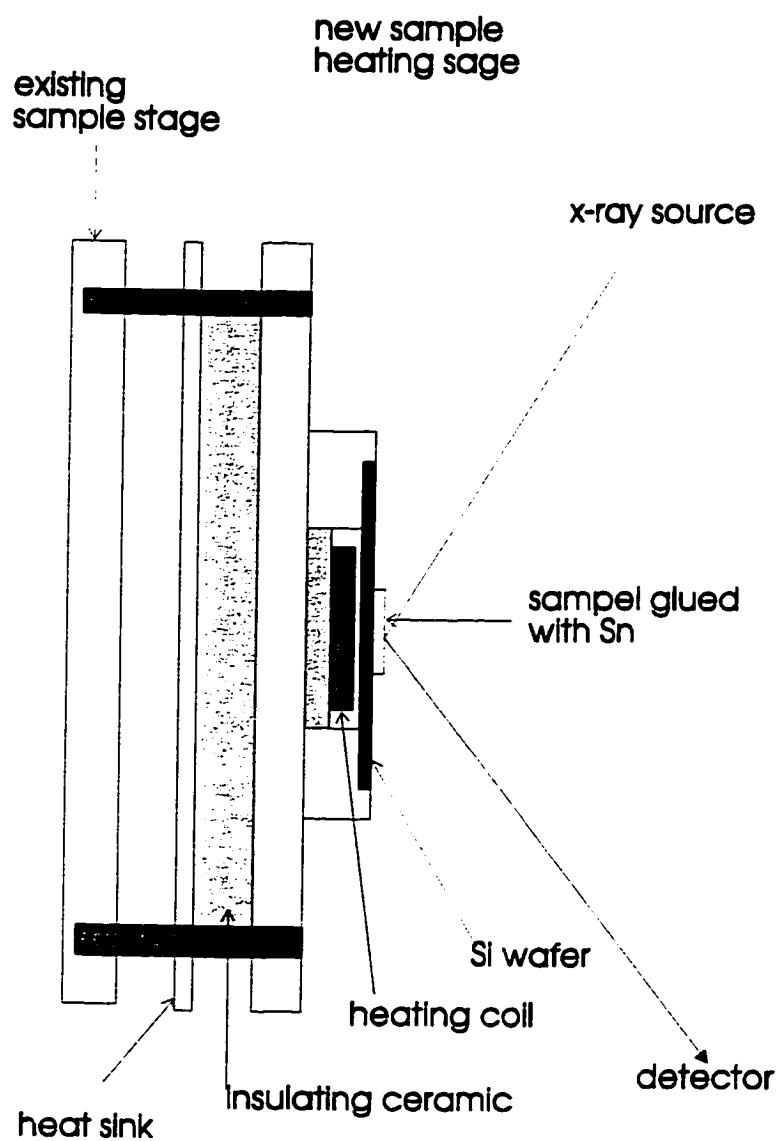
Figure 4.2.   A schematic of the sample heater attached to the cradle of the HRXRD
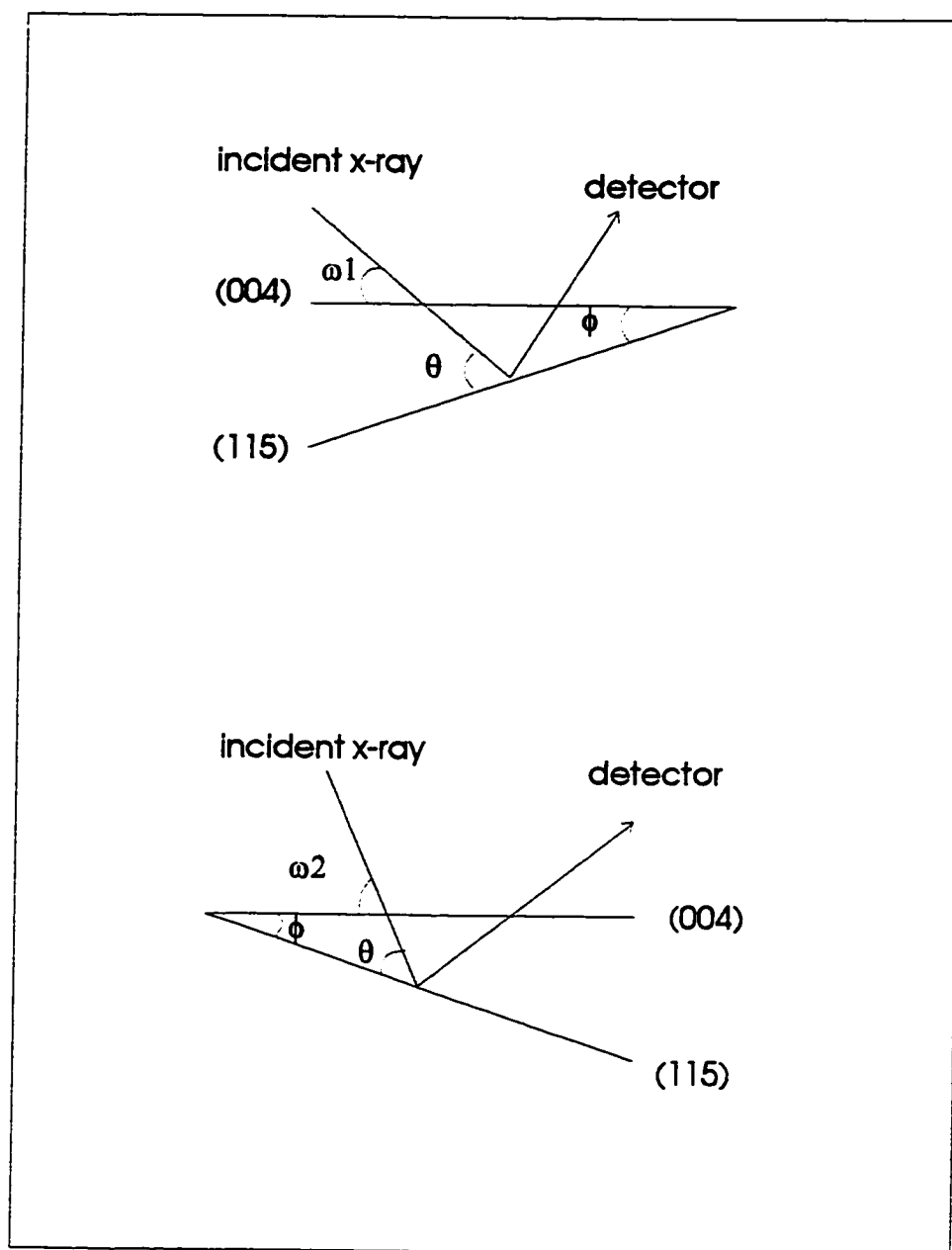
Figure 4.3.   Geometry for the asymmetric reflection from (115) plane
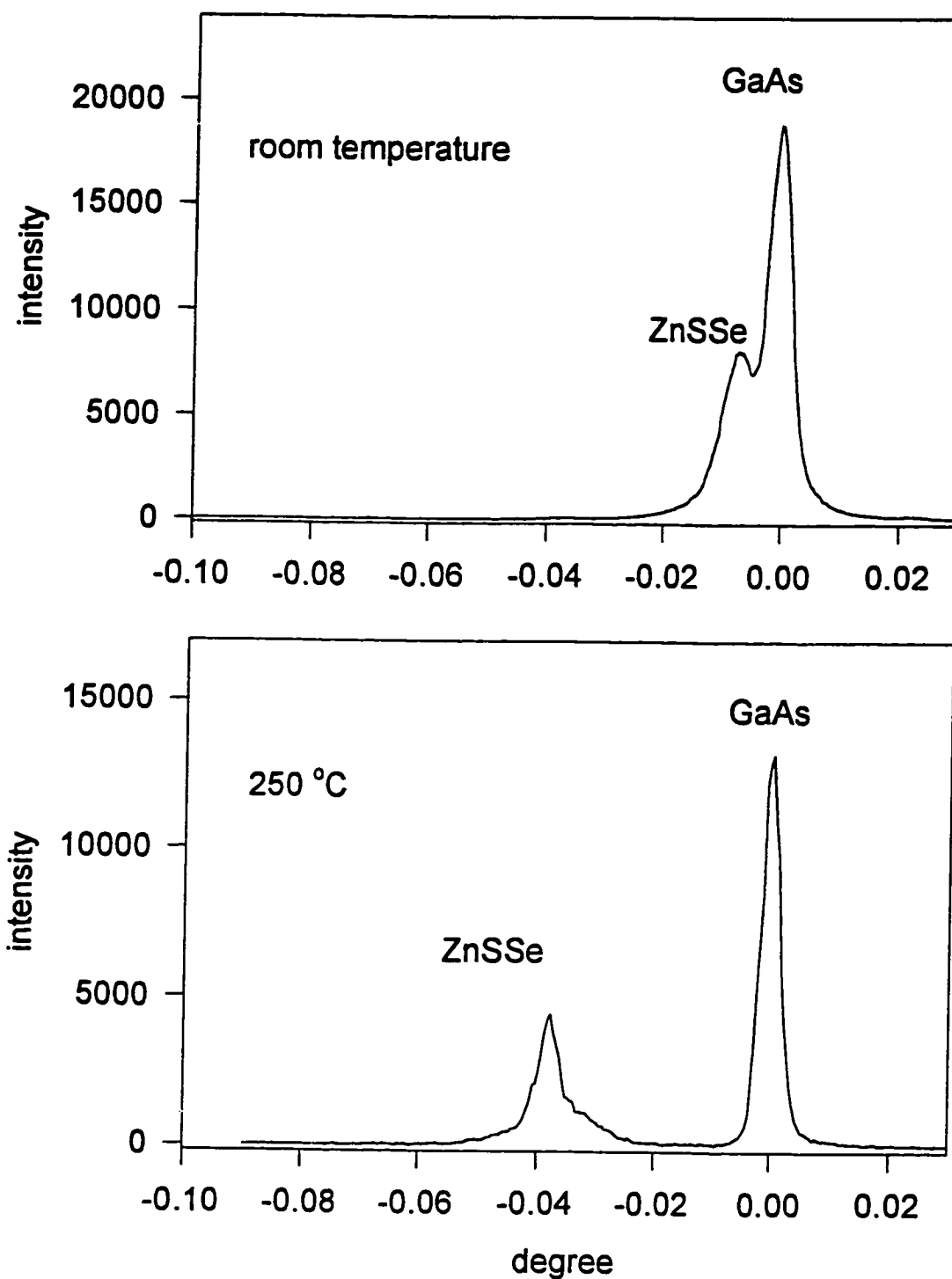
Figure 4.4. Symmetric reflections from the (004) plane at the room temperature (above) and at 250 °C (below)
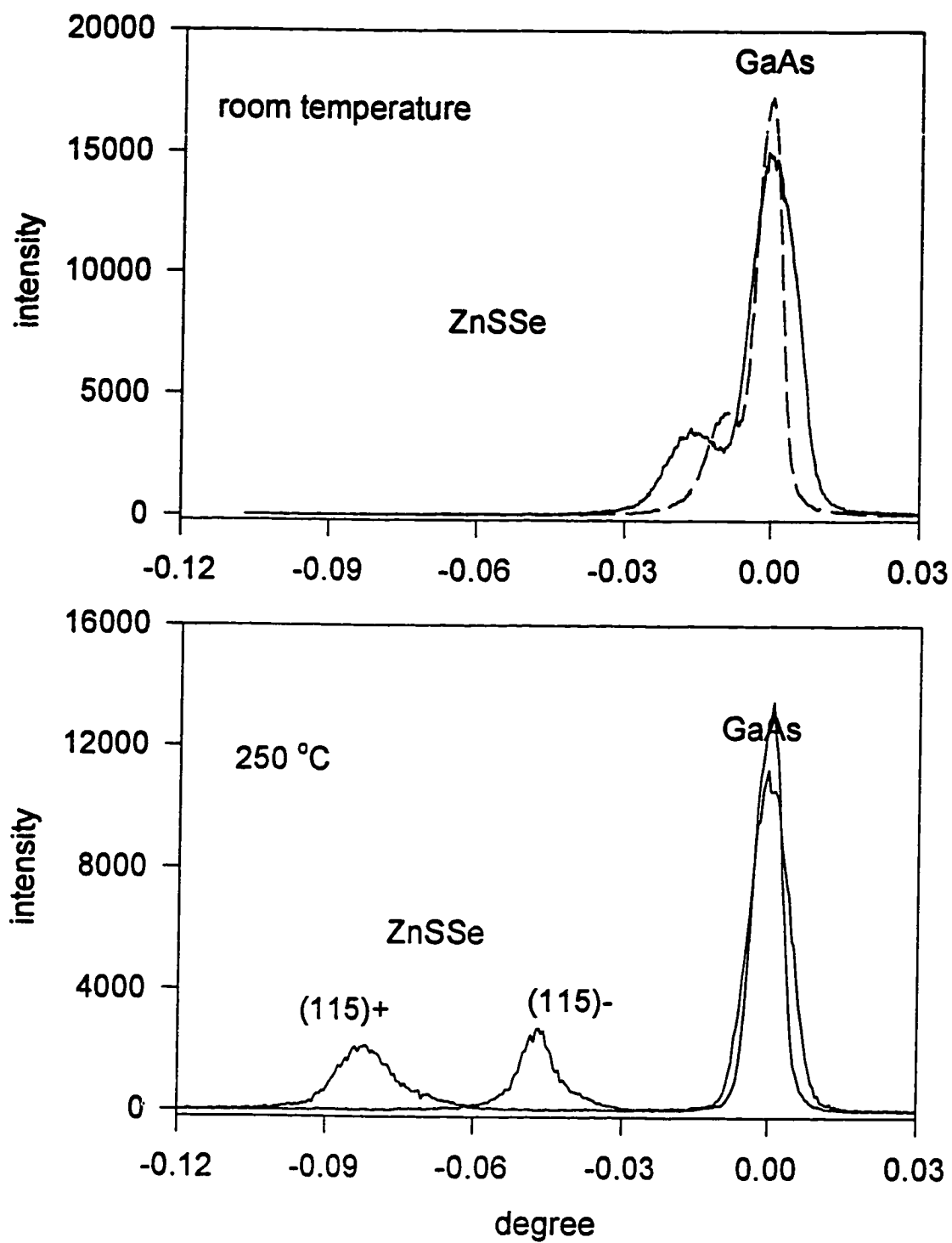
Figure 4.5.   Asymmetric reflection from the (115) plane at the room temperature (above) and at 250 °C (below)
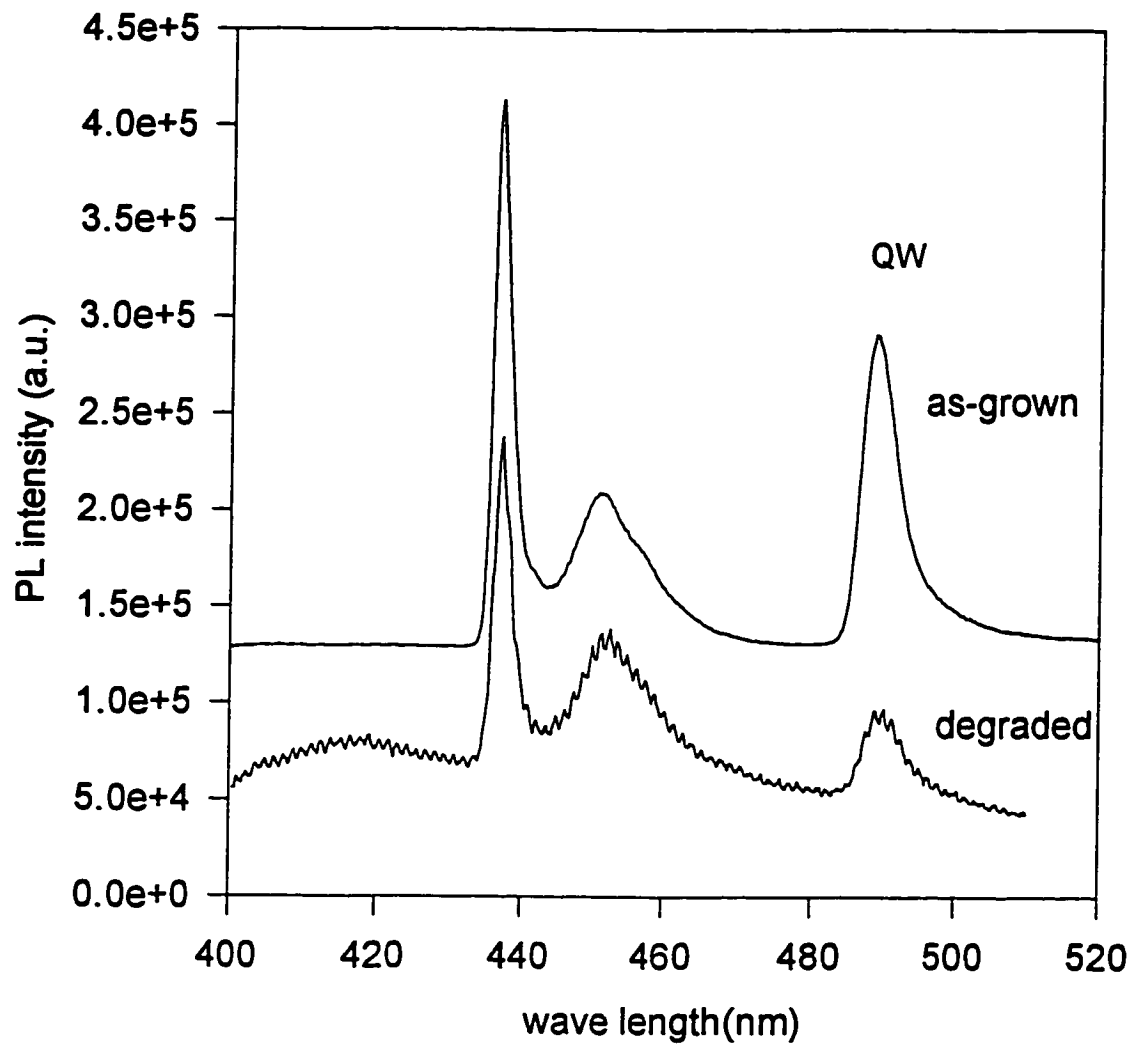
Figure 4.6. Comparison of Low temperature PL spectra between as-grown and 50%-degraded LEDs for the simplified ternary-based heterostructure
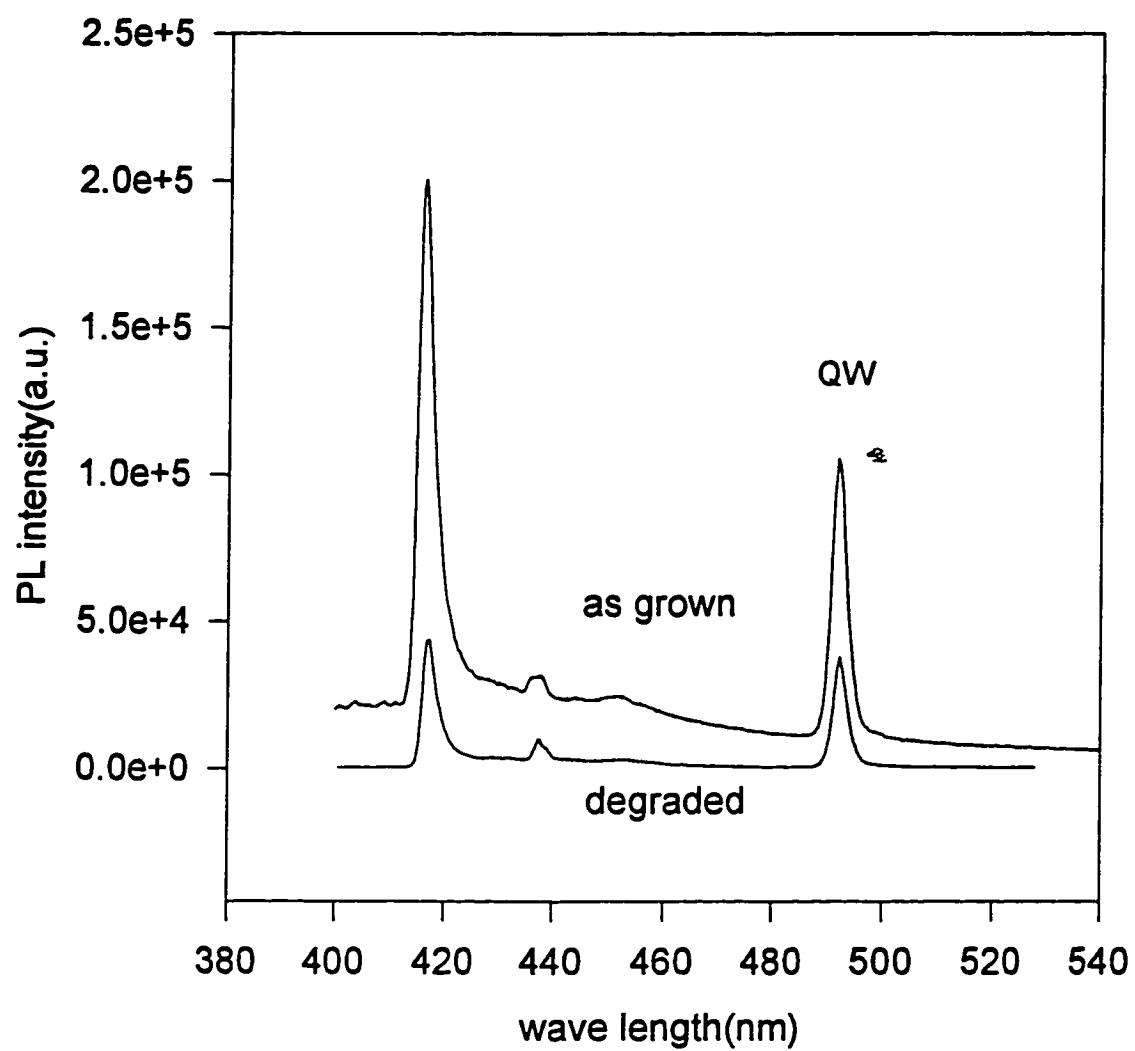
Figure 4.7. Comparison of Low temperature PL spectra between as-grown and 50%-degraded LEDs for quaternary-based SCH.
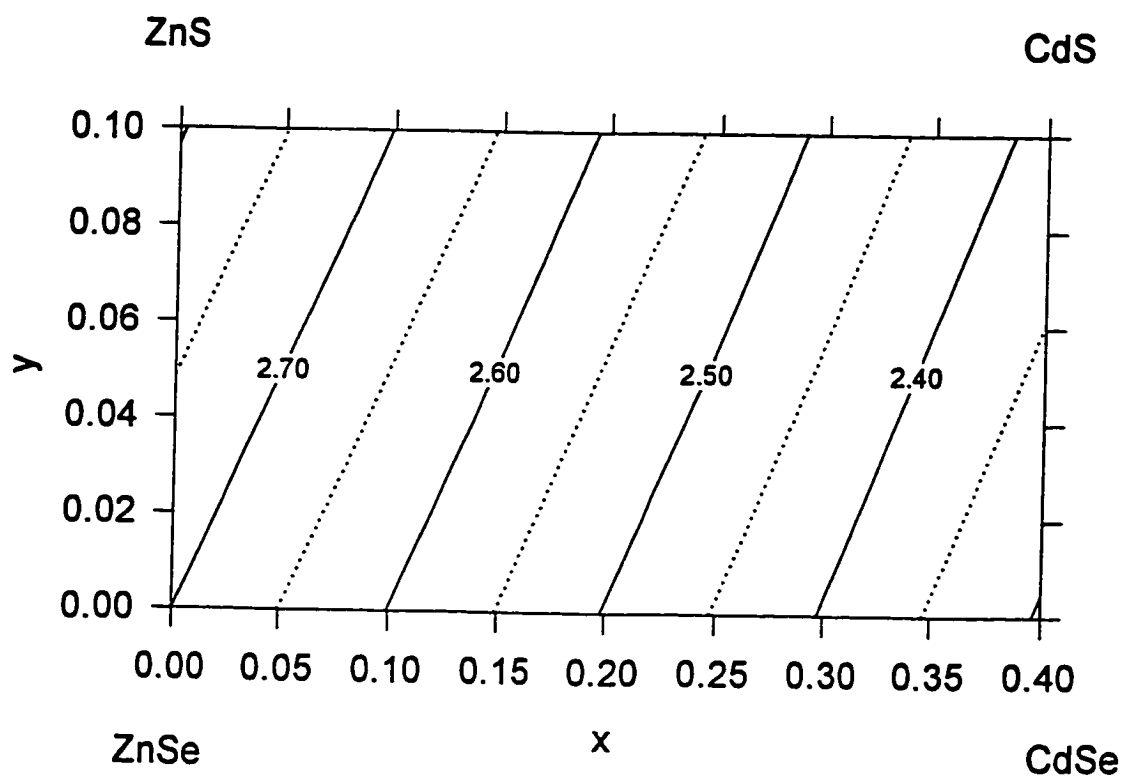
Figure 4.8. Calculated band-gap energy (eV) for $Zn_{1-x}Cd_xS_ySe_{1-y}$ quaternary
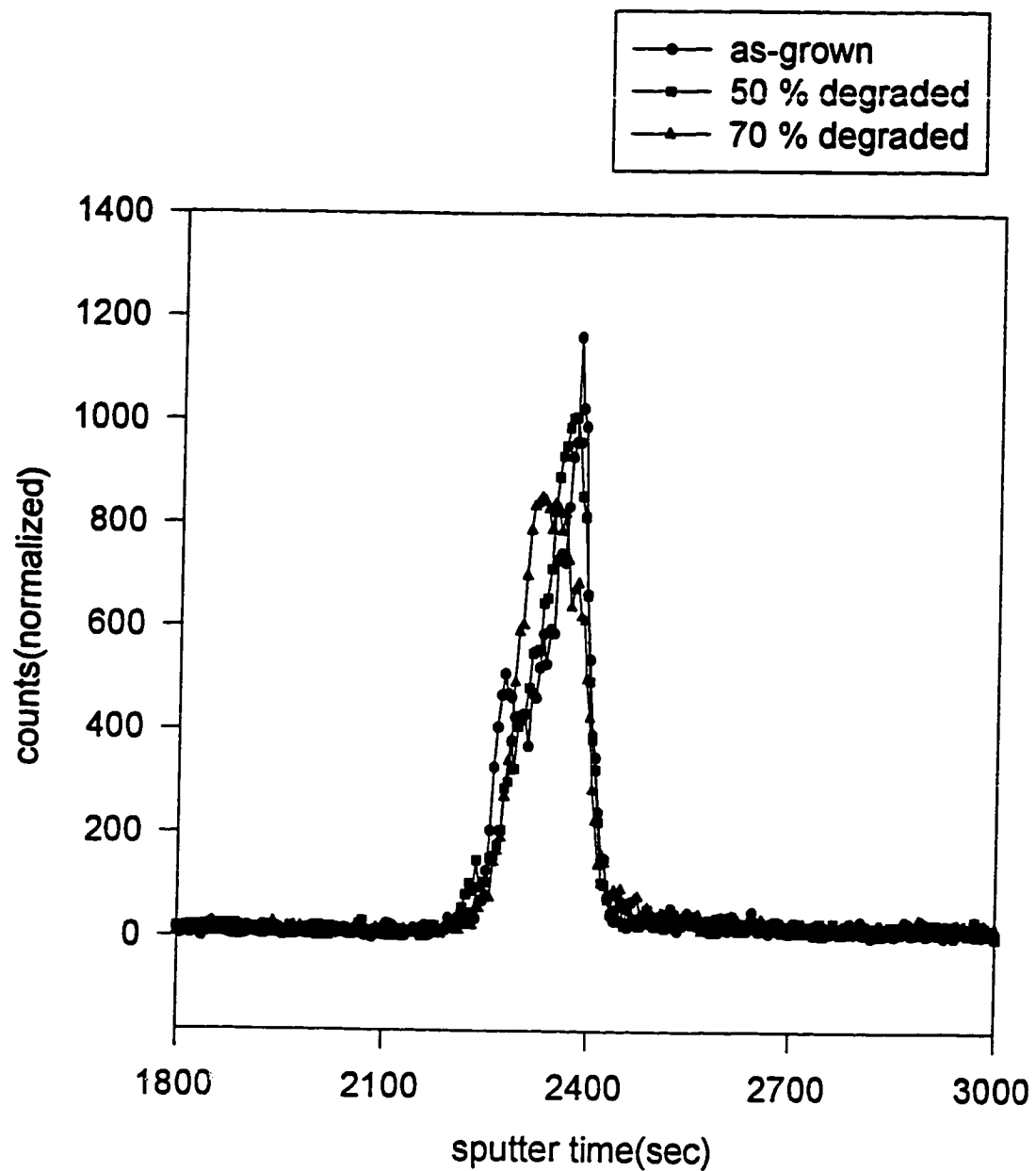
Figure 4.9.   SIMS profile of Cd in the as- grown, 50%-degraded and 70%-degraded LEDs. No Cd outdiffusion was observed.

(a) unstrained

(b) under biaxial compression
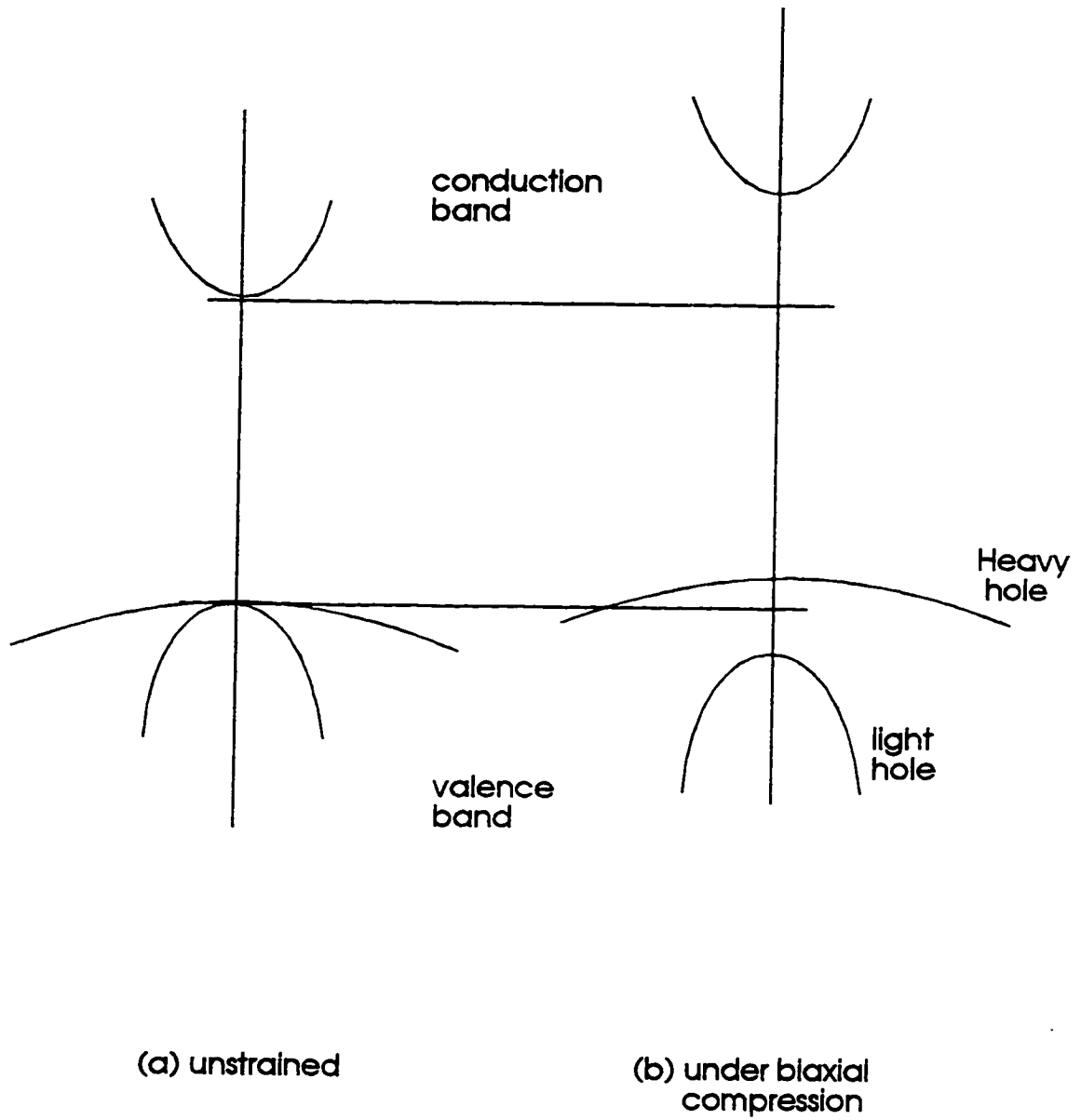
Figure 4.10. Schematic representation of the conduction and valence-band edge changes in the quantum-well under a biaxial compression
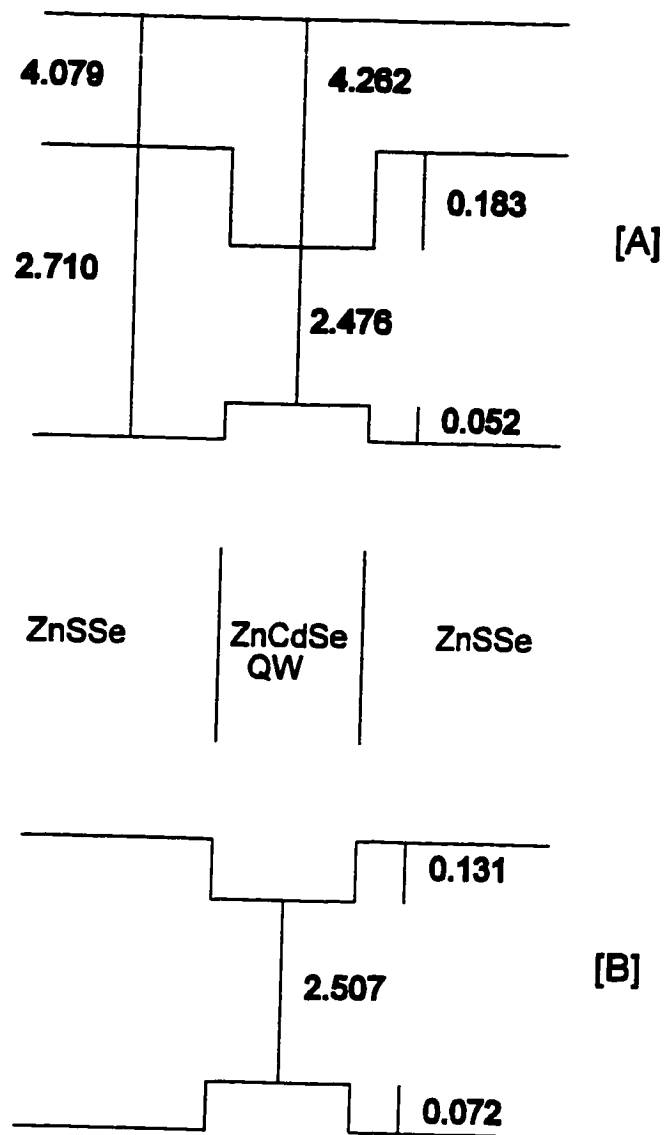
Figure 4.11.   Calculated band lineups for unstrained ZnCdSe quantum-well (a), and strained ZnCdSe quantum well (b). The unit of all the numeric values is eV.
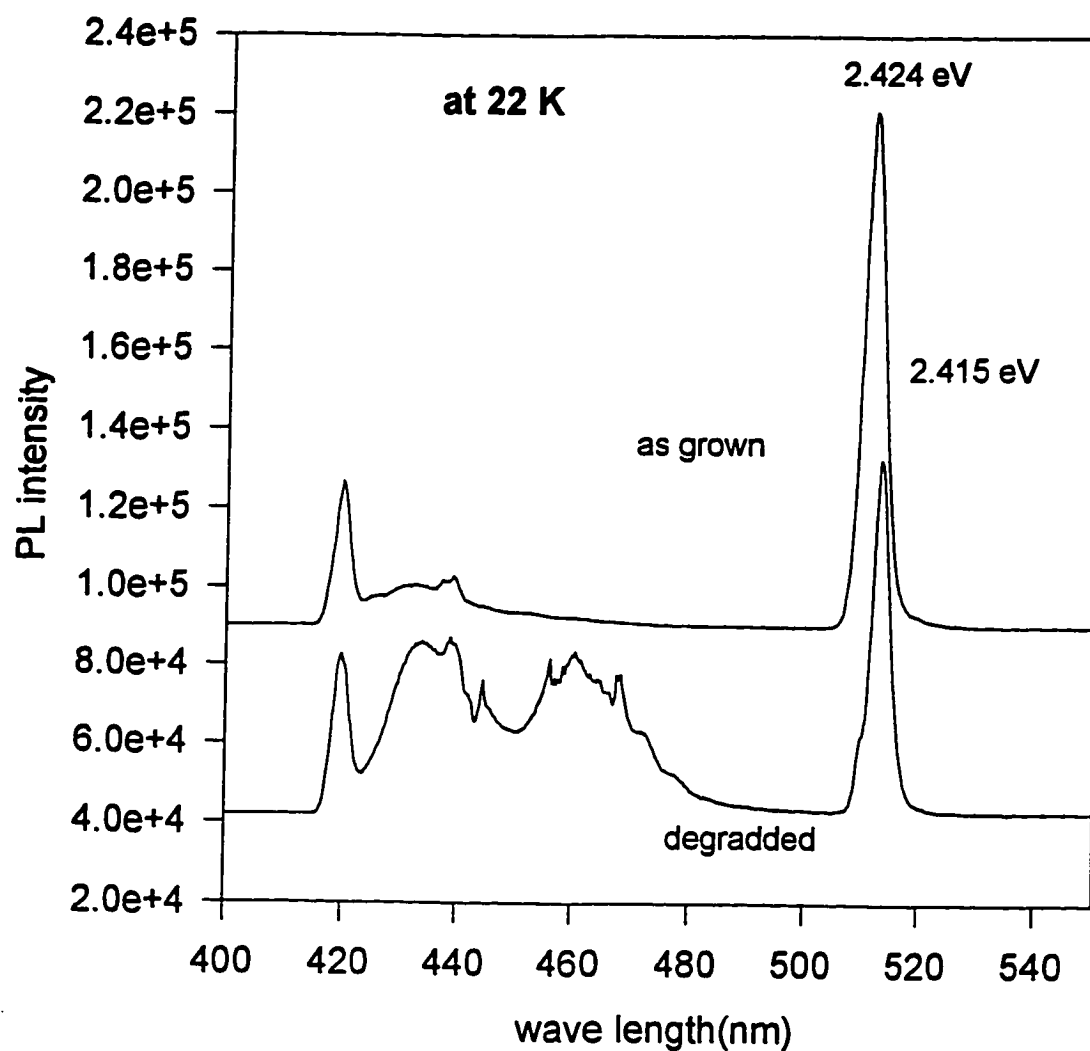
Figure 4.12. Photoluminescence spectra at 22K before degradation and after 80% degradation of quaternary-based SCH (structure III)

CHAPTER 5
DEGRADATION INDUCED DEFECTS

During the electrical degradation of II-VI ZnSe-based light emitters, dark line defects (DLDs) were observed and were considered as the major cause of degradation. In the case of [001] grown materials these DLDs lie along the <100> directions. These DLDs are believed to be evolving at or near the active region. As a result of such defects, the light emission decreases because DLDs act as nonradiative recombination centers. In lasers these defects are generated very rapidly reducing the device life time. In order to understand this rapid degradation phenomenon one needs to further understand the nature of these defects.

In order to characterize the DLDs, electroluminescence (EL) microscopy and TEM were used. LEDs were degraded under the electroluminescence microscope to observe the development of dark defects. The experimental set up used has been described in the chapter 2. After degradation, cross-sectional and plan-view TEM analyses were performed on these samples. Also, pre-existing defects, that is, growth related defects which already exist in the structure, are believed to act sources for degradation-induced defects. However, the relation between

109

the pre-existing defects and degradation-induced defects has been ambiguous. There has not been any direct observation of <100> dark line defects associated with grown-in defects. Even though crystal growers have focused on reducing structural defects with promising results, the pre-existing defect density still remains high (> 10^5/cm^2). The nature and characteristics of grown-in defects need to be studied prior to the studying degradation induced defects.

5.1 Pre-existing Defects

The extended defects which exist in the as-grown structure were characterized using TEM. In the ternary-based SCH (structure I) many stacking faults were observed in the structure. One of the reasons for the presence of such defects is the lattice mismatch between various layers. Many of these stacking faults originate at the GaAs/ZnSe buffer interface and propagate through the entire epilayer and to the surface. Many more stacking faults were found in the upper p-type layer than in the lower n-type layer, because some of them originate at the interface in the middle of epilayers. A cross sectional TEM image of the structure is shown in Figure 5.1. Figure 5.2 shows a typical image of plan-view TEM for the upper p-type ZnSSe layer. The number of triangular stacking faults is about 20 per 10 μm^2. This dense population of stacking faults is equivalent to a defect density of 1.5×10^9 /cm^2 when calculated using the length of partial dislocations enclosing the stacking fault.

In the simplified ternary-based heterostructure (structure II), almost no stacking faults were observed which indicates an extended defect density of less than $10^6/cm^2$. A cross-sectional TEM image of this sample is shown in Figure 5.3(a). A (004) high resolution x-ray reflection is shown in Figure 5.3(b) for this ternary-based heterostructure. ZnSSe peaks are separated from the GaAs peak, which means the ZnSSe lattice constant is slightly larger than the GaAs lattice constant. Although there exists a slight mismatch, the defect density in this structure is quite low.

A cross-sectional TEM image of the quaternary-based SCH (structure III) is shown in Figure 5.4(a). This figure shows typical triangular stacking faults. Threading dislocations appear to be generated at the stacking fault and terminate at the surface. Misfit dislocations can be seen near the ohmic contact area. The epilayers in quaternary based SCH are not perfectly lattice-matched each other at room temperature as shown in the high resolution x-ray rocking curves in Figure 5.4(b). Peaks of ZnSSe and ZnMgSSe layers are separated from the GaAs peak and they appear to be separated each other.

The major types of extended defects observed in the as-grown structures of quaternary based SCH sample are (a) misfit dislocations in the area of ohmic contact, (b) [110] dislocations developed near the ZnSSe/ZnMgSSe interface and (c) stacking faults through out structure. Among these defects stacking faults are the main extended defect that exist in the quantum-well. Although the quantum-well (ZnCdSe) is highly strained, no

misfit dislocations were observed in the quantum-well since the thickness of the quantum-well is well below the critical thickness. The three types of defects were further analyzed as follows.

5.1.1   Misfit and threading dislocations

To obtain plan-view TEM images near the top surface, a specimen was ion milled from only the GaAs substrate side. A typical plan-view TEM image near the top ohmic contact is shown in Figure 5.5(a). The misfit dislocations develop due to the lattice-mismatch between ZnTe, ZnSe and ZnMgSSe. The dislocation density in this region is very high, around 1.6×10^9 /cm^2. To determine the volume of the specimen for the defect density, the thickness of the foil was estimated utilizing the thickness fringes.   In a bright field image, white fringes occur at $t / \xi_g^w = 0$, 1, 2, *etc*, where t is the thickness of the specimen and ξ_g^w is the effective extinction distance. Another method used to confirm the correct thickness was utilizing the dimension of a stacking fault assuming one knows the location of its origin. The vertical thickness of the specimen can be evaluated when the stacking fault ends on each of the ion-milled surfaces.

Two types of dislocations were observed in this contact area, misfit dislocations and threading dislocations. Some of the misfit dislocations develop along the [110] direction and have been identified as 60° mixed [110] dislocations. These are typically observed in ZnSe epilayers on the mismatched substrate, i.e. GaAs [83].   However, most of the misfit

dislocations appear to be developed in zigzag shapes at random orientations. The steps in these zigzagged dislocations lie along in the <110> directions. Such zigzagged dislocations, that on an average are oriented along a <100> direction, would be an energetically favorable configuration from a misfit relief perspective [84]. These dislocations may evolve by repeated cross slip of threading segments of dislocations on adjacent {111} glide planes as they move across the epilayer leaving a misfit segment during growth [85]. As a result of this cross slip, the misfit dislocation may attain a zigzag shape. The resulting configuration is more efficient in relieving misfit strain since it has a <100> orientation, which is not attainable by glide alone. Such a zigzag motion of misfit dislocations has not been observed in III-V and IV-IV systems and therefore suggests that cross-slip may be easier in II-VI compounds.

In addition to dislocations, stacking faults were also observed in this region, which appear to terminate at the misfit dislocations. They show the typical nature of a stacking fault of ZnSe based epilayers. The detailed analysis of the stacking faults follows in section 5.1.3.

5.1.2 [110] Dislocations in the middle layer

The plan-view specimen, which was initially milled from the GaAs substrate, was subsequently ion-milled from the top surface to analyze the p-type top layer after removal of the contact region. For the underlying p-type layer [110] type dislocations were observed. Most of these

dislocations were aligned along only one of the <110> directions as shown in Figure 5.5(b). This indicates that the strain relief was anisotropic for this sample. The dislocations appear to be located in the middle of upper ZnMgSSe layer, i.e. at the interface between ZnMgSSe cladding layer and ZnSSe barrier layer. Some of these dislocations appear to terminate at triangular stacking faults lying just below the contact layer. Other dislocations appear as elongated half loops starting and ending within the ohmic contact layer. Most of these dislocations seem to end at the edge of the structure. The length the elongated segments was found to be typically greater than 15 -20 μm with a mean spacing about 5 -10 μm.

Most of these [110] type dislocations were identified as 60° dislocations and this result is consistent with that of Choi et al. [86] who reported a lack of 90 degree perfect edge dislocations at the ZnSe/GaAs interface. In zincblende structures, the lattice $a/2<110>$ dislocations are commonly observed to be narrowly dissociated into pairs of $1/6<112>$ partial dislocations. A typical dissociation is that a 60° lattice dissociation (i.e., with angle between line direction and Burgers vector of 60°) is dissociated into two partial dislocations with angle between line direction and Burgers vector of 30° and 90°. The partial dislocations bound a stacking fault [87]. The dissociation of [110] dislocations can be observed by comparing images from g220 and g$\bar{2}$20 two beam conditions as shown in Figure 5.7.

5.1.3 Stacking faults

Stacking faults were the major defect type observed in every structure. Since most researchers suggest that these stacking faults are the cause of the fast degradation of II-VI lasers, a through characterization of these stacking faults is reported in this section.

In the upper p-type layers, stacking faults originate at the quantum-well region and terminate at the surface. The size of the stacking faults appear to be uniform implying they originate at the same depth. Almost all of them appear in pairs that are connected by narrow stacking faults. The spacing between pairs is about 0.8 - 1.0 μm. Figure 5.6(a) shows a cross-sectional TEM image of these stacking faults and plan-view TEM images are shown in Figure 5.6(b) after removal of the ohmic contact region. When we observe the stacking faults using different two beam conditions, the connection between the stacking fault pairs is much apparent. The connection of stacking fault pairs is shown in Figure 5.7. The connecting stacking faults are enclosed by partial dislocations. One unique characteristic of these stacking faults is their anisotropic formation. All of the pairs are aligned in only one of the <110> directions, i.e. all the stacking faults are on the (111) and ($\bar{1}\bar{1}$1) planes and the stacking fault pairs are all parallel to the [110] type dislocations as shown in Figure 5.5.(b). This anisotropy might arise from the tilt of the substrate prior to

growth. During the ion milling procedure, these stacking faults were used to evaluate the milling depth from the surface.

In the lower n-type epilayers, density of stacking faults is much lower than that in the upper p-type layers. A typical plan view TEM image is shown in Figure 5.8. These faults also occur in pairs and are connected by a very small segment. The stacking fault pairs in this region is aligned in the perpendicular $[1\bar{1}0]$ direction to the stacking fault observed in the p-type layer. The fault planes are $(\bar{1}11)$ and $(1\bar{1}1)$, respectively.

One of the reason why so many stacking faults exist in II-VI ZnSe based layers would be the low stacking fault energies. The stacking fault energy in II-VI compounds has been estimated experimentally [88]. In contrast to the III-V compounds, the stacking fault energy of II-VI compounds are substantially lower as shown in the following table.

Table 5.1. Stacking fault energy of II-VI compounds [91]

Material	Stacking fault energy γ (mJ/m2)
GaAs	55
ZnSe	13
ZnTe	16
ZnS	<6
CdSe	14

<u>Type of stacking fault</u>   The type of stacking faults in ZnSe based epilayers reported previously were not consistent.   Some authors have reported extrinsic stacking faults [89][90], while other have reported the stacking faults are intrinsic [91]. In order to determine the type of stacking fault, a bright field image and a centered dark field (CDF) image were taken and they are shown in Figure 5.8 and Figure 5.9. The bright field image consists of a series of alternate dark and bright fringes running parallel to the intersection of the fault plane and the sample surface. The dark field image is also a series of fringes but the outer fringes are not the same. Normally, centered dark field imaging is performed using opposite g vector to the bright field (BF) mode and the top fringes are then of opposite contrast. This behavior enables the sense of inclination of the fault plane to be determined. On a positive print the first fringe at the top of the foil in BF is bright for $g \cdot R_F$ positive and dark for $g \cdot R_F$ negative, which is the basis of the method for determination of extrinsic/intrinsic nature of a fault. Here, R_F is the displacement vector. In the case of zinc-blende structure, stacking faults have a displacement vector of $R_F = 1/3 <111>$ or $1/6 <211>$. $R_F = 1/3 <111>$ is the displacement vector of the Frank type fault originating from partial dislocations with $b = 1/3 <111>$. $R_F = 1/6 <211>$ is that of the Shockley type fault with $b = 1/6 <211>$. R_F can be easily determined by examining the cross-sectional TEM images (Figure 5.4) and it is $1/3 <111>$. Most of the stacking faults in this material are Frank type in nature.

The type of the stacking fault can be determined by examining plan-view TEM images. For example, in Figure 5.9 the zone axis was [001] and the g vector for the two beam condition is [220]. So the upper drawn normal direction is [111] since Rf=1/3[111]. If the stacking fault is intrinsic, the product of R_F and g is positive, and the image contrast will be bright -bright in BF mode, i.e., both the top surface side and the bottom side is bright. If the stacking fault is extrinsic, the $g \cdot R_F$ product is negative and thus the contrast will be dark-dark. As it is can be seen in Figure 5.9 stacking faults in the upper p-type layer show dark-dark contrast and are therefore extrinsic. However, the stacking faults in the lower n-type layer intrinsic, because the value of $g \cdot R_F$ is negative and they have dark-dark contrast in BF mode as shown in Figure 5.8.

<u>Type of partial dislocation</u>   From the cross-sectional TEM image of stacking faults (Figure 5.4) which lie along a [110] direction, the edge-on stacking faults would meet at a point near the ZnSe/GaAs interface. The angle between the (001) plane of the epilayer and each stacking fault is 54.7°, which corresponds to the angle between the (001) and the (111) planes of a cubic crystal. It shows that stacking faults lie on the {111} planes. Four kinds of Burgers vectors are expected to correspond to the types of partial dislocations on the (111) fault planes, which can be described as

$$1/2[\bar{1}10] = 1/6[\bar{1}2\bar{1}] + 1/6[\bar{2}11]$$
$$1/2[\bar{1}01] = 1/6[\bar{1}\bar{1}2] + 1/6[\bar{2}11]$$
$$1/2[0\bar{1}1] = 1/6[\bar{1}\bar{1}2] + 1/6[1\bar{2}1]$$
$$1/3[111]$$

Similar types of Burgers vectors can be expressed on the $(\bar{1}\bar{1}1)$ plane. These Burgers vectors and the corresponding values of g·b for some reflection vectors are listed in Table 5.2. From the fact that partial dislocations are invisible for g·b=0 and/or $\pm 1/3$ and the Burgers vectors were determined to be $1/2[\bar{1}10] = 1/6[\bar{1}2\bar{1}] + 1/6[\bar{2}11]$ on the (111) plane. Thus the type of partial dislocations are Schockley types.

Table 5.2. Burgers vectors of partial dislocations expected for the (111) fault planes

b =	$1/3[111]$	$1/6[1\bar{2}1]$	$1/6[\bar{1}2\bar{1}]$	$1/6[\bar{1}\bar{1}2]$	$1/6[\bar{2}11]$
g			g·b		
200	2/3	1/3	-1/3	-1/3	-2/3
220	4/3	-1/3	1/3	-2/3	-1/3
$2\bar{2}0$	0	1	-2/3	0	-1
131	5/3	-2/3	2/3	-2/3	1/3
$1\bar{3}1$	1	-1	1	-1	0

5.2 Degradation-Induced Defects

5.2.1 Dark defects observed in EL Microscope

During degradation electroluminescence images were captured by a CCD camera through the thin gold contact. This enabled the observation of any changes in the light emitting region, i.e. the quantum-well region. For the LEDs fabricated from ternary-based SCH (structure I), the worst sample in terms stacking fault density, only dark spot defects (DSD) were observed which grew larger covering the entire region upon degradation as shown in Figure 5.10. These EL pictures show the successive stages of degradation of an LED and degradation defect development during operation. Driving conditions used for degradation were the same as in Table 3.1. There were no dark line defects (DLD) observed in this sample. The reason would appear to be associated with the high density of pre-existing defects.

LEDs from the simplified ternary-based heterostructure (structure II) and quaternary-based SCH (structure III) showed both dark spot defects and dark line defects during degradation.   In the initial stages of operation, the dark line defects showed up near the thick gold pad and seemed to propagate to the center of the thin gold layer defining the LED. One of the reasons for this observation may be a greater current density under the gold pad and thus increased the generation of DLDs. Another reason may be related to a greater amount of strain under the gold

contact. As shown in Figure 5.11 and Figure 5.12 dark lines and dark spot damage increases as the degradation progresses. The dark spot defects and dark line defects seem to appear almost simultaneously. The appearance of DLDs in the simplified ternary-based heterostructure (structure II) in electroluminescence microscope was different from that in quaternary-based SCH (structure III). DLDs in simplified ternary-based heterostructure are more straight than those in quaternary-based SCH. There are more dark spot defects in the EL image for quaternary-based SCH. This indicates that dark spot defects are related to the preexisting defects around the quantum-well active region since the quaternary-based SCH has more pre-existing defects and the highest density of dark spot defects occurred as mentioned for ternary based SCH which had the highest stacking fault density. Some DLDs are slightly misoriented from the <100> directions and very few DLDs were even oriented in the [110] direction in the degraded quaternary based SCH. The misorientation may be come from the connection of the DSDs located closely.

The dark defects lie in the region of active quantum well area, because the non-radiative recombination takes place in the degradation defects and appear to be dark in the EL microscope. They appear very early in the degradation stage. The DLDs appeared after about 10% degradation, i.e. when the output intensity decreased to 90% of the initial output intensity. When a higher current density was applied, DLDs formed very rapidly. Figure 5.13 shows the time for DLDs to appear at the driving

conditions of 10 KHz repetition rate, 20% duty cycle and different current densities. The current density appears to be a major factor in the generation of DLDs during operation. As shown in Chapter 3, the higher current density causes the device to degrade faster.

A peculiar aspect of these DLDs is that the direction of the dark line is along the <100> directions as seen from the top surface. If the highly strained quantum-well is relaxed by plastic deformation, then the usual <110> misfit dislocations would be generated. The most common slip system is <110>{111} in a zinc blend structure. The <100> directions of DLDs indicate that DLDs may not be related to the strain relaxation process in the quantum-well. As described in chapter 4 the strain in the quantum-well had remained the same until 50% degradation. This supports the hypothesis that the DLDs are not related plastic deformation due to strain relief. Also as mentioned AlGaAs/GaAs lasers can degrade by [100] DLDs. And the dislocation climb is responsible for these defects. However, to date no one has reported what is the micro-structural source of the [100] DLD's in ZnSe-based lasers. The spacing between DLDs was estimated to be about 8 μm for structure II and 4-5 μm for structure III after 50% degradation as shown in Table 5.3. This data indicates that most of DLDs form in the early stages of degradation.

5.2.2 TEM Analysis

In order to study further the micro-structural source of DLDs, specimens for plan-view and cross-sectional TEM were prepared. No

Table 5.3. Spacing and number of DLDs for quaternary-based SCH

	Degradation			
	10 %	30 %	50 %	80 %
DLD Spacing (micron)	10-15	5-10	5	5
# of DLDs in 200 microns	15-20	20-35	35-40	35-40

defects were observed in the TEM for the slightly or moderately degraded samples (until 50% degradation) for both structure II and structure III. Defects were observable only in the sample that was heavily degraded, i.e. down to 30% of initial output intensity (70% degradation). One reason might be that DLDs in their early stages of degradation may be caused by point defect accumulation and they had not yet transformed into extended defects. From this observation, DLDs may be related to point defect generation, diffusion and agglomeration. In the early or even the moderate degradation stage (50% degradation), no strain relief was observed in the quantum-well as described in chapter 4. The generation and accumulation of point defects may not be contributing to significant strain relaxation of the quantum-well. As more DLDs nucleate and grow as in the heavily degraded LEDs, the quantum-well strain may be relaxed.

Degradation-induced defects observed in TEM in 70-80% degraded LEDs comprise of not only <100> dark line defects but also other various defects, such as dislocation tangles, dislocation helices and dislocation half loops.

<u><100> dark line defects in structure II</u>.   In the 80% degraded simplified ternary-heterostructure (structure II), dislocation-like <100> dark line defects were observed. The line direction is about 3^0 off from the <100> direction as shown in Figure 5.14. This figure shows a cross section area of two DLDs. Burgers vector analysis on these lines was not possible, because the defects exhibited very little strain contrast and were hence difficult to image. Figure 5.15 shows these defects at a higher magnification. On this fine scale in most cases 2-3 lines of contrast were closely packed to each other (0.1 μm apart) and these bundled lines were spaced about 0.6 μm apart. It is not believed these are simple dislocations as seen in degraded AlGAs/GaAs devices. In fact the fractured contrast suggests they might even be fine rows of clusters of point defects.

<u><100> dark line defects in structure III</u>.   In the 70-80% degraded quaternary-based SCH, a different type of <100> dark line defects was observed.   A relatively low magnification image of DLDs is shown in Figure 5.16. The spacing between these <100> dark line defects is about 4-6 microns on average and this distance is about the same as that measured in the electroluminescence microscope. The orientation of these defects is exactly along the [100] and [010] directions. These defects appear to be

connected lines among oval defects newly developed during operation along the <100> directions. The size of these oval defects is about 0.1μm × 0.15μm, usually elongated in the <100> directions. There exist many shorter dark line defects which are not connected, and appear to be aligned in the <100> directions. When a diffraction pattern was taken at the region of the degradation defect island, a ring pattern was observed as shown in Figure 5.17. This single halo surrounding a diffraction spot normally corresponds to distortion of crystalline structure. This suggests that the region about these <100> dark line defects is not single crystal. Somehow the crystalline nature of the structure was destroyed during the degradation and those islands of the <100> DLDs became regions of dense, small size of dislocations. Another nature of DLDs can be seen from a weak beam dark field TEM image shown in Figure 5.18. Here dark defect islands resembling dislocation loops are seen and some of them appear to be connected with short dislocations.

The nucleation point of some <100>DLDs appears to be at pre-existing stacking faults. Figure 5.19 shows a stacking fault with a clump of dislocations around it and a DLD that appear to be connected to it. This implies that the stacking faults would be the origins of DLDs during device operation. Kuo et al. [92] observed that stacking faults that were partially collapsed during photodegradation. A part of the stacking fault became a dense tangle of dislocations. They speculated that the stacking fault has transformed to a dense tangle of dislocations after

photodegradation. The dense dislocation tangle was observed elongated along the <100> directions. In our study the stacking fault transformation occurred after electrical degradation. The tangled dislocation may appear as dark spot defects in electroluminescence images. Figure 5.20 shows another type of nucleation site of DLD. The circular defects resemble a molten area, which appear to be connected to a DLD. It could be speculated that a defect site in the quantum well might be melted during operation. The possibility of melting during operation will be discussed more in detail in chapter 6.

In order to know where the DLDs lie in the structure, an Auger depth profile was obtained from the plan-view TEM specimen in which we observed DLDs. The detection area was near the edge of the thinned specimen in which DLDs were found. As shown in Figure 5.21 sulfur content has a large valley in the middle that represents ZnSSe barrier layers cladded by ZnMgSSe layers. This Auger profile indicates DLDs are at least within the ZnSSe barrier layers. We believe the surface ion-milling procedure used successfully exposed the quantum well region to PTEM investigation. The Cd content would not be detected due to the small thickness of the quantum well and the rough surface of the ion-milled specimen.

<u>Other types of degradation defects</u>. Although the major type of degradation-induced defects in the early stage of operation is <100> dark line defects and dark spot defects, additional extended defects such as

dislocation helices, dislocation tangles, dislocation half loops and newly generated stacking faults were observed after degradation.

(a) Dislocation helix: Many small helices were developed in the heavily degraded sample especially near the <100> dark line defects. A typical area near a dark line defect is shown in Figure 5.22. A dislocation helix can be produced by vacancy absorption and emission in the climb bow-out of a dislocation segment. In the study of whiskers, Webb [93] observed dislocation helices in palladium whiskers and he deduced that helices formed by vacancy condensation. The general rule for formation of a helix is described by Hirth et al. [94]. The formation of helices in metals involves with vacancy absorption or emission. In semiconductors of zinc blend structure, high concentration of interstitials and vacancies is possible. The presence of such helices in the degraded LEDs is therefore consistent with the formation of high concentration of point defects during degradation.

(b) Tangled dislocation: Many tangled dislocations were also found in both plan-view and cross sectional TEM. They appear to develop near pre-existing stacking faults and in the upper p-type layer. A TEM micrograph of such defects is shown in Figure 5.23(a).

(C) Dislocation half loop: Dislocation half loops also formed during operation. They appear to grow along the ZnSSe and ZnMgSSe interface and end up at the ohmic contact where dense misfit dislocation networks exist. Some dislocations are located along the quantum-well. Typical

dislocation half loops are shown in the cross sectional TEM image in Figure 5.23 (b). It is noted that degradation-induced defects occurred in much greater numbers in the upper p-type layer relative to the lower n-type layer. The tangled dislocations exist almost exclusively in the upper layers and dislocation half loops are also located only in the upper layer. This can be clearly seen in Figure 5.24. The resistivity in the p-type layer is higher due to low net carrier density may cause more heating and contribute to the easier defect formation. The poorer initial crystalline quality (more pre-existing defects), the proximity to the surface and the proximity to the ohmic contact with its high defect density may contribute to the higher density of degradation defects in the upper p-type layer.

(d) Stacking fault: In certain areas of degraded LED stacking faults were generated. Much more damages can be seen in the upper p-type layers and degradation induced stacking faults are shown in Figure 5.24(b). The size of these stacking faults was much smaller than the pre-existing faults. The average size when viewed on edge is about 0.3-0.4 μm on the {111} planes.

Source region of degradation defects. When we look at the degradation induced defects in the cross sectional TEM image as shown in Figure 5.25, the main dislocation is generated along the quantum well. This TEM image was taken from the 80%-degraded structure II. In order to see if the dislocation is confined in the quantum-well, the specimen was tilted in the TEM so as to take a look at the quantum-well plane in a two

dimensions. This main dislocation along the quantum-well lies within the quantum-well plane. This indicates that the quantum well is the most susceptible to formation of extended defects. Many dislocation branches were developed from the main dislocation in the quantum well. This figure implies that the defects may be start from the quantum well first and develop into the outer layers. However, degradation induced defects in structure III shows different characteristics. As described previously most of degradation induced defects are located in the upper p-type layers and the ohmic contact region also seems to act as the source for those degradation defects. In other words, defects may be start to form at the ohmic contact area and propagate to the quantum well.

5.3. Summary

The major pre-existing defects are as follows: (a) misfit dislocation networks in the ohmic contact area, whose density is about 10^9 /cm2 and most of them are in zigzag shapes which are not common in other III-V system. (b) [100] dislocations in the middle of the upper p-type layers, which are identified as typical 60° dislocations and mostly develop in one of the <110> directions and (c) stacking faults through out the whole structure, which are all Frank type in nature, and most of them in the upper p-type layer are intrinsic and those in the lower layers are extrinsic. They all occur in pairs and form in one direction of <110>. The strong anisotropic distribution of defects was observed.

The major defects induced during LED operation is <100> dark line defects. TEM analyses showed that DLDs appeared to be rows of clusters of point defects aligned in the <100> direction in the 80% degraded simplified ternary heterostructure (structure II). However, DLDs in the 80%-degraded quaternary-based SCH (structure III) appeared to be regions of distorted crystalline material, such as dense area of small dislocations, connected in the <100> directions. The nucleation site of the DLDs appeared to be the stacking faults. The pre-existing stacking fault was transformed into a dislocation tangle that may as the origin of DLDs. DLDs seem to form by accumulation of point defects generated during degradation. DLDs act as non-radiative recombination sites at or near the active quantum-well and appear to be dark in EL microscopy.

Other degradation-induced defects such as dislocation helices, dislocation tangles, dislocation half loops and stacking faults were also generated during electrical degradation. Dislocation helices are formed through the vacancy emission and absorption which is also consistent with the generation of point defects during electrical degradation.
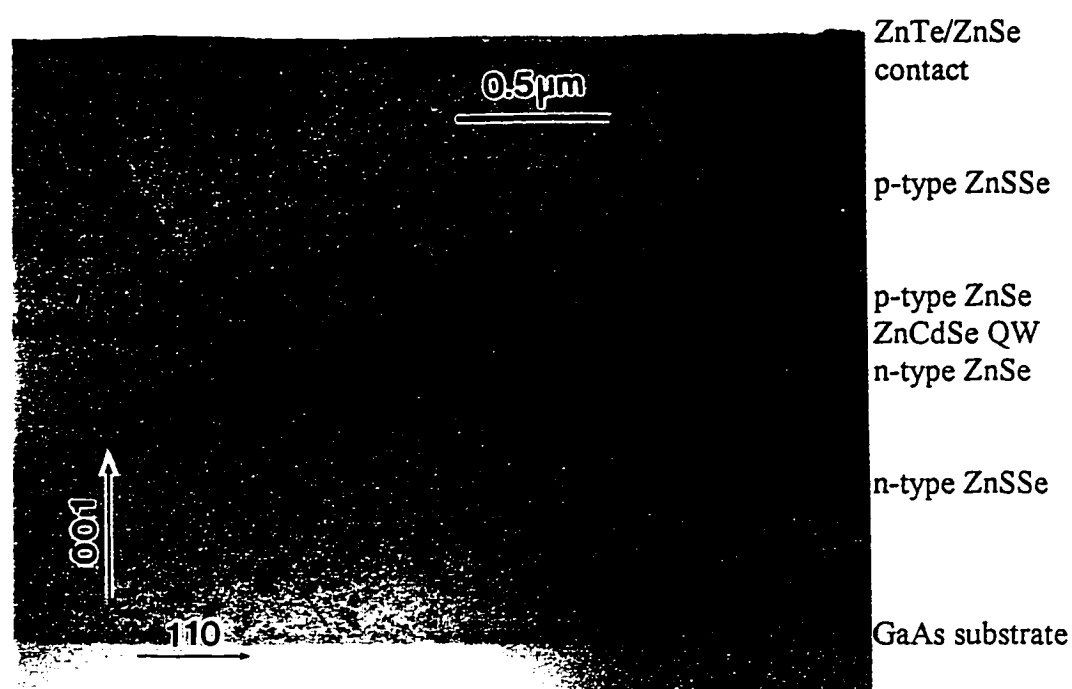
Figure 5.1. Cross-sectional TEM image in bright field mode showing typical stacking faults residing on the {111} planes for as-grown ternary-based SCH (structure I)

g220
→
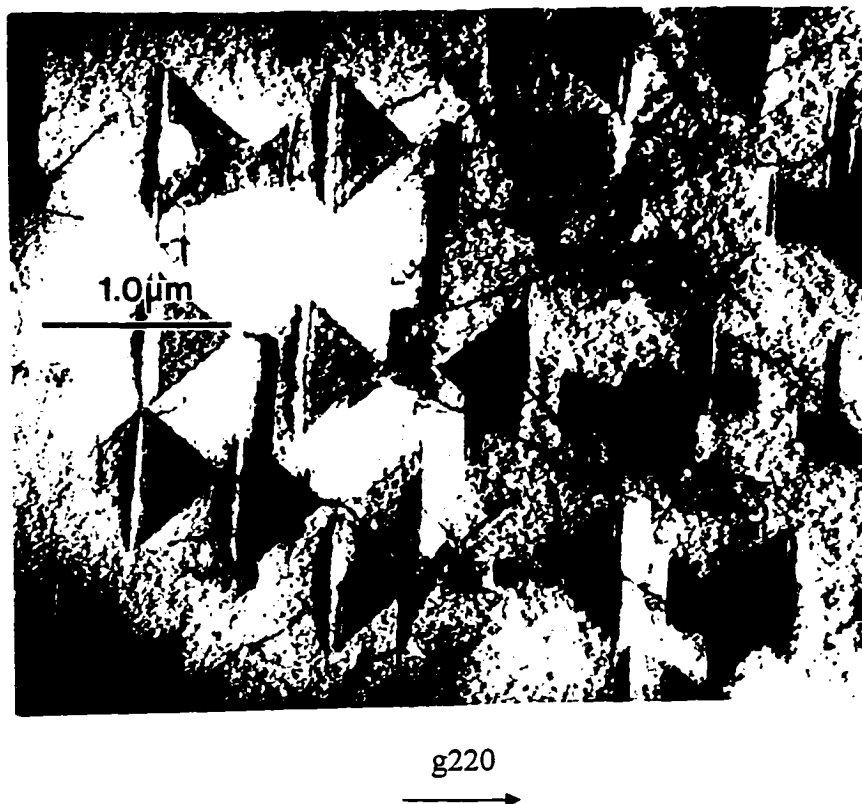
Figure 5.2.   Plan-view TEM image at BF of the upper p-type layers for ternary-based
SCH (structure I)
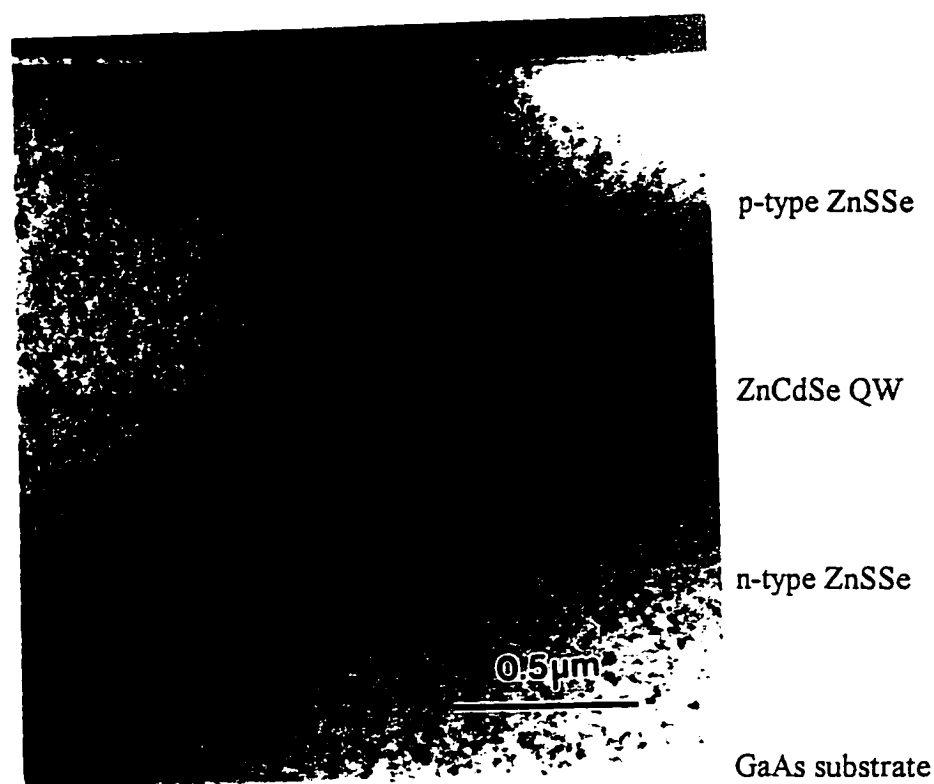
Figure 5.3(a). Cross sectional TEM image for the simplified ternary-based heterostructure (structure II). No defects were observed and thus the defect density is less than TEM resolution limitation.
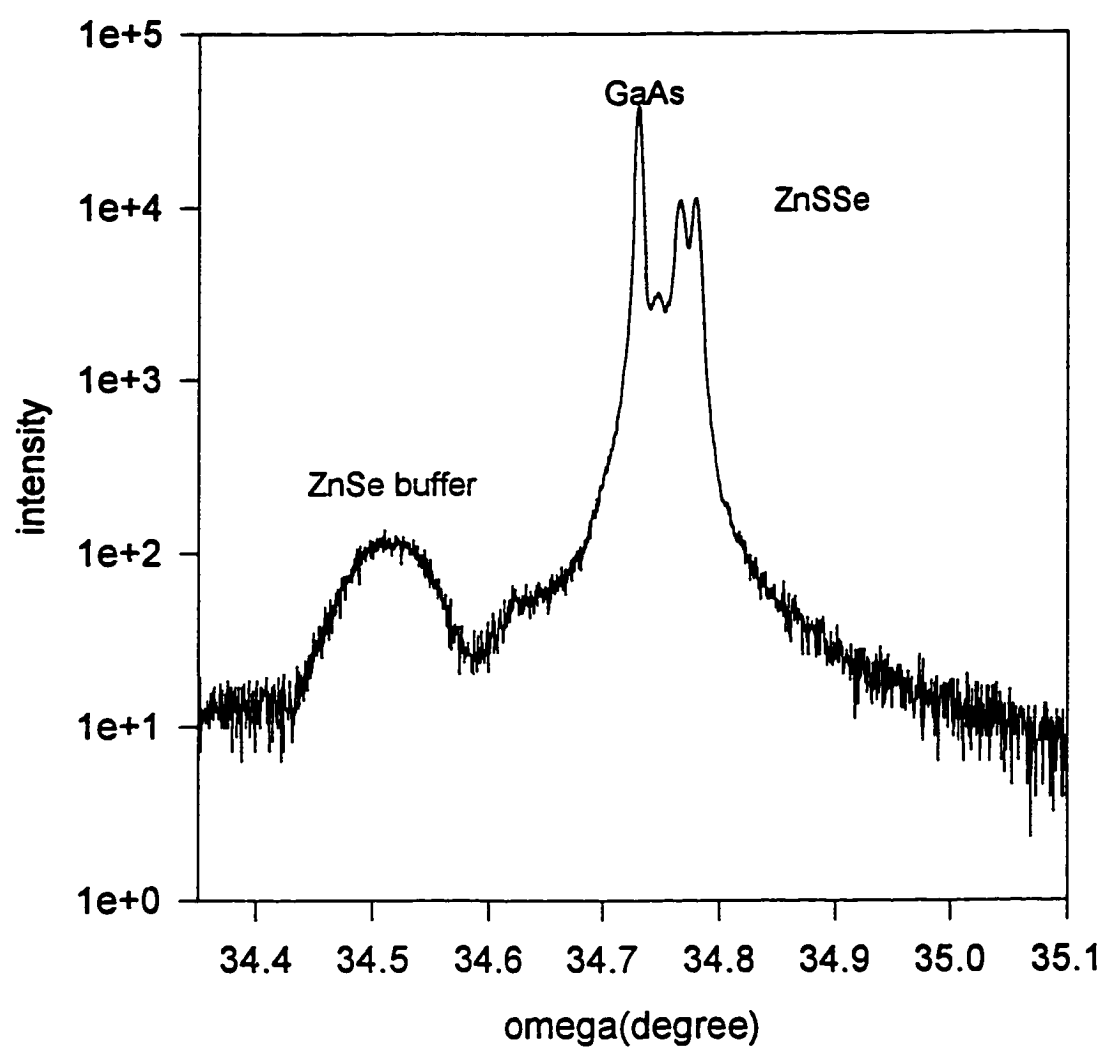
Figure 5.3(b)   X-ray rocking curve for (004) reflection from the simplified ternary-based heterostructure

ZnTe/ZnSe contact

p-type ZnMgSSe

p-type ZnSSe
ZnCdSe QW
n-type ZnSSe

n-type ZnMgSSe

ZnSe buffer
GaAs substrate
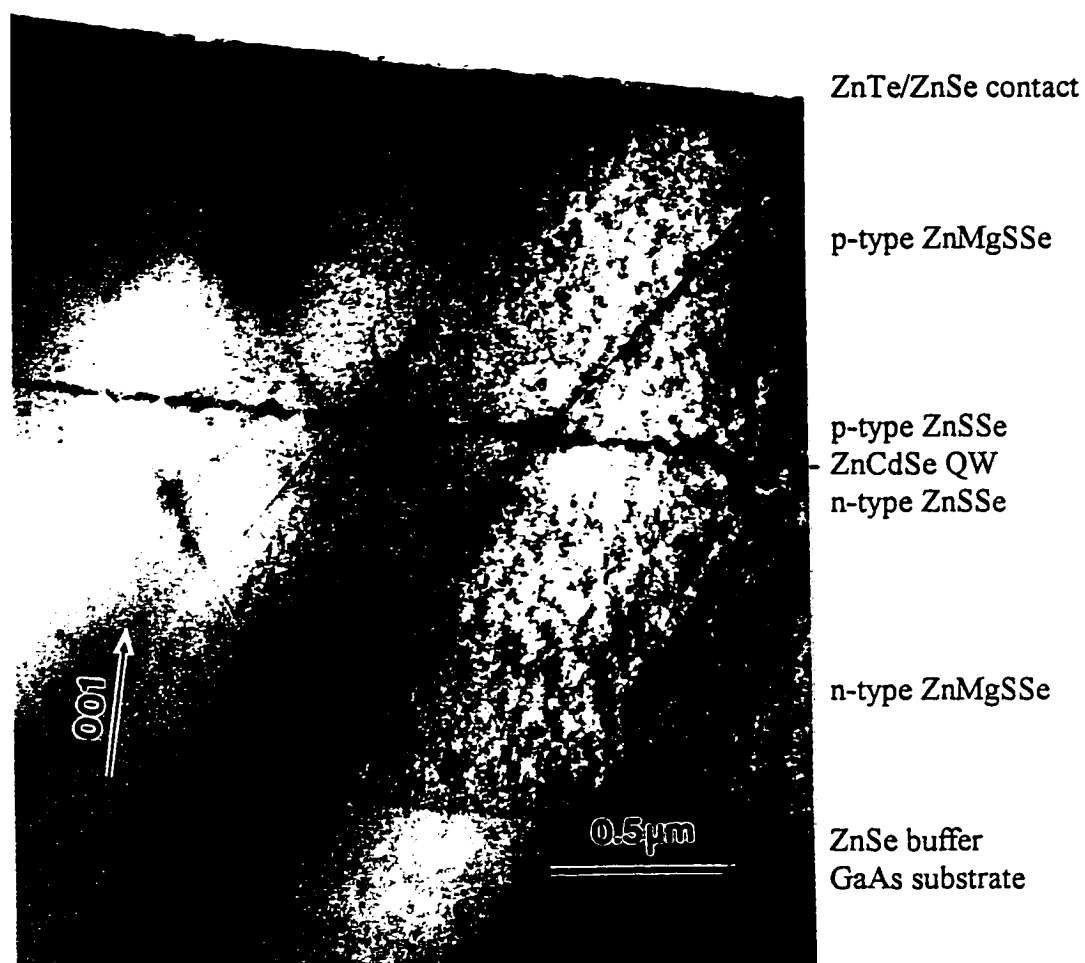
Figure 5.4(a). Cross-sectional TEM image of quaternary-based SCH (structure III) showing typical stacking faults in the as-grown structure
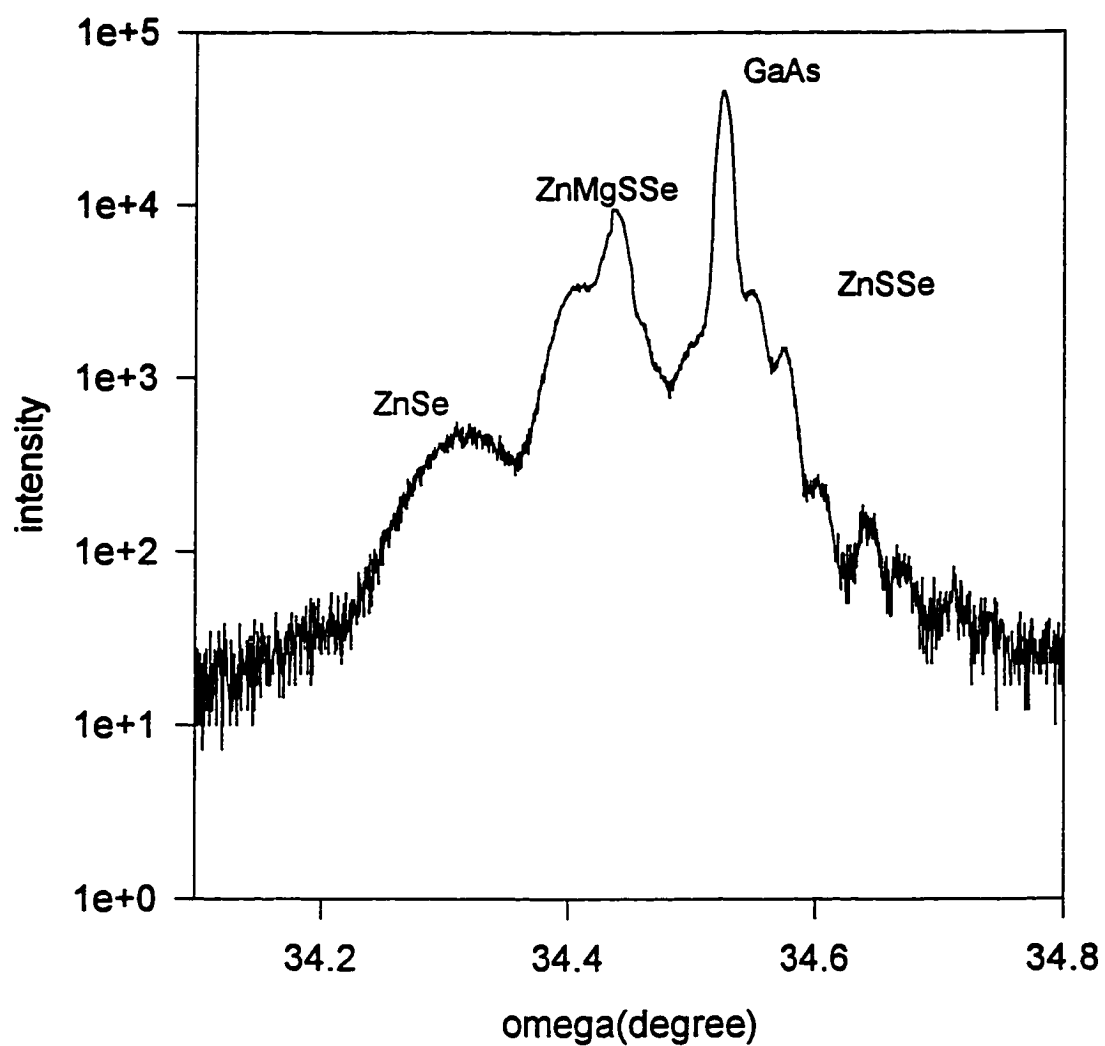
Figure 5.4(b). X-ray rocking curves for (004) reflection from the quaternary-based SCH

(a)

(b)
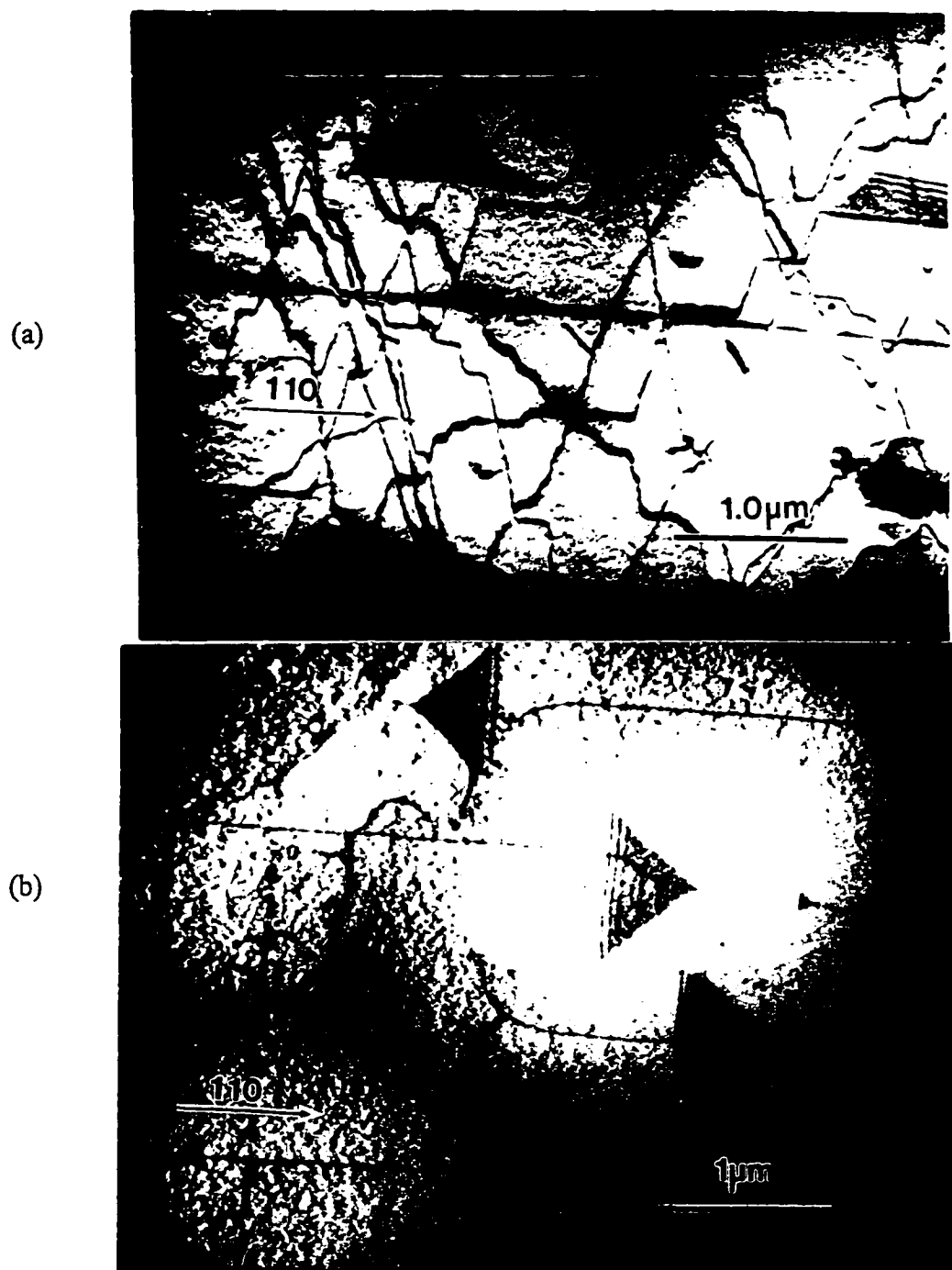
Figure 5.5.   Plan-view TEM images of quaternary-based SCH: (a) ohmic contact area showing zigzag misfit dislocation networks and (b) the upper p-type layers showing stacking faults and [110] dislocations

(a)

(b)
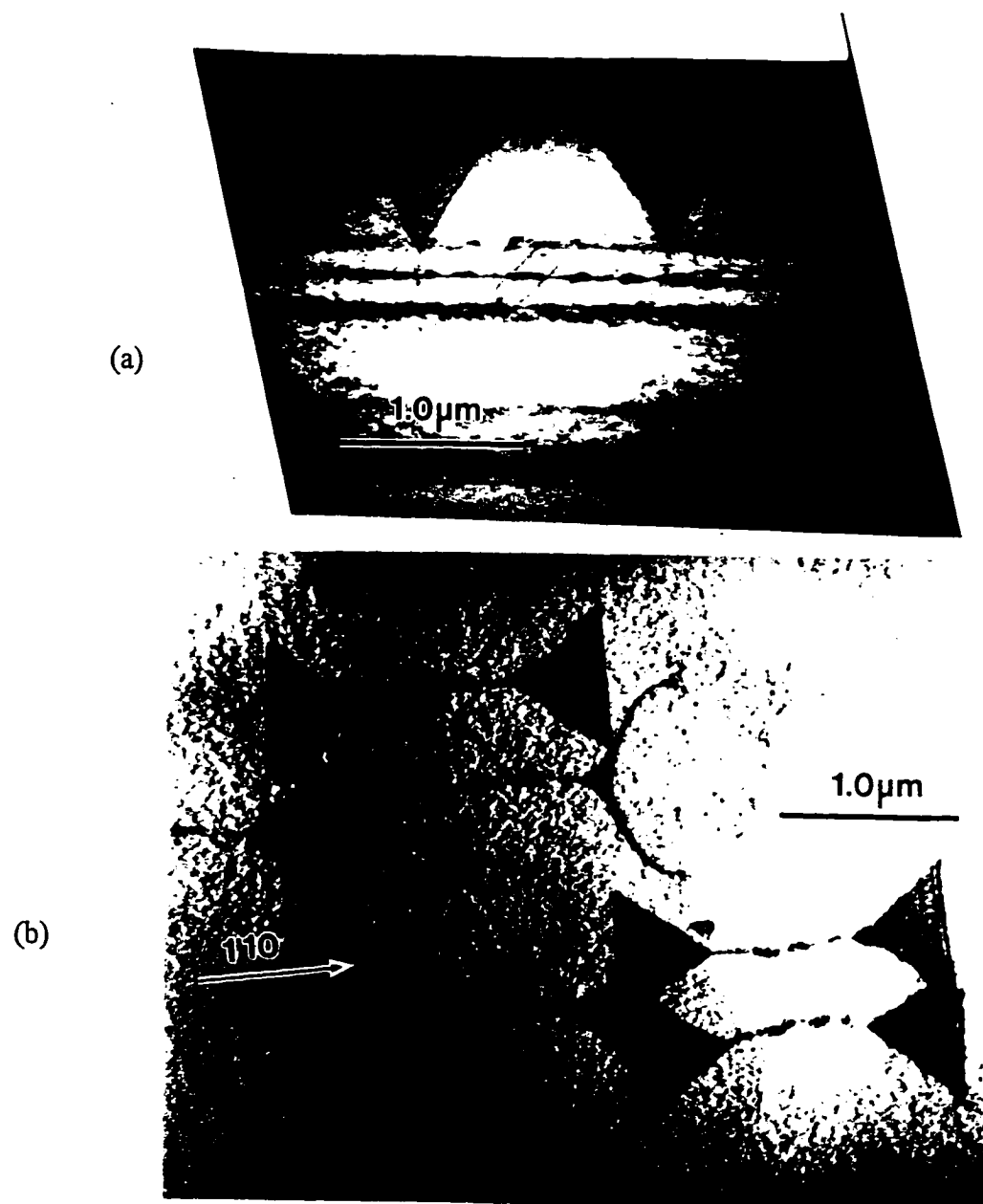
Figure 5.6.   Stacking fault images of the upper p-type layers in quaternary-based
SCH: (a) cross sectional TEM and (b) plan-view TEM

(a)

(b)
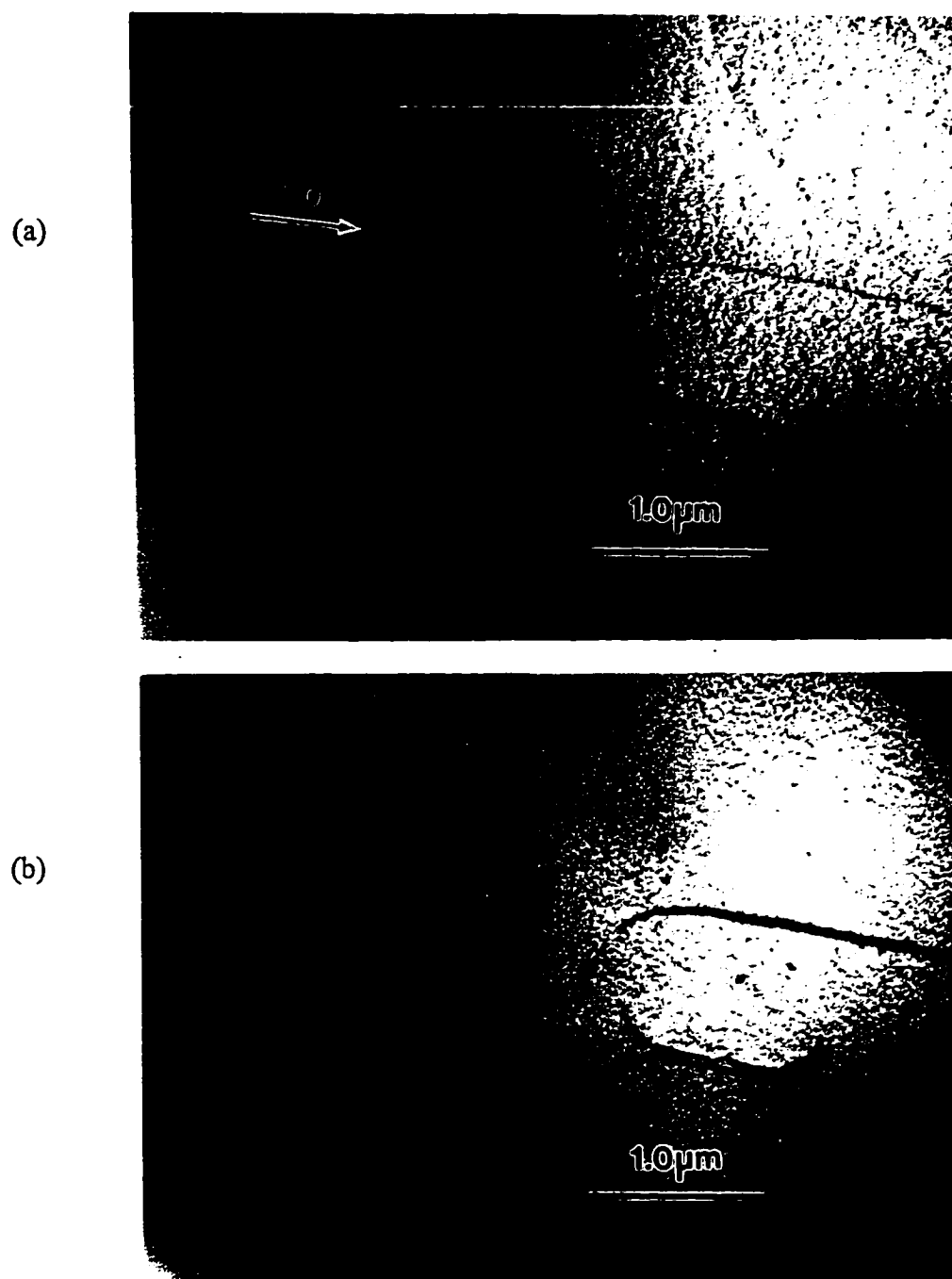
Figure 5.7.   Plan-view TEM images of stacking faults and [110] misfit dislocation taken at (a) g220 and (b) $g\bar{2}20$ two beam conditions in quaternary-based SCH
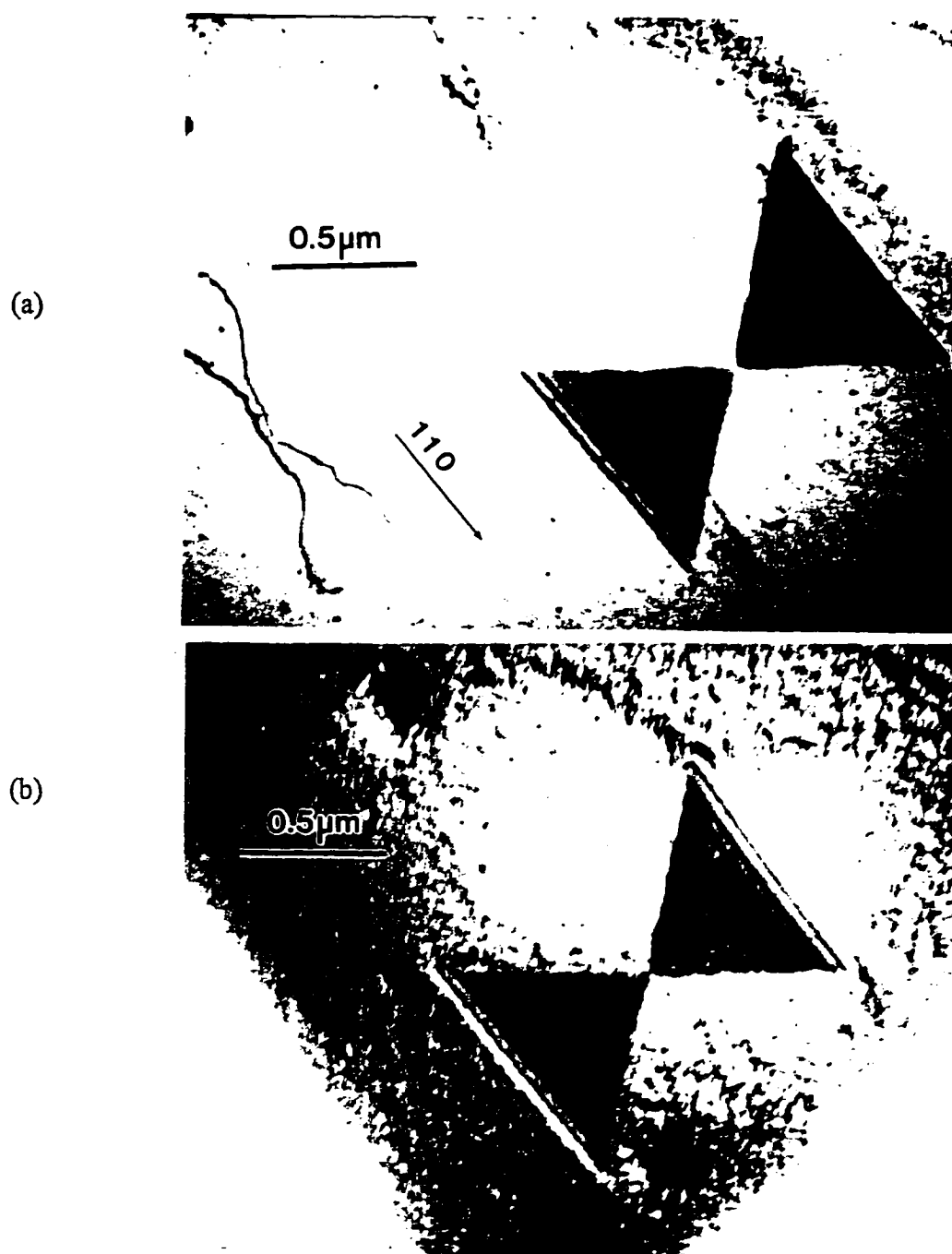
Figure 5.8. Plan-view TEM images of a stacking fault pair in the lower n-type layers of quaternary-based SCH taken at (a) BF and (b) CDF mode
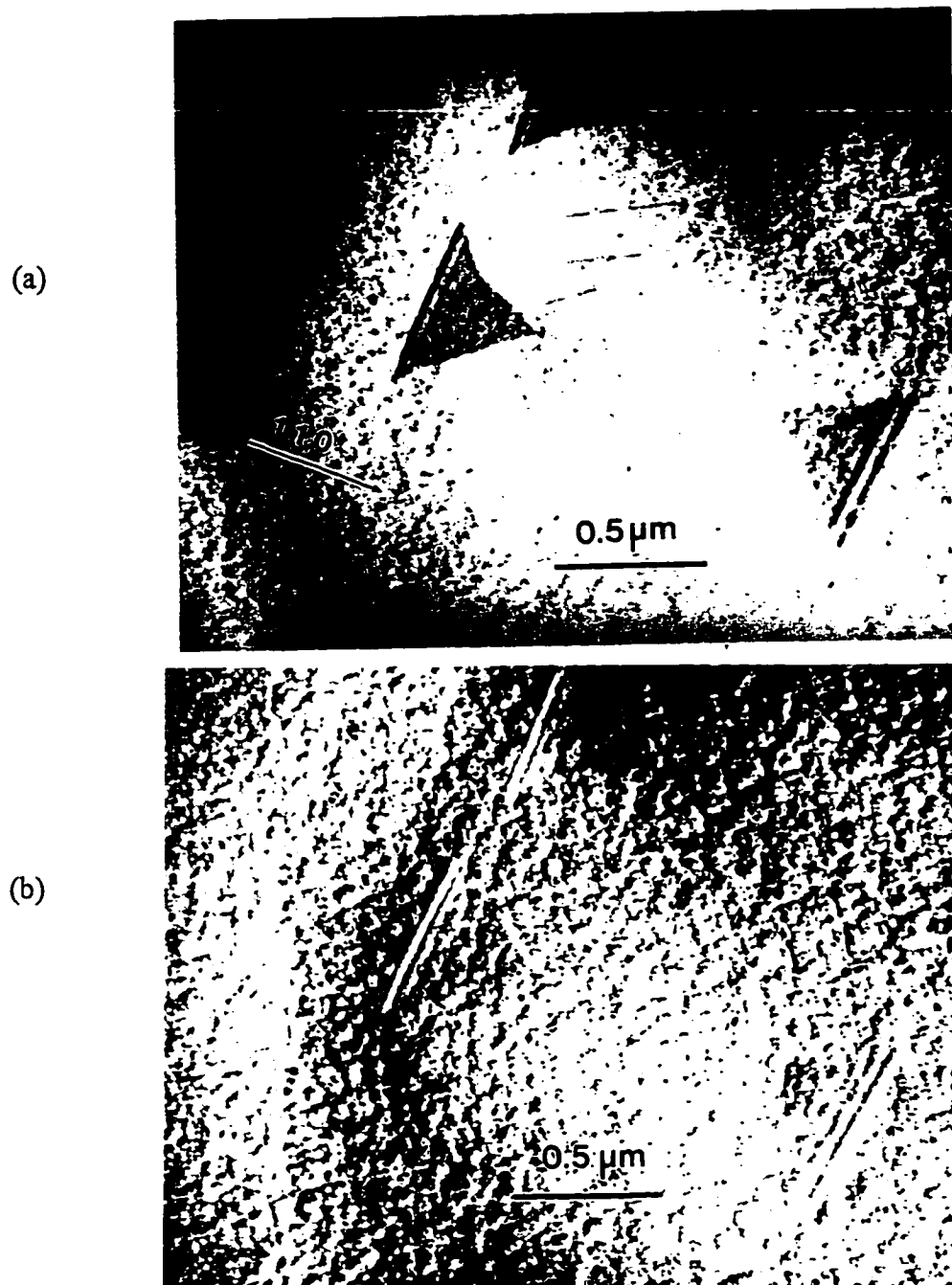
Figure 5.9.   Plan-view TEM images of stacking fault pairs in the upper p-type layers of quaternary-based SCH taken at (a) BF and (b) CDF mode
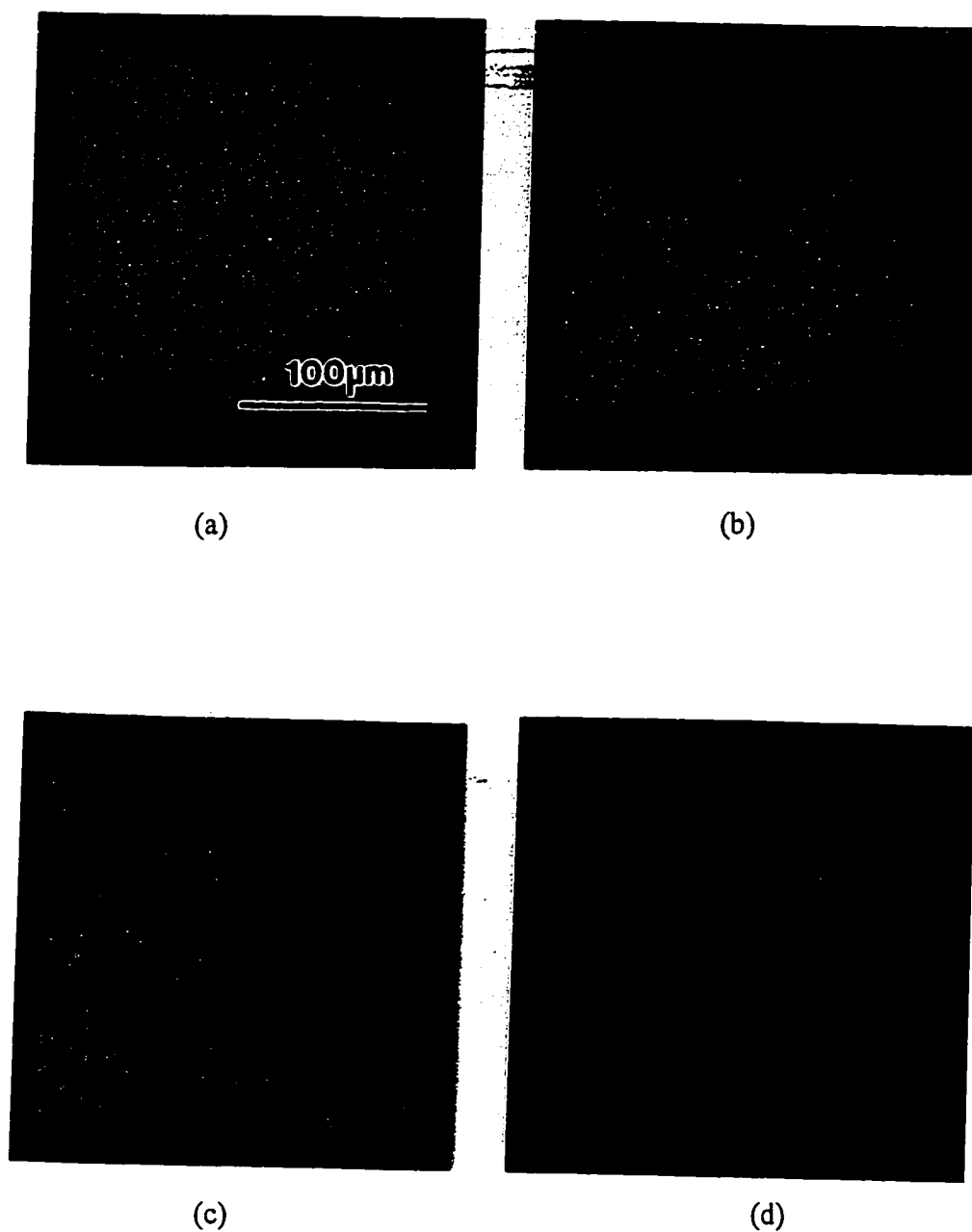
Figure 5.10. Electroluminescence images of the ternary-based SCH taken at (a) 0%, (b) 20%, (c) 50%, (d) 80% degradation at the driving conditions in Table 3.1

(a)   (b)

110

(c)   (d)
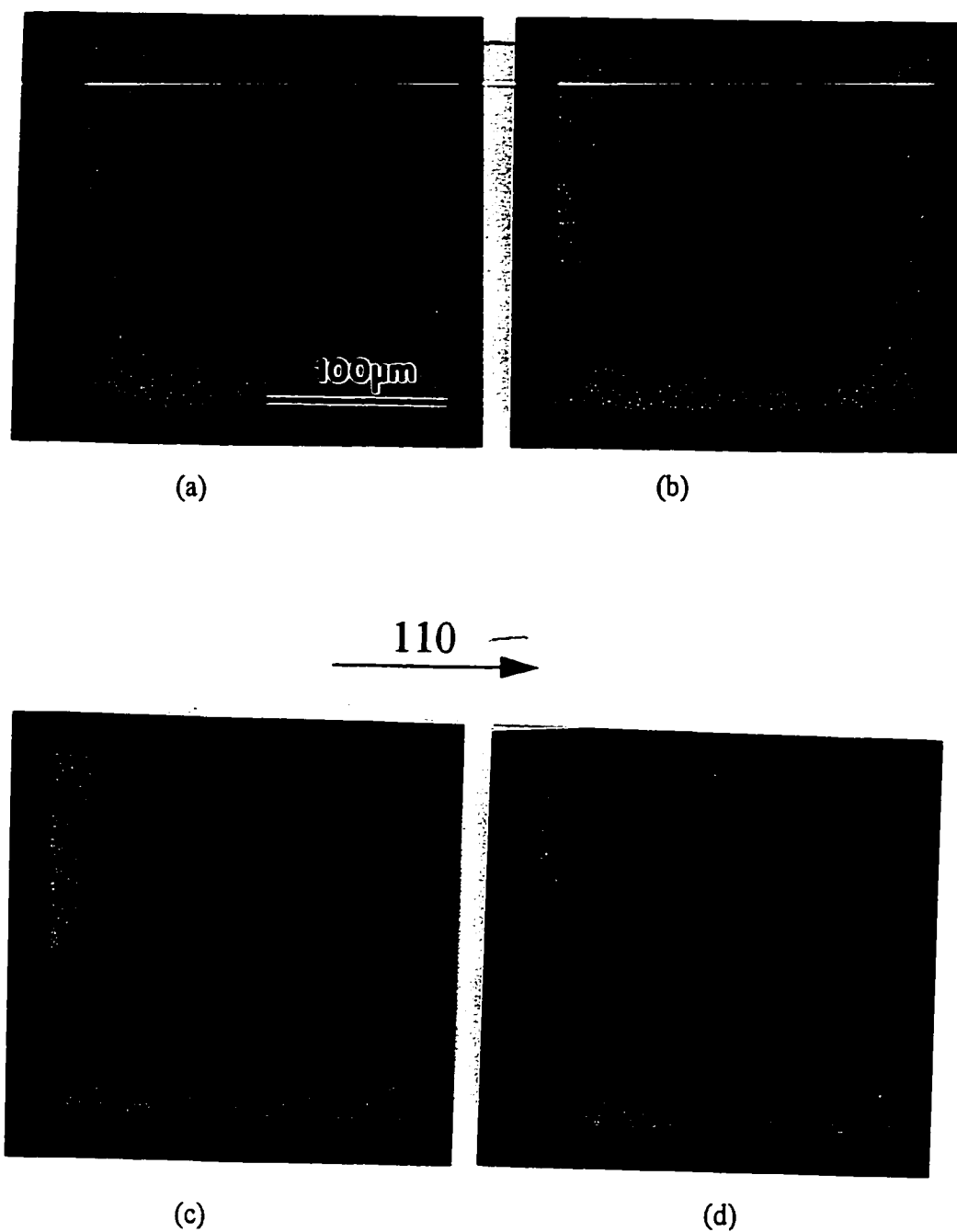
Figure 5.11. Electroluminescence images of the quaternary based SCH (structure I) taken at (a) 0% ,(b) 20%, (c) 50%, (d) 80% degradation. The driving conditions were 20 % duty cycle, 10 KHz and 6 A/cm^2 current density

(a)

110

(b)
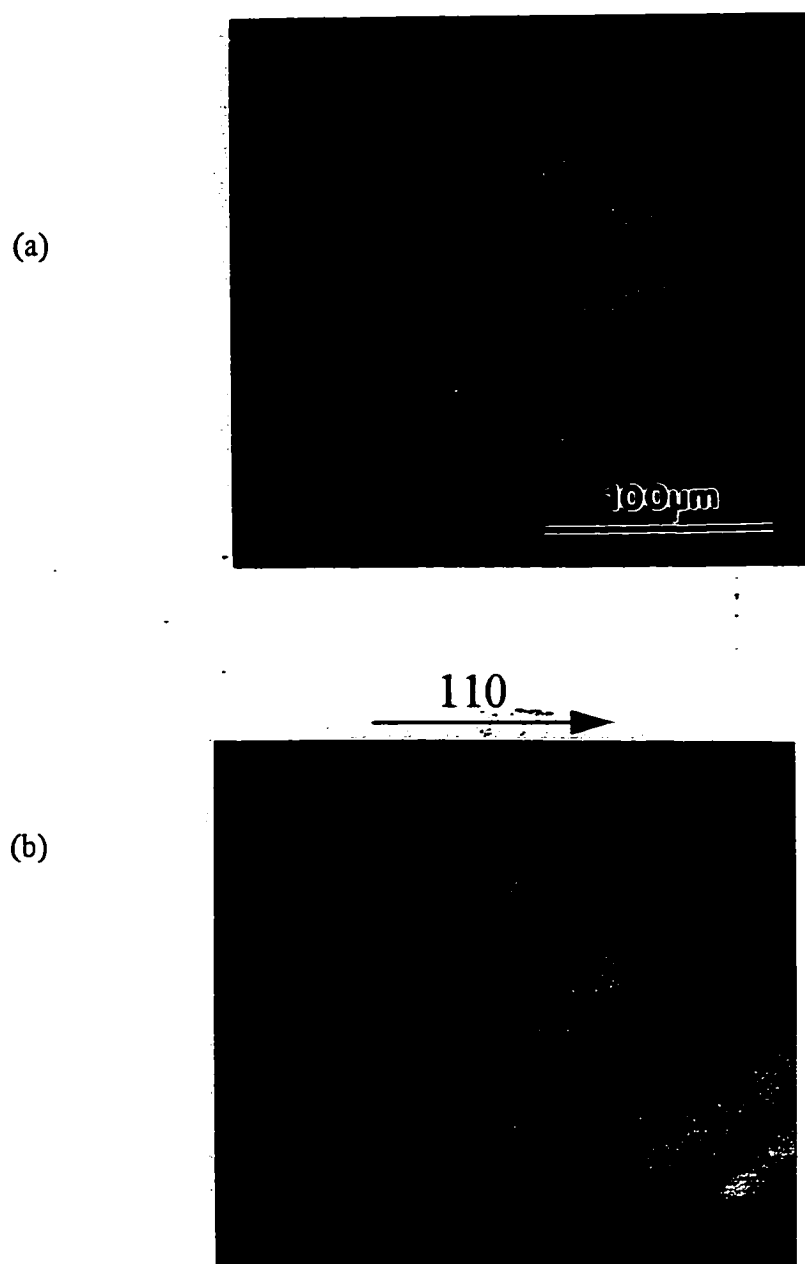
Figure 5.12.   EL images of DLDs in the simplified ternary-based heterostructure
(structure II) at (a) 30 % degradation and (b) 70 % degradation
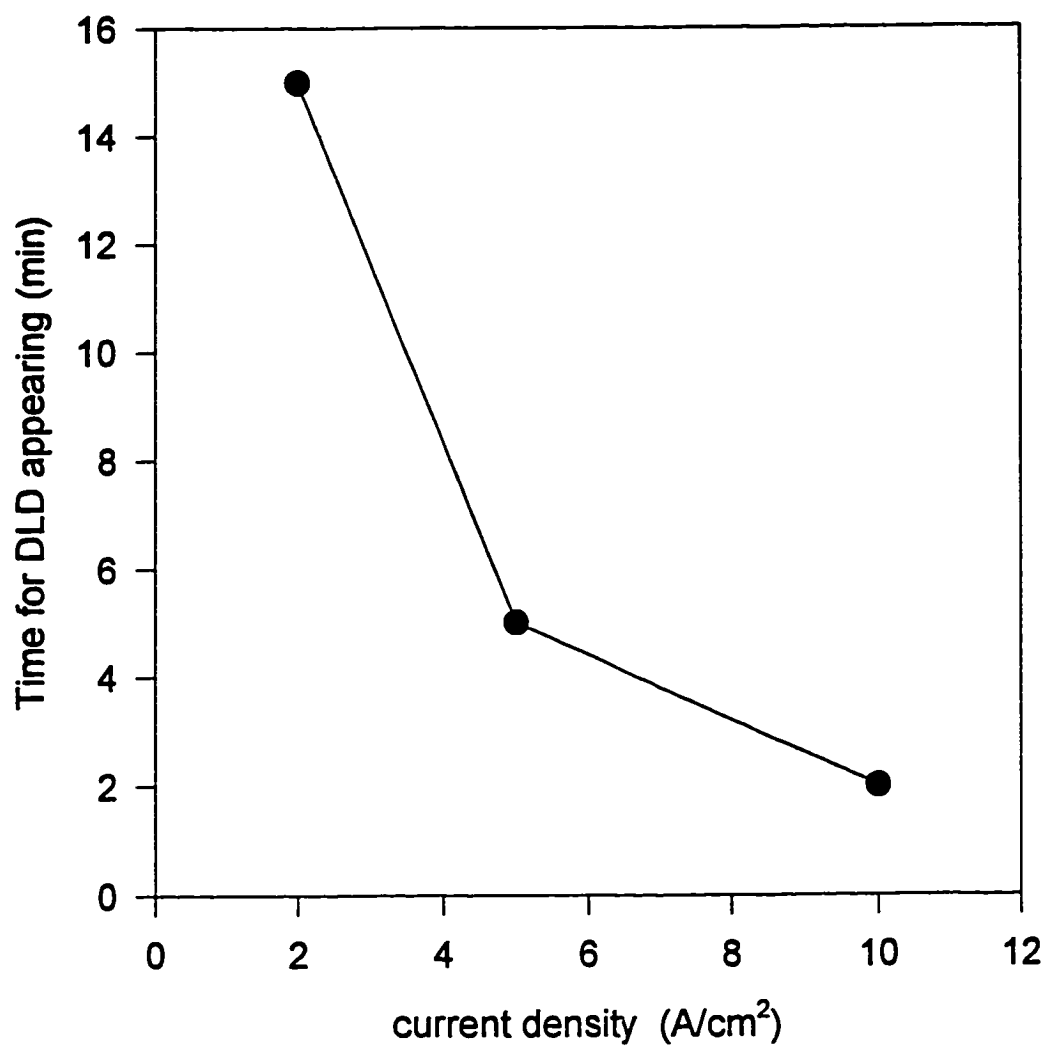
Figure 5.13.   Time for DLD appearance in EL microscopy at different current density at the driving conditions of 10 KHz, 20 % duty cycle for the quateernary-based SCH
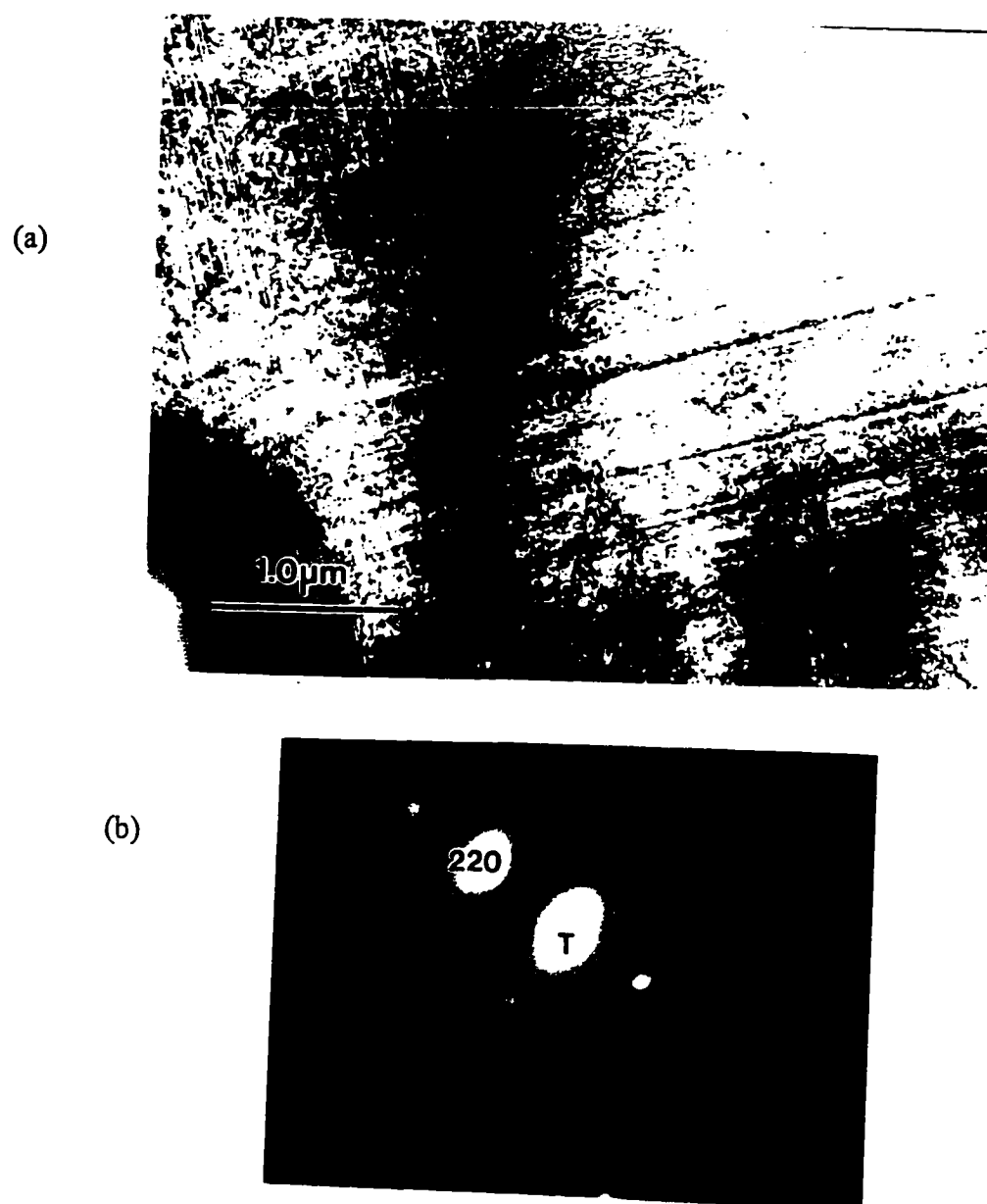
(a)

(b)

Figure 5.14. (a) Plan-view TEM images of DLDs in the 80%-degraded LED of the simplified ternary-based heterostructure, (b) two beam condition (g220) used in the electron diffraction pattern for this picture (angle between the image and diffraction pattern is 1° at 20X magnification and 200 KV, by which the pictures was taken)
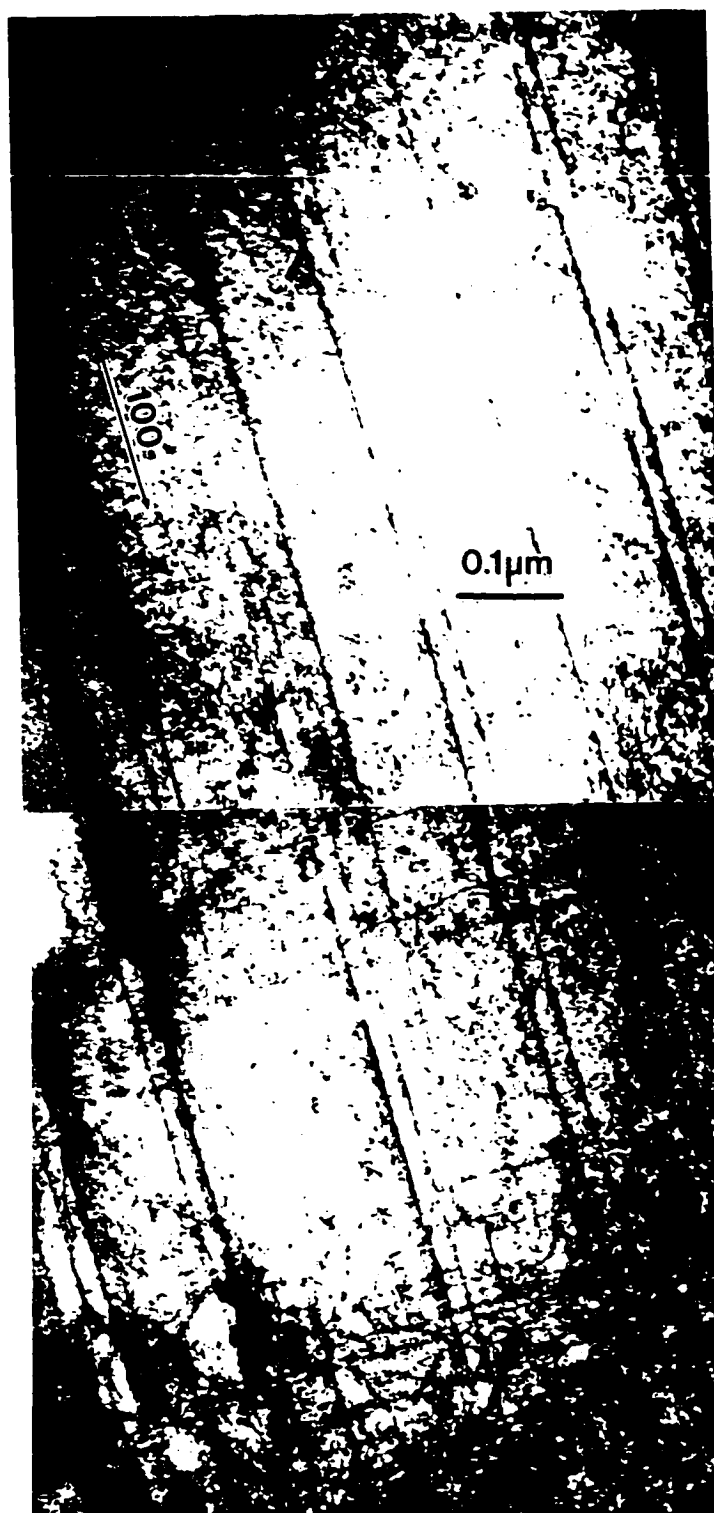
Figure 5.15. Degradation-induced line defects in simplified ternary-based heterostructure. At a distance from the cross section, DLDs are aligned only in one of the <100> directions.
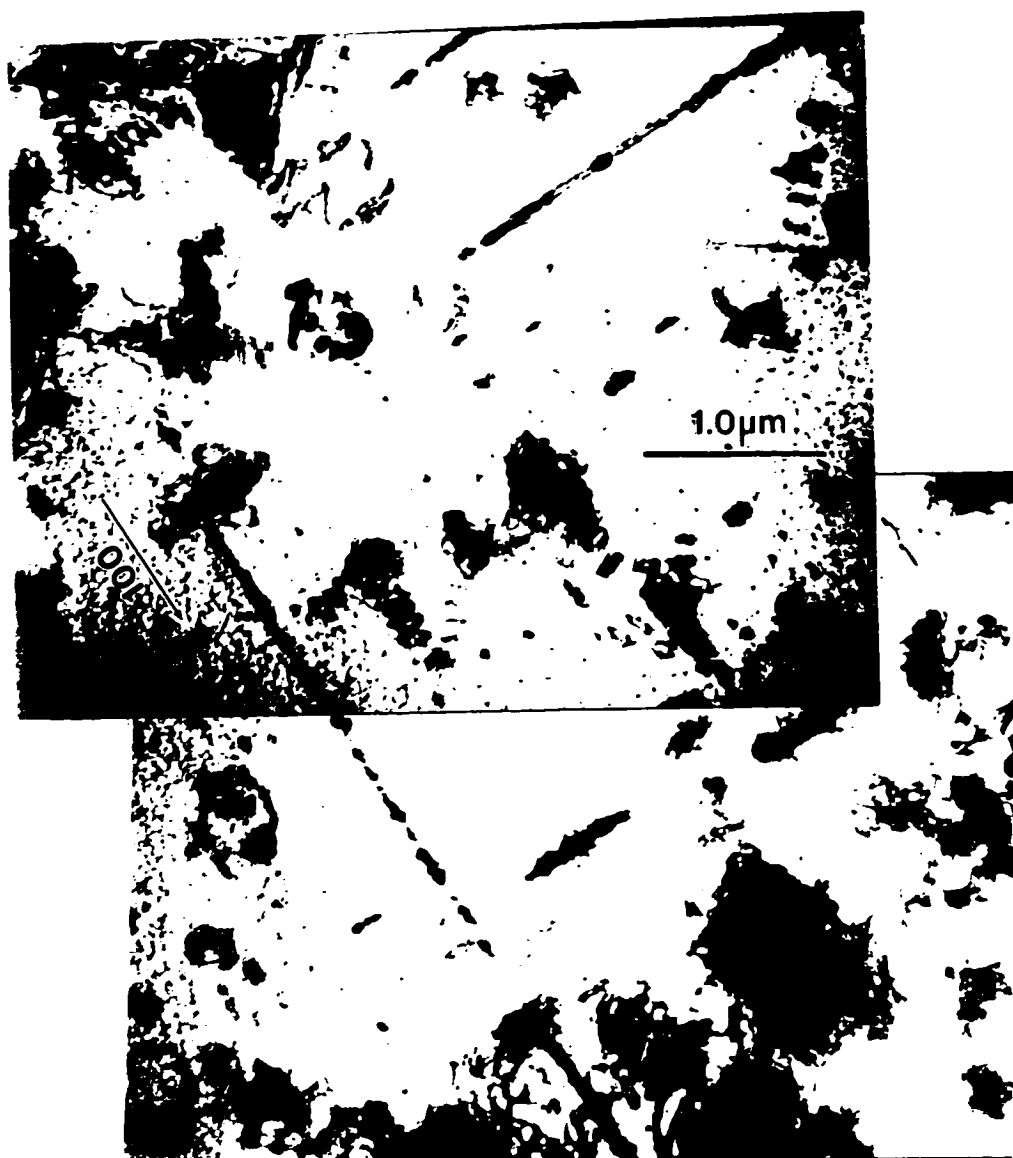
Figure 5.16.   DLDs developed in LEDs fabricated from quaternary-based SCH.   Long DLDs are aligned in the <100> directions and even shorter DLDs were also aligned in <100>.
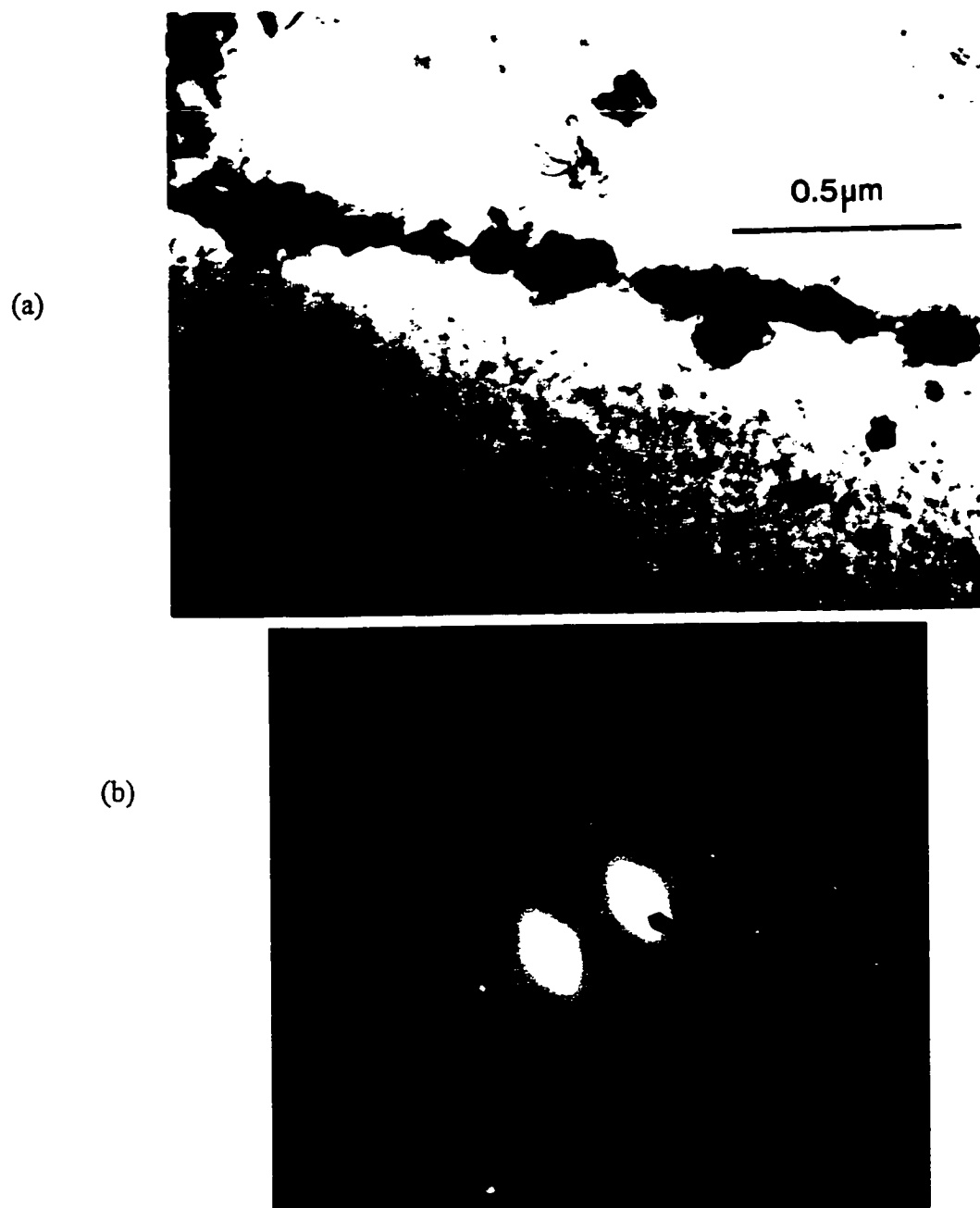
Figure 5.17.   (a) A large scale TEM image of a DLD and (b) diffraction pattern taken at the DLD for quaternary-based SCH. A ring pattern is observable.
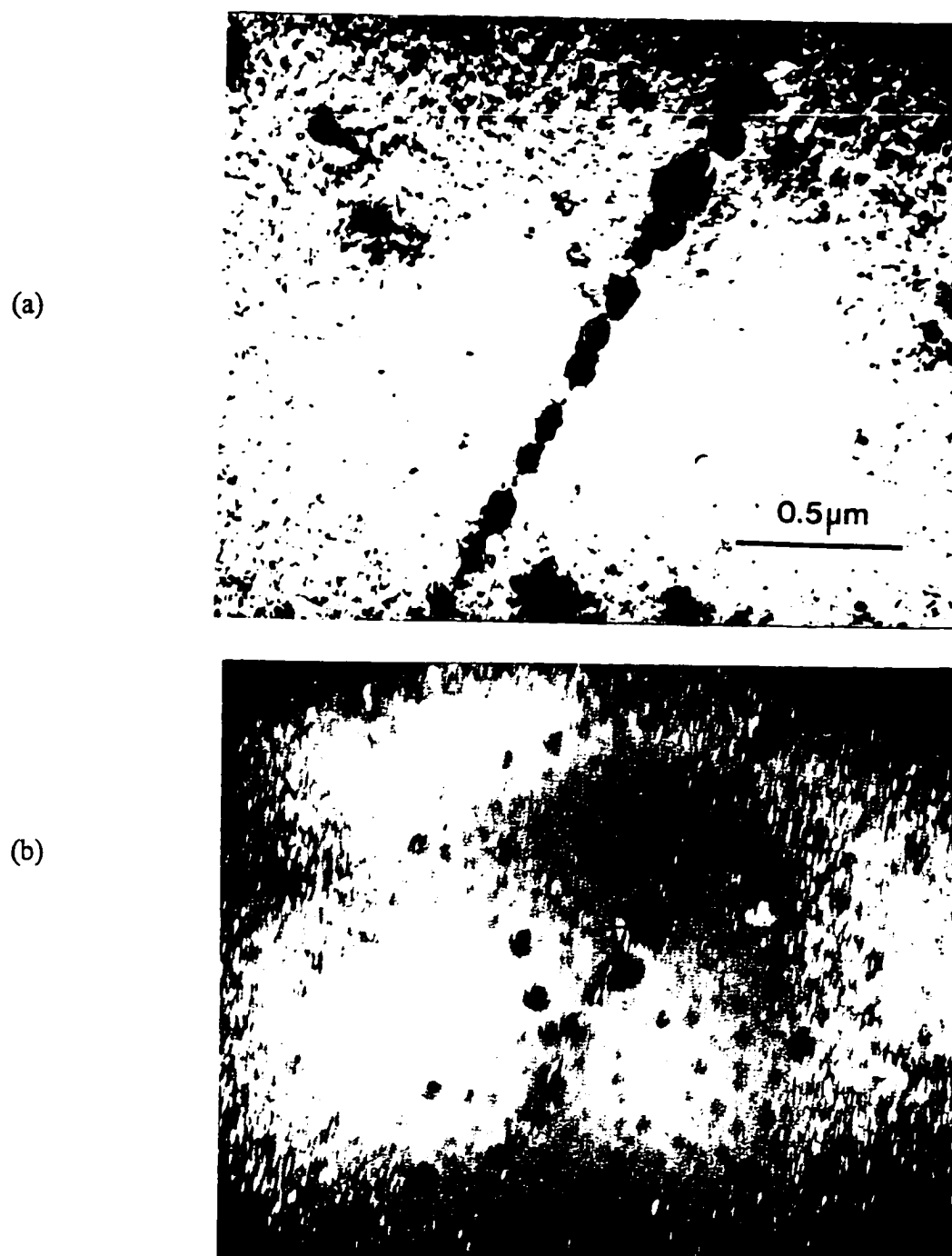
Figure 5.18.   Plan-view TEM images of a DLD at (a) BF and (b) weak beam dark field (WBDF) modes for quaternary-based SCH
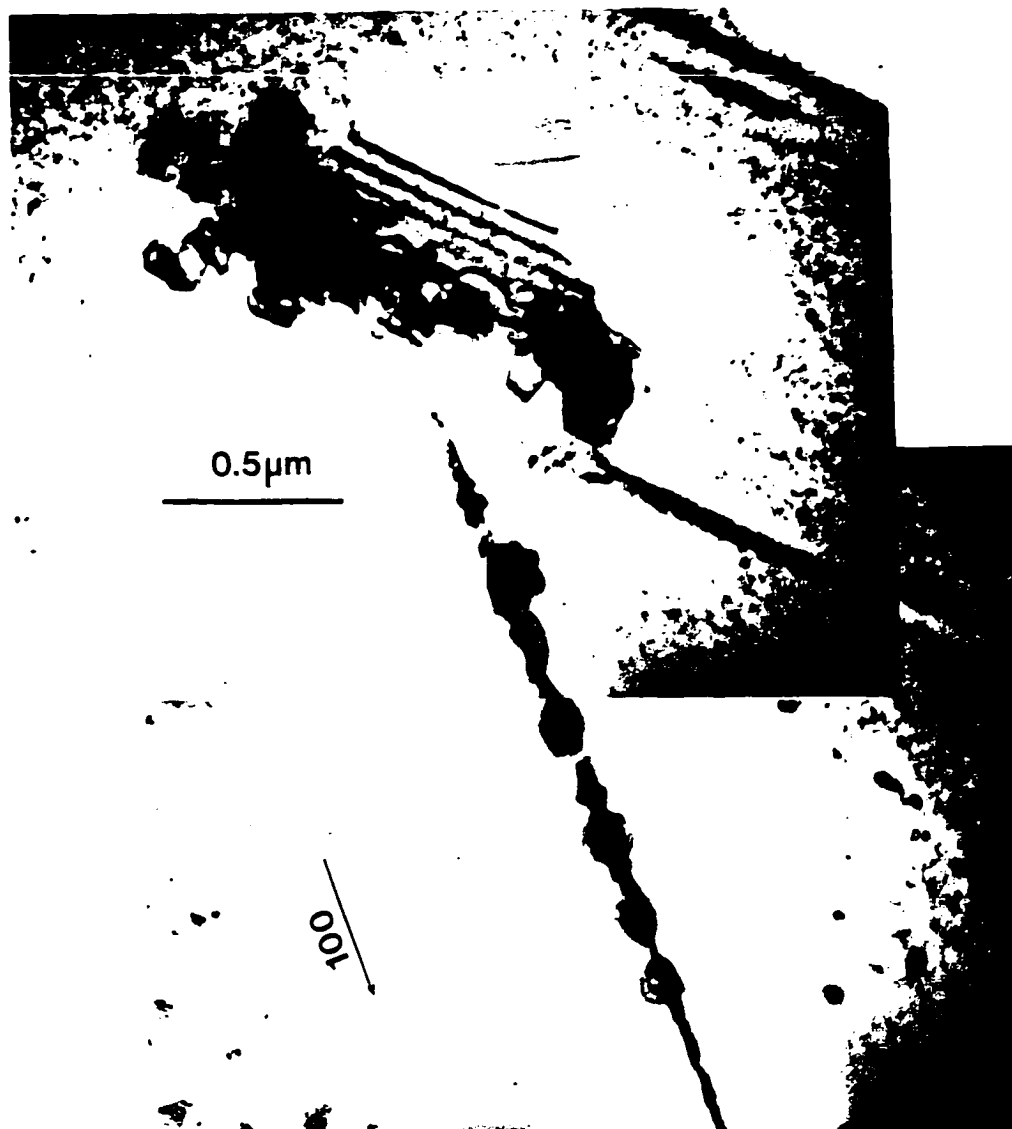
Figure 5.19.   Transformed stacking fault near a DLD. A stacking fault is transformed to tangled dislocations and appears to be a nucleation site of DLD in quaternary-based SCH.
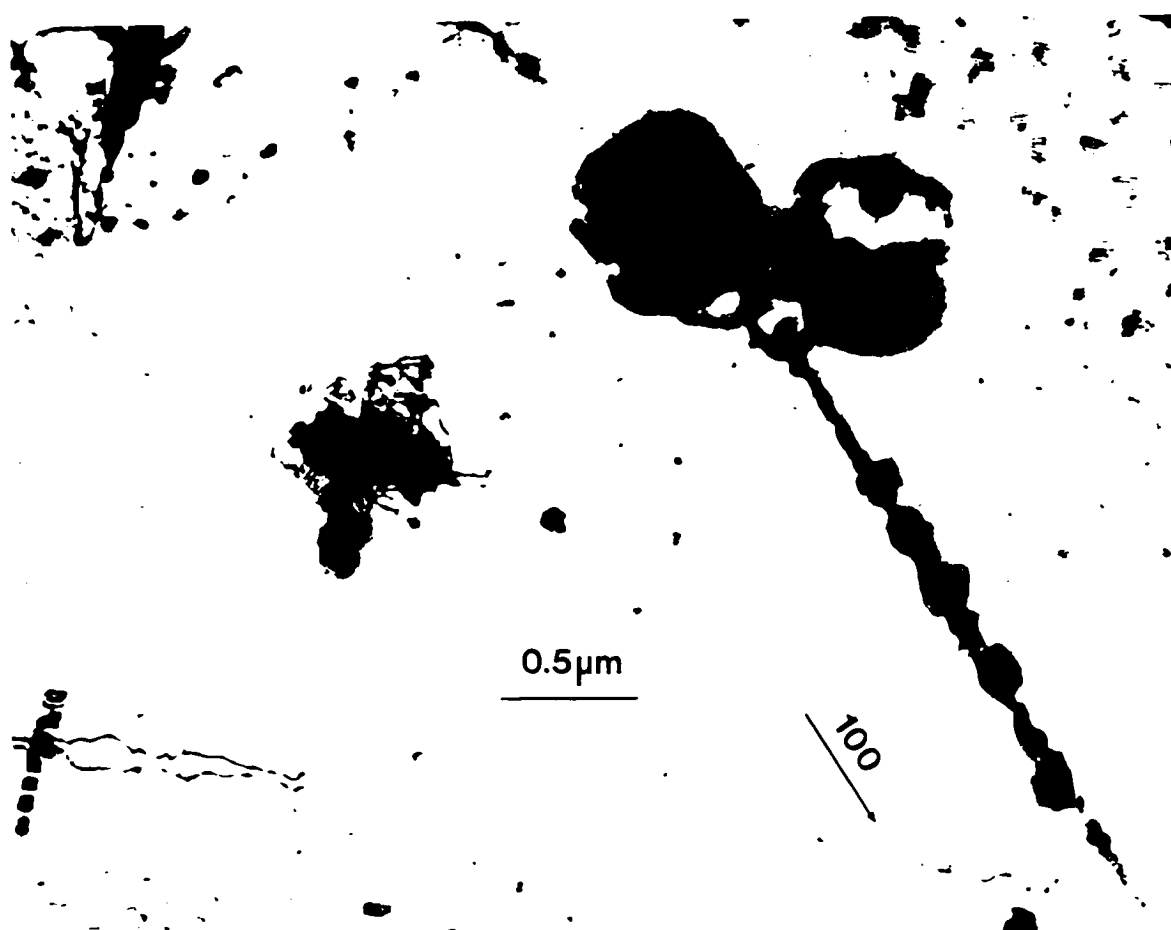
Figure 5.20. A precursor for DLD appears to be melted in quaternary-based SCH
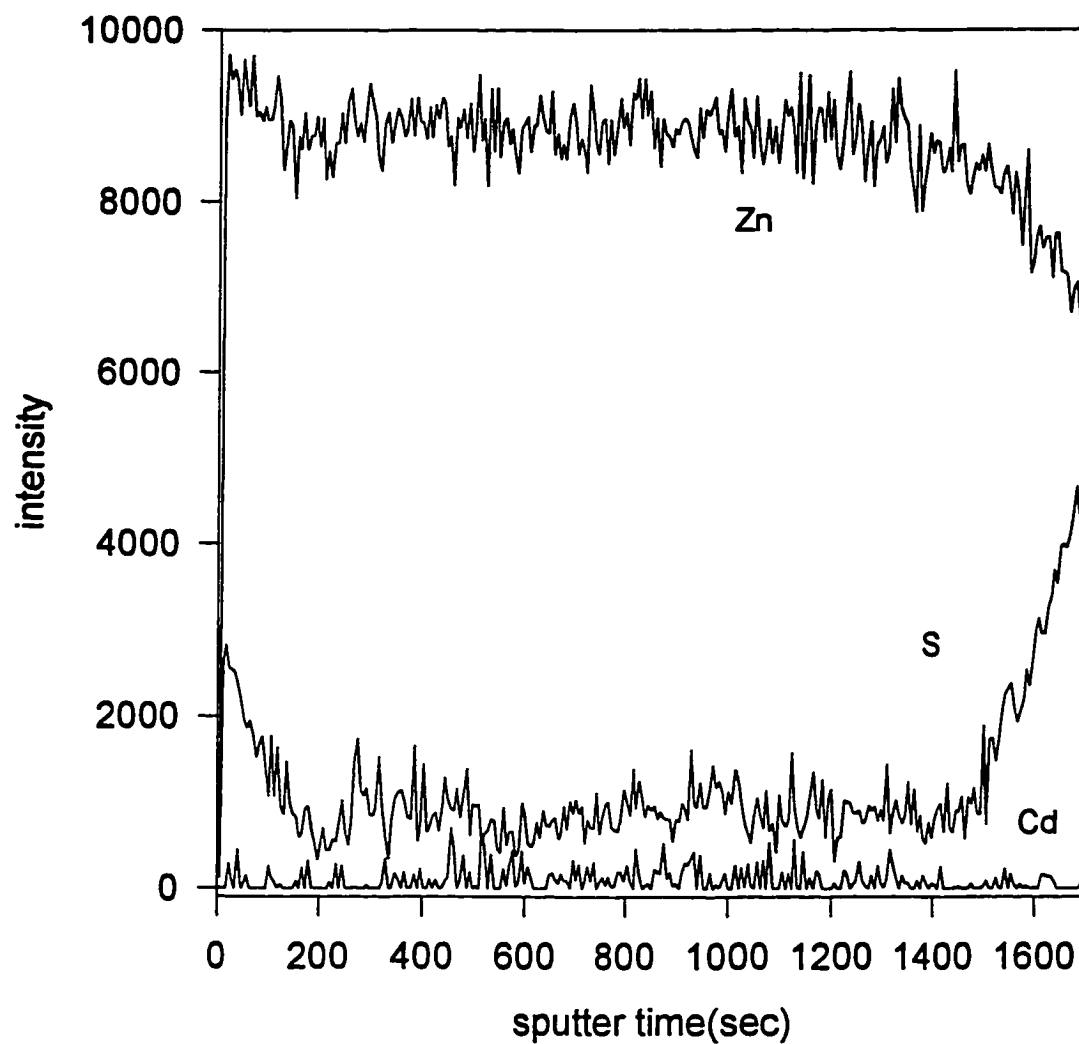
Figure 5.21.   Auger depth profile obtained from the TEM specimen in which DLDs were observed in quaternary based SCH
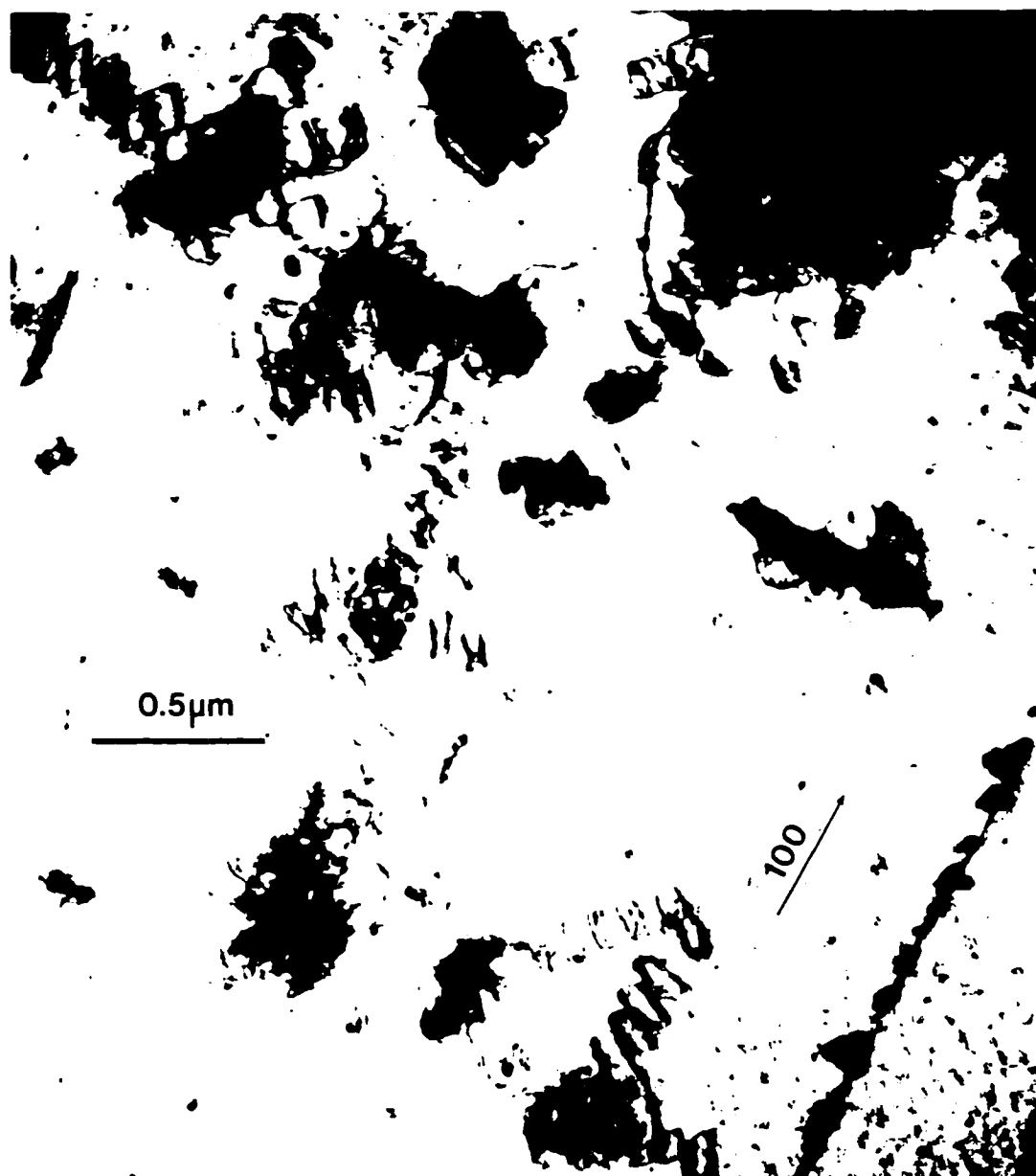
Figure 5.22.   Typical plan-view TEM image near DLD. Relatively large number of dislocation helices were developed and shorter DLDs and dislocation tangles were also observable in degraded quaternary-based SCH.

(a)

QW

0.5µm

(b)

QW

0.5µm
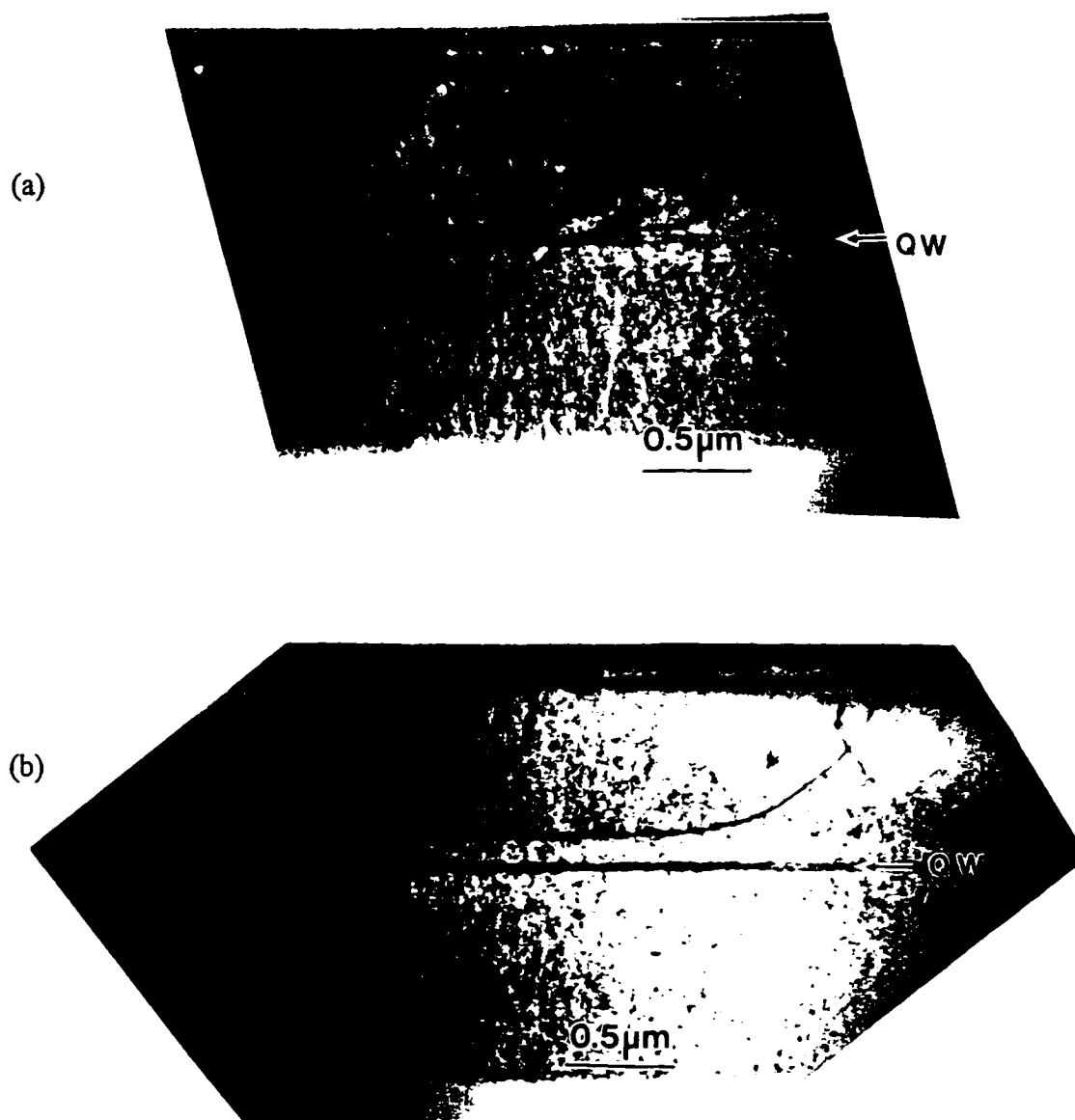
Figure 5.23.   Cross-sectional TEM images of (a) tangled dislocations and (b) dislocation half loops generated in degraded quaternary-based SCH

(a)

0.5μm

(b)

Figure 5.24.   Cross-sectional TEM images of (a) dislocations half loops and (b) stacking faults generated during LED operation in quaternary-based SCH

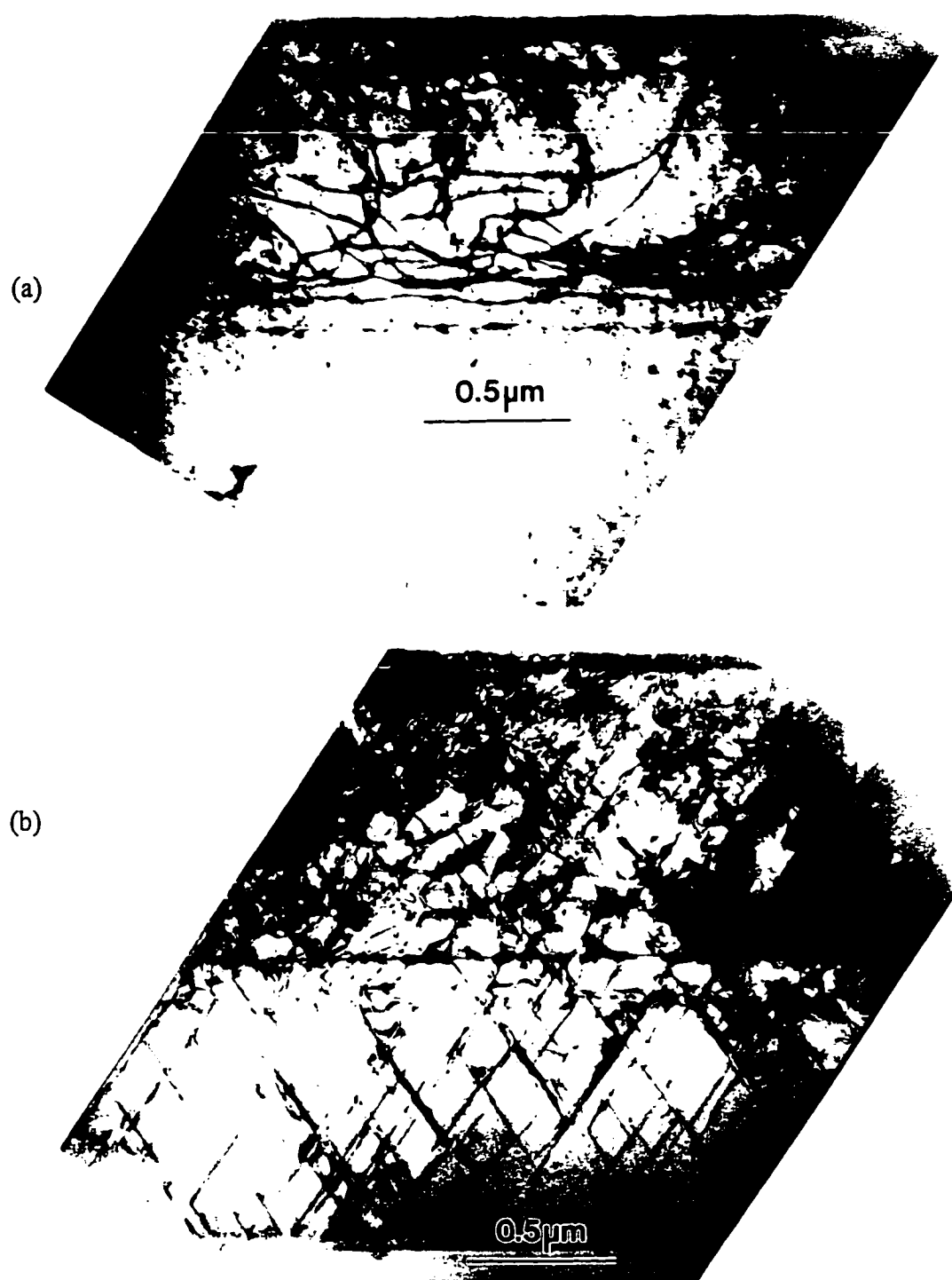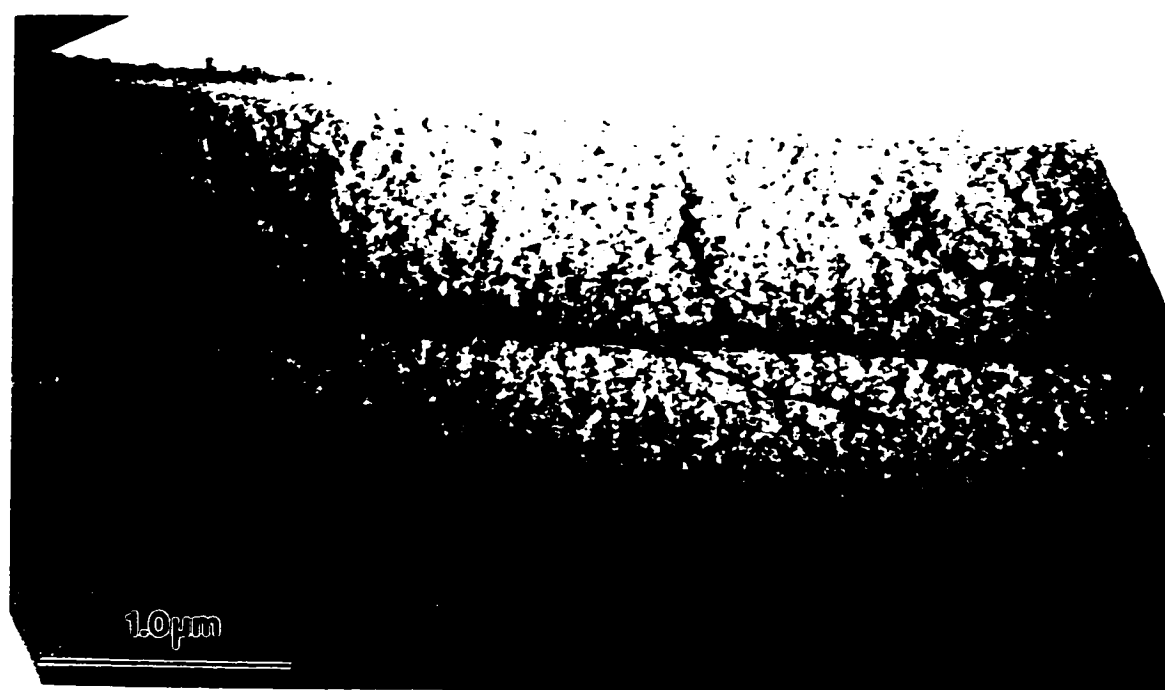Figure 5.25.   Cross-sectional TEM image of degraded ternary-based heterostructure showing that a main dislocation confined in the QW and other dislocation branches developed from the QW

CHAPTER 6
DEGRADATION MECHANISM

The following observations were recorded during the course of this study:

(a) LEDs degrade rapidly at current density levels that are well below the lasing level for lasers. The degradation proceeds with the generation of DSDs and DLDs in the active quantum-well region during operation.

(b) LEDs degrade more rapidly with increasing density of preexisting defects and current density.

(c) The temperature of the active region during a typical LED operation is about 250 °C and this value is higher than that of III-V devices.

(d) No atomic interdiffusion takes place during LED operation and the abruptness of the quantum-well is maintained during the early stages of degradation. The strain in the quantum-well is not relaxed in the 50%-degraded LEDs, however it is partially relaxed in the 80%-degraded LEDs.

(e) DSDs and DLDs appear in the early stages of degradation but are not detected in TEM. The EL intensity decreases as the size of DSDs and DLDs increases. The degradation induced extended defects are observable only in the heavily degraded LEDs. Other types of extended defect formation (dislocation helices) indicate that point defects were generated

158

during degradation.

(f) For structures that have a low pre-existing stacking fault density ($<10^6$/cm^2), DLDs appear to be straight lines which may be strings of point defect clusters.

(g) For quaternary-based separate-confined heterostructures that have many stacking faults ($5*10^6$/cm2), an unusual extended defect structure that is not a simple dislocation area appears to correspond to the DLDs. These elongated degradation-induced defects appear to be distorted crystalline material consisting dense tangles of small dislocations and connected along the <100>directions.

(h) Stacking faults appear to be the nucleation sites for many DLDs. Melted regions may be another possible nucleation site for DLDs.

Based on these facts degradation can be divided into two stages. In the first stage of degradation, point defects are generated and DSDs and DLDs are formed. In the second stage, extended defects are formed and strain in the quantum well relaxes. One mechanism of DSDs and DLDs formation may be due to point defect generation and their subsequent clustering. In the early stages of degradation, nonradiative recombinations occur at the pre-existing defect sites in the quantum-well. Point defects could be generated because of the following; (1) Existence of relatively large concentration of impurities and/or crystal defects (intrinsic point defects, stacking faults, and dislocations) from the growth (2) Release of larger amount of energy due to nonradiative recombination at these sites

(3) Low activation energy of self diffusion, interdiffusion, impurity diffusion for II-VI compounds. Point defects could be generated in the quantum-well or/and diffuse from sources such as the interface or the surface. Dark spot and line defects could be then formed by condensation of the generated point defects. The point defects and their clusters are too small or the strength of the associated strain field is too weak to be detected by TEM. A second possibility may be that DLD could nucleate due to melting of a defect site. During this fast melting and quenching a large concentration of point defects can be created and condensed into DLDs. In the second stage of degradation, extended defects such as dislocations are developed through point defect condensation and dislocation climb. They are primarily developed in the quantum-well and mostly in the p-type layer that is near to the ohmic contact. The quantum well is highly strained and thus is the weakest junction in the entire heterostructure. Some amount of strain in the quantum-well could then be relieved in the second stage through to the formation of the observed line defects. In the p-type layer it is easier for dislocations to grow by climb from the abundant defect density in the contact region.

The point defect creation, diffusion and annealing during operation due to nonradiative recombination will be further discussed in later sections. The thermal stability of the quantum-well and the possibility of melting during operation are also discussed. Finally a model of the degradation cycle is proposed.

6.1 Point Defect Generation

The creation of point defects was speculated to account for the slow degradation of III-V devices. During the operation, point defects are created continuously for a long period of time at deep level defects with the energy from nonradiative recombination. Point defects created appeared to disperse homogeneously through out the active region. Uji et al. observed the formation of micro-dislocation loops rather than large dislocation networks in gradually degraded AlGaAs lasers [95]. Despite these observations, point defect creation in III-V devices during the long periods of operation has not yet been confirmed.

<u>Energy dissipation during Non-radiative recombination (Multiphonon emission)</u>. The ground state of deep defects is separated from the band by a high energy which is larger than the energy of lattice or of the local phonons. Therefore, carrier capture by such centers is accompanied by the simultaneous emission of many phonons. The basis for the theory of multiphonon transitions was laid by Huang and Rhys in 1950 [96]. They proposed an adiabatic potential of a defect without an electron (U2) and that with an electron (U1) as shown in Figure 6.1. In this one dimensional configuration-coordinate diagram, the coordinate x is called nuclear coordinate and U represents the potential energy of the nucleus. Nonradiative recombination at an impurity center occurs in two steps. For example, in a p-type material an electron in the conduction band is first

captured in a bound state and a certain amount of energy ε_1 is released. The atom with the bound electron is displaced to a new equilibrium position. Then the bound electron recombines with a hole in the valence band and an amount of energy ε_2 is released. During these two transitions, energy equal to the band-gap must be dissipated. The multiphonon emission has been considered a major energy dissipation mechanism in GaAs and GaP. Immediately after the capture of the electron the lattice is displaced far from the equilibrium position giving rise to a violent lattice vibration at the defect. The vibration damps rapidly down to the amplitude of thermal vibration at the defect after a small number of vibration periods. During the damping, the localized energy propagates away from the defect as lattice phonons.

In devices made from wide band gap II-VI materials, point defect creation by nonradiative recombination is theoretically easier because of the larger band gap. As will be discussed below, the formation energy of point defects is about the same as GaAs. Further more, there are many grown-in nonradiative recombination sites in the as-grown structure. Therefore, it is more susceptible to generating point defects during device operation by multiphonon emission in wide gap II-VI devices.

The vacancy formation energy (ΔH) in GaAs has been calculated to be 1.6 or 2.3 eV depending on the charge state [97]. For II-VI compounds the enthalpy of formation of vacancy was calculated by J.A. Van Vechten

[98]. The formation energy of vacancies varied between 2.6 and 3.5 eV for the II-VI's systems.

The energy for Frenkel (interstitial-vacancy pair) defect formation is usually smaller than that of Schottky (vacancy) defect formation. For Si the energy of formation of a Schottky defect, i.e. the energy required to move an atom from its lattice site within the crystal to a lattice site on its surface is 2.3eV. However, the energy of formation of a Frenkel defect is about 1.1 eV, which is about half of that of Schottky defect [99]. The energy for vacancy formation in a compressed layer has been shown to be reduced compared to an unstrained structure by Hopgood [100]. In a layer of $In_{0.2}Ga_{0.8}As$ on GaAs the drop in the energy of formation of a vacancy was calculated to be as large as 0.5 eV. The formation energy of a Frenkel defect would be much less than the values in Table 6.1. for a strained ZnCdSe quantum-well.

Table 6.1. Enthalpy of single vacancy formation[98]

materials(AB)	$\Delta H(V_A)$[eV]	$\Delta H(V_B)$ [eV]
Si	2.66	
GaAs	2.59	2.59
ZnS	3.47	3.13
ZnSe	3.09	3.09
CdSe	3.18	2.65

Dow et al. [101] proposed that the rapid degradation of III-V semiconductor lasers may be initiated by trapping and non-radiative e-h recombination assisted by the deep dangling bond levels of an anion vacancy or vacancy complex. The recombination events provide a mechanism of energy localization that eventually leads to the production of other vacancies or vacancy complexes. A dangling bond energy level associated with a daughter vacancy becomes another excitation trap. This self-reproducing dangling bond trap eventually may grow into a dislocation and becomes an excitation trap of macroscopic dimensions.

In order to try to determine if point defects are generated at/near the quantum-well region in the early stages of operation, two methods were used. The first involved using SIMS to look for any diffusion enhancement of constituent elements due to excess point defect creation. The second involved looking at the PL intensity decay at higher temperatures.

6.1.1 Diffusion Enhancement due to Point Defects

An indirect method of studying the generation of point defects during operation is done by measuring diffusivity of a solute during high temperature annealing. Solvent and solute atoms migration through a crystal lattice can be enhanced by excess point defects. This has been studied extensively in silicon as excess point defects can result in phenomena ranging from oxidation enhanced diffusion to transient enhanced diffusion [102][103]. Therefore the hypothesis was, if point defects are generated near the quantum-well during degradation, then

depending on the diffusion mechanisms of the solute the diffusion of the solute atoms might be enhanced due to the higher concentration of interstitials or vacancies or their complexes.

LEDs made out of the ternary-based SCH (structure I) were degraded 30% and 60% (down to 70% and 40% of the initial output intensity) and then annealed in an ambient of forming gas (10% H_2 + 90% N_2) at a temperature of 500 °C for 10 minutes. Composition depth profiling was performed by SIMS. The PL spectra were obtained before the SIMS measurements.

As-grown structures were annealed at 500 °C for 10 minutes. The SIMS depth profiles of Cd were obtained from the annealed and nonannealed as-grown samples. Figure 6.2. shows the Cd profile at the ZnCdSe quantum-well region. This figure indicates that there is no outdiffusion of Cd even after annealing at 500 °C for 10 minutes.

The 30% degraded LED was annealed at 500 °C for 10 minutes. Cd depth profiles were obtained from the annealed and nonannealed LEDs which were 30%-degraded. Figure 6.3 shows Cd outdiffusion for the 30%-degraded LEDs comparing the annealed and nonannealed ones. Cd appears to diffuse out to the barrier layers from the quantum-well for the degraded LED at this annealing condition. Cd diffusion enhancement is obvious in the degraded sample. The diffusion enhancement factor (D_{Cd}/D^*_{Cd}) was determined to be about 20 by fitting Gaussian functions to normalized SIMS profiles in Figure 6.2 and Figure 6.3.

The nondegraded LED, 30% and 60% degraded LEDs were annealed at 500 °C and for 10 minutes. SIMS depth profiles of Cd were obtained on these samples. Figure 6.4 shows Cd depth profiles. The Cd outdiffusion was enhanced in the degraded samples. However, the Cd outdiffusion appears to be less enhanced between 30%- and 60%-degraded at this annealing conditions. Photoluminescence spectra were taken from these annealed samples at room temperature. Figure 6.5 shows the results of the photoluminescence measurement. The barrier peaks (ZnSe) were reduced, however, the quantum well peak was broadened more as the degree of degradation increased. This indicates that the interdiffusion in the quantum well region was more enhanced in the more degraded LEDs.

The enhanced outdiffusion of Cd from the quantum well was observed in the sample which were 30% and 60% degraded. The enhancement of Cd diffusion may come from the large number of point defects created during operation at/near the quantum well.

6.1.2 PL Intensity Decay at High Temperatures due to Point Defects

Since thermally activated nonradiative recombination centers have been associated with point defects [104], temperature dependent photoluminescence intensity quenching measurements can be used to evaluate changes in the point defect concentration. This method was used to estimate the concentration of point defects for MBE grown ZnSe by Grillo et al. [105].

LEDs from the simplified ternary-based heterostructure (structure II) were degraded down to 30% of the initial intensity and PL spectra was obtained at temperatures between 22 K and 150 K. The results are shown in Figure 6.6, which shows the PL intensity quenching of the quantum-well peak for the as-grown and degraded structures at higher temperatures. The increased quenching of the quantum-well PL spectrum suggests that point defect concentration in the active region has increased during degradation. This indicates that point defects are generated in the quantum well during operation. Another indication of point defect generation is shown in Chapter 5. TEM images of degraded structures show that these dislocation helices develop near DLDs during degradation. The helices can not form without point defects in the absence of applied stress.

The remaining question is whether the point defects are created within the quantum well or diffuse from the surface, that is, the mechanism of point defect generation is conservative or non-conservative. This should be further investigated. However, it is more likely that a conservative mechanism take place when the relatively short time period for the 30% degradation is considered. It takes about 10 minutes at the current density of $10A/cm^2$ for 30% degradation and the point defects may not be able to diffuse about 0.02 microns. Because the value of $\sqrt{Dt}$ for Cd in ZnSe at 250 °C for 10 minutes is around 0.02 µm. Also if the point defects diffused in from the surface, the quantum well would show broadening after degradation without additional 500 °C annealing.

6.2 Nonradiative Recombination-Enhanced Diffusion

An interesting question is if point defects do form then why are they so mobile when the intrinsic diffusion is so small between RT and 250 °C. One answer is their motion is enhanced by nonradiative recombination enhanced diffusion. The second possibility is the temperature of the quantum-well is too higher than 250 °C. The third possibility is they do not have to travel far to produce degradation.

Lang and Kimerling[106] had shown that nonradiative recombination leads to the low temperature annealing of radiative recombination damage centers in GaAs. They observed a sharp rise in the annealing rate when they applied a forward bias current to the radiation damaged p-n junction of GaAs. The activation annealing energy, Ea, which is equal to 1.4 eV for zero bias, decreased to a value of 0.34 eV at forward bias. This annealing rate increase was interpreted as the result of the local vibration heating due to multiphonon emission. The mechanism of nonradiative recombination gives rise to violent, short-lived lattice vibrations localized at the defect site which greatly enhances the probability of defect motion.

Two major mechanisms of enhanced diffusion due to nonradiative recombination were proposed. (1) The activation energy for the atom to jump depends on the charge state of a defect. For example, the defect was neutral in the initial state and its activation energy was Ea. On capturing an electron, the defect acquires a negative charge. Thus its activation

energy may be less than that of a neutral center. In the course of recombination the centers recharge, and the charged centers are more mobile than the neutral ones, so the recombination results in enhanced diffusion. (2) Recombination enhanced diffusion can also assisted by the energy released in multiphonon capture of carriers. This energy released would reduce the activation energy for a defect to jump out to the next site. In a similar model labeled 'thermal flash', the energy released in the course of multiphonon recombination leads to a local rise of the crystal temperature in the vicinity of the defect thus increasing the probability of jumps.

In our devices there are pre-existing defects, such as dislocations, stacking faults and possibly point defects(vacancies, interstitials, antisites, impurity atoms) which can be introduced during the growth. Nonradiative recombination can take place at these defect sites especially those in the quantum well. Trapping of a carrier at a defect whose energy level resides within the bandgap would result in a release of energy in the form of phonons which would locally enhance the mobility of a defect.

Any point defects that are grown into the quantum-well during the growth or generated during operation may have their diffusivity enhanced by nonradiative recombination enhanced motion. Weeks et al. [107] developed a theory of nonradiative recombination defect reactions. When we apply this model to our devices, the calculated diffusion enhancement is in the order of 10^3-10^6. The calculation is as follows:

The diffusion coefficient of the defect is proportional to the rate at which it hops to the adjacent site, and the frequency of jumping is given by

$$\nu = \nu_o \exp(-E_a/kT) \qquad (6\text{-}1)$$

where ν is the frequency of the successful jump out of the jump attempt frequency ν_o at the temperature T and Ea is the activation energy for an atom to overcome a potential barrier. If a carrier is captured at a defect site, the defect is in an excited state and the activation energy is reduced to the amount of $(E_a\text{-}E_{nr})$ for a time τ. E_{nr} is the energy released due to the trap and τ is the typical time scale in which the defect transfers energy to the lattice. If R is the nonradiative recombination rate, then the jumping rate ν_r only due to non radiative recombination can be expressed by

$$\nu_r = R\tau\nu_1\exp[-(E_a\text{-}E_{nr})/kT] \qquad (6\text{-}2)$$

Finally, the effective frequency of jumping under the nonradiative recombination enhanced conditions could be expressed by

$$\nu_e = (1\text{-}R\tau)\nu_o\exp(-E_a/kT) + R\tau\nu_1\exp[-(E_a\text{-}E_{nr})/kT] \qquad (6\text{-}3)$$

Because the diffusion coefficient D and D_e are directly proportional to ν and ν_e respectively, the enhancement of diffusion under nonradiative recombination can be indicated by

$$D_e/D = \nu_e/\nu = R\tau \exp(E_{nr}/kT) \qquad (6\text{-}4)$$

assuming ν_o and ν_1 are about the same. The known deep levels in ZnSe are typically within 0.5-0.8 eV of the conduction band edge [108][109][110].

Assuming the same for $Zn_{0.8}Cd_{0.2}Se$ quantum well compound, E_{nr} is about 0.5-0.8 eV. Typical values of R and τ are assumed to be the same as those of GaAs ($R=10^{11}$ /sec and $\tau = 10^{-13}$ sec). The value of diffusion enhancement, D_e/D, is about 10^3-10^6 at the operating temperature of 250 °C and this is a significant enhancement. Once defects have arrived at the quantum well, no more thermal energy is needed for hopping around in the quantum well. Another reason for this nearly athermal movement is due to their low activation energies. The self diffusion coefficients of II-VI materials are known to be higher and the activation energies are lower than those of III-V's as shown in Figure 6.7. For example, the self diffusion coefficient of S in ZnS is expressed by $D*(S)=2.14*10^3exp(1.44$ eV/kT) [111][112]. Based on these observations it would appear wide band-gap II-VI materials are particularly susceptible to recombination enhanced diffusion.

6.3 Nonradiative Recombination-Induced Annealing

Germanium doped AlGaAs LEDs showed an annealing process under accelerated aging [113]. At the low aging temperatures (120-160 °C), light output initially decreases and then begins to increase. This increase appears earlier in time and is of greater magnitude as the aging temperature increases. The data are interpreted as an increase in injection efficiency due to the annealing out of nonradiative centers by a recombination-enhanced defect reaction.

The same phenomenon appears to occur in the II-VI LEDs used in this study. The light output intensity increased at the very early stage of degradation and then decreased exponentially. The ternary based SCH (structure I) was degraded under the driving conditions of 18 A/cm^2 and 7 A/cm^2 current densities, 40% duty cycle, and 10 KHz repetition rate. The changes of peak intensity were monitored every minute in the very early stages of degradation. Figure 6.8 shows two sets of data. The output intensity increases for the first few minutes and then decays. This can be interpreted as recombination induced annealing of pre-existing point defects in the quantum-well layer. Ichimura et al. [114] observed that the light emission efficiency of II-VI ZnSe-based LEDs improved after annealing at 300-400 °C for 5 minutes. The thermal annealing of their ZnCdSe/Zn(S)Se quantum-well structures appeared to improve the crystal quality of ZnCdSe quantum-wells. The improved efficiency of light emission may come from the reduction of the nonradiative recombination defect sites. During the early operation of LEDs the same phenomenon of defect annealing could happen due to nonradiative recombination at defect sites.

6.4 Thermal Stability of the Quantum Well

The operating temperature is estimated to be around 250 °C in the active region. The local temperature at the defect sites may be much higher due to nonradiative recombination. In order to see the effect of high

temperature on the quantum well, the as-grown samples of a simple quantum-well structure (ZnSSe /ZnCdSe-QW /ZnSSe on GaAs) were annealed at higher temperatures in flowing forming gas. The samples were annealed at 400 to 600 °C for 10 minutes. SIMS depth profiles, PL spectra and high-resolution XRD data were obtained from these annealed samples. Figure 6.9 shows the PL spectra taken at room temperature. The shape of PL spectra start to change even after 400 °C for 10 minutes annealing. The PL peak from the quantum-well has dropped and additional peaks in the higher wavelength range appeared. After annealing at 550 °C for 10 minutes the quantum-well peak disappeared and the other peaks that may be arising from the intermixed interface of ZnSSe/GaAs dominated. Figure 6.10 shows that there is no quantum-well peak after 550 °C - 10 min annealing. The SIMS depth profile of the quantum-well region showed Cd outdiffusion in the 600 °C -10 minute annealed sample. Figure 6.11 shows the SIMS results. The high resolution x-ray diffraction patterns also show that the distinct peak of ZnSSe barrier layers disappears after 550 °C-10 min annealing. This result is shown in Figure 6.12. This indicates that atomic interdiffusion occurs at each interface and the compositional abruptness has been destroyed.

The above experiments show that the structure of II-VI QW layers on GaAs is not stable at temperatures above 450 °C. During operation the local temperature could have been close to this temperature due to multiphonon emission at nonradiative recombination sites. The DSD and

DLD regions would have higher temperatures. In the area of DSDs and DLDs the interface of the quantum well may lose the compositional abruptness during operation. The electronic confinement near those dark defects would be poor and thus the output power could decrease as the DSD and DLDs get denser during operation.

The thermal escape of the free carriers or excitons were observed at higher temperature by Toutnie et al. [115]. In order to see the reduction of electrical confinement in degraded LEDs, LEDs from quaternary-based SCH (structure III) was degraded down to 20% of the initial intensity (80% degradation) and the PL spectra were taken at various temperatures. The measurements were obtained as the sample temperature increased at a fixed power of laser source. The PL peak intensity decreases as the temperature increases since the carrier escape from the quantum well increases at higher temperatures. As it can be seen in Figure 6.13, the PL peak from the quantum-well remained until 150K for the as-grown structure. However, the quantum-well peak from the 80%-degraded LED is in the noise background level at 150 K as shown in Figure 6.14. This is more clearly seen in Figure 6.15 which compares the quantum-well peaks at 22 K and 150 K. The same result was obtained from the another degraded quaternary-based SCH (structure III). Figure 6.16 shows that the quantum well PL peak from the 80%-degraded LED is invisible at 150 K. When we compare the quantum well peak to the cladding layer (ZnMgSSe) peak, the PL intensity ratio (ZnCdSe/ZnMgSSe) remains almost same for the as-

grown sample as the temperature increases. On the other hand the PL intensity ratio between ZnCdSe and ZnMgSSe for 80% degraded LED decreases rapidly as the temperature increases as shown in Figure 6.17. This indicates that the free carriers easily escape thermally from the degraded quantum well. This is consistent with the DSDs and DLDs reducing the electronic confinement significantly.

6.5 Why are DLDs in the <100> directions ?

The reason why the dark line defects are aligned in the <100> directions is puzzling. One answer may be that there are pre-existing defects along the <100> directions and DLDs simply develop along these defects. The fact that DLDs are developed in the very early stages of degradation may support this hypothesis. The other reason may be that the point defects could accumulate in the <100> directions easily in terms of the required energy.

The directionality of DLD formation may be related to the modulated structure in the epilayers. Ueda et al. [116] observed quasi-periodic diffraction contrast under a two beam condition. In LPE grown InGaAsP on (001) GaAs, the modulated structures develop in the two equivalent directions of [100] and [010]. They are columnar shaped in the [001] growth direction. For Alloys which have asymmetry in elastic coefficients, modulated waves extend so as to minimize the strain contribution to free energy in the solid solution. The modulated structures

are induced in the direction of [hkl], which minimize the elastic coefficient Y_{hkl}. It has been found that $Y_{100} < Y_{110} < Y_{111}$ in InGaAsP [117]. This can explain the preferential direction of elongation of the structure.

A similar contrast modulation was observed in ZnMgSSe film on GaAs [118][119][120]. It is believed that a variation in the S and Mg concentration exists in the modulated structure. The composition modulation was developed only in the <100> directions. The Young's modulus can be calculated by the following equation [121]

$$Y_{[hkl]} = \frac{C_{11} + 2C_{12}}{2}\left[3 - \frac{c_{11} + 2c_{12}}{c_{11} + 2(2c_{44} - c_{11} + c_{12})(l^2 m^2 + m^2 n^2 + n^2 l^2)}\right] \quad (6\text{-}5)$$

where c's are the elastic constants and l,m,n are the directional cosines between [hkl] and the three cubic axes. $c_{11} = 87$ GPa, $C_{12} = 54$ GPa, and $C_{44} = 39$ GPa for the ZnSe epilayer [122]. The Young's modulus for the [100], [110], and [111] directions can be calculated as follows:

$Y_{[100]} = (c_{11} + 2c_{12})(c_{11} - c_{12})/C_{11}$

$Y_{[110]} = (c_{11} + 2c_{12})(12c_{11} - 5c_{11} + 5c_{12})/(8c_{44} - 3c_{12} + 4c_{12})$

$Y_{[111]} = 6(c_{11} + 2c_{12})c_{44}/(4c_{44} + c_{11} + 2c_{12})$

The calculated Young's modulus plot is shown in Figure 6.17. The Young's modulus in the [100] direction is the least and composition modulation would be therefore develop in this direction during growth.

Initially more pre-existing point defects may be dwell in the <100> directions than other directions due to composition modulation or growth

abnormalities. In this case DLD formation from excess point defect condensation on preexisting defects would result in heterogeneous formation in those directions. In a second mode (homogeneous nucleation) point defects are either created or diffuse into the quantum well and because of the very high mobility and super saturated conditions condense in the <100> directions.

In the TEM images of degraded quaternary based SCH, dislocation loops were observed to align in the both [100] and [010] directions. As shown in Figure 6.18(a) the partial dislocations enclosing a stacking fault were transformed to dislocation tangles during electrical degradation. When they were imaged in weak beam dark field(WBDF) in TEM, some of them appear to be dislocation loops aligned in the <100> directions as shown in Figure 6.18(b). The WBDF images of dislocation loops developed on the stacking faults appear to be similar to the oval defect images of <100> DLDs in Figure 5.18(b).

6.6 Possibility of Melting at Defects

In III-V lasers a catastrophic degradation takes place at the mirror surface. When the output power density reaches a critical value, strong optical absorption occurs at the mirror surface and this gives rise to the temperature of melting of the crystal. This is termed catastrophic optical damage (COD). In InGaAs and AlGaAs lasers, the critical output power density is 9-20 MW/cm^2 and 5-8 MW/cm^2, respectively for COD [123].

COD has also been observed at defect sites in the middle of quantum-well during lasing [124]. In LEDs there is no mirror surface, and it is assumed that there is no COD related degradation. However, the extended defects such as stacking faults in the quantum-well may act as local heating areas during LED operation.

Firstly, it is necessary to determine the amount of heat generated by nonradiative recombination that is sufficient for melting to occur. Assume, for the sake of argument, a local region is melted and let the melted region be a sphere. Consider the heat generated at nonradiative recombination sites which will raise the temperature ΔT of a uniformly heated sphere 50 angstrom in radius. The melting point of ZnSe is 1793 K. When we consider the operating temperature is 250 °C thus the ΔT is about 1270 K. The energy required to melt a sphere of 50 angstrom radius can be calculated by [125]

$$\Delta T = \frac{a^2 F_o}{2K}\{1+(\frac{2kt}{a^2}-1)erf(\frac{a}{2\sqrt{2kt}})-2\sqrt{\frac{kt}{\pi a^2}}\exp(-a^2/4kt)\} \qquad (6-6)$$

where a is the radius of sphere, F_o is the heat produced, K is the thermal conductivity, k is the thermal diffusivity ($=K/c_p\rho$) and t is the time for heat generation. For ZnSe K=1.9 W/cm sec, c_p=5420 mJ/mol K and ρ is 5.26 g/cm^3 [126]. If we take t=10^{-9} sec which is the typical value of nonradiative recombination time for the deep level in ZnSe [127], the heat (Fo) for raising the temperature(ΔT =1270 K) is calculated to be 10^{11}

W/cm^3. The heat flux for the 50 angstrom thick quantum well is therefore about $5*10^4$ W/cm^2.

Secondly, it is necessary to determine whether nonradiative recombination can produce this amount of heat flux. The necessary rate of nonradiative recombination to generate the heat flux of $5*10^4$ W/cm^2 can be simply calculated as $5*10^4$ W/cm^2 /1.8 eV = $1.7*10^{23}$ $cm^{-2}sec^{-1}$. If this rate of nonradiative recombination is maintained, the 50 angstrom sphere in the quantum well can be melted. At a typical current driving condition of 50 A/cm^2, if all the electron and holes injected into quantum-well near the defect sites are trapped, the maximum rate can be calculated to be around $3*10^{18}$ $cm^{-2}sec^{-1}$ using the following equation.

$$J = qn_{inj}d / \tau \qquad\qquad (6-7)$$

where J is the current density applied, q is the charge of electron, d is the quantum well thickness and τ is the recombination life time. This rate of nonradiative recombination can not generate enough heat for melting. However, assuming the nonradiative recombination rate in the core of dislocation follows that of the surface [128], i.e. R (nonradiative recombination rate)=$s_o(np)^{1/2}$, the maximum rate can be over the required rate for melting. Here s_o is the recombination velocity and n (p) is the free electron (hole) density. The value for s_o in the interfacial misfit dislocations was estimated about 10^5 cm/sec for InGaP/GaAs [129]. Assuming the s_o value is about the same for the partial dislocations in our

devices, the maximum nonradiative rate is about 10^{24} cm^{-2} sec^{-1}, which is enough for melting.

Therefore it is theoretically possible to allow nonradiative recombination heating to raise the local temperature to the melting point during typical LED operation only under the following conditions: (a) all the injected free carriers near the defect sites are trapped (b) the nonradiative recombination rate of a dislocation core follows that of the surface (c) the recombination velocity s_o is of the order of 10^5 cm/sec.

6.7 Degradation Cycle

We can conclude from previous discussions that one of direct sources of degradation is the pre-existing defects. The nature of point defects in ZnSe have been extensively studied [130][131]. One of the oldest and most popular explanations for the difficulty in doping p-type materials is that the doping of wide band-gap semiconductors is compensated by native defects. Laks et al. calculated native point defect concentrations in ZnSe at T=600 K (growth temperature) and concluded that the concentration of native point defect is too low in stoichiometric ZnSe to cause compensation. The calculated values are shown in Table 6.2 and 6.3. However it was pointed out that a deviation from stoichiometry as small as 10^{-4} implies a defect concentration of about 10^{18} cm^{-3}.

After taking strain into consideration, the energy of vacancy formation is reduced as described in section 6.1. If there is a reduction of 0.5 eV, the equilibrium concentration of a vacancy would increase by a factor of more than 1.6×10^4 at a temperature of 600 K. In addition to those intrinsic native defects, there exist some impurities and dopants which are not activated near the quantum well. Qiu et al. [132] showed that the doping of ZnSe with active nitrogen is limited to Na-Nd $\approx 10^{18}$ cm^{-3} despite the fact that greater than 10^{19} $/cm^3$ nitrogen can be incorporated into the material. Those unactivated dopants would remain as interstitials. Further more the lattice matched hetero-interfaces have higher nonradiative recombination centers. Studies of AlGaAs/GaAs heterojunctions reveal substantial interfacial nonradiative recombination centers [133].

Table 6.2. Calculated native defect concentrations in stoichiometric p-type ZnSe at 600 K[130]

Defect	charge	concentration($/cm^3$)
Zni(Tse)	2+	2.48e9
V (Zn)	0	2.14e9
Se(Zn)	2+	1.46e8
Se(Zn)	1+	1.71e7
V(Zn)	1-	8.7e6
V(Zn)	2-	1.17e6
Zni(Tzn)	2+	2.21e6
Vse	2+	8.58e5

Table 6.3. Calculated native defect concentrations in stoichiometric
n-type ZnSe at 600 K [130]

Defect	charge	concentration($/cm^3$)
Zni(Tse)	2-	1.37e13
V (Zn)	1-	5.23e12
Se(Zn)	0	1.26e12
Se(Zn)	2-	3.54e11
V(Zn)	0	3.65e9
V(Zn)	0	5.07e8
Zni(Tzn)	1+	6.19e7
Vse	1+	1.70e5

In addition to the point defects, extended line or plane defects, such as stacking faults and threading dislocations are introduced during the growth process as shown in chapter 5.

Degradation starts in those grown-in defect sites near and in the quantum well due to nonradiative recombination as the electrons and holes are injected. The multiphonon-emission process transfers enough energy to generate additional point defects and diffuse those defects. The degradation process can be escalated as more point defects are generated in the active region. The excess point defects may condense in <100> directions. The accumulation of point defects eventually forms DLDs in the quantum well and other extended defects also form. This degradation cycle would be repeated during the operation as shown in Figure 6.20.

In order to cut off one of those chains in the degradation process, the first step would be to reduce the defects in the structure during the

growth. The next step would be to use a quantum-well composition that is more resistant to point defect formation i.e. one with a stronger bonding of the constituent elements. The bonding should be strong enough to withstand the energy released by nonradiative recombination. This could possibly be done by adding an impurity or alloying element or using entirely different materials. In order to solve these problems, the nature of pre-existing point defects and energetic consideration of creation of point defects should be investigated further for a variety of potential materials. The understanding of intrinsic properties of materials used in II-VI devices also needs to be continued along with further efforts to reduce grown-in defects. Finally reducing the defects in the ohmic contact will be necessary if the growth of half loops on the p-type side into the quantum well is to be reduced.

6.8 Summary

The point defect were generated during LED operation due to nonradiative recombination. This was confirmed with diffusion enhancement of Cd in the degraded LEDs. The higher PL quenching rate at higher temperatures also showed point defect generation in the quantum well during degradation. Point defect generation may be escalated as more nonradiative recombination sites are created.

Once point defects were generated, diffusion of point defects could be athermal during operation because of nonradiative recombination

enhancement. During the early stage of degradation some defects were even annealed out of nonradiative recombination centers. The point defects may accumulate along the <100> directions since less energy is required for them to be located in those directions. The condensation of point defects eventually form DSDs and DLDs and other defects. The pre-existing defects both in the quantum well and in the ohmic contact should be reduced to reduce degradation. However it is not clear that a long lived lasers or LEDs based on this material will ever be realized without a change in composition that reduces the generation rate of intrinsic point defects.
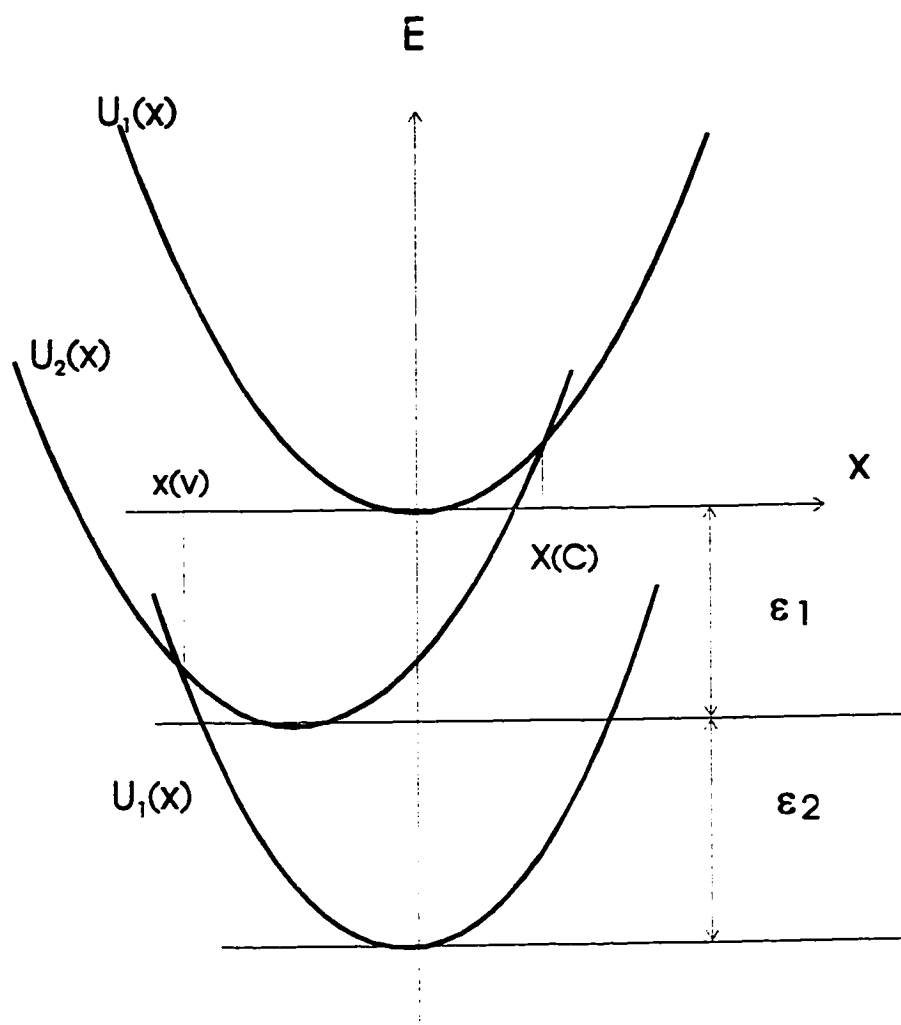
Figure 6.1. Schematic representation of potential curves: U1 and U2 represent the potential energy of a nucleus without an electron and with an electron, respectively. $\varepsilon_1 + \varepsilon_2 = Eg$ (energy gap)
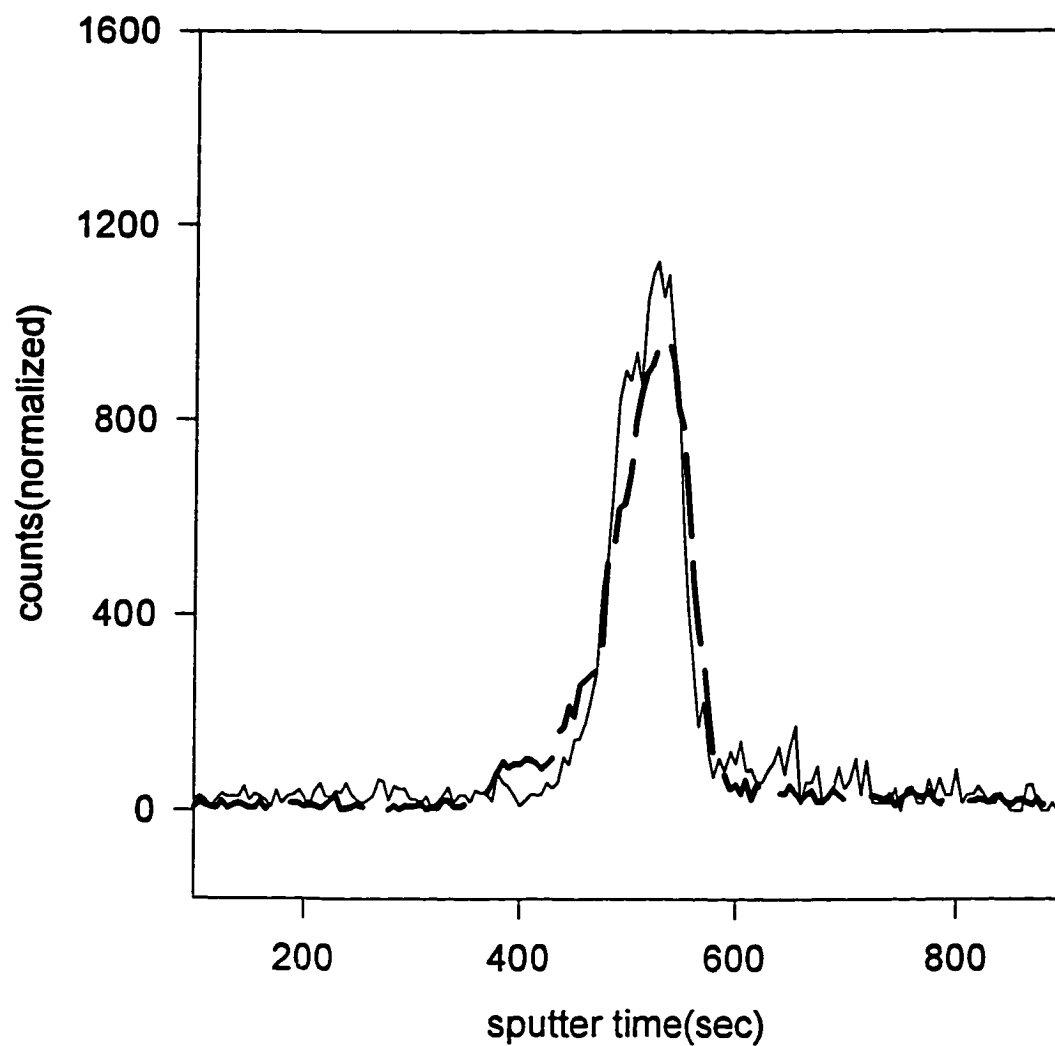
Figure 6.2. SIMS depth profile of Cd near the ZnCdSe QW: solid Line is for the as-grown structure (nonannealed), and dashed line is for the annealed as-grown sample at 500 °C for 10 minutes.
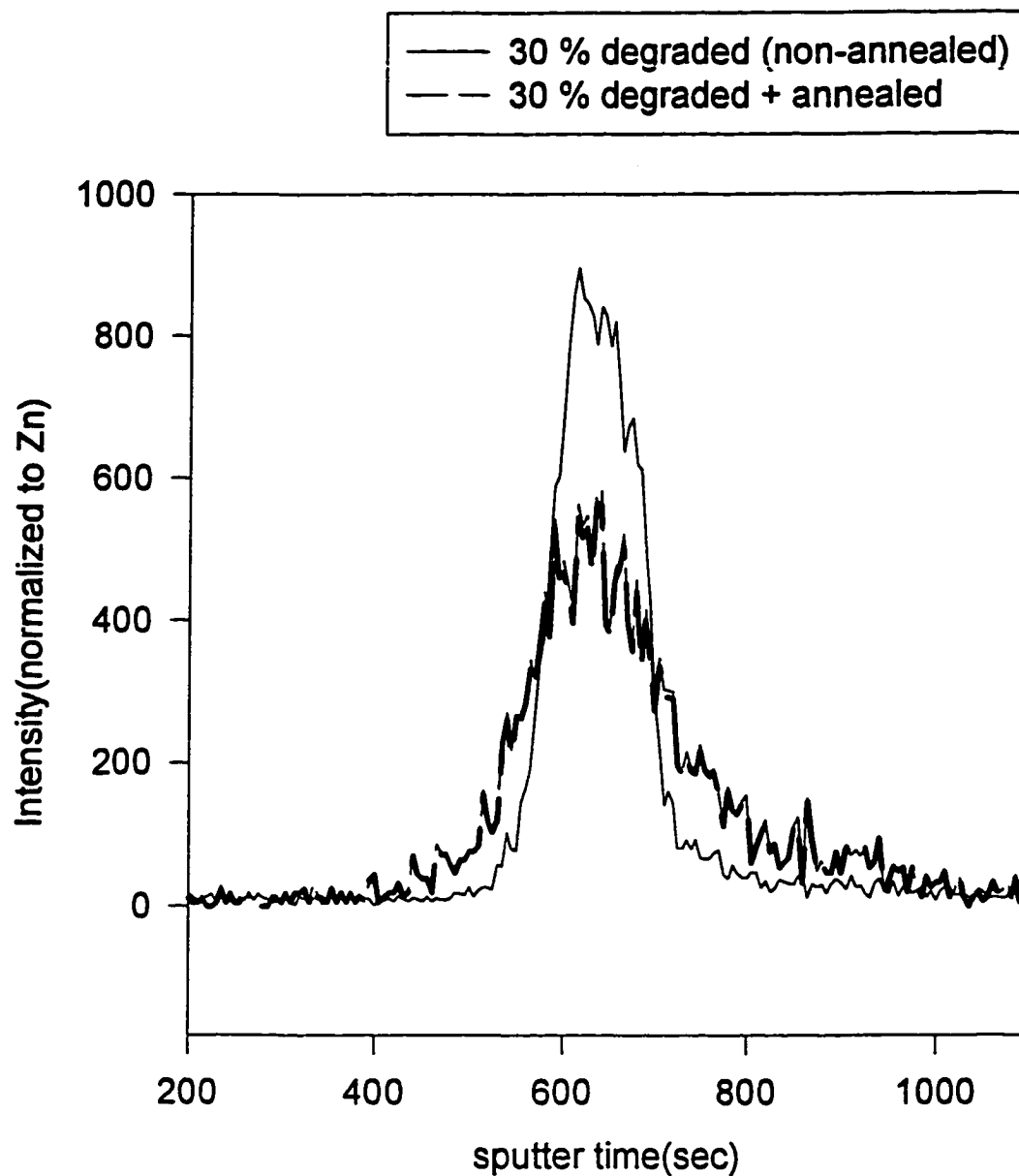
Figure 6.3. SIMS depth profile of Cd near the ZnCdSe QW: solid line is for the 30%-degraded (nonannealed) LED, and thick-dashed line is for the annealed at 500 °C for 10 minutes after 30% degradation.
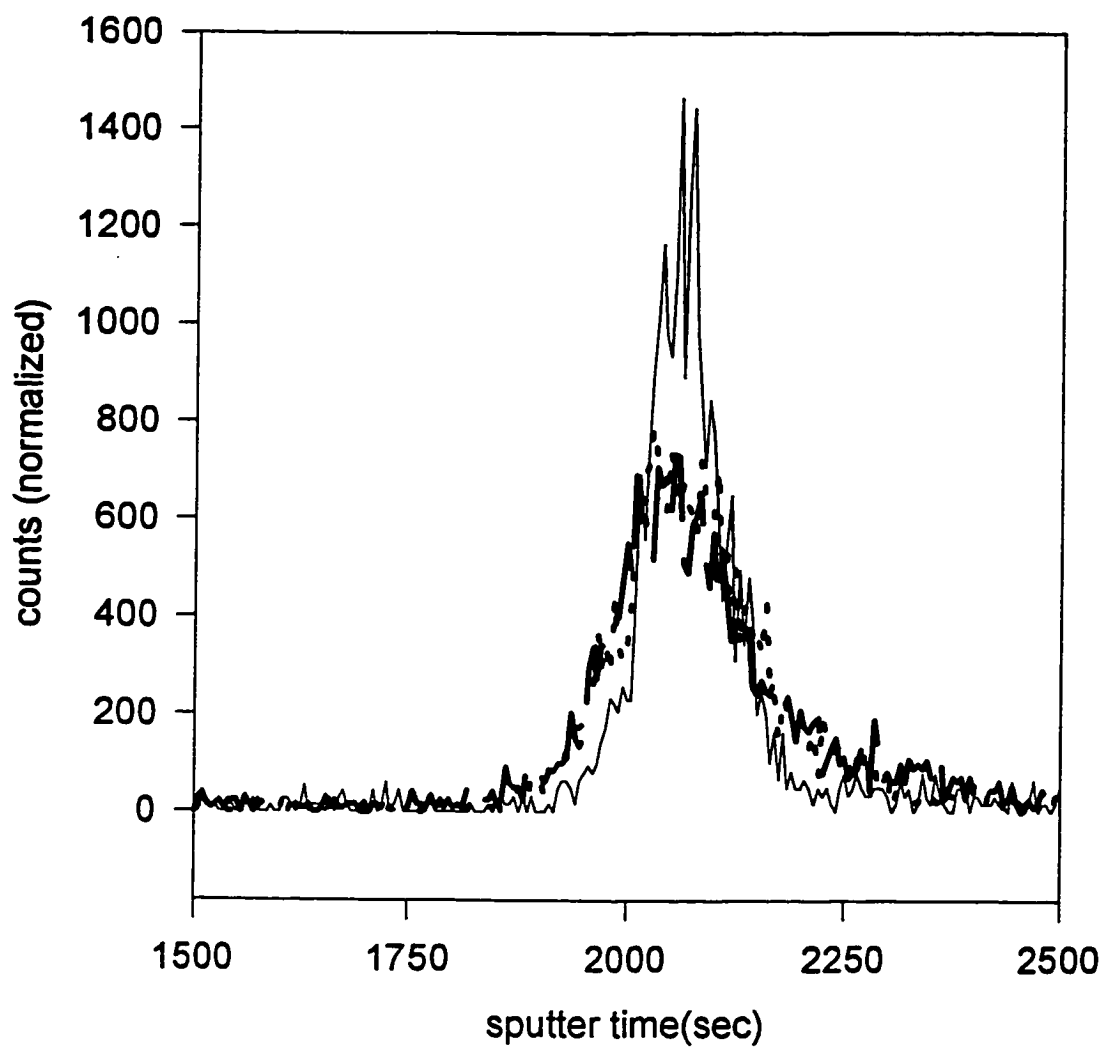
Figure 6.4. SIMS depth profile of Cd near the ZnCdSe QW: solid line is for the as-grown structure, and dashed lines are for 30% and 60%-degraded LEDs. All samples were annealed at 500 °C for 10 minutes.
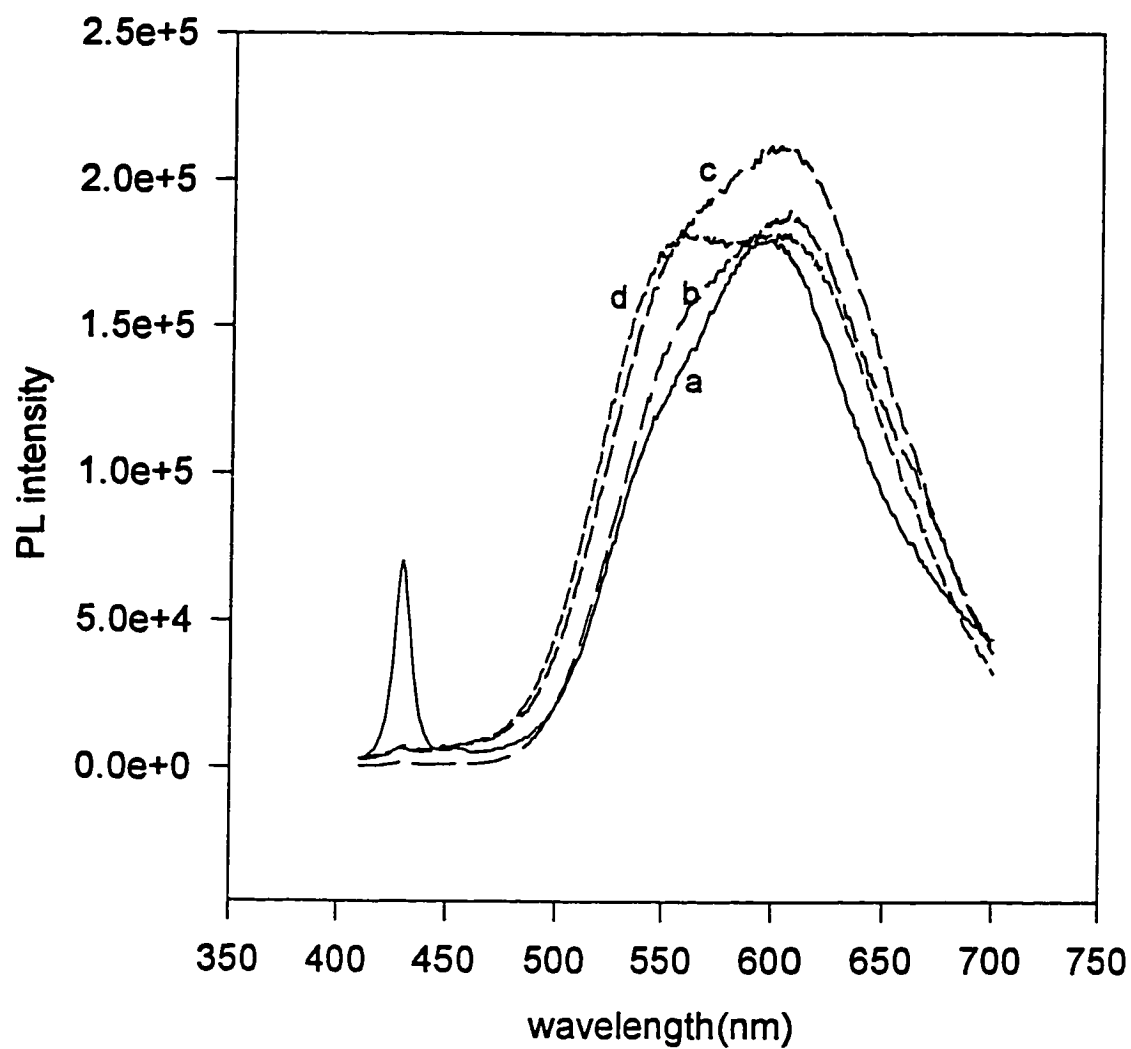
Figure 6.5. PL spectra obtained at the room temperature from (a) the as-grown (nonannealed), (b) as-grown (annealed), (c) 30% degraded (annealed) and (d) 60% degraded. Annealing conditions were 500 °C for 10 minutes.
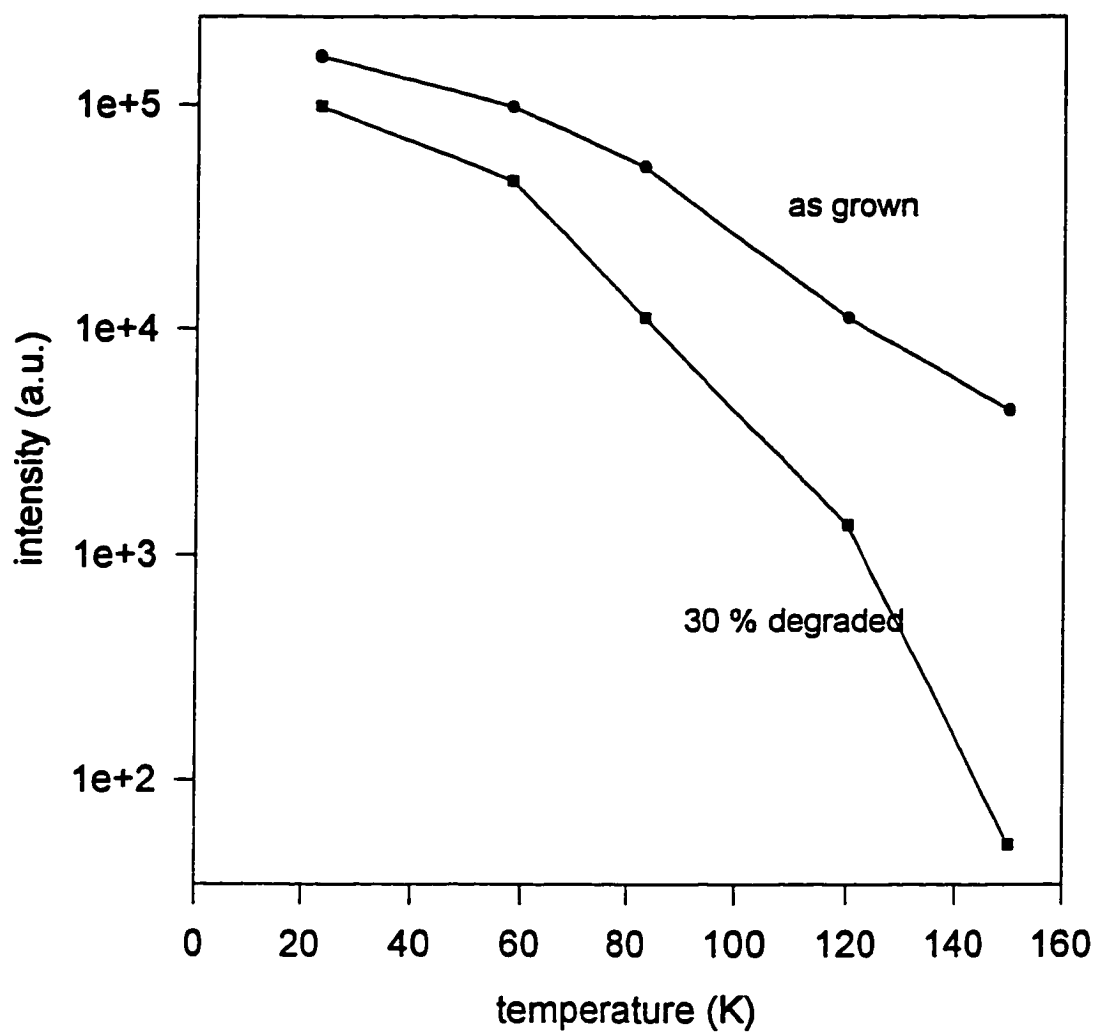
Figure 6.6. PL intensity decays at higher temperatures comparing between the as-grown structure and 30%-degraded LED.
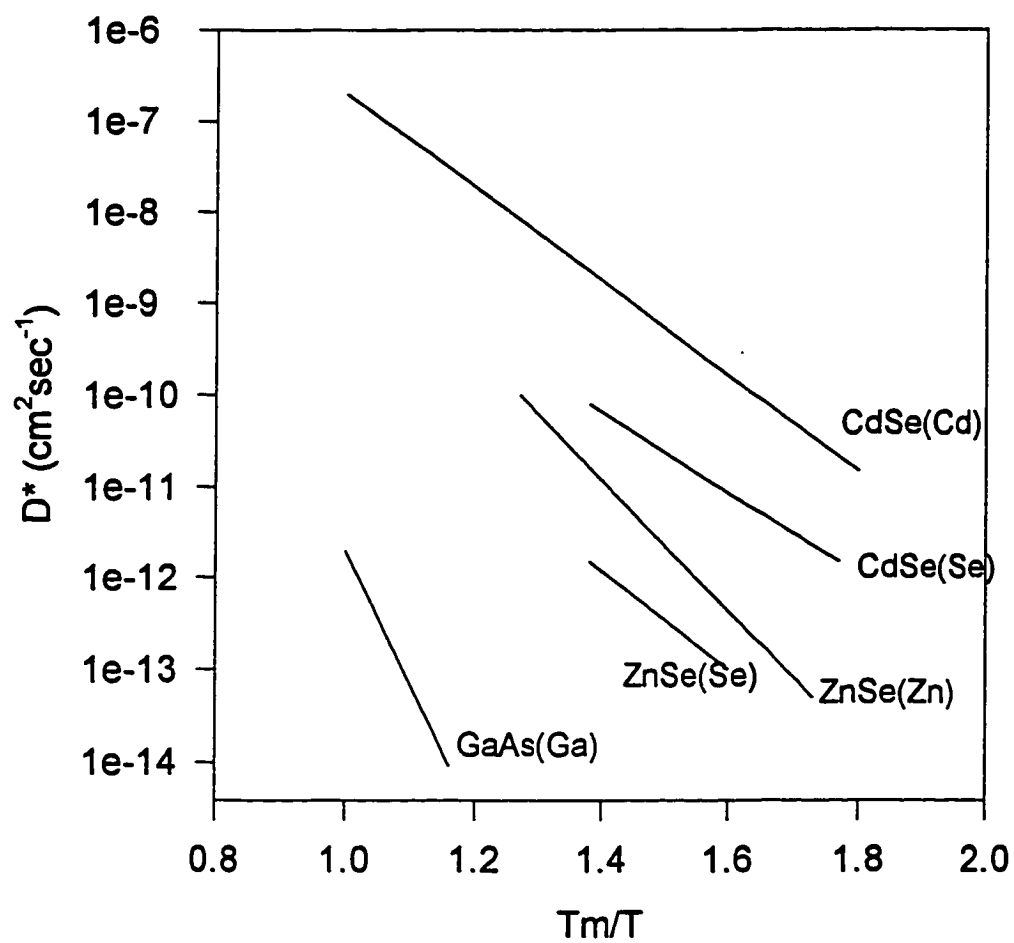
Figure 6.7. Self diffusion coefficients of various species in II-VI semiconductors
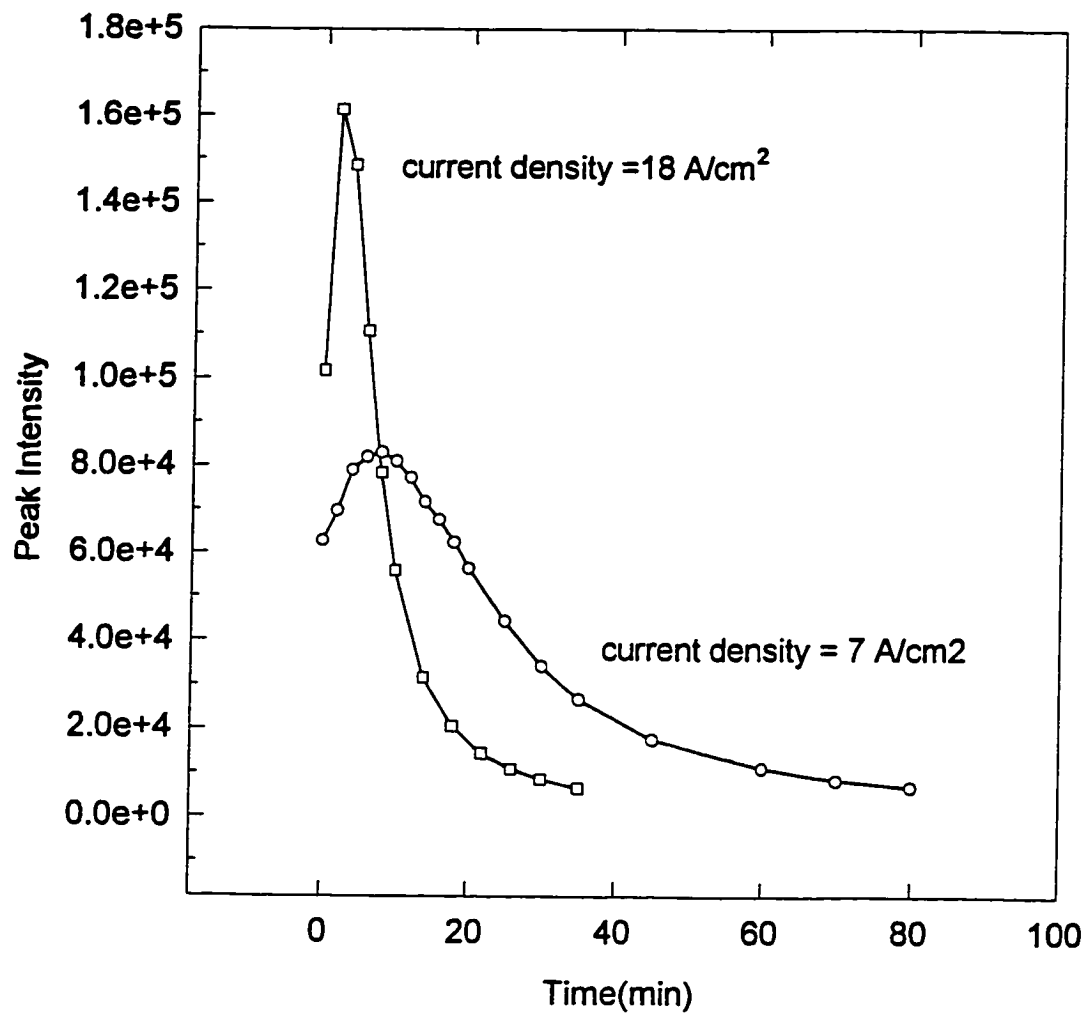
Figure 6.8. Nonradiative recombination-induced defect annealing occurred in the early stage of degradation
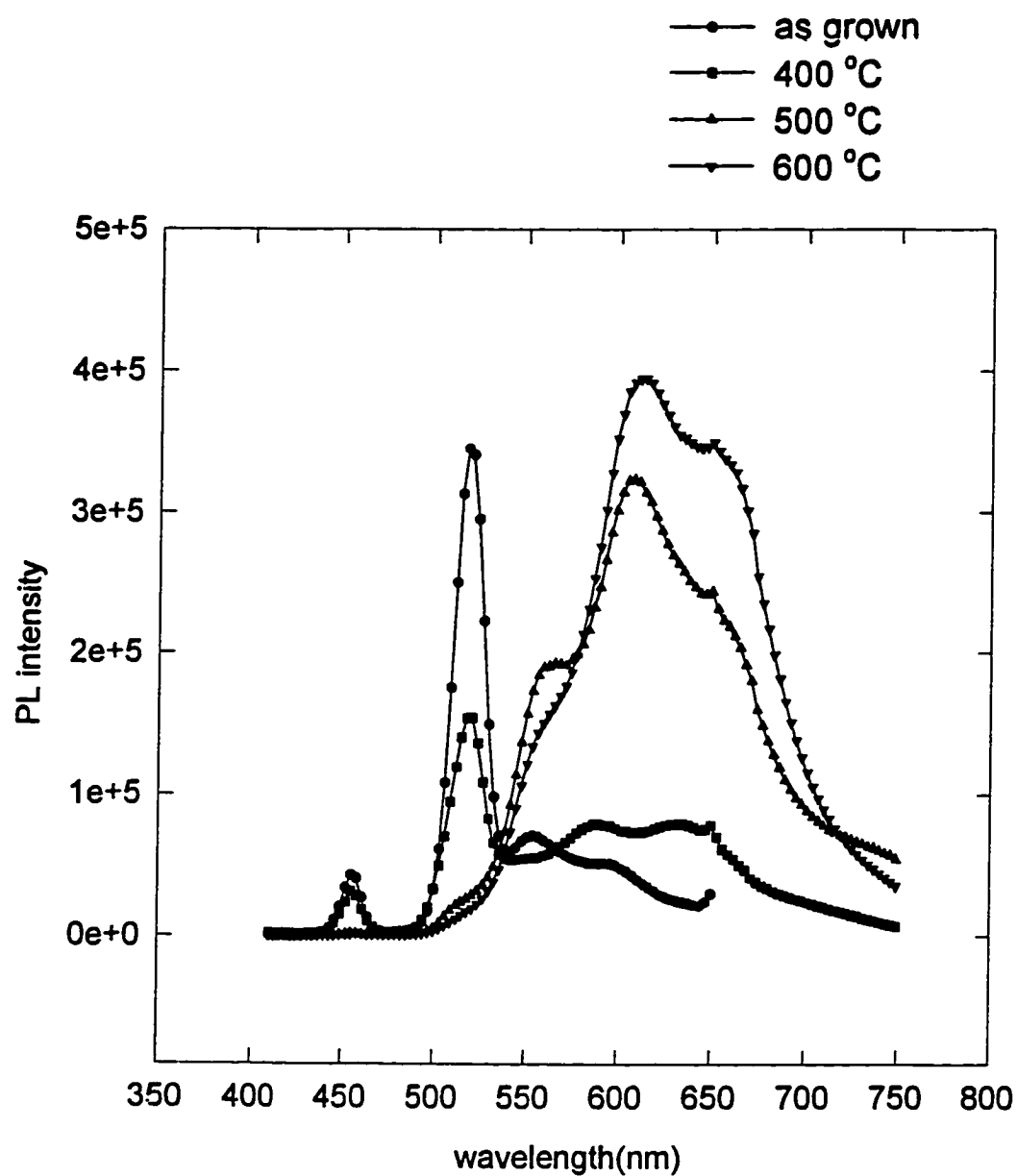
Figure 6.9. PL spectra taken at the room temperature after annealing as-grown samples at 400-600 °C for 10 minutes
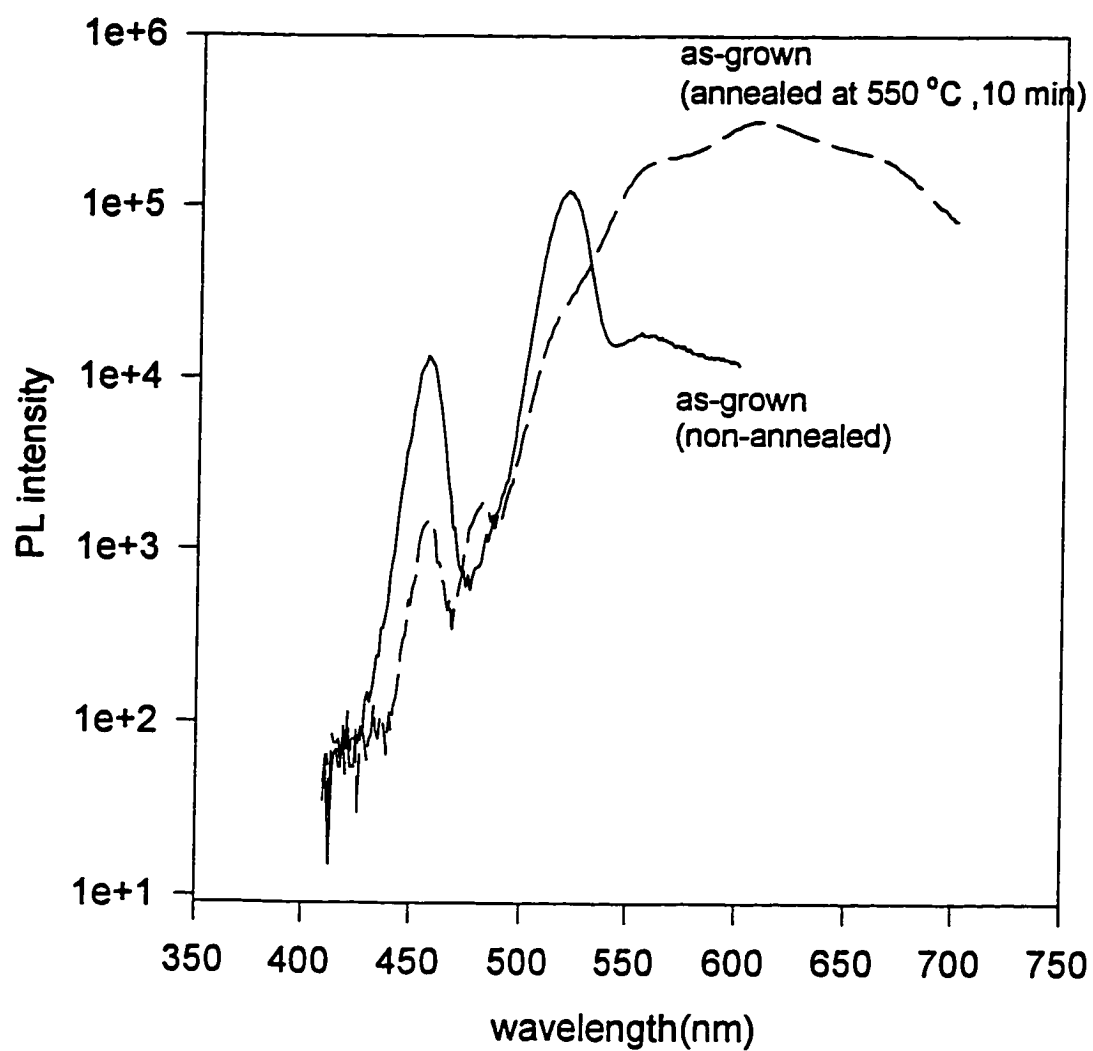
Figure 6.10. PL spectra comparison between nonannealed and annealed at 550 °C for 10 minutes
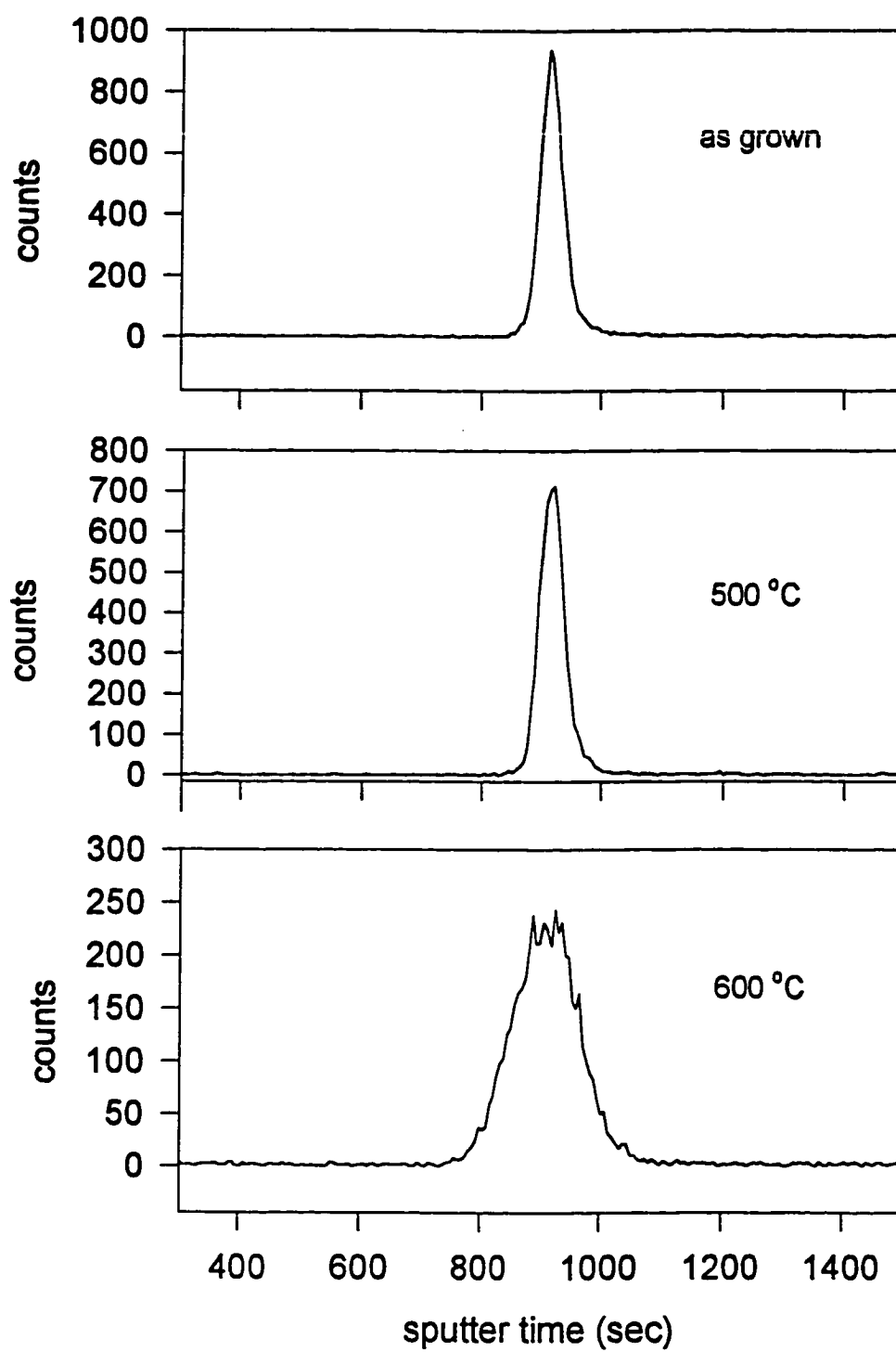
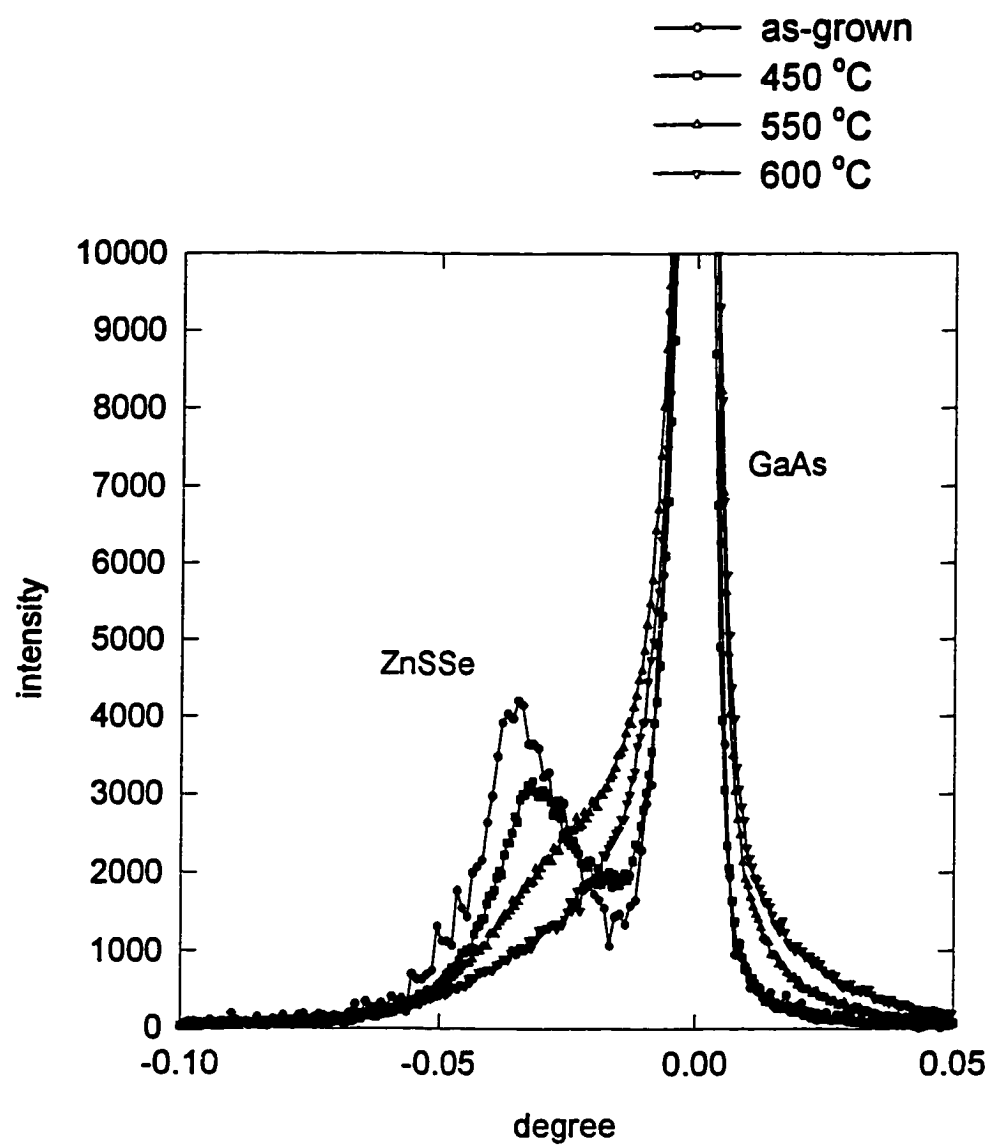Figure 6.11. SIMS profile of Cd at the ZnCdSe QW before and after annealing at 500-600 °C for 10 minutes

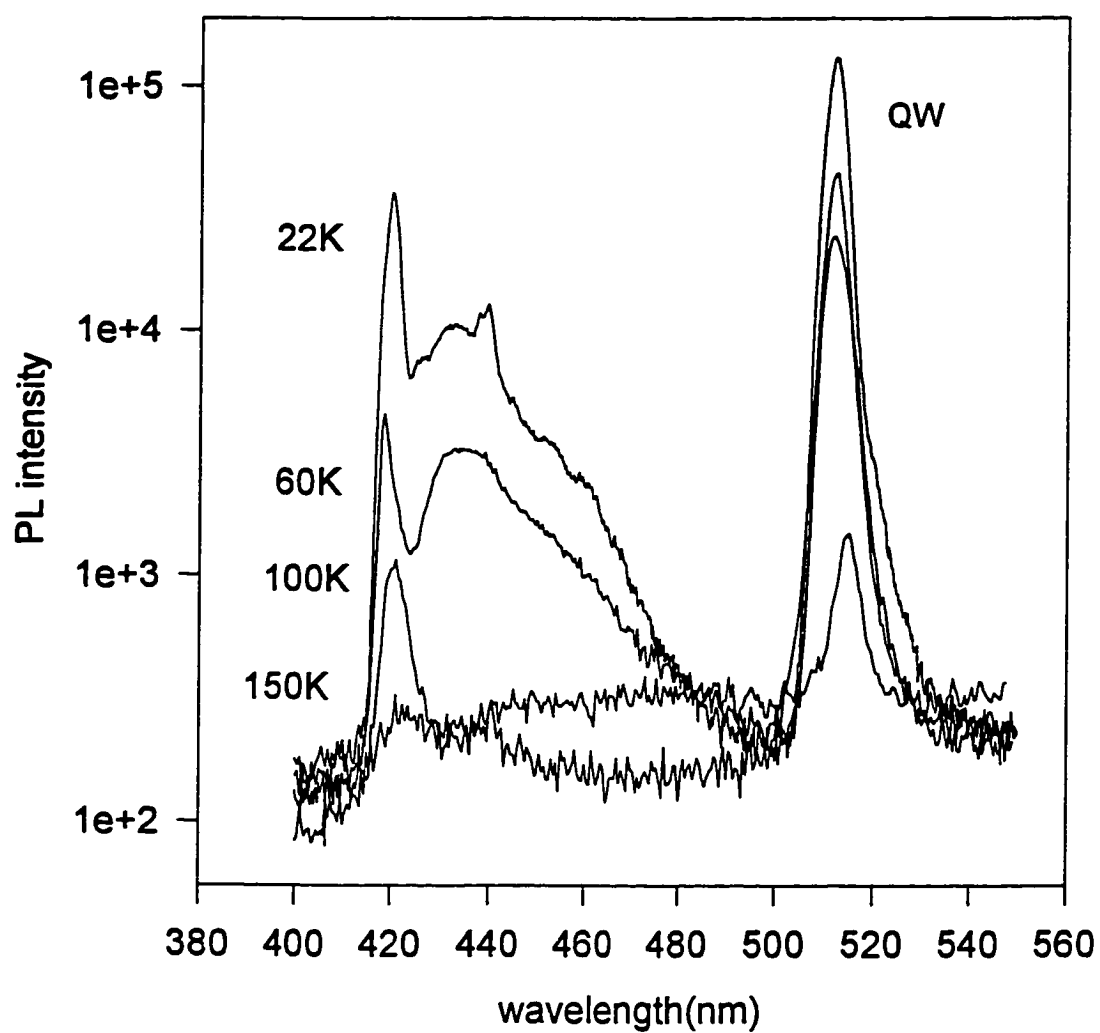Figure 6.12. High resolution x-ray diffraction patterns before and after annealing

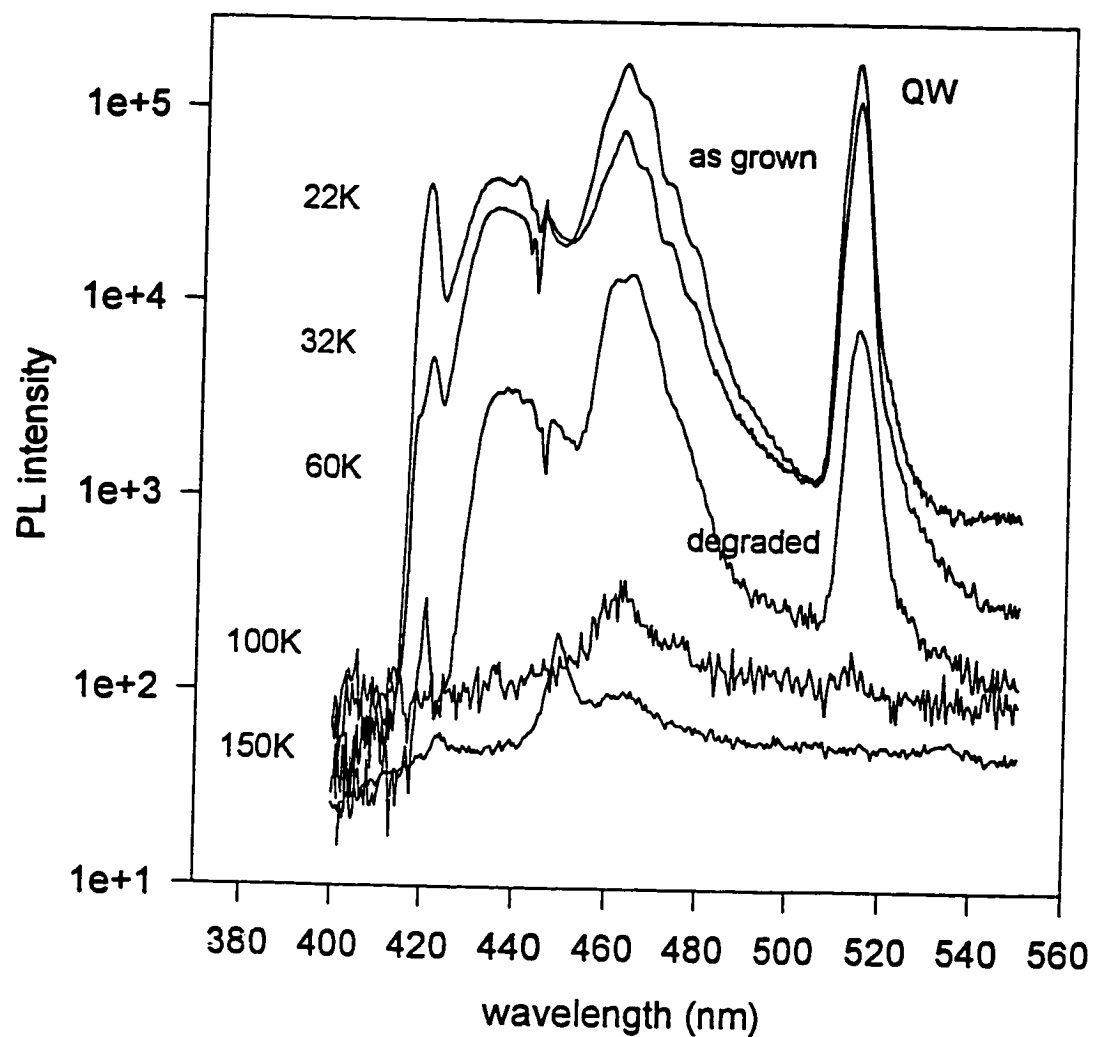Figure 6.13. PL intensity quenching at higher temperatures for as-grown quaternary-based SCH

Figure 6.14. PL quenching at higher temperatures for the 80%-degraded LED from quaternary-based SCH
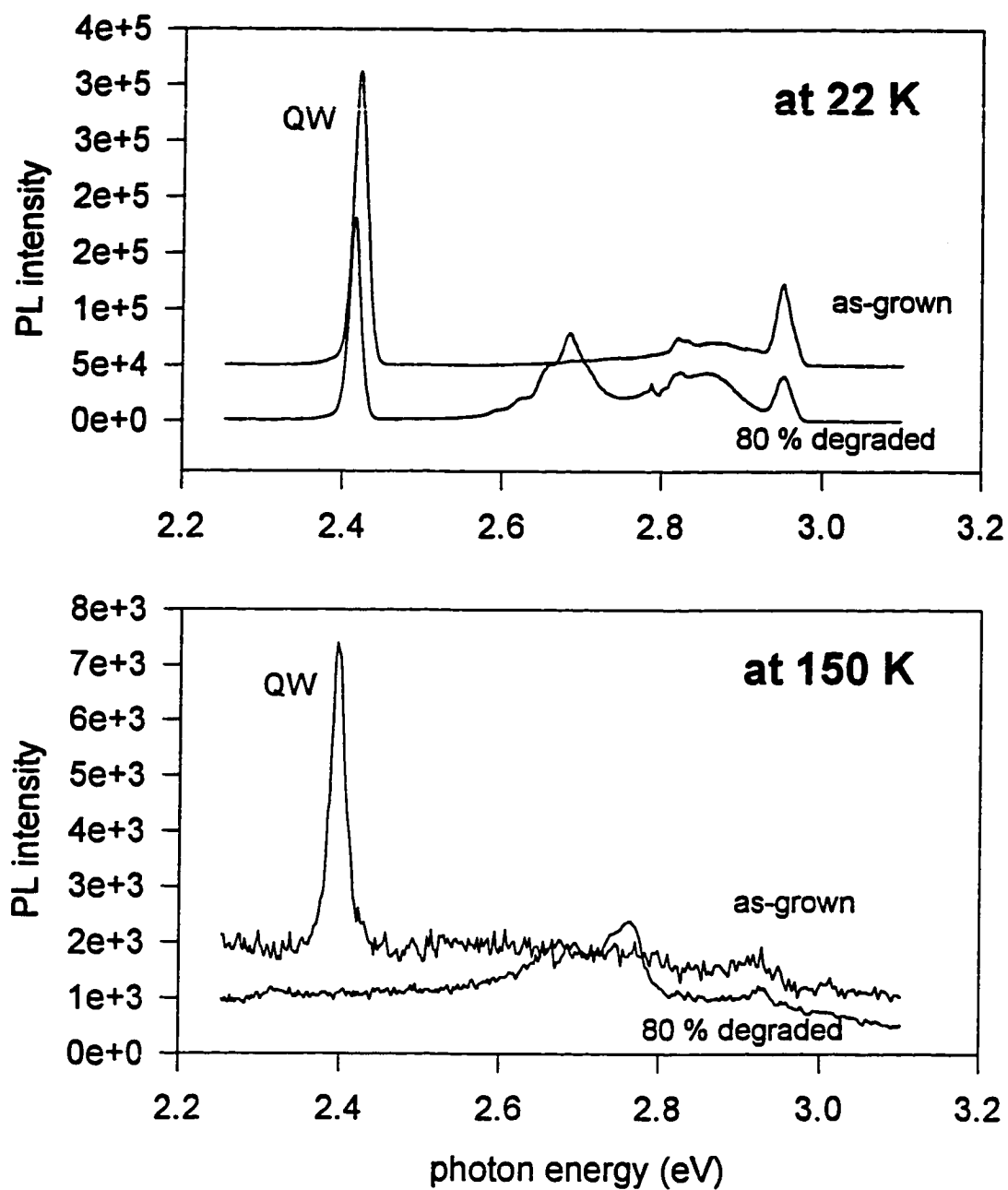
Figure 6.15. PL spectra taken for the as-grown structure and 80%-degraded LED at the temperature of 22 and 150 K
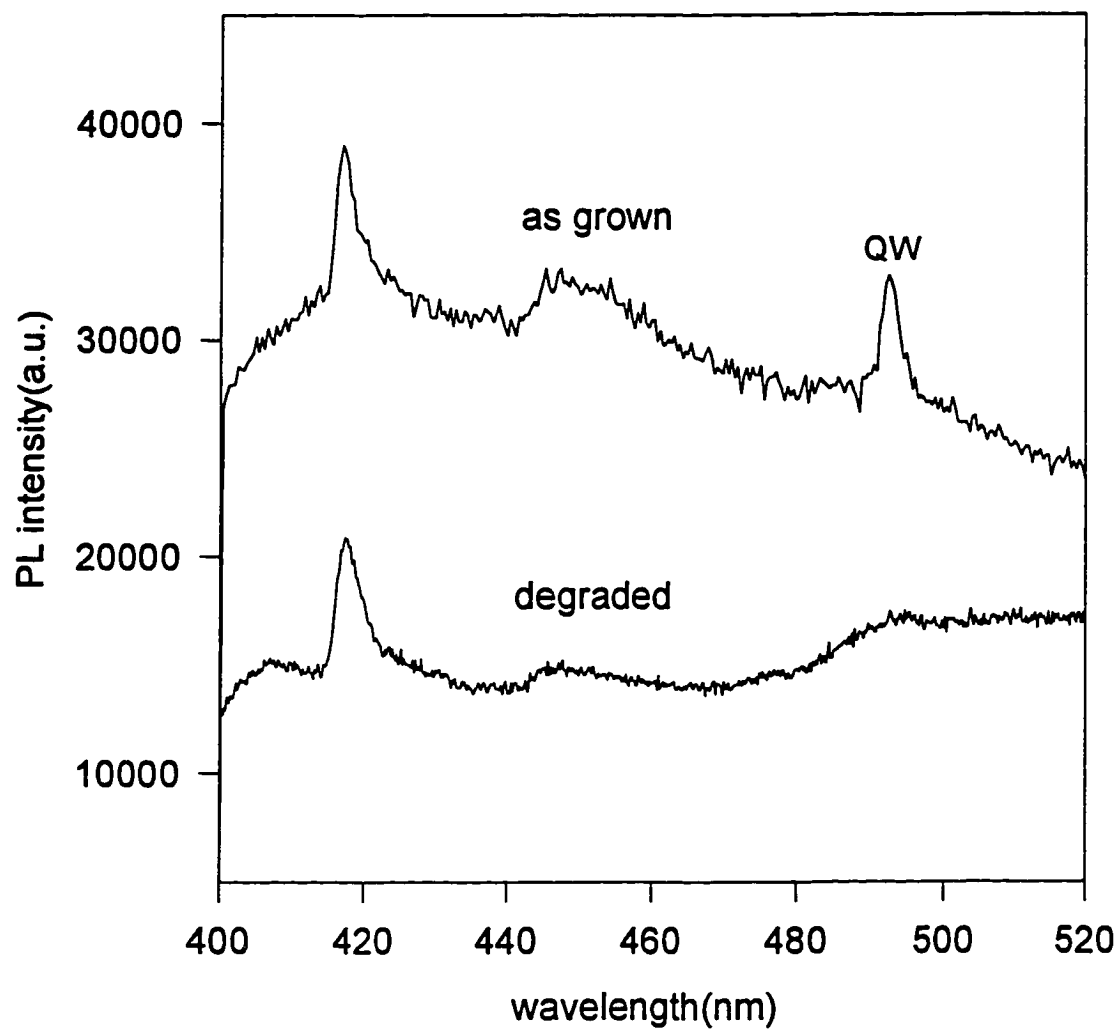
Figure 6.16. PL spectra taken at 150 K from the as-grown structure and 80%-degraded quaternary-based SCH
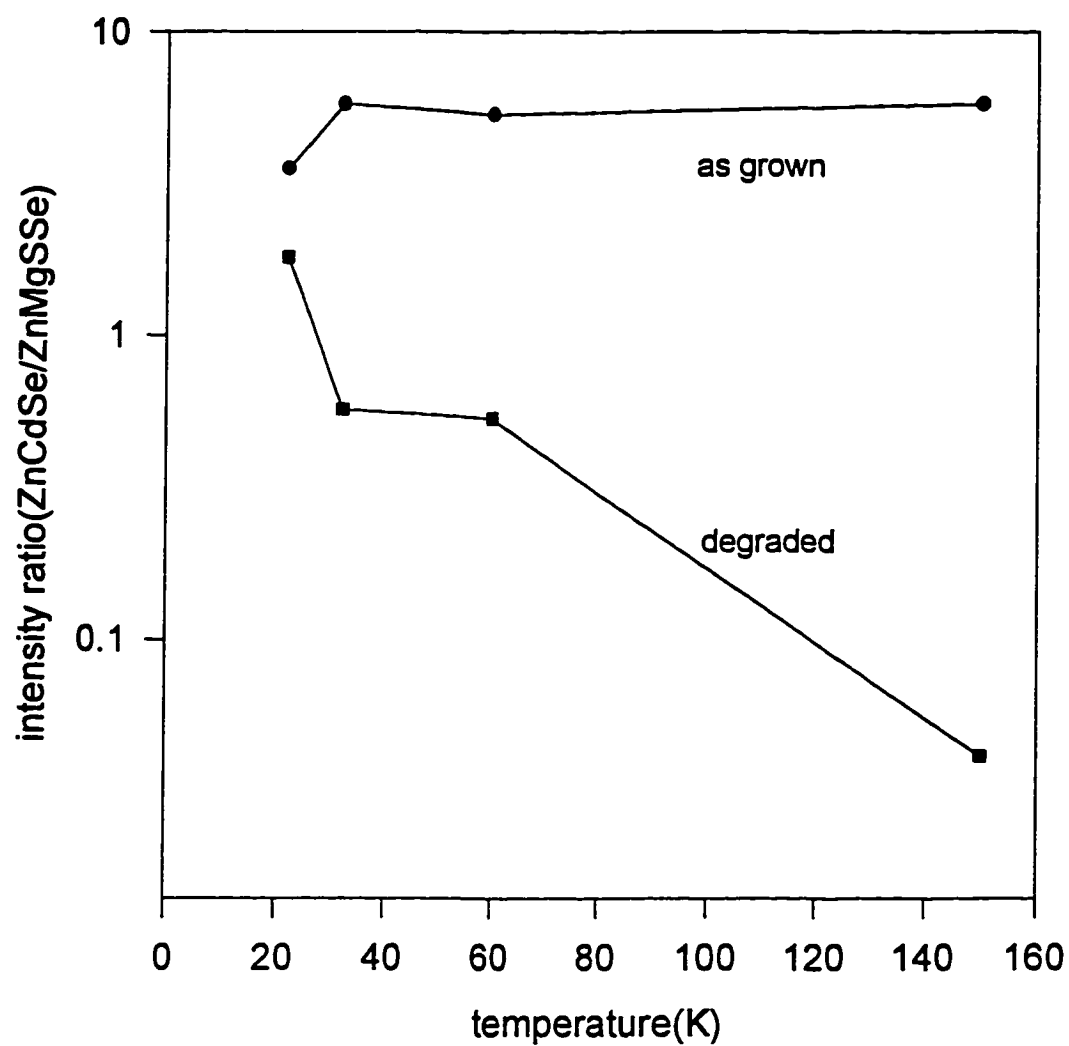
Figure 6.17. PL intensity ratio between the cladding layer (ZnMgSSe) and the QW(ZnCdSe) at higher temperatures
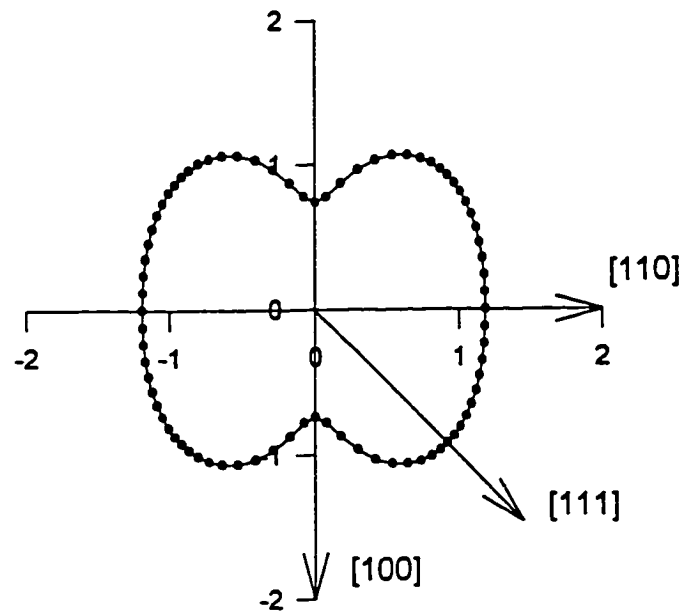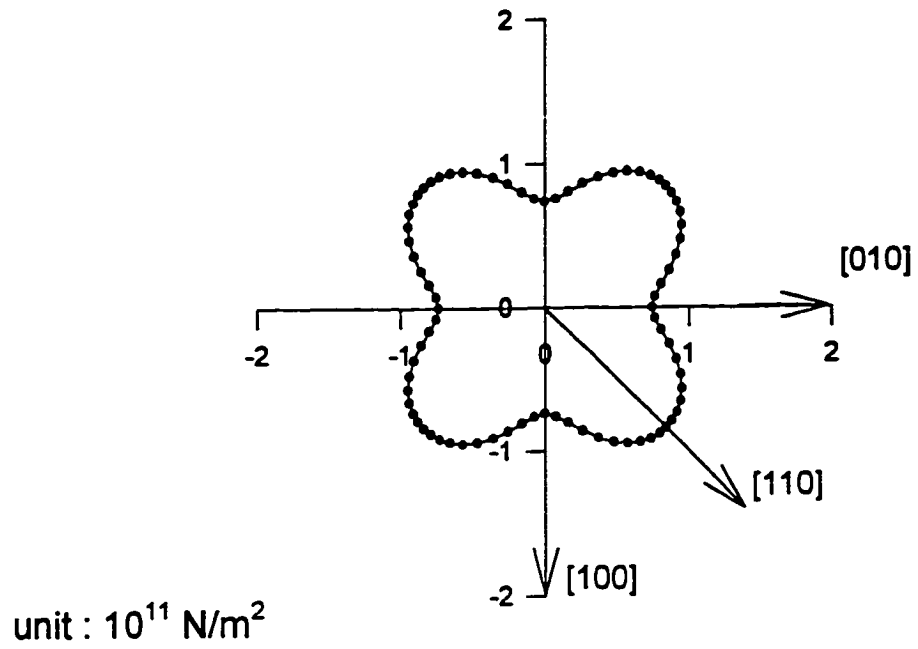
unit : 10^{11} N/m^2

Figure 6.18. 2-dimensional Young's Modulus surface for ZnSe calculated using equation (6-5)

(a)

(b)

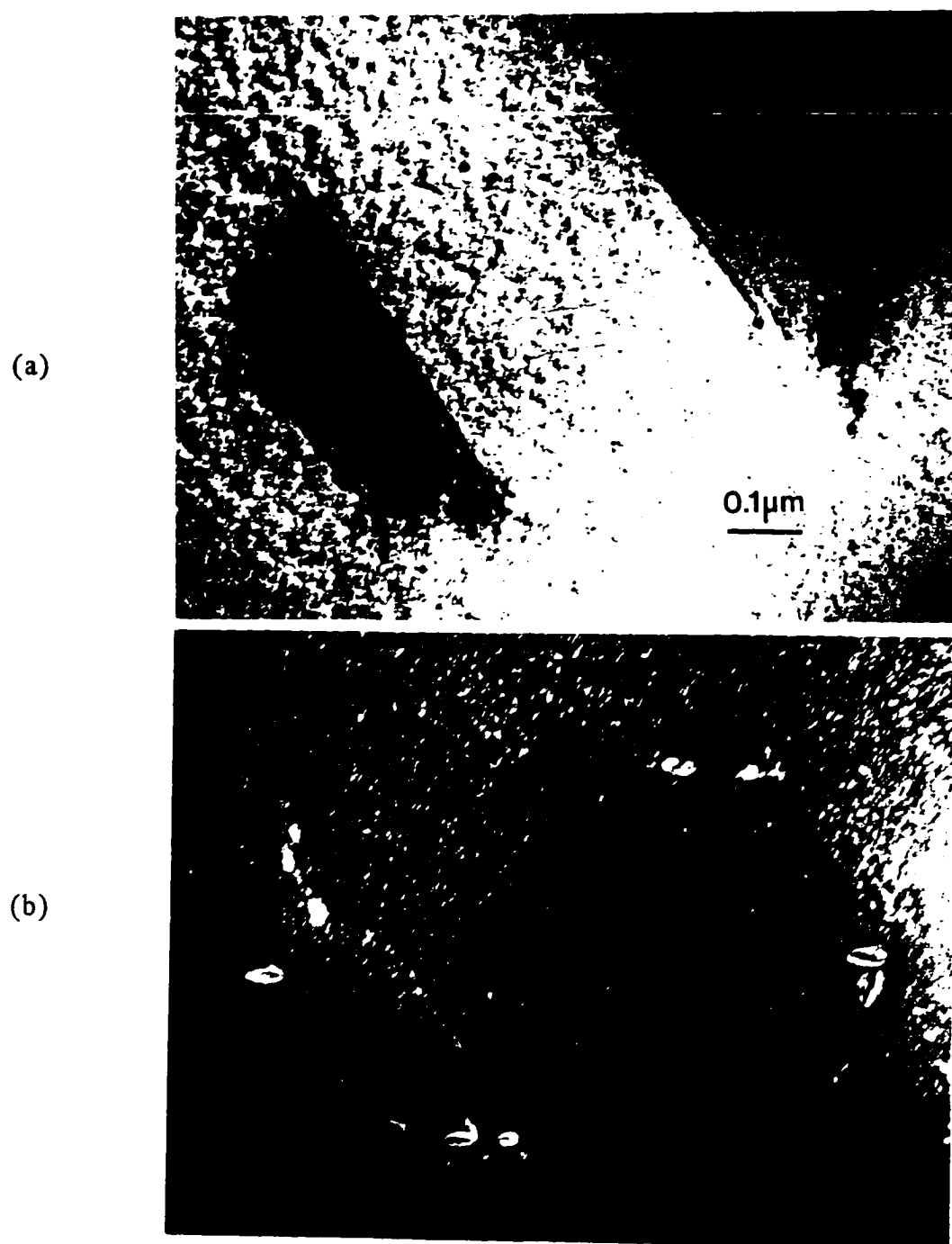Figure 6.19. TEM images of transformed partial dislocations enclosing the stacking fault in the BF mode (a) and weak beam dark field mode (b)

<u>Degradation cycle</u>

electron-hole injection
↓
nonradiative recombination ←———————
  at defect sites
↓
Phonon emission (local heating)
↓
bond breaking /
point defect generation
↓
point defect accumulation ———————

↓
extended defect formation
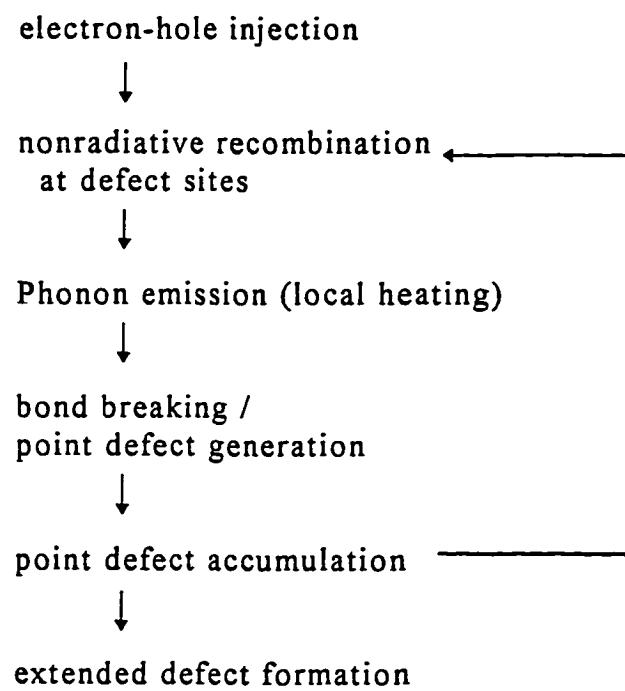
Figure 6.20. A degradation cycle

CHAPTER 7
CONCLUSIONS

The degradation of II-VI ZnSe-based light emitters is important to understand short life time of devices. Nevertheless little work has been done to understand degradation mechanisms. In this study, the characteristics of electrical degradation of ZnSe light emitting devices and microstructural changes after degradation were investigated and a degradation mechanism was proposed.

Three types of structures were grown by MBE: (structure I) $Zn_{0.8}Cd_{0.2}Se$ single-quantum-well /ZnSe /$Zn_{0.94}S_{0.06}$ on GaAs, (structure II) $Zn0.8Cd_{0.2}Se$ single QW / ZnSSe on GaAs and (structure III) $Zn_{0.8}Cd_{0.2}Se$ single QW / $Zn_{0.94}S_{0.06}Se$ / $Zn_{0.9}Mg_{0.1}S_{0.12}Se_{0.88}$ on GaAs. The epilayers are all lattice-matched to the GaAs substrate except for structure (I). LEDs were fabricated by deposition of gold on the surface and degraded by supplying a pulsed direct-current.

The degradation depended predominantly on the current density applied to the LEDs. The output intensity of emitted light decayed more rapidly as the current density increased. The degradation depended also on the pre-existing defect density near/at the quantum-well. The light emission decreased faster with the larger grown-in defect density. The decrease in

205

efficiency of light emission during degradation was due to the increase of nonradiative recombination rate. An analytical calculation was performed to obtain the change in the nonradiative recombination rate after 50% degradation. It turned out that the radiative recombination rate decreased by 1/3 and the rate of nonradiative recombination increased 2.5 times.

A method to estimate the temperature of the active region during operation was developed utilizing the temperature dependence of band-gap for the quantum well material. The relationship between the energy band-gap and temperature was obtained by raising the external ambient temperature. The typical operation temperature was estimated to be 250 °C. This high temperature appears to a contributing factor to rapid degradation.

The thermal expansion behavior of epilayers at the temperature of 250 °C was examined using a high resolution x-ray diffractometer with a sample heater. The thermal expansion was almost entirely accommodated in the perpendicular direction in the lattice matched system. This thermal behavior increases the strain in the compressed quantum-well by 15% at 250 °C.

The possible atomic interdiffusion in the active region and strain relaxation in the quantum well were investigated using secondary ion mass spectroscopy and low temperature photoluminescence. After 50% degradation, SIMS and PL results indicated that no significant outdiffusion occurs near the quantum well. However, after post degradation it was

shown through diffusion studies that a high concentration of point defects were indeed produced in the quantum well after only 30% degradation. The strain in the quantum-well remained constant even after 50% degradation consistent with the lack of extended defect formation and also consistent with point defects being the primary source of degradation. Upon additional degradation 1/3 of the strain relaxed in 80%-degraded LEDs. This is consistent with the observation of dislocation formation in the quantum-well after this amount of degradation.

Structural defects were investigated for the as-grown structure and degraded LEDs with cross-sectional and plan-view TEM. The major pre-existing defects were zigzag shaped misfit dislocation networks in the ohmic contact area, [110] dislocations which were identified as typical 60° dislocations developing in the middle of upper cladding layer / barrier layer interface, and stacking faults through out the entire structure. The major pre-existing defect in the quantum well was the stacking fault. All of the faults were Frank type in nature and most of them in the upper p-type layer were intrinsic and those in the lower n-type layers are extrinsic. The stacking faults formed in triangular pairs and these pairs are aligned only in the [110] direction.

Degradation-induced defects were observed using electro-luminescence (EL) microscopy. Dark spot defects (DSD) and dark line defects (DLD) were developed as degradation proceeded. DLDs were developed mostly in the <100> directions as seen from the top surface.

Output power decreased as the DSDs and DLDs increased in number and size. Dark images in EL microscopy indicate that DSDs and DLDs lie at the active region.

The major defects induced during LED operation were <100> DLDs. They act as non-radiative recombination sites at or near the active quantum well. Although DLDs appeared in the very early stage of degradation in EL microscopy, these degradation-induced defects were observable only in the heavily degraded LEDs (70 % degradation) in TEM. Bundled line defects were generated in the degraded structure II, in which the pre-existing defect density is less than 10^6 /cm^2. DLDs in the structure II are not simple dislocations and they appeared to be rows of clusters of point defects developed in the <100> directions. DLDs in the structure III (5 × 10^6 initial defect density) showed different characteristics. DLDs appeared to consist of many small oval defects connected in the <100> directions. These oval-shaped, degradation-induced defects were found to be regions of distorted crystalline material composed of dense dislocation tangles. The pre-existing stacking faults were transformed and appeared to be the nucleation sites of DLDs. The location of the degradation-induced defects such as, dislocation tangles and dislocation half loops, indicate that the ohmic contact area may contribute significantly to the formation of extended defects. Dislocation helices also formed, which is another indication of point defect generation during operation.

Nonradiative recombination provides necessary energy by multiphonon emission at the defect sites for additional point defects to generate during degradation. This was confirmed with diffusion enhancement of Cd near the quantum well and the higher PL quenching rate at higher temperatures for degraded LEDs. Diffusion of point defects in the active region would be almost athermal during operation because of nonradiative recombination heating. In the very early stage of degradation, defect annealing was also observed, which is a direct consequence of nonradiative recombination during operation. Some defects were annealed out of nonradiative recombination centers.

A possible degradation mechanism was proposed as follows: Once the free carriers are driven into the quantum well, degradation starts in the pre-existing defect sites due to nonradiative recombination. This multiphonon process transfers enough energy to generate additional point defects and to diffuse those defects. The escalation of degradation process takes place as the more point defects are generated. The accumulation of point defects form DSDs and DLDs near or in the quantum well. The generated point defects eventually condense into extended macroscopic defects.

In order to increase lifetime of the II-VI light emitters, the grown-in defects should be reduced. The quantum well composition should be changed to a material more resistant to point defect generation. Determining such a material will require further investigations into point

defect generation in possible candidate. Finally defect formation in the ohmic contact needs to be reduced.

REFERENCES

1. R.M. Park, M.B. Troffer, C.M. Rouleau, J.M. DePuydt, and M.A. Haase, Appl. Phys. Lett., vol. 57, p.2127 (1990)

2. N. Nakayama, S. Itoh, K. Nakano, H. Okuyama, M. Ozawa, A. Ishibashi, M. Ikeda and Y. Mori, Electron. Lett., vol. 29, p. 2194 (1993)

3. A. Ishibash and Y. Mori, J. Cryst. Growth, vol. 138, p. 667 (1994)

4. A, Ishibash and M. Ikeda, 7th International Conference on II-VI Compounds and Devices, abstract p. Mo-1 (1995)

5. A.Salokatve, H. Jeon, J.Ding, M.Hovinen, A.V.Nurmikko, D.C.Grillo, Li He. J.Han, Y.Fan, M.Ringle and R.L.Gunshor, Electron.Lett. Vol.29, P. 2192 (1993)

6. S. Guha, J.M. DePuydt, M.A. Haase, J. Qiu, and H.Cheng. Appl. Phys. Lett., vol. 63(23), p. 3107 (1993)

7. G.C. Hua, N. Otsuka, D.C. Grillo, Y. Fan, J. Han, M.D. Ringle and R.L. Gunshor, M. Hovinen, and A.V. Nurmikko, Appl. Phys. Lett. vol. 65(11), p. 1331 (1994)

8. G.M. Haugen, S. Guha, H. Cheng, J.M. DePuydt, M.A. Haase, G.E. Hofler, J. Qiu, and B.J. Wu, Appl. Phys. Lett., vol. 66(3), p. 358 (1995)

9. S. Yomiya, E. Morita, M. Ukita. H. Okuyama, S. Itoh, K. Nakano, and A.Ishibashi, Appl. Phys. Lett., vol. 66(10), p.1208 (1995)

10. I. Hayashi, M.B. Panish, P.W. Foy, and S. Sumski, Appl. Phys. Lett., vol. 17, p.109 (1970)

11. B.C. DeLoach, Jr., B.W. Hakki, R.L. Hartman, and L.A. D'Asaro, Proc. IEEE, p. 1042 (1973)13.P.M. Petroff and R.L.Hartman, Appl. Phys. Lett., vol. 23, p.469, (1973)

12. P.M. Petroff and R.L.Hartman, Appl. Phys. Lett., vol. 23, p.469, (1973)

211

13. P.M. Petroff and L.C. Kimerling, Appl. Phys. Lett., vol. 29, p. 8 and 46 (1976)

14. P.M. Petroff, *Semiconductors and Insulators*, vol. 5, p. 307, Gordon & Breach, New York (1983)

15. W.T. Tsang, *Semiconductors and Semimetals*, vol. 22, p.379, Academic Press Inc., New York (1985)

16. P.W. Hutchinson and P.S. Dobson, Phil. Mag., vol. 32, p. 745, (1975)

17. D.V. Lang, Annu. Rev. Mater. Sci., vol. 12, p. 377 (1984)

18. P.M.Petroff and L.C. Kimerling, Appl.Phys.Lett., vol. 29, p. 461, (1976)

19. S.O'Hara, P.W.Hutchinson, and P.S.Dobson, Appl.Phys.Lett., vol. 30, p. 368, (1977)

20. K. Ishida., T. Kamejima, Y. Matsumoto, Appl. Phys. Lett., vol. 54, p. 16 (1982)

21. J.J. Hsieh, Appl. Phys. Lett., vol. 28, p. 283 (1976)

22. T. Kamejima, K.Ishida, and J. Matsui, Jpn. J. Appl. Phys., vol. 16, p. 233 (1977)

23. H. Yonezu, Y. Yuasa, T. Shinohara, T. Kamejima, and I. Sakuma, Jpn. J. Appl. Phys., vol. 15, p. 2393 (1976)

24. S. Yamakoshi, M. Abe, O. Wada, S. Komiya, and T. Sakurai, IEEE J. Quantum Electron., vol. QE-17, p.167 (1981)

25. O. Ueda, S.Yamakoshi, and T. Yamaoka, Jpn. J. Appl. Phys., vol.19, p. L251 (1980a)

26. M. Seki, M. Fukuda, and K. Wakita, Appl. Phys. Lett., vol. 40, p. 115 (1982)

27. A.K. Chin, C.L. Zipfel, S. Mahajan, F. Ermanis, M.A. Digiuseppe, Appl. Phys. Lett., vol. 41, p.555 (1982)

28. C.H. Henry, P.M. Petroff, R.A. Logan and F.R. Meritt, J. Appl. Phys., vol. 50, p. 3721 (1979)

29. H. Yonezu, T. Kamejima, M. Ueno, and I. Sakuma, Japn. J. Appl. Phys., vol.13, p. 1679 (1974)

30. M. Fukuda, M. Okayasu, J. Temmyo, and J.I. Nakano, IEEE Quant. Electeron., vol. 30, p. 471 (1994)

31. M. Okayasu, M. Fukuda, T. Takeshida and S. Uehara, IEEE Photonics Tech. Lett., vol. 2(10), p. 689 (1990)

32. J.A. Baumann, A.H. Shepard, R.G. Waters, S.L.Yellen, C.M. Harding, and H.B. Serreze, SPIE vol. 1418, *Laser Diode Technology and Applications III*, p. 328 (1991)

33. H.Yonezu, M.Ueno, T. Kamejima, and I. Hayashi, IEEE J. Quantum Electron., vol. QE-15, p.775 (1979)

34. R.G. Waters, Pro. Quant. Electr., vol. 15, p. 153 (1991)

35. K. Kondo, O. Ueda, S. Isozumi, S. Yamakoshi, K. Akita, and T. Kontani, IEEE Trans. Electron Devices, ED-30, p. 321 (1983)

36. T. Uji, T. Suzuki, and T. Kamejima, Appl. Phys. Lett., vol. 36, p. 655 (1980)

37. M. Fukuda, *Reliability and Degradation of SemiconductorLasers and LEDs*, Artech House, Inc., Norwood (1991)

38. *Quantum Well Lasers*, edited by Peter S. Zory, Jr., Academic Press, Inc., San Diego (1993)

39. K. Huang and A. Rhys, Proc. Roy. Soc., vol. A204, p. 406 (1950)

40. P.T. Landberg, *Recombination in Semicondutors*, Cambridge University Press, Cambridge (1991)

41. S.M. Sze, *Phyics of Semiconductor Devices*, Wiley-Interscience, New York (1983)

42. L.R. Weisberg, J. Appl. Phys., vol. 39, p. 6096 (1968)

43. I.N. Yassievich, Semicond. Sci. Technol. vol.9, pp.1433-1453 (1994)

44. V.N. Abakumov, V.I. Perel and I.N. Yassievich, *Nonradiative Recombination in Semiconductors*, North-Holland, Elsevier Science Publishers B.V., Amsterdam (1991)

45. R.M. Park, M.B. Troffer, C.M. Rouleau, J.M. DePuydt and M.A. Haase, Appl. Phys. Lett., vol. 57, p. 2127 (1990)

46. M.A. Haase, J. Qiu, J.M. DePuydt, and H. Cheng, Appl. Phys. Lett., vol. 59, p.1272 (1991)

47. Y. Fan, J. Han, L. He. J. Saraie, R.L. Gunshor. G.C. Huha, and N. Otsuka, Appl. Phys. Lett., vol. 61, p. 3160 (1992)

48. J.E. Yu, K.S. Jones, and R.M. Park, J. Electron Microscopy Technique., vol. 18, p. 315 (1991)

49. J.M. DePuydt, M.A. Haase, S. Guha, J. Qiu, H. Cheng, B.J. Wu, G.E. Hofler, G. Meis-Haugen, M.S. Hagedorn, and P.F. Baude, J. Cryst. Growth, vol. 138, p. 667-676 (1994)

50. C.L. Zipfel, *Semiconductors and Semimetals*, vol 22. part c, chap.6 (1985)

51. A. Ishibashi, and Y. Mori, J. Cryst. Growth, vol. 138, p. 677 (1994)

52. C.W. Walker, J.M. DePujdt, M.A. Haase, J. Qiu, and H. Cheng, Physica B, vol. 185, p. 27 (1993)

53. Henry Kressel, *Semiconductors and Semimetals*, vol. 16, chap. 1, p. 17, Academic Press Inc., New York (1981)

54. Quantum Well Lasers, edited by Peter S. Zory, Jr. Academic press Inc. San Diego (1993)

55. R. Nagarajan, T. Kamiya, and A. Kurobe, IEEE J. Quan. Electron., vol. QE-25, p. 1161 (1989)

56. I. Seumune, Appl. Phys. Lett. vol. 63, p. 2612 (1993)

57. M. Fukuda, K. Wakita, and G. Iwane, Jpn. J. Appl. Phys., vol. 20 No.2, pp. L87-L90 (1981)

58. K.G. Merkel, V.M. Bright, M.A. Marciniak, C.L.A. Cerny, and M.O. Manasreh, Appl. Phys. Lett. vol.65(19), p. 2442 (1994)

59. T. Kobayashi, T. Kawakami, and Y. Furukawa, Jpn. J. Appl. Phys. vol. 14, No.4, pp.508-515 (1975)

60. P.J. Parbrook, B. Henderson, K.P. O'Donnell, P.J. Wright, and B. Cockayne, Semicon. Sci. Technol., vol. 8, p.818 (1991)

61. I.N. Yassievich, Semicon. Sci.Technol. vol.9, p.1433 (1994)

62. J.R. Troxell, A.P. Chatterjee, G.D.Watkins, and L.C. Kimerling, Phys. Rev. B., vol. B19, p. 5336 (1979)

63. L.C. Kimerling, Solid-state Electron., vol. 21, p. 1391 (1978)

64. A. Sibille, J. Electron. Mat., vol. 14a, p.1155 (1985)

65. R.Bhargava, J.Cryst.Growth, vol.59, p.15 (1982)

66. A.G.vMilnes and D.L. Feucht, *Heterojunctions and Metal-semiconductor Junctions*, Cargie-Mellon University, Pittsburgh (1976)

67. Y. Tonami, T. Nishino, Y. Hamakawa, T. Sakamoto, and S.Fujita, Jpn. J. Appl. Phys., vol.27, p. L506 (1988)

68. W.L. Bond, Acta. Cryst., vol. 13, p.814 (1960)

69. W.J. Bartels, J. Vac. Sci. Technol., vol. B1(2), p. 338 (1983)

70. P van der Sluis, J. Phys. D: Appl. Phys., vol. 26, p. A188 (1993)

71. PC-MRD User Guide, first edition, Philips (1993)

72. J. Bak-Misiuk, J. Wolf, and U. Pietsch, Phys. Stat. Sol.(a), vol. 118, p. 209 (1990)

73. M. Leszczynski, A. Kulik, and P. Ciepielewski, Phys. Stat. Sol. (a), vol. 119, p. 495 (1990)

74. *Numerical Data and Functional Relationships in Science and Technology*, vol. 17.b, edited by K.H. Hellwege, Springer-Verlag, Berlin-Heidelberg (1982)

75. S. Adachi, J. Appl. Phys., vol.58(3), p. R1 (1985)

76. L.M. Woods, P. Silvestre, P. Thiagarajan, G.A. Patrizi, G.Y. Robinson, K.M. Jones, and M. Al-Jassm, J. Electron. Matl., vol. 23, no.11, p.1229 (1994)

77. W.A. Harrison, *Electronic Structure and Properties of Solids* Freeman, San Francisco, p. 77 (1980)

78. C.G. Van De Walle, K. Shahzad and D.J. Olego, J. Vac. Sci. Technol. B, vol.6, p. 1350 (1988)

79. M. Chandrasekhar and F.H. Pollak, Phys. Rev. B, vol. 15, p. 2127 (1977)

80. F.H. Pollak and M. Cardona, Phys. Rev., vol.172, p.816 (1968)

81. M. Chandrasekhar and F.H. Pollak, Phys. Rev. B, vol.15, p. 2127 (1977)

82. Shizuno Fujita, Y. Kawakami, and Shigeo Fujita, Physica B, vol. 191, p. 57 (1993).

83. C. Choi and N. Otsuka, *Dislocations and Interfaces in Semiconductors*, 1988 TMS annual meeting, Phoenix (1988)

84. S. Guha, H. Munekata and L.L. Chang, J. Appl. Phys., vol. 73, p. 2294 (1993)

85. J. Petruzello, B.L. Greenberg, D.A. Cammack, and R. Dalby, J. Appl. Phys., vol. 63, p. 2299 (1988)

86. C. Choi, N. Otsuka, L.A. Kolodziejski, M.R. Melloch, and R.L. Gunshor, *Dislocations and Interfaces in Semiconductors*, Proceedings of 1988 TMS annual meeting, p. 141 (1988)

87. E.P. Kvam and R. Hull, J. Appl. Phys., vol. 73, p. 7407 (1993)

88. S. Takeuchi, K. Suzuki, and K. Maeda, Philos. Mag. A, vol.50, p.171 (1984)

89. J. Tanimura, O. Wada, T. Ogama, Y. Endoh, and M. Imaizumi, J. Appl. Phys., vol.77, p. 6223 (1995)

90. J. Petruzzello, B.L. Greenberg, D.A. Cammack, and R. Dalby, J. Appl. Phys, vol. 63, p. 2299 (1988)

91. C.Y. Chen and W.M. Stobbs, Inst. Phys. Conf. Ser. no.134, Semicond. Mater. Conf., Oxford (1993)

92. L.H. Kuo, L. Salamanca-Riba, B.J. Wu, G.M. Haugen, J.M. DePuydt, G. Hofler, and H. Cheng, J. Vac. Sci. Technol. B, vol. 13, p. 1694 (1995)

93. W.W. Webb, J. Appl. Phys., vol. 36, p. 214 (1965)

94. J.P. Hirth and J. Lothe, *Theory of Dislocations*, Second Edition, p. 624, John Wiley and Sons, New York (1982)

95. T. Uji, T. Suzuki, and T. Kamejima, J. Appl. Phys., vol.36, p.655 (1980)

96. K. Huang and A.Rhys, Proc. Royal Soc.A, vol. 204, P. 406 (1950)

97. J.F. Wager, J. Appl. Phys., vol. 69, p.3022 (1991)

98. J.A. Van Vechten, J. Electrochem. Soc., vol.122, p.419 (1975)

99. Sorab K. Ghandi, *VLSI Fabrication Principles*, John Wiley & Sons, NewYork, p.18-19 (1983)

100. A.A. Hopgood, J. Appl. Phys., vol.76, p.4068 (1994)

101. J.D. Dow and R.E. Allen, Appl. Phys. Lett., vol. 41, p.672 (1982)

102. P.M. Fahey, P.B. Griffin, and J.D. Plummer, Reviews of Modern Physics, vol. 61, p. 289 (1989)

103. T.O. Sedgwick, A.E. Michel, V.R. Deline, S.A. Cohen and J.B. Lasky, J. Appl. Phys. Vol. 63, p. 1452 (1988)

104. C.H. Henry and D.V. Lang, Phys. Rev. B, vol.15, p. 989 (1977)

105. D.C. Grillo, M.D. Ringle, G.C. Hua, J. Han, R.L. Gunshor, M. Hovinen, and A.V. Nurmikko, J. Vac. Sci. Technol. B, vol.13(2), p.720 (1995)

106. D.V. Lang and L.C. Kimerling, Phys. Rev. B, vol.12, p.3286 (1975)

107. J.D. Weeks, J.C. Tully and L.C. Kimerling, Phys. Rev. B, vol.12, p. 3286 (1975)

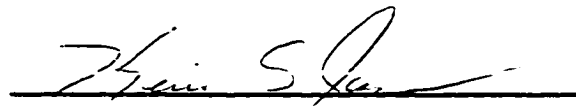108. B. Hu, G. Karczewski, H. Luo, N. Samarth, and J.K. Furdyna, J. Appl. Phys., vol.74, p.4153 (1993)

109. G. Karczewski, B. Hu, A. Yin, H. Luo, and J.K. Furdyna, J. Appl. Phys., vol.75, p.7382 (1994)

110. K. Ando, Y. Kawaguchi, T. Ohno, A. Ohki, and S. Zembutsu, Appl. Phys. Lett, vol. 63, p. 191 (1993)

111. D. Shaw, J. Cryst. Growth, vol.86, p.778 (1988)

112. B.L. Sharma, Defect Diffus. Forum, vol. 64-65, p.77 (1989)

113. C.L. Zipfel, R.H. Saul, A.K. Chin, and V.G. Keramidas, J. Appl. Phys., vol.53, p.1781 (1982)

114. Y. Ichimura, K. Kishino, M. Kuramoto, M. Satake, and A.Yoshida, J. Electron. Mat., vol.24, p. 171 (1995)

115. E. Tournie, C. Morhain, M. Leroux, C. Ongaretto, and J.P. Faurie, Appl. Phys. Lett., vol. 67, p.103 (1995)

116. O. Ueda, Mat. Res. Soc. Symp. Proc., vol.184, p.125 (1990)

117. O. Ueda, S. Komiya, and S. Isozumi, Jpn. J. Appl. Phys., vol.23, p.L241 (1984)

118. L.H. Kuo, L. Salamanca-Riba, B.J. Wu, J.M. DePuydt, G.M. Haugen, H. Cheng, S. Guha, and M.A. Haase, Appl. Phys. Lett., vol.65, p. 1230 (1994)

119. D.C. Grillo, M.D. Ringle, G.C. Hua, J. Han, R.L. Gunshor, and A.V. Nurmikko, J. Vac. Sci. Technol. A, vol.13, p.681 (1995)

120. B.J. Wu, J.M. DePuydt, G.M. Haugen, G.E. Hofler, M.A. Haase, H. Cheng, S. Guha, L.H. Kuo, and L.Salamanca-Riba, Appl. Phys. Lett., vol. 66, p.3462 (1995)

121. J.W. Cahn, Acta Metallurgica, vol.10, p.179 (1962)

122. S. Lee, B. Hillebrands, G.I. Stegeman, H. Cheng, J.E.Potts, and F. Nizzoli, J. Appl. Phys., vol.63, p.1914 (1988)

123. O. Ueda, J. Electrochem. Soc., vol.135, p.11C (1988)

124. S.N.G. Chu, S. Nakahara, M.E. Twig, L.A. Koszi, E.J. Flynn, A.K. Chin, B.P. Segner, and W.D. Johnston Jr., J. Appl. Phys., vol. 63, p.611 (1988)

125. H.S. Carslaw and J.C. Jarger, *Conduction of Heat in Solids*, 2nd ed.,Oxford Univ. Press, London, p.349 (1959)

126. K.H. Hellwege, Landolt-Bornstein: *Numerical Data and Functional Relationships in Science and Technology*, vol. 17, subvolume b, p.149, Springer-Verlag, New York (1982)

127. J.S. Massa, G.S. Buller, A.C. Walker, J. Simpson, K.A. Prior, and B.C. Cavenett, Appl. Phys. Lett., vol.64, p.589 (1994)

128. C. Henry, R.A. Logan, and F.R. Merritt, J. Appl. Phys., vol.49, p.3530 (1978)

129. M. Ettenberg and G.H. Olsen, J. Appl. Phys., vol. 48, p. 4275 (1977)

130. D.B. Laks, C.G. Van de Walle, G.F. Neumark, P.E. Blochl, and S.T. Pantelides, Phys. Rev. B, vol. 45(19), p. 10965 (1992)

131. *Widegap II-VI Compounds for Opto-electronic Applications*, edited by Harry E. Ruda, chap. 11, Chapman & Hall, New York (1992)

132. J. Qiu, J.M. DePuydt, H. Cheng, and M.A. Hasse, Appl. Phys. Lett., vol. 59, p.2992 (1991)

133. *Semiconductors and Semimetals*, vol. 16, p. 35, Academic Press, Inc. New York (1981)

BIOGRAPHIC SKETCH

Lt. Col. Jong Ryul Kim was born on December 1, 1957, in the southern part of the Repulic of Korea. He graduated from Korea Military Academy with a Bachelor of Science in 1980. After graduation he started to serve in the Army as an engineer officer. When he was captain, he was selected to take the officers' advanced course at Ft. Belvoire, the US Army Engineer School. He completed company commander in the 6th Engineer Brigade near the front line in 1986. In the spring of 1987 he enrolled in the department of physics at the US Naval Postgraduate School in California. He was working on flash x-ray generation. In December 1989 he was awarded his Master of Science degree in physics. He went back to Korea and served in the army headquarters. In the fall of 1991, he enrolled in the Department of Materials Science and Engineering at the University of Florida and was admitted as a Ph.D. candidate in January 1994. After graduation he will participate in projects to improve weapon systems for the Korea Army as an active duty officer.

I certify that I have read this study and that in my opinion it conforms to acceptable standards of scholarly presentation and is fully adequate, in scope and quality, as a dissertation for the degree of Doctor of Philosophy.
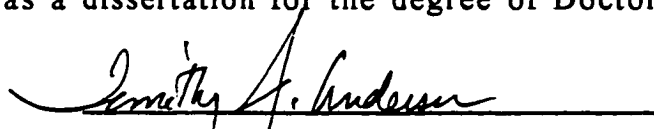
Kevin S. Jones, Chairman
Associate Professor of Materials
    Science and Engineering

I certify that I have read this study and that in my opinion it conforms to acceptable standards of scholarly presentation and is fully adequate, in scope and quality, as a dissertation for the degree of Doctor of Philosophy.
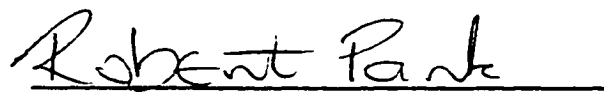
Paul H. Holloway
Professor of Materials Science and
    Engineering

I certify that I have read this study and that in my opinion it conforms to acceptable standards of scholarly presentation and is fully adequate, in scope and quality, as a dissertation for the degree of Doctor of Philosophy.
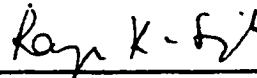
Timothy J. Anderson
Professor of Chemical Engineering

I certify that I have read this study and that in my opinion it conforms to acceptable standards of scholarly presentation and is fully adequate, in scope and quality, as a dissertation for the degree of Doctor of Philosophy.

Robert M. Park
Professor of Materials Science and
    Engineering

I certify that I have read this study and that in my opinion it conforms to acceptable standards of scholarly presentation and is fully adequate, in scope and quality, as a dissertation for the degree of Doctor of Philosophy.
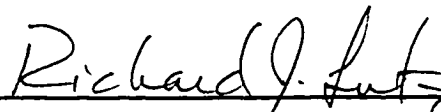
Rajiv K. Singh
Associate Professor of Materials
Science and Engineering

This dissertation was submitted to the Graduate Faculty of the College of Engineering and to the Graduate School and was accepted as partial fulfillment of the requirements for the degree of Doctor of Philosophy.

May, 1996

Winfred M. Phillips
Dean, College of Engineering

Karen A. Holbrook
Dean, Graduate School